

Charles University

Faculty of Science

Ph.D. Study Program: Physical Chemistry



Zahid Ali Zafar

Water-in-Salt Electrolytes for Dual-ion Batteries

Doctoral Thesis

Supervisor: Ing. Jiří Červenka, Ph.D.

Prague, 2023

We the undersigned committee hereby approve the attached thesis,

“Water-in-Salt Electrolytes for Dual-ion Batteries.”

by

Zahid Ali Zafar

Ing. Jiří Červenka, Ph.D.
Senior Scientist
Department of Thin Films and Nanostructures,
FZU - Institute of Physics of the Czech Academy of Sciences
Supervisor

_____, Ph.D.
Professor
Department of Physical and Macromolecular Chemistry,
Charles University in Prague

_____, Ph.D.
Professor
Department of Physical and Macromolecular Chemistry,
Charles University in Prague

_____, Ph.D.
Professor
Department of Physical and Macromolecular Chemistry,
Charles University in Prague

Prof. RNDr. Tomáš Obšil, Ph.D.
Professor and Committee Chairman
Department of Physical and Macromolecular Chemistry,
Charles University in Prague

Declaration of the Originality

I declare that this doctoral thesis has been conducted by me independently and with the use of only cited sources, literature, and professional materials and methods. I confirm that this thesis has not been previously submitted for the purpose of obtaining another academic degree at this or any other institution.

My contributions to the research presented in this thesis are indicated by the authorship order of the publications included and elaborated upon in the "Results and discussion" chapter of the present thesis. Additionally, all literary works referred to in the preparation of this thesis have been appropriately cited.

In Prague, June 2023

Signatures of the author:



Author's Contribution Statement

The following outlines author's contributions to the publications listed in the appendices upon which this thesis is based.

Appendix I: Z.A. Zafar, G Abbas, M Silhavik, K Knizek, O Kaman, FJ Sonia, P Kumar et al. Reversible anion intercalation into graphite from aluminum perchlorate “water-in-salt” electrolyte, *Electrochimica Acta*, 2022, **404**, 139754.

Contribution: Conceptualization, Methodology, Investigation, Formal analysis, Validation, Writing – original draft, Writing – review & editing.

Appendix II: G Abbas, F. J. Sonia, Z.A. Zafar, K Knížek, J Houdková, P Jiříček, M Bouša, Influence of structural properties on (de-) intercalation of ClO_4^- anion in graphite from concentrated aqueous electrolyte, *Carbon*, 2022, **186**, 612-623.

Contribution: Investigation, Formal analysis, Validation, Writing – original draft, Writing – review & editing.

Appendix III: G Abbas, Z.A. Zafar, F.J. Sonia, K Knížek, *et al.*, The Effects of Ultrasound Treatment of Graphite on the Reversibility of the (De)Intercalation of an Anion from Aqueous Electrolyte Solution, *Nanomaterials*, 2022, **12**, 3932.

Contribution: Investigation, Formal analysis, Validation, Writing – original draft, Writing – review & editing.

Appendix IV: Z.A. Zafar, G. Abbas, K. Knizek, M. Silhavik, P. Kumar, P. Jiricek, J. Houdková, et al., Chaotropic anion based “water-in-salt” electrolyte realizes a high voltage Zn–graphite dual-ion battery, *Journal of Materials Chemistry A*, 2022, **10**, 2064-2074.

Contribution: Conceptualization, Methodology, Investigation, Formal analysis, Validation, Writing – original draft, Writing – review & editing.

Zahid Ali Zafar:

Ing. Jiří Červenka, Ph.D (Supervisor)

The work presented in this Doctoral thesis was financially supported by the Czech Science Foundation (GACR, Grant No. 19-23986S and 23-05895S), the Czech Ministry of Education Youth and Sports (MEYS) and European Structural and Investment Funds (SOLID21 – CZ.02.1.01/0.0/0.0/16_019/0000760 and CARAT – CZ.02.1.01/0.0/0.0/16_026/0008382), and the Czech Academy of Sciences.

Abstrakt (Czech)

Vodné elektrolyty nabízejí vysokou bezpečnost, vysokou iontovou vodivost a nízké náklady, což je činí velmi atraktivními pro systémy skladování elektrochemické energie. Nicméně jejich největším úskalím je velmi úzké potenciálové okno elektrochemické stability vody (1,23 V), mimo které se voda začne rozkládat na vodík a kyslík. To omezuje výběr vhodných elektrodových materiálů a dosažitelnou energetickou hustotu v těchto vodných systémech. Například vodné multivalentní baterie na bázi hliníku a zinku, které slibují vysokou hustotu energie díky multivalentní redoxním reakcím kovových iontů (Al^{3+} , Zn^{2+}), v reálu vykazují mnohem nižší hustotu energie kvůli malému potenciálovému oknu vodných elektrolytů, které neumožňuje použití vysokonapěťových katod.

V této dizertační práci jsou studovány vodné elektrolyty založené na konceptu voda v soli (WiSE) a řešena problematika nízkého elektrochemického potenciálového okna ve vodných elektrolytech v multivalentních kovových bateriích. V práci je ukázáno, že ve WiSE elektrolytech dochází k výrazné modifikaci struktury vody a rozšíření potenciálového okna v důsledku minimalizace obsahu volných molekul v těchto roztocích. Jsou studovány též vlastnosti aniontů při expanzi potenciálového okna s ohledem jejich umístění v Hofmeisterově řadě, která třídí anionty dle jejich vlivu na strukturu vody. Tato práce demonstruje, že chaotropní (hydrofobní) anionty rozšiřují elektrochemické potenciálové okno v důsledku omezení molekul vody v solvatačních obalech kationtů. Na druhou stranu kosmotropní (hydrofilní) anionty mají negativní dopad na potenciálové okno, protože narušují solvatační obal protikationtů. V důsledku toho jeví WiSE elektrolyty založené na vysoké koncentraci chaotropních chloristanových aniontů široké potenciálové okno, které je 4 V pro elektrolyty na bázi Al a 2,8 V pro elektrolyty na bázi hliníku, čímž překonávají výrazně termodynamický limit pro rozklad vody. Široké potenciálové okno WiSE elektrolytů má též výhodu, že umožňuje použít vysokonapěťové grafitové katodové materiály, což není možné s konvenčními vodnými elektrolyty.

V práci byla zkonstruována a prozkoumána vysokonapěťová Zn-grafitová duální iontová (ZnG-DIB) baterie využívající WiSE elektrolyt na bázi $\text{Zn}(\text{ClO}_4)_2$. V rámci baterie bylo ukázáno, že dochází k reverzibilní elektrochemickému pozinkování a odleptání při minimálním přepětí a reverzibilní interkalaci chloristanových aniontů do grafitu s vysokou coulombickou účinností. ZnG-DIB baterie poskytuje vysoké napětí 1,95 V, vybíjecí kapacitu 45 mAh g^{-1} při

100 mA g⁻¹ a živssotnost po více než 500 cyklů. Výsledky této práce přináší nové poznatky, které pomohou při vývoj systémů pro ukládání elektrochemické energie, zejména pro vývoj levných, bezpečných a vysokonapěťových duálních iontových baterií.

Klíčová slova:. elektrolyt voda v soli; duální iontové baterie, interkalace aniontů, chaotropní aniont

Abstract

Aqueous electrolytes offer high intrinsic safety, high ionic conductivity, and low costs, which makes them very attractive for electrochemical energy storage systems (EESS). Nevertheless, their biggest bottleneck is the narrow electrochemical stability window (ESW) of water of 1.23V, beyond which water undergoes hydrogen and oxygen evolution reactions. This restricts the choice of electrode materials within the H₂ and O₂ evolution potentials and limits the achievable energy and power densities of aqueous-based EESS. For instance, aqueous multivalent aluminum- and zinc-based batteries promise high energy density due to the multivalent redox chemistry of metal-ions (Al³⁺, Zn²⁺), but they exhibit much lower energy density owing to the small ESW of the aqueous electrolytes, which does not allow using high-voltage cathodes.

In this thesis, the issue of the narrow ESW for these multivalent batteries has been addressed by using the concept of “water-in-salt” electrolytes (WiSE). This concept is based on using high concentrations of salts in aqueous electrolytes, which results in strong modifications of the water structure and widening of the ESW by restricting the free water content in WiSE. More importantly, the role of anion in the expansion of ESW has been investigated based on the Hofmeister series, which sorts different anions according to their effect on the water structure. The present thesis demonstrates that the chaotropic (hydrophobic) anions increase the ESW by confining the water molecules in the solvation shells of the cations. On the other hand, kosmotropic (hydrophilic) anions have a negative impact on the ESW by disturbing the solvation shell of the counter-cations. Consequently, Al- and Zn-based WiSE containing highly chaotropic ClO₄⁻ anion demonstrated wide ESW of 4 V and 2.8 V, respectively, which are way beyond the thermodynamic limit of water decomposition. The expanded ESW enabled using high-voltage graphite cathodes in the WiSE systems, which has not been possible with the conventional aqueous electrolytes.

A high voltage Zn-graphite dual-ion battery (ZnG-DIB) based on Zn(ClO₄)₂ WiSE has been constructed and investigated. The battery demonstrates a reversible Zn plating/stripping with minimum overpotential, and ClO₄⁻ anion intercalation into the graphite with high stability and high Coulombic efficiency. The ZnG-DIB has delivered a discharge capacity of 45 mAh g⁻¹ at 100 mA g⁻¹ with a high mean discharge voltage of 1.95 V and a cycle life of over 500 cycles.

This has significant implications for the development of electrochemical energy storage systems, particularly for low-cost, safe, and high-voltage DIBs.

Key Words: water-in-salt electrolytes; dual-ion batteries; anion-intercalation; chaotropic anion

Contents

| | |
|--|----|
| Abstrakt (Czech)..... | 11 |
| Abstract..... | 14 |
| Contents | 17 |
| Acknowledgements | 22 |
| List of Abbreviations and Symbols | 24 |
| List of Figures | 27 |
| 1 Aims and structure of the thesis..... | 29 |
| 2 Introduction..... | 30 |
| 2.1 Dual-ion batteries (DIBs): An overview..... | 31 |
| 2.2 Electrolytes for DIBs | 33 |
| 2.3 Electrodes for DIBs..... | 38 |
| 2.4 Graphite and Graphite Intercalation Compounds (GICs) | 40 |
| 3 Results and discussion | 45 |
| 3.1 Al- and Zn- perchlorate-based WiSE..... | 45 |
| 3.1.1 Characterization of WiSE..... | 46 |
| 3.2 Half-cell studies of perchlorate anion intercalation into graphitic materials from Aluminum-WiSE | 50 |
| 3.3 Zn-graphite dual-ion battery based on Zn-perchlorate WiSE | 58 |
| 3.3.1 Stripping plating of Zn | 58 |
| 3.3.2 Performance of full-cell..... | 60 |
| 4 Conclusions | 64 |
| References | 67 |
| Complete list of journal publications..... | 75 |
| Conference proceedings..... | 77 |
| Patents | 78 |
| List of Appendices..... | 79 |

| | |
|-----------------------|-----|
| Appendix I..... | 80 |
| Appendix II | 90 |
| Appendix III..... | 103 |
| Appendix IV..... | 118 |
| Curriculum Vitae..... | 130 |

Dedication

To my grandfather, who had great insight,
And taught us the power of determination right.
Though he couldn't read or write,
He planted education's seed to ignite.

To my dear parents, my greatest source of light,
Your unwavering love kept me in flight,
Through ups and downs, you were always there,
My success I owe to your constant care.

To all those who believed in me,
Encouraged and pushed me to be,
The best version of myself, day by day,
Your faith and trust, I will always display.

This thesis is a tribute to you all,
For every time you picked me up when I'd fall.
I dedicate this work to your names,
And hope to honor your legacies with my future gains.

Acknowledgements

I would like to take this opportunity to express my heartfelt gratitude to all those who have contributed toward the completion of my PhD.

First and foremost, I would like to express my sincere appreciation to my supervisor, Dr. Jiri Cervenka, for his invaluable guidance, unwavering support, and encouragement throughout my research journey. His mentorship and expertise have been instrumental in shaping my professional and personal growth.

I would also like to extend my gratitude to my colleagues Martin Silhavič and Prabhat Kumar, who have been my constant companions, providing both technical and moral support. Martin's support, particularly in social matters, as a local has been invaluable. I am also grateful to my other colleagues and friends who have provided their support and encouragement during this journey and stay in the Czech Republic, and whose friendship has enriched my life in countless ways.

To my family, especially my parents, I owe an immeasurable debt of gratitude for their steadfast love, unwavering encouragement, and constant support. Their guidance and motivation have been the driving force behind my success. To my loving wife, whose unwavering support and patience have been my anchor through all the highs and lows of my PhD journey, and to my daughter, whose smiles have brought me boundless joy and happiness even during the most challenging times, I am eternally grateful.

Finally, I would like to acknowledge the financial support received from the Czech Science Foundation (GACR), the MEYS and European Structural and Investment Funds (SOLID21 and CARAT projects), and Charles University in Prague. Without their support, this study would not have been possible.

Thank you all for your kindness, support, and encouragement. Your contributions have been invaluable, and I will always cherish them as a source of inspiration and motivation.

Zahid Ali Zafar

In Prague, June 2023

List of Abbreviations and Symbols

| Abbreviation | Description |
|----------------------------|------------------------------------|
| ESS | Energy storage systems |
| LIBs | Li-ion batteries |
| DCBs | Dual-graphite batteries |
| DIBs | Dual-ion batteries |
| ZnG-DIB | Zn-graphite dual-ion battery |
| GICs | Graphite intercalation compound |
| ILs | Ionic liquids |
| ESWs | Electrochemical stability windows |
| WiSE | Water-in-salt electrolyte |
| WiBS | Water-in-bisalt electrolyte |
| DoG | Degree of graphitization |
| CEI | Cathode-electrolyte interphase |
| SEI | Solid-electrolyte interphase |
| BET | Brunauer-Emmett-Teller |
| ClO_4^- | Perchlorate anion |
| CF_3SO_3^- | Triflate anion |
| AlCl_4^- | Aluminum trichloride |
| PF_6^- | Hexafluorophosphate |
| BF_4^- | Tetrafluoroborate |
| VC | Vinylene carbonate |
| VEC | Vinyl ethylene carbonate |
| ES | Ethylene sulfite |
| CEC | Chlorethylene carbonate |
| PC | Propylene carbonate |
| EC | Ethylene carbonate |
| DMC | Dimethyl carbonate |
| EMS | Ethyl methanesulfonate |
| EMC | Ethyl methyl carbonate |
| FEC | Fluoroethylene carbonate |
| SL | Sulfolane |
| MP | Methyl propionate |
| PVDF | Polyvinylidene fluoride |
| PTFE | Polytetrafluoroethylene |
| NMP | N-methyl-2-pyrrolidone |
| MOF | Metal-organic frameworks |
| CV | Cyclic voltammetry |
| LSV | Linear cyclic voltammetry |
| C.E. | Coulombic efficiency |
| Pyr14^+ | 1-butyl-1-methylpyrrolidinium |
| TFSI | bis(trifluoromethanesulfonyl)imide |
| LiOTf | trifluoromethanesulfon |
| HOPG | Highly oriented pyrolytic graphite |

| | |
|------|------------------|
| NG | Natural graphite |
| KG | Kish graphite |
| D.I. | Deionized water |
| GP | Graphite paper |

| Symbols | Description |
|------------------------------|-------------------------------------|
| λ | Wavelength |
| θ | Angle of incidence |
| σ | Ionic conductivity |
| Å | Ångström (10^{-10} m) |
| i | Peak currents |
| v | Scan rate |
| α, β and γ | (Inter)intralayer hopping integrals |

List of Figures

| | |
|--|----|
| Figure 2.1 Working mechanism of dual-ion batteries vs. "rocking-chair" batteries..... | 33 |
| Figure 2.2. Electrolyte stability window (ESW) illustration. | 34 |
| Figure 2.3. Pourbaix diagram for water decomposition potentials with respect to pH values.. | 37 |
| Figure 2.4. Illustration of the expanded ESW achieved by WiSE, demonstrated by LiMn_2O_4 cathode and Mo_6S_8 anode..... | 38 |
| Figure 2.5. Schematic presentation of the reported anode/cathode materials for DIBs..... | 39 |
| Figure 2.6. Structures of graphite and effect of heat-treatment on the degree of graphitization, and its cation/anion intercalation capacity..... | 41 |
| Figure 2.7. Schematic illustration of Rüdorff and Daumas–Hérolld models for the staging mechanism of ion intercalation into graphite. | 43 |
| Figure 3.1. Hofmeister Series of anions and cations..... | 45 |
| Figure 3.2. ESW of $\text{Al}(\text{ClO}_4)_3$ -WiSE, and $\text{Zn}(\text{ClO}_4)_2$ -WiSEs | 46 |
| Figure 3.3 Water-ion interaction energy as function of the ions charge density..... | 47 |
| Figure 3.4 Raman spectra OH-stretching vibrations region of pure water vs WiSE systems. 48 | |
| Figure 3.5 Temperature dependence of ionic-conductivity of $\text{Al}(\text{ClO}_4)_3$ - and $\text{Zn}(\text{ClO}_4)_2$ -WiSE | 50 |
| Figure 3.6. Long-cycling test up to 2000 cycles of $\text{Al}(\text{ClO}_4)_3$ -WiSE half cell.. | 51 |
| Figure 3.7. Operando- XRD for HOPG in $\text{Al}(\text{ClO}_4)_3$ -WiSE half cell.. | 52 |
| Figure 3.8 The CV kinetic analysis for ClO_4^- (de-)intercalation into NG and KG. | 56 |
| Figure 3.9. CV and (dis)charge curves of NG and US-NG in $\text{Al}(\text{ClO}_4)_3$ -electrolyte..... | 57 |
| Figure 3.10.Stripping/plating analysis of Zn^{2+}/Zn from 8 <i>m</i> $\text{Zn}(\text{ClO}_4)_2$ -WiSE..... | 59 |
| Figure 3.11.Schematic of a Zn-graphite dual-ion battery (ZnG-DIB) working mechanism... 60 | |
| Figure 3.12 Charge-discharge and cycling performance of ZnG-DIB. | 62 |
| Figure 3.13.Schematic of anion (de)intercalation (from)into graphite on (dis)charging, and <i>Operando</i> -XRD results of a ZnG-DIB..... | 63 |

1 Aims and structure of the thesis

This work was done within the doctoral program at the Faculty of Science, Charles University in Prague, and conducted at the FZU – Institute of the Physics of the Czech Academy of Sciences in Prague.

The present thesis aims to design and investigate safe, non-flammable, and low-cost electrolytes with a wide electrochemical stability window for aqueous dual-ion batteries. It investigates fundamental electrochemical processes in highly concentrated aqueous electrolytes. Furthermore, it studies the interactions, electrochemical kinetics and charge-storage mechanisms of high voltage electrodes in the electrolytes and dual-ion batteries by means of electrochemical, ex-situ, and operando-spectroscopic techniques.

The text of this thesis is organized into an introduction, results and discussions, conclusions, and appendices. The chapter on results and discussions is based on the original findings of the author, which are based on articles either authored or co-authored by the author of this thesis. Each section of this chapter begins with a brief overview of the main results, followed by the enclosed as-published publications embedded in the *Appendices*.

Chapter 2 presents the introduction of the present thesis. It provides an overview of the dual-ion batteries, their working principle, and a historical overview of their development. It summarizes important components of DIBs, including electrodes and electrolytes.

Chapter 3 presents a summary of the key-results of the author's publications. The chapter has been divided into 3 main sections. *Section 3.1* presents the electrochemical and physical properties of the Zn and Al-based water-in-salt electrolytes (WiSEs). *Section 3.2* showcases the results of the half-cell studies of the graphite-based materials in an Al-based WiSE. *Section 3.2* demonstrates the results of the stripping/plating of Zn and a zinc-graphite dual-ion battery (ZnG-DIBs) based on Zn-perchlorate WiSE.

Chapter 4 provides a conclusion to the experimental findings of this work and suggests prospects of the work.

Appendices provide the published articles on which the present thesis is based, a list of the publications, patents, and conference, and finally a complete curriculum vitae of the author is provided.

2 Introduction

The energy transition from fossil fuels to intermittent renewable resources involves indispensable component – batteries – for its storage and utilization in modern-life applications, such as electric vehicles (EVs) and energy storage systems (ESS) ¹. Rechargeable batteries have been proven to be the most feasible and efficient due to the success of Li-ion batteries (LIBs) which were first commercialized by SONY in 1991 ². These batteries are widely used in portable electronic devices, EVs, and ESS due to their high energy density, low self-discharge, and long lifespan ³. However, LIBs can also be dangerous if not handled properly and have been known to catch fire or explode if damaged or overcharged. The main culprit involved in the fire hazard of LIBs is the organic electrolytes ^{4,5}. Furthermore, current LIBs utilize critical materials like cobalt, nickel, and lithium itself which are geographically less distributed, hard to recycle, toxic, prone to environmental hazards, and involve exploitation of labor ⁶⁻¹⁰. The electrochemical energy storage demand is forecasted to exponential growth, whereby 2022 demand levels are expected to double by 2050 ^{11,12}. Further, uneven distribution of critical battery raw materials can critically affect the supply chain due to different geopolitical conflicts, for instance, Russia's war in Ukraine. Prices of raw materials such as cobalt, lithium, and nickel have surged seven times higher than at the start of 2021 ¹². This means a battery based on non-sustainable and less abundant elements will not be able to cope with future energy storage demands. Therefore, electrochemical energy storage systems based on sustainable materials with global abundance and safety would be an appropriate substitute to current LIBs.

Rechargeable multivalent metal batteries, such as those using Zn, Ca, or Al, meet these merits for the development of high-energy-density and sustainable EESS ^{13,14}. However, practical applications of these batteries are hindered by several issues, such as low electrochemical reversibility, dendrite growth, sluggish multivalent-ion kinetics, and gas-evolution in (non)aqueous electrolytes ¹⁵. Dual-ion battery (DIB) concepts that employ different combinations of multivalent metal and non-metal ions to overcome these challenges can be a viable option ¹⁶. Furthermore, the development of safe batteries is also impeded by the flammability of organic solvent-based electrolytes. Ionic liquids and solid-state electrolytes are considered to mitigate the issues of flammability, low stability window, and dendrites, however, each of these has its own drawback. For instance, ionic liquids are costly and often toxic, while solid-state electrolytes have low ionic conductivity at ambient temperatures ¹⁷.

Aqueous electrolytes offer high safety and ionic conductivity but suffer from low operating voltages due to the narrow electrochemical stability window of water¹⁸. Therefore, it is crucial to develop new, improved non-flammable electrolytes that do not possess these issues and offer a wide-electrochemical stability window.

The present thesis is focused on non-flammable and low-cost electrolytes for beyond-Li secondary batteries, specifically on multivalent DIBs. In the next section, an overview of DIB concepts will be presented along with their components, like electrolyte and cathodes, their status, and prospects. *Chapter 3* will showcase the summaries of the main results, which have been published in peer-reviewed scientific articles provided in *Appendices I-IV*. Finally, the conclusion of the thesis will be given along with the prospects of the current study.

2.1 Dual-ion batteries (DIBs): An overview

The batteries that can be recharged by applying electrical current to reverse the chemical reactions that occur during discharge are known as secondary batteries or rechargeable batteries. On the other hand, primary batteries can only be used once and then discarded. Some common examples of secondary batteries include nickel-cadmium batteries, lead-acid batteries, and LIBs¹⁹.

LIBs use lithium ions (Li^+) as the charge-carrying particles. LIBs, like all other batteries, consist of a positive electrode, a negative electrode separated by a dielectric material (an electronic insulator but ionic conductor material), and an electrolyte. They work by using the migration of Li^+ ions, also known as the “rocking-chair mechanism” between the electrodes through the electrolytes to store and supply energy^{20,21}. Currently, rechargeable LIBs do not contain lithium metal, due to dendrite formation that makes Li metal not safe as an anode²². However, in recent years tremendous efforts have been made to use Li metal as an anode in batteries because of its high specific capacity (3862 mAh g^{-1}), and lowest reduction potential (-3.04 vs SHE)²³. Alternatively, graphite as an anode is used in commercial LIBs as it forms a reversible Li^+ intercalated compound (LiC_6) with a theoretical maximum capacity of 372 mAh g^{-1} ²⁴. On the cathode side, Li^+ ions are (de)intercalated from layered metal oxides, for instance, LiCoO_2 , or others^{24,25}.

In contrast to LIBs, DIBs can avoid the use of critical materials which are precious, environmentally harmful, or difficult to recycle, such as nickel and cobalt. DIBs use two different types of ions to store and release electrical energy^{21,26}. This allows the development

of more advanced battery systems with improved performance and safety characteristics. Principally, DIBs differ from the “rocking-chair” LIBs and others involving similar mechanisms like sodium and potassium-ion batteries. **Figure 2.1** displays the difference between traditional LIBs and DIBs. In DIBs, one type of ion is used for the positive electrode, and another type of ion is used for the negative electrode ^{4,27}. Further, the electrolyte serves as an active material in DIBs, and both cations and anions of the electrolyte participate in energy storage and supply ¹⁵. Briefly, during the charging, both the cations and anions from the electrolyte incorporate into the anode and cathode, respectively. They are released from the electrodes into the electrolyte during discharge. Therefore, electrolytes are the key components in DIBs.

The term “dual-ion battery” was first proposed by Winter *et al.* in 2012 and is inspired by dual-graphite batteries (DCBs) where both positive and negative electrodes are based on graphite ^{3,28}. Such batteries are based on the concept of graphite intercalation compounds (GICs), which will be described in detail in **section 2.4**. The history of DIBs can be traced back to the discovery of GICs of the acceptor type ²⁹. In 1938, Rudolf and Hofmann investigated the process of intercalation of anions into graphite using a concentrated sulfuric acid electrolyte ³⁰. In the 1970s, Armand and Touzain conducted a systematic study of the electrochemical properties of acceptor-type GICs, paving the way for their later use in DIBs ³¹. Around the same time, Dunning *et al.* successfully achieved reversible intercalation of anions such as ClO_4^- , BF_4^- , and CF_3SO_3^- into graphite using a Li/graphite cell ^{32,33}. The inception of the concept of utilizing GICs in a non-aqueous electrolyte for battery applications was first proposed by McCullough *et al.* in their patent of 1989 ²⁸. The feasibility of this idea was later demonstrated by Carlin *et al.* in 1994, utilizing a molten salt electrolyte and graphite as the positive and negative electrodes ³⁴. In recent years, there has been a surge in interest in DIBs among researchers, owing to their potential advantages over traditional LIBs and the possibility of combining multiple ionic chemistries ³⁵. In 2014, a liquid electrolyte-based DIB was successfully developed, showcasing stable cycling ^{36,37}, and in 2015, Dai *et al.* reported the use of an ionic-liquid (IL) electrolyte in an Al-graphite DIB, which exhibited reversible intercalation of AlCl_4^- anions at the graphite cathode ³⁸.

Recently, the working concept of DIBs has been applied to other abundant metals including Na, K, Zn, Al, Mg, etc. ³⁹⁻⁴⁹. However, most of the reported work is based on non-aqueous electrolytes ^{50,51}. More recently, aqueous-based dual-ion systems have been developed such as

anion conversion-based and reverse DIB, and from our group Al- and Zn-based aqueous dual-ion battery systems^{15, 18, 52, 53}.

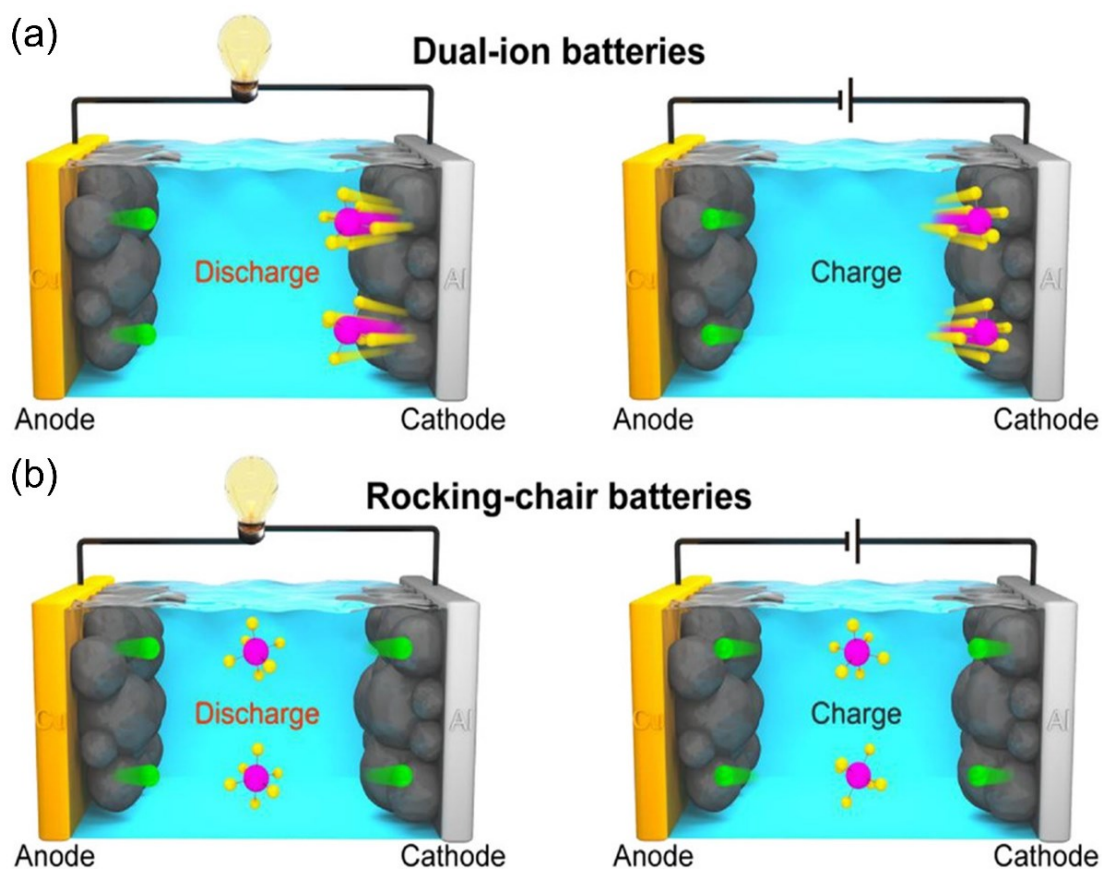


Figure 2.1 Schematic working mechanism of dual-ion batteries vs. conventional "rocking-chair" batteries,²⁷.

2.2 Electrolytes for DIBs

Designing electrolytes for DIBs is a critical aspect, as the electrolyte supplies active ions for energy storage and serves as the charge transfer medium during operation. The electrolyte's stability at high oxidizing potentials is the most significant contributing factor, as such stability is intrinsic to the solvent or achieved through electrolyte engineering⁵⁴. The electrochemical stability window (ESW) is defined as the difference between the highest occupied and lowest unoccupied molecular orbitals of the electrolyte, as illustrated in **Figure 2.2**. The electrolyte is oxidized when the cathode's electrochemical potential is below the highest occupied molecular orbital (HOMO), and the electrolyte is reduced when the anode's electrochemical potential is above the lowest unoccupied molecular orbital (LUMO) of the electrolyte^{55, 56}.

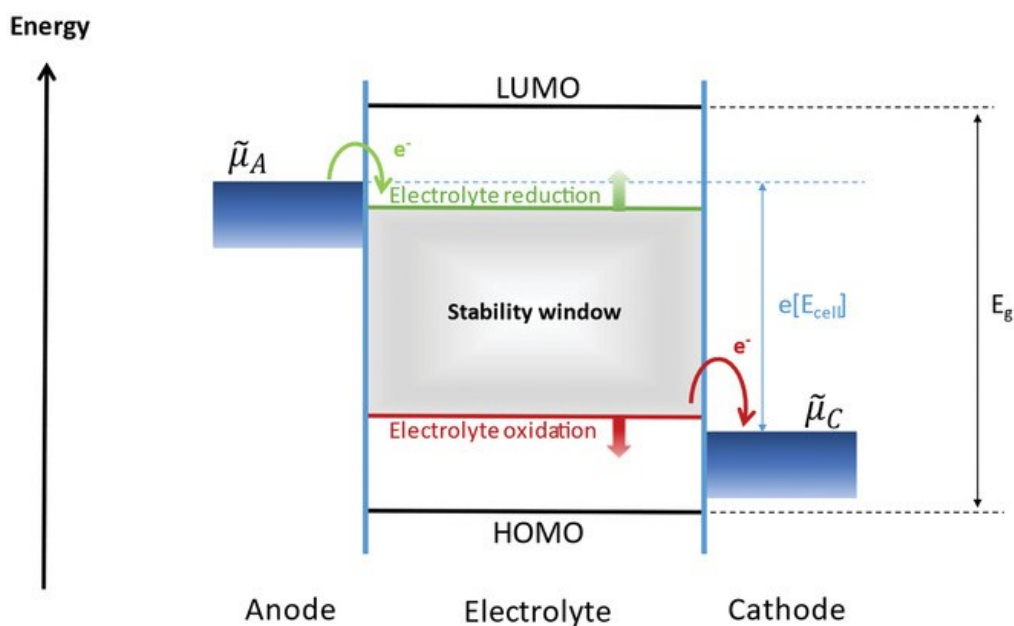


Figure 2.2. Electrolyte stability window, illustrating the ranges for electrolyte reduction at negative potentials and oxidation at positive potentials ^{56, 57}.

Electrolyte composition requires careful consideration when designing DIBs, given that the electrolyte supplies the active ions for energy storage whilst simultaneously serving as the charge migration medium during operation. The main contributing factor is the stability of the electrolyte at high oxidizing potentials (> 4.5 V vs. Li^+/Li) for anion intercalation at cathodes (for instance, graphite), such high oxidative stability is imperative and can be intrinsic to the solvent or achieved through the electrolyte design as mentioned earlier.

A plethora of solvents, salts, and additives are available for DIBs to withstand high voltage and ensure stable electrochemical behavior with graphite-and other positive electrodes ^{58, 59}. The high working potential of both DIBs and conventional LIBs presents a challenge for electrolyte compatibility. Electrolytes and additives have been extensively studied that are compatible with these high potentials in conventional LIBs ⁶⁰. This research can serve as a reference for selecting appropriate electrolytes for reversible cyclic processes in DIBs. Strategies such as highly concentrated electrolytes IL electrolytes can be utilized to create a wide electrochemically stable range for DIBs. Below is provided a summary of different electrolytes systems utilized in (non)aqueous DIBs.

Organic solvents and additives-based electrolytes:

Organic solvents are a practical and feasible option for commercializing DIBs due to their long history of use in LIBs, variety, low cost, comparatively high ionic conductivity, and ability to

form an SEI layer for protection ^{4, 61}. However, using organic solvents in DIBs faces a major challenge of stability under high oxidizing potentials for anion uptake into the positive electrodes. This potential exceeds the upper limit of frequently used electrolytes in LIBs, causing the electrolyte to oxidize and decompose ⁶². Additionally, other factors, such as the stability of the decomposition interphase layer on electrode surfaces, electrolyte ionic conductivity, wettability with electrodes and separator, and thermal stability, also affect cell performance ⁶³. To improve performance and ensure good cyclic stability/reversibility solvent/additive compositions are being explored extensively. Several solvents and additives have been tested to improve the stability and cyclic performance of DIBs ^{58, 64, 65}. Examples of these include propylene carbonate (PC), ethylene carbonate (EC), dimethyl carbonate (DMC), ethyl methanesulfonate (EMS), ethyl methyl carbonate (EMC), methyl propionate (MP), and fluoroethylene carbonate (FEC), sulfolane (SL), etc ^{62, 63, 66}. Among them, EMC is a promising solvent due to its high stability towards reduction and low viscosity, making it suitable for the smooth intercalation of anions (PF_6^-) into graphite. However, EMC has a compatibility issue with BF_4^- anions, which exhibit sluggish mobility and high initial intercalation voltage into the graphite electrode ^{4, 67}.

To improve cyclic stability, highly concentrated electrolytes are used to enhance anodic and cathodic stability, improve the uniformity of the electrode-electrolyte interface layers, and suppress the corrosion of current collectors ⁶⁸. Although this approach results in a loss of ionic conductivity and increased costs, it has shown good performance ⁶⁹. For instance, using a high concentration of 2 M $\text{LiPF}_6/\text{EMC}:\text{SL}$ (1:4, V:V) as the electrolyte and graphite as both electrodes, over 94% of the initial capacity was retained after 1000 cycles at a high rate of 5C ⁷⁰. Furthermore, higher oxidization stability by using highly concentrated electrolytes allows higher working potential and higher salt concentration could improve the specific capacity to some extent, contributing to the higher energy density of cells ⁶⁰.

Ionic liquids-based electrolytes:

Ionic liquids (ILs) are a promising alternative to organic solvents for use in high-voltage DIBs due to their wide ESW range and other advantageous properties, such as excellent thermal stability, non-flammability, low volatility, and a broad liquid range with ionic conductivity comparable to that of organic solvents ^{59, 71}. However, the use of ILs in DIBs requires addressing compatibility issues with graphite-negative electrodes due to the formation of a thinner SEI layer compared to organic solvent-based electrolytes ³⁷. One solution is to add

electrolyte additives, such as vinylene carbonate (VC), vinyl ethylene carbonate (VEC), fluoroethylene carbonate (FEC), chlorethylene carbonate (CEC), and ethylene sulfite (ES), etc., which assist in the formation of a thicker SEI layer on the negative electrode surface via electrochemical reduction-polymerization⁷². A DIB based on IL electrolyte was reported in 2014 with stable cycling^{36,37}. Further, IL based electrolytes have extensively been reported for Al-graphite based batteries since 2015⁷³⁻⁷⁶. However, the use of ILs brings up issues related to cost and sustainability.

Aqueous electrolytes:

Non-aqueous electrolytes, specifically organic and ILs electrolytes, are utilized in DIBs and LIBs due to their wide ESW. However, the drawbacks of these electrolytes, including slow ion diffusion, high cost, safety concerns, and environmental pollution, necessitate the development of new and improved electrolytes³⁵. Aqueous electrolytes, on the other hand, are a promising alternative due to their low cost, ease of handling, and high ionic conductivity^{77,78}. However, the narrow ESW of aqueous electrolytes is a major limitation, resulting from the low thermodynamic decomposition potential of water (1.23 V), **Figure 2.3**⁷⁹. Although the overpotential for redox-process and adding salts to a diluted solution can extend the stability window to ~1.5 V, aqueous systems still fall short when compared to organic electrolytes⁸⁰. Therefore, the Li-aqueous batteries introduced by Dahn in 1994 have not been commercialized⁸¹.

Another approach to address this limitation is to reduce the working potential of anion-hosting materials, such as alternative positive electrode materials like metal-organic frameworks (MOF), polycyclic aromatic hydrocarbons (PAH), and p-type organic materials that exhibit lower working potentials than graphite⁸². However, this approach sacrifices working voltage and potential for increased energy density⁸³. To address the limitations of aqueous electrolytes, Suo *et al.* proposed the use of superconcentrated aqueous electrolytes with a salt concentration of 21 mol kg⁻¹, known as water-in-salt electrolytes- (WiSE), in 2015⁸⁴. WiSE are high-concentration salt solutions in water used in batteries to increase their efficiency and safety. This approach allowed for an expansion of the operating potential window to 3 V while maintaining ionic conductivity similar to that of conventional organic electrolytes (approximately 10 mS cm⁻¹). The authors demonstrated the feasibility of this approach by creating a 2.3 V battery with Mo₆S₈ and LiMn₂O₄ as the negative and positive electrodes, respectively, **Figure 2.4**.

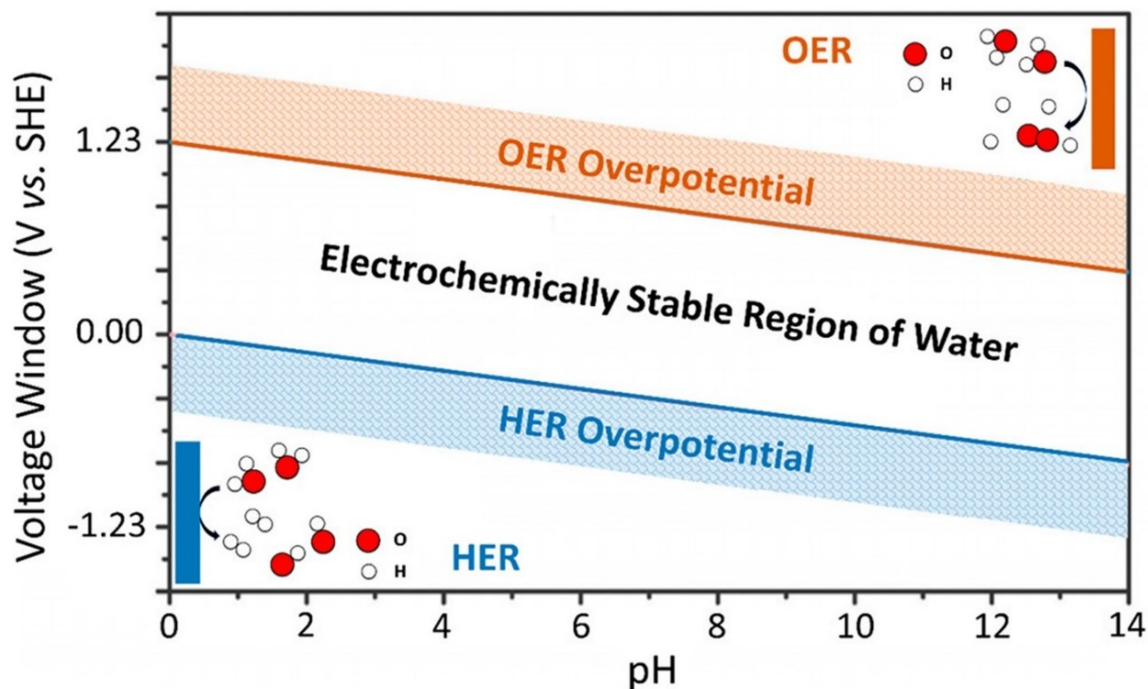


Figure 2.3. Pourbaix diagram for water showing pH values of aqueous electrolytes and their corresponding potentials (V vs SHE) on the y-axis, with upper and lower thermodynamically stable potentials represented by orange and blue lines. Areas above and below the lines indicate overpotentials for water oxidation and reduction,⁸⁰

Building on this work, Yamada *et al.* later reported that combining two organic lithium salts to form a water-in-bisalt electrolyte (WiBS) could enable the assembly of aqueous batteries with a working potential as high as 3.1 V⁸⁵. However, the limited energy density resulting from the low working potential of electrodes and electrolytes remains a significant obstacle to the further development and widespread application of aqueous electrolytes. To use the high voltage of graphite, Wang *et al.* developed a WiBS electrolyte containing 21 mol kg⁻¹ LiTFSI and 7 mol kg⁻¹ LiOTf dissolved in water. They used a composite of lithium halide salts (LiBr and LiCl) and graphite with a mass ratio of 2:1:2 as the positive electrode material. Both lithium halide salts in the electrode form a hydrated layer on the electrode surface, which supports the fast diffusion of Li⁺ and helps reserve anions within the electrodes. The Br⁻ and Cl⁻ intercalate into graphite inter- layers in sequence during charging and de-intercalate in reverse sequence during discharging with an average potential of 4.2 V⁸⁶.

In summary, to achieve stable and reversible cycling in DIBs using graphite as a positive electrode, it is important to find electrolytes that can withstand high working potential and develop well-engineered high-voltage electrodes. Further, it is crucial to find a balance between the amount of excess salt added and the performance output, as adding an excessive amount of

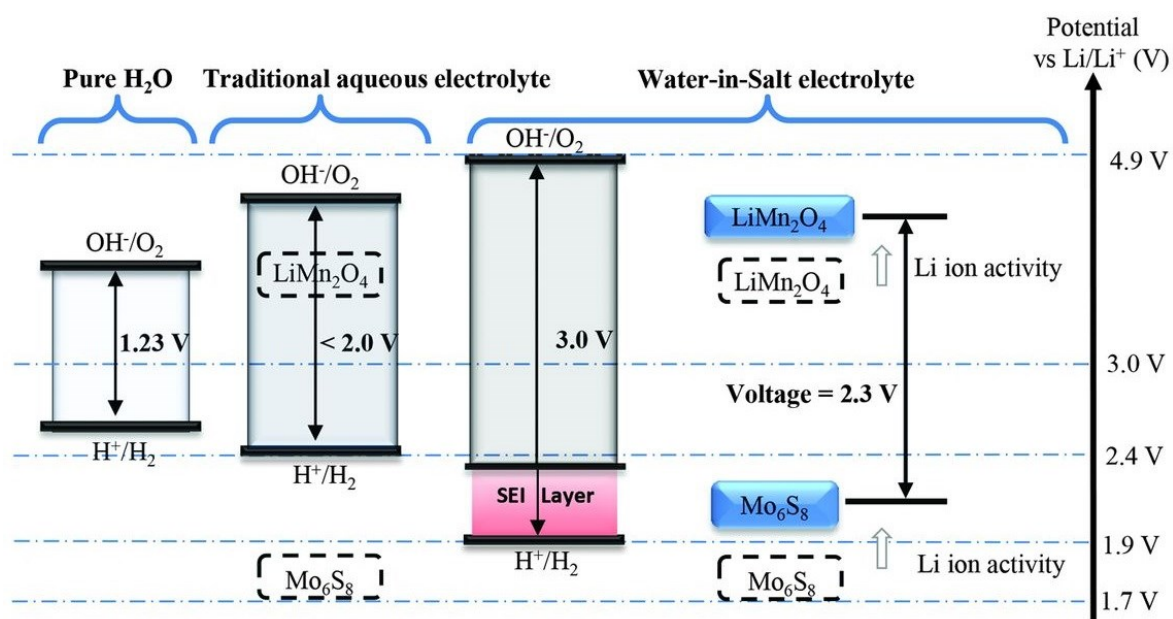


Figure 2.4. Illustration of the expanded electrochemical stability window achieved by WiSE, demonstrated by LiMn_2O_4 cathode and Mo_6S_8 anode,⁸⁴.

salt can lower the energy density of the cell and ionic-conductivity and increase the cost of the electrolyte. Aqueous electrolytes are a promising option because they allow anions intercalation at relatively low voltage and have advantages like high conductivity, sustainability, and low cost. However, a major disadvantage of aqueous electrolytes is their narrow ESW, which limits their energy and power capabilities. This issue still needs to be well-addressed for attaining practical high-energy density aqueous batteries⁸⁷.

2.3 Electrodes for DIBs

As described, in DIBs both anions and cations are involved in the energy storage process. The choice of anode and cathode materials depends on the available charge-carrying ionic species in electrolytes and properties of electrolytes, for instance, ESW, ionic conductivity, etc.²⁴. The reductive (cathodic) stability of the electrolyte and available cations determines if a particular material can be used as an anode or not. For instance, lithium metal can be used as an anode if the available cation is either Li^+ or can form reversible alloy or plating/stripping at or close to the reduction potential of Li^+/Li (-3.04 V vs SHE). Similarly, the electrolyte should also not decompose at such low potentials.

The electrochemical performance of DIBs is strongly influenced by the anode material used, such as energy density, rate capability, and cycling stability⁸⁸. Alkali and alkaline earth metals or materials that can reversibly store cations (Li^+ , Na^+ , K^+ , Mg^{2+} , Ca^{2+} , Al^{3+} , etc.) and can be

utilized as anodes in DIBs. The reaction mechanism of anodes in DIBs is quite similar to that of traditional “rocking-chair” batteries such as LIBs. However, given the unique anion-intercalation process in the cathode and different electrolyte requirements⁸⁸. Other mechanisms, such as alloying, conversion, based anode materials for DIBs are depicted in **Figure 2.5**. Ideally, an anode should have high capacity and the lowest reduction potential with fast kinetics. However, the choice highly depends on the type of electrolytes, as mentioned earlier, as anode material must also be compatible with the electrolyte. For instance, in the case of aqueous electrolytes alkali and alkaline earth metals (Li^+ , Na^+ , K^+ , Mg^{2+} , Ca^{2+}) cannot be used directly due to their abrupt side reactions with water and hydrogen evolution⁸⁹.

On the other hand, the capacity and relatively high voltage in DIBs are attributed to the intercalation/insertion of the anions into cathode materials⁹⁰. Anion intercalation and deintercalation are strongly affected by the structural and chemical properties of the cathode materials⁹¹. Therefore, the electrochemical performance of DIBs is significantly determined by choice of the cathode material and involved anion in the charge storage mechanism. As a result, a thorough knowledge of anionic intercalation in cathodes, especially in graphitic cathodes, is essential for improving and understanding the kinetics of anions intercalation in DIBs. The schematic in **Figure 2.5** summarizes the reported cathode materials for DIBs. Most reported cathode materials in DIBs are carbon-based due to the ease of intercalation of anions. However, other layered materials such as metal chalcogenides, oxides, Mxenes, and organic materials have recently been reported in DIBs^{27, 55, 92-94}

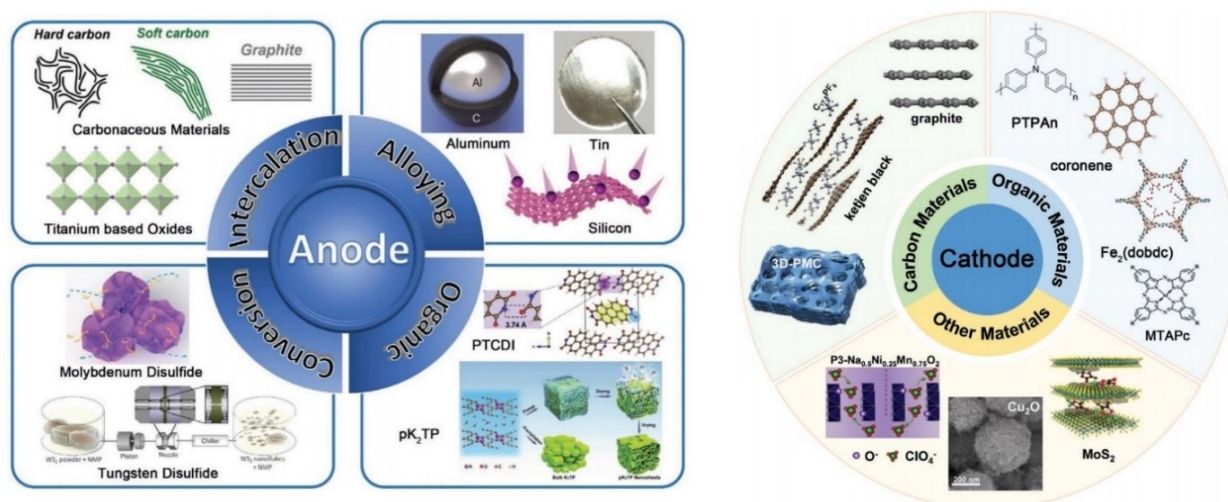


Figure 2.5. Schematic presentation of the reported anode/cathode materials for DIBs²⁶.

It is also worth noting that major work on DIBs has been done in non-aqueous electrolytes, including organic and IL-based electrolytes^{4, 6, 14, 38, 43, 83}. There are limited reports of DIBs using graphite as a cathode in aqueous electrolytes due to the formation of GICs at high potentials $\sim 1.5 - 1.7$ V vs Ag/AgCl, which is beyond the oxidative stability of conventional aqueous electrolytes^{15, 16}.

2.4 Graphite and Graphite Intercalation Compounds (GICs)

Graphite has been the preferred anode material in LIBs since their inception, due to its advantageous combination of low cost, abundant availability, high energy density, and power density^{2, 21, 31}. To this day, graphite remains a widely used material for negative electrodes in LIBs. For the same reasons and its attractive properties, graphite has been extensively utilized in DIBs, where it can be used both as a negative and positive electrode^{36, 37, 72}.

Carbon exists in two main forms in nature: diamond and graphite. These forms are associated with two different hybridization states, sp^3 (as in diamond) and sp^2 (as in graphite)⁹⁵. In the case of graphite, the basal planes are usually parallel to the graphene layer, while the edge planes expose the end of the graphene layer. As a result, the edge planes exhibit higher reactivity to intercalation and deintercalation compared to the basal planes. This difference results in the anisotropy of graphite, impacting its electronic, mechanical, and other physicochemical properties⁹⁶. The graphene layers in graphite are stacked in three distinct modes: hexagonal (AA-stacking), Bernal (ABA-stacking), and rhombohedral (ABC-stacking), as illustrated in **Figure 2.6 (a-c)**⁹⁷. The distance between the layers is 3.35 \AA ^{1, 20}. The unit cells are represented by dark shadows for the three structures, where the symbols α , β and γ indicate the interlayer and intralayer hopping integrals⁹⁶. The sp^2 hybridized graphene layers in graphite are held together by weak van der-Waals forces from the delocalized electron orbitals. The "2p_z" orbitals perpendicular to the graphene plane hybridize to form a partially filled, delocalized band structure that allows for high electron mobility (approximately $200,000 \text{ cm}^2 \text{ V}^{-1} \text{ s}^{-1}$)⁹⁸. This property also accounts for the redox amphoteric nature of graphite, enabling it to function as both the negative and positive electrodes in DIBs^{99, 100}. This is achieved through the stabilization of excess electrons in its antibonding π^* -band, forming donor-type GICs, or stabilization of extra holes in its bonding π -band, forming acceptor-type GICs, due to delocalization¹⁰⁰. A variety of cations and anions (such as cations like Na^+ and Li^+ , or Pyr14^+ , anions, like PF_6^- and BF_4^- , AlCl_4^- , ClO_4^- , FSI^- , TFSI^- , etc.) can overcome the weak van der Waals forces between graphene sheets when charged to specific potentials^{24, 99, 101, 102, 103}.

However, recent studies have explored the correlation between graphitic carbon cathode characteristics and corresponding electrochemical performance for anion intercalation, including reversible capacity and Coulombic efficiency¹⁰⁴⁻¹⁰⁶.

On the basis of the reported literature, the current understanding of carbon-based cathodes for anion intercalation from both aqueous and non-aqueous electrolytes suggests that a high degree of graphitization (DoG) is necessary for reversible anion intercalation/deintercalation. Increasing DoG can enhance specific discharge capacity¹⁰⁷. This is schematically shown in **Figure 2.6 (d)**. Furthermore, the crystallite height (L_c) has only a minor impact on capacity. Brunauer-Emmett-Teller (BET)-specific surface area and the 'non-basal plane' surface area of graphite particles and surfaces strongly affect capacity and rate performance for anion intercalation, and smaller particle sizes and/or higher surface areas can enhance performance³. Other than the graphite's structural properties, the anion (de)intercalation depends on various factors, such as the type of anion, electrolyte composition, the cut-off potential of the graphite cathode, charge rate, and operation temperature^{2, 103, 108}.

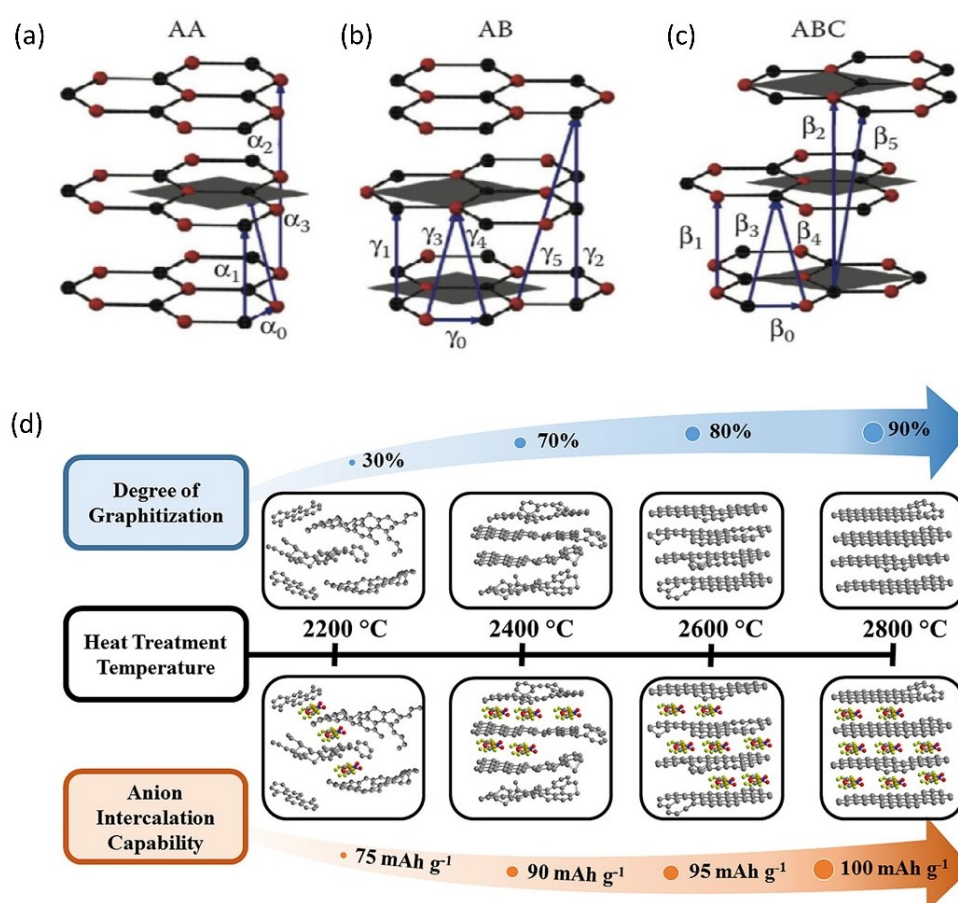


Figure 2.6. Structures of (a) AA, (b) AB, (c) ABC-stacked graphite⁹⁵, and (d) show the effect of heat-treatment on the degree of graphitization, and its effect on anion intercalation capacity^{107, 109}.

Limitations of Graphite in DIBS

Although graphite-based DIBs offer higher operation voltage than LIBs, there are still some limitations to graphite cathodes. One of the limitations is the severe volume expansion of the cathode (>130%) caused by the intercalation of anions with large sizes, which may lead to graphite exfoliation and capacity loss¹⁰⁹. Additionally, solvent molecules may co-intercalate into the cathode during the anion intercalation process, which can accelerate structural collapse and capacity loss^{109, 110}. Another limitation is that graphite can only store anions via intercalation, which limits its theoretical capacity. For instance, in the case of the intercalation of PF₆⁻ anion, the theoretical capacity for stage 1 C₁₆PF₆ is 140 mAh g⁻¹^{111, 112}. To overcome these limitations and improve DIB performance, modifications and optimizations of the graphite cathode structure and properties and the introduction of new anion storage mechanisms are necessary.

Staging Phenomenon

The concept of GICs was demonstrated as early as 1840¹¹³. Graphite's weak van der Waals forces between its graphene layers and the ability to expand its interlayer distance make it possible for the intercalation of ionic and molecular species. This process usually leads to a restacking of the graphene layers and the formation of a well-arranged structure that enables the reversible insertion and removal of charge carriers^{113, 114}. The insertion of ions into the layers of graphite occurs in a specific sequence rather than all at once. This phenomenon, referred to as "staging," was first documented by Rüdorff and Hofmann in 1940¹¹⁵⁻¹¹⁷. It is believed that the intercalant gradually fills the interlayer spaces of the graphene without causing any structural disruptions to the graphene layer. The stage number in GICs is a measure of the number of graphene layers separating the intercalated layers. The original staging model proposed by Rüdorff and Hofmann in 1940 suggested that anions insert into the graphene layers sequentially, without inducing any structural distortions in the graphene layer. However, this model oversimplifies the process, and later in 1969, Daumas and Hérold proposed a more realistic model, in which ions insert simultaneously into the graphene layers and then deform the layers around them^{114, 117}. This allows for subsequent diffusion of the intercalant ions, which is more accessible compared to diffusion along the c-axis in the Rüdorff model. This model also explains the coexistence of domains with different stages in the same crystallite. **Figure 2.7** presents a schematic illustration of Rüdorff and Daumas–Hérold models for the staging mechanism of ion intercalation into graphite¹¹⁸.

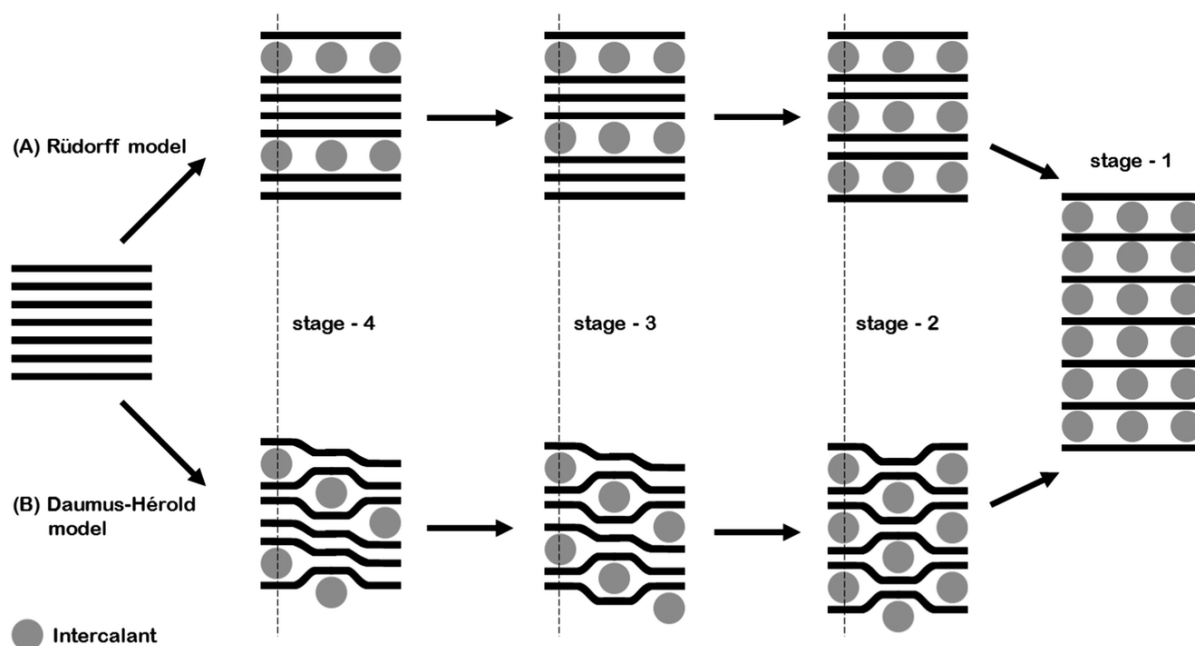


Figure 2.7. Schematic illustration of Rüdorff and Daumas–Hérol models for the staging mechanism of ion intercalation into graphite,¹¹⁸.

Observation of staging phenomenon in GICs

Galvanostatic charging/discharging can provide insight into the intercalation and deintercalation processes of GICs, but it can be challenging to quantify the stages using this method¹¹⁹. X-ray diffraction (XRD) and Raman spectroscopy are more explicit in identifying the stage value of GICs^{15, 118}. These methods provide structural information about the intercalated species and the arrangement of graphene layers, allowing for a more accurate determination of the staging process. XRD can determine the interlayer spacing and the degree of ordering in GICs, while Raman spectroscopy can provide information on the degree of electronic interaction between the graphene layers and the intercalant¹²⁰. Both XRD and Raman spectroscopy are non-destructive techniques¹²¹, making them valuable tools for studying the properties of GICs. In this thesis, XRD is also used for *In-situ/Operando* XRD measurements during the charging and discharging processes.

X-ray diffraction (XRD)

X-ray (Powder) Diffraction (XRD), especially in an *Operando* mode, is an effective and fast measurement tool to characterize crystalline material, for instance, GICs. It provides information on unit cell dimensions, where crystal lattice planar spacing (d-spacing) is used for sample identification and characterization. The d-spacing is defined through the wavelength of

the incident X-rays (λ) and the angle of incidence (θ). The general relationship is known as Bragg's law expressed as ¹²²,

$$n\lambda = 2d\sin\theta$$

X-ray -Diffraction of GICs

XRD patterns of graphite electrodes show an initial independent peak at 26.5° (002), which belongs to pristine graphite. Upon anion intercalation, this peak disappears, and new peaks emerge at lower angles for (00(n+1)) reflections and higher angles for (00(n+2)) reflections, where n represents the dominant stage number. The intensity order is commonly $I(00(n+1)) > I(00(n+2)) > I$ (all other reflections). The appearance of these peaks indicates the successful intercalation of anions into the graphene sheets, leading to the lattice expansion of graphite ¹²². Schmuelling *et al.* studied this phenomenon for TFSI intercalation and determined the dominant stage (n), gallery height (d_i), and experimentally obtained capacity correlated with theoretical specific discharge capacities for different graphite stages ¹⁸. The spacing of (00n) planes (d_{00n}) can be determined using the equation below. In the case of graphite, this equation can be used to derive other parameters, such as periodic repeating distance (I_c), gallery expansion (Δd), intercalant gallery height (d_i), and dominant stage number (n), where l represents the index of (00l) planes in the stacking direction and d_{obs} are the observed distance between two adjacent graphene planes ^{18, 123}.

$$d_{00n} = \frac{I_c}{n} = \frac{\lambda}{2d\sin\theta_{00n}}$$

$$I_c = d_i + 3.35\text{\AA} \cdot (n - 1) = \Delta d + 3.35\text{\AA} \cdot n = l \cdot d_{obs}$$

As the voltage consistently increases, the peak at the lower angle shifts to the left, and the peak at the higher angle shifts to the right. When anion deintercalation starts, the (00(n+2)) peak shifts to lower 2θ values, and the (00(n+1)) peak shifts to higher 2θ values. When the graphite electrode is discharged to a certain potential, the newly emerged peaks do not disappear completely, and the pristine peak decreases in intensity and becomes wider. This is due to the presence of remaining anions between the graphene sheets, which causes a decrease in long-range order and a broader peak ²⁴.

3 Results and discussion

3.1 Al- and Zn- perchlorate-based WiSE

Multivalent zinc and aluminum perchlorate-based WiSE are the focus of the present thesis. These metals are abundant, low-cost, and safe for use in energy storage systems. Further, the physical and chemical properties of the electrolytes, such as solvation structure, transport property of ions, and viscosity, have been linked with the anion's nature¹²⁴. The Hofmeister series ranks the relative influence of ions on the behavior of aqueous solutions^{125,15}. The Hofmeister series has been well-studied, with ions classified as either kosmotropes or chaotropes. Kosmotropic ions, such as SO_4^{2-} , PO_4^{3-} , Al^{3+} , and Zn^{2+} , have a high charge density and strengthen the hydrogen-bonding network of water molecules, while chaotropic ions, like NH_4^+ , SCN^- , and ClO_4^- , have a low charge density and break the network^{125, 126}. Notably, recent studies have shown that the position of an anion in the Hofmeister series has a strong correlation with the resulting ESW of highly concentrated electrolytes^{15, 127}. The kosmotropic or chaotropic nature has been linked with the interaction energy between water and ions, and it has been elucidated that the ions for which interaction energy (function of the ions charge density) with water is stronger than water-water interaction ($-24.48 \text{ kJ mol}^{-1}$) are hydrophilic (kosmotropic). Whereas the ions are considered hydrophobic (chaotropic) if the interaction energy between the ion and one water molecule is more positive than $-24.48 \text{ kJ mol}^{-1}$ ¹²⁴.

Therefore, the chaotropic strength of the counter anion is a crucial factor in selecting suitable zinc or aluminum salts for WiSE, as a high-voltage WiSE should have a strong chaotropic anion to reduce hydrolysis and attain a wide ESW. The perchlorate anion, which is one of the most chaotropic ions in the Hofmeister series (**Figure 3.1**) and has been found to form reversible intercalation compounds with graphite, is a promising candidate for developing high-voltage WiSE electrolytes and graphite-based dual-ion batteries^{102, 128}s. Therefore, zinc and aluminum perchlorates have been chosen as model systems for the investigation in this thesis.

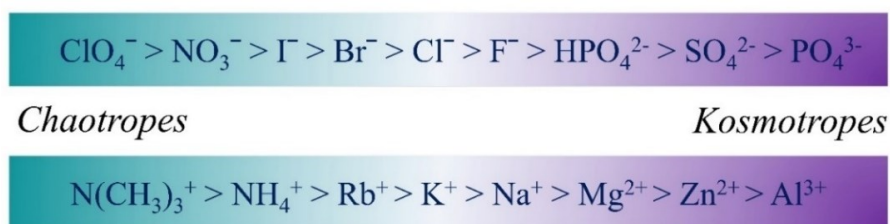


Figure 3.1. Hofmeister Series of anions and cations.

3.1.1 Characterization of WiSE

a) Determination of ESW

All electrolytes used in the present thesis were prepared by mixing the respective quantities of the aluminum- and zinc- salts (perchlorates and sulfates) and deionized water (conductivity $< 0.26 \mu\text{Scm}^{-1}$) under continuous stirring to obtain dilute ($0.5 m$) and concentrated ($5 m$, $8 m$ and $15 m$ (mol/kg)) aqueous electrolytes. It is worth mentioning that the $15 m$ and $8 m$ electrolytes of $\text{Al}(\text{ClO}_4)_3 \cdot 9\text{H}_2\text{O}$ and $\text{Zn}(\text{ClO}_4)_2 \cdot 6\text{H}_2\text{O}$ were supersaturated and named Al- and Zn-WiSE, respectively. The ESW of the as-prepared electrolytes was evaluated by linear cyclic voltammetry (LSV) using a glassy carbon working electrode, platinum counter electrode, and Ag/AgCl reference electrode. The LSV results of $\text{Al}(\text{ClO}_4)_3$ and $\text{Zn}(\text{ClO}_4)_2$ -based WiSEs are presented in **Figure 3.2**.

Figure 3.2 (a) compares the electrochemical stability of the Al-WiSE ($15 m$) to other concentrations ($0.5 m$, and $5 m$) of the same salt at a scan rate of 5 mVs^{-1} . The $\text{Al}(\text{ClO}_4)_3$ -based WiSE demonstrated a stable and wide ESW in the voltage range of 2.0 to -2.0 V vs. Ag/AgCl. The electrochemical window of the $15 m$ WiSE was found to be approximately double the window obtained with the diluted aqueous electrolyte ($0.5 m$), which is a function of the increasing salt concentration. Similarly, the ESW of differently concentrated Zn-based electrolytes was also determined by LSV in a 3-electrode electrolytic cell, as given in **Figure 3.2 (b)**. The LSV spectra of the $\text{Zn}(\text{ClO}_4)_2$ -based WiSE showed a wide ESW of 2.8 V , which is wider than the electrochemical window of the $0.5 m \text{ Zn}(\text{ClO}_4)_2$ electrolyte. In contrast, the ZnSO_4 -based WiSE

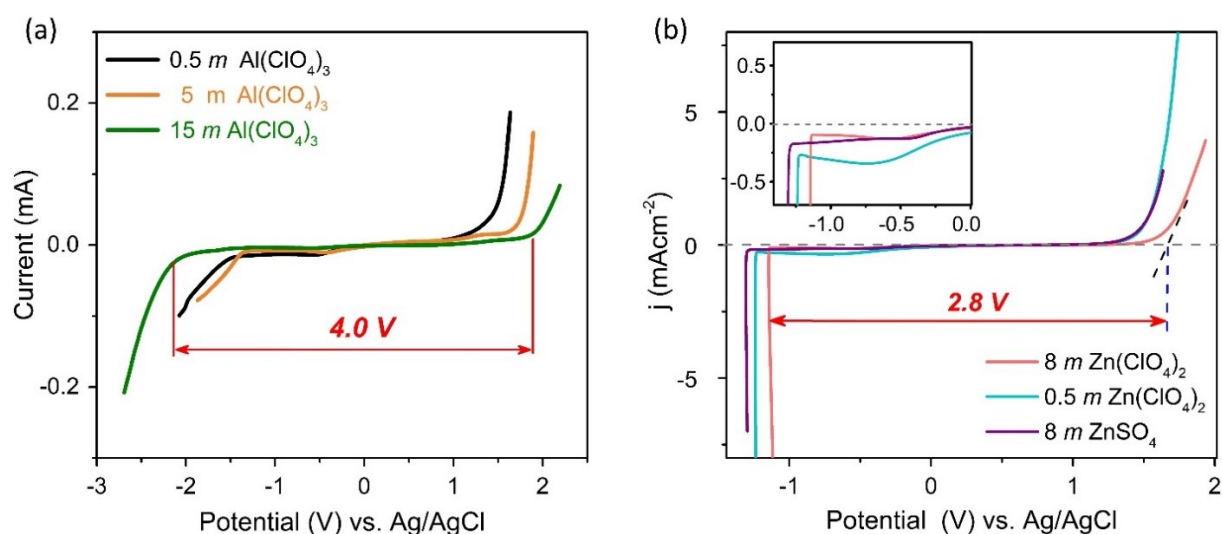


Figure 3.2. ESW of (a) $\text{Al}(\text{ClO}_4)_3$ -WiSE, and (b) $\text{Zn}(\text{ClO}_4)_2$ -WiSE compared to diluted aqueous electrolytes.

showed a narrower ESW, which was attributed to the presence of the kosmotropic sulfate anion that disrupted the solvation shell of the Zn^{2+} ions and increased the possibility of hydrolysis reactions. Nevertheless, the reductive stability window reduces for perchlorate-based Zn-WiSE as the overpotential for Zn-plating shifts towards the standard reduction potential of Zn (-0.76 V vs SHE).

The interaction (hydration) energies (ΔG^{int}) of ions with water can help in interpreting the kosmotropic (hydrophilic) or chaotropic (hydrophobic) nature of anions and their effect on the water-structure. Recently, Han *et al.* performed DFT simulations to achieve a better understanding of the molecular interactions of water and ions based on ionic charge densities¹²⁴. The hydration energy increases sharply with the ion charge density, as presented in **Figure 3.3**. Based on the ΔG^{int} , hydrophilic or hydrophobic ions can be identified by comparing the ΔG^{int} between one ion and one water molecule with the ΔG^{int} between two water molecules (-24.48 kJ mol⁻¹, red dotted line in **Figure. 3.3**).

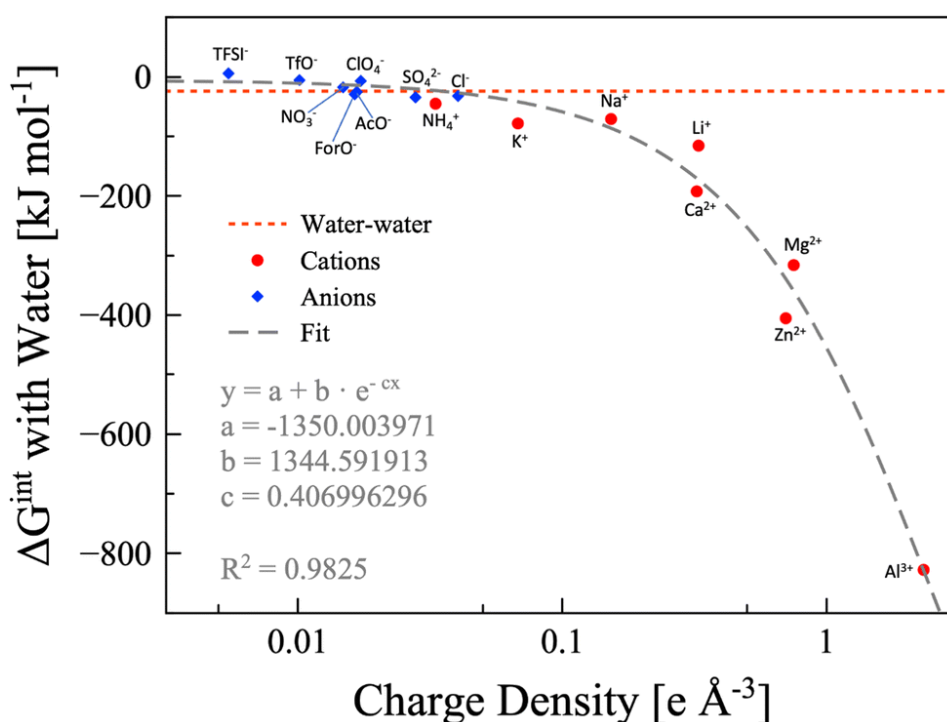


Figure 3.3 "Water-ion interaction energy as a function of the ions charge density" - A graph displaying the relationship between water-ion interaction energy and the charge density of ions, with anions depicted as blue diamonds and cations as red circles. The dashed grey line represents an exponential fit, with the equation and parameters shown, while the red dotted line represents the water-water interaction energy¹²⁴.

Therefore, an ion is hydrophobic (chaotropic) if the ΔG^{int} between the ion and one water molecule is higher than -24.48 kJ mol⁻¹, otherwise it is hydrophilic (kosmotropic). Hence, the effect of ClO_4^- and SO_4^{2-} on ESW in Zn-WiSE can be assigned to their chaotropic and

kosmotropic natures, as ΔG^{int} of ClO_4^- anion is much higher ($-7.02 \text{ kJ mol}^{-1}$) than water-water $-24.48 \text{ kJ mol}^{-1}$ and SO_4^{2-} anion ($-34.7564 \text{ kJ mol}^{-1}$). The results are in line with the Hofmeister series (**Figure 3.1**). These results indicate that the choice of counter anion is critical for achieving a wide ESW in WiSEs. On the other hand, Al and Zn are highly kosmotropic in nature, which suggests they interact strongly with water molecules and trap them in their solvation shells.

Raman spectroscopy was used to examine the hydration of Zn^{2+} and Al^{3+} cations in the WiSE in **Figure 3.4 (a-b)**. Raman spectra OH-stretching vibrations region of pure water, dilute electrolytes and ZnSO_4 -WiSE with the kosmotropic SO_4^{2-} anion demonstrate wide peaks at 3530 cm^{-1} . In contrast, a narrow peak is observed for the chaotropic ClO_4^- based Al and Zn-WiSE. This suggests that water molecules are primarily located within the solvation sheath of Zn^{2+} cations in the concentrated WiSE system ¹²⁹.

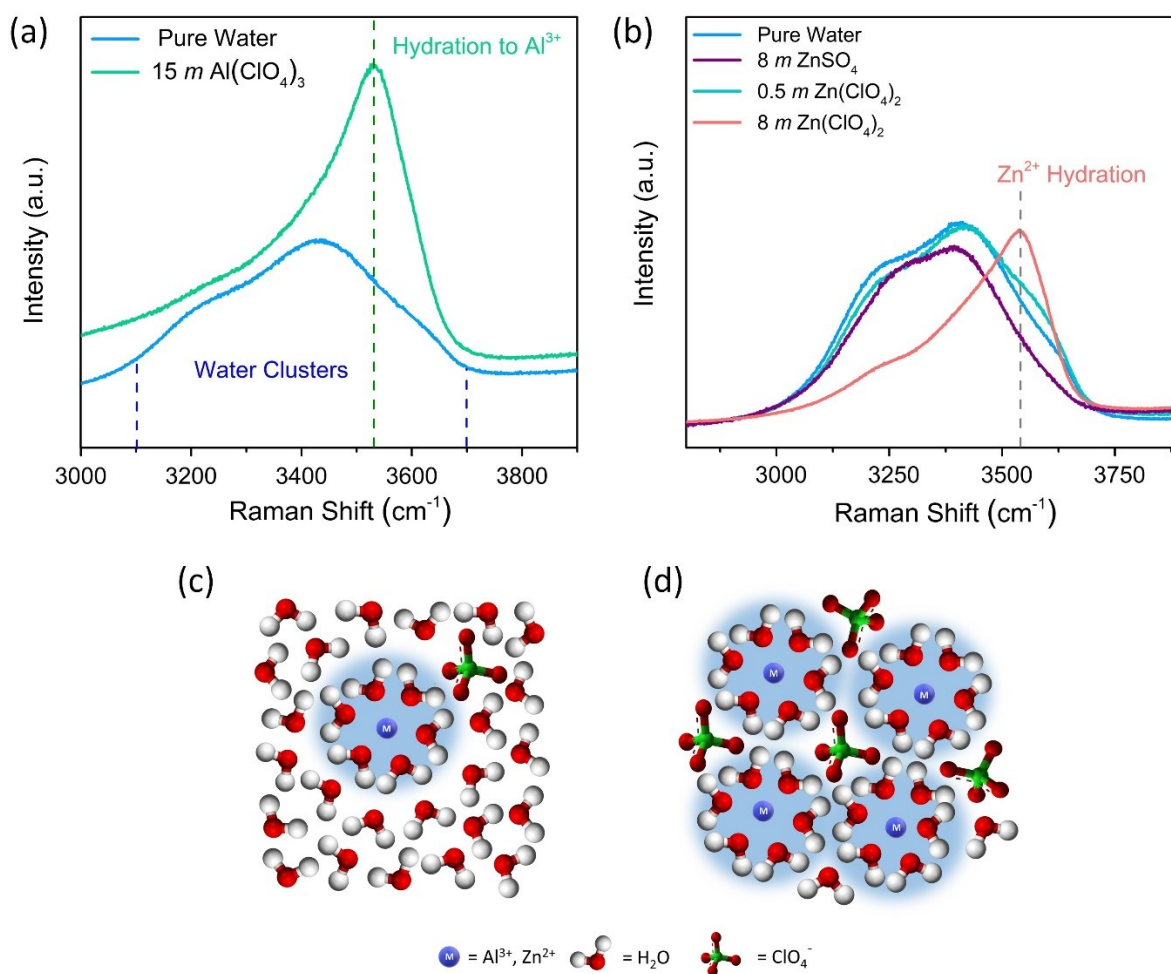


Figure 3.4 Raman spectra OH-stretching vibrations region of pure water vs (a) $\text{Al}(\text{ClO}_4)_3$ WiSE, and (b) $\text{Zn}(\text{ClO}_4)_2$ WiSE, the dilute electrolyte of $\text{Zn}(\text{ClO}_4)_2$ and ZnSO_4 -WiSE, and (c) illustration water-ions solvation of dilute (salt-in-water) and, (d) concentrated electrolyte (WiSE).

The chaotropic anion modifies the hydrogen-bonding network of water and forces water molecules toward the cation. This results in a decrease of free water in the WiSE and the widening of the ESW. **Figure 3.4 (c & d)** illustrates the water-cation solvation shells and free water in the diluted electrolytes and WiSE, respectively. Water molecules are bounded within the solvation shells of the cations in WiSE. A similar phenomenon has also been observed by other research groups in other WiSE systems¹²⁵. In summary, the wide ESW in Al- and Zn-based WiSE is attributed to the high salt concentrations and the interplay between ion-water interactions between multivalent kosmotropic (hydrophilic) cations and strong chaotropic (hydrophobic) ClO₄⁻ anions.

b) Ionic conductivity measurements of WiSE

Ionic conductivity is a crucial property of electrolytes and their potential use in energy storage systems. To measure the ionic conductivity of the as-prepared WiSEs, electrochemical impedance spectroscopy (EIS) was employed. The electrolyte resistance (R_s) was measured in an electrolytic tank with two symmetric Pt electrodes of a specific surface area and a fixed distance (L) between them, over a frequency range of 0.1-10⁵ Hz. Ionic conductivity (σ , mS cm⁻¹) was calculated using

$$\sigma = L / (R_s * A)$$

where A is the area of the platinum electrode immersed in the electrolyte. To calibrate the conductivity measurement system, standard conductivity calibration solutions of 12,880 $\mu\text{S cm}^{-1}$ and 80,000 $\mu\text{S cm}^{-1}$ (Atlas Scientific, LLC) were used. **Figure 3.5 (a)** and **(b)** displays the temperature-dependent ionic conductivity of 15 *m* Al(ClO₄)₃ and 8 *m* Zn(ClO₄)₂ WiSE in the range of -30 to 60 °C and -45°C to 60°C, respectively. Both electrolytes have a significantly higher ionic conductivity than ionic liquids. At room temperature, the Al(ClO₄)₃-based WiSE has a ionic conductivity of 25.5 ± 0.07 mS cm⁻¹, and the Zn(ClO₄)₂-based WiSE has $32.5 (\pm 0.07)$ mS cm⁻¹. Remarkably, the ionic conductivity of the WiSEs remains high even at extremely low temperatures, making them suitable for energy storage applications in cold climates. A comparison of the ionic conductivity and stability window of the Al(ClO₄)₃-WiSE with previously reported WiSE systems is presented in **Appendix I (Figure 1 (c))**.

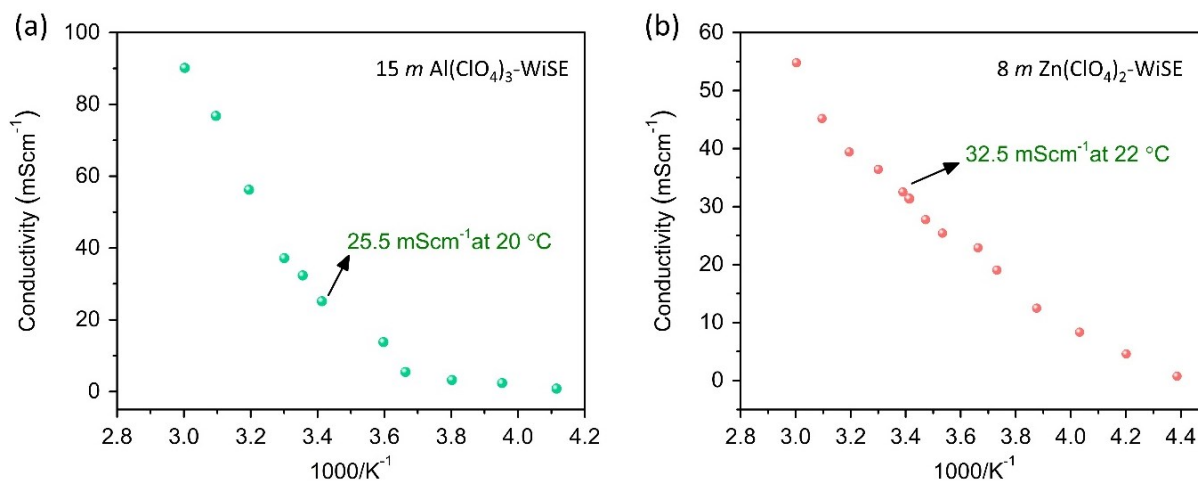


Figure 3.5 Temperature dependence of ionic-conductivity of (a) $\text{Al}(\text{ClO}_4)_3$ -WiSE, and (b) $\text{Zn}(\text{ClO}_4)_2$ -WiSE.

3.2 Half-cell studies of perchlorate anion intercalation into graphitic materials from Aluminum-WiSE

a) *Highly Oriented Pyrolytic Graphite (HOPG)*

To investigate electrochemical anion intercalation into graphite, HOPG was first utilized as a positive electrode material due to its well-defined ordered crystal structure and high purity^{128, 130}. To avoid the disintegration of the bulk HOPG upon anion intercalation, a uniform HOPG slurry was prepared and used as the working electrode. Initially, HOPG was exfoliated by tip-ultrasonication (Hielscher UP200S, 24 kHz, Germany) in N-methyl-2-pyrrolidone (NMP) (ROTH®, Germany), at 80% power for 6 hours, using 30 mg of HOPG flakes in 60 ml of NMP. The exfoliated HOPG flakes were separated by centrifugation, and NMP was washed with ethanol. Subsequently, the HOPG flakes were mixed with conductive carbon and polyvinylidene fluoride (PVDF) binder dissolved in an NMP disperser to form a homogenous slurry. The resulting HOPG slurry was pasted onto a polytetrafluoroethylene (PTFE) treated hydrophobic carbon paper current collector and dried in air at 80 °C overnight prior to the electrochemical measurements. The active mass density of the resulting HOPG electrodes was approximately 2.5 mg cm^{-2} .

CV of a HOPG-based electrode and the bare current collector in the $\text{Al}(\text{ClO}_4)_3$ -based WiSE at a scan rate of 10 mV s^{-1} is presented in **Appendix I** (Figure 2 (a)). The CV voltammogram for the HOPG electrode demonstrates two oxidation peaks (O and O') and two corresponding reduction peaks (R and R'). The oxidation peaks at around 1.48 V and 1.6 V vs. Ag/AgCl

correspond to the intercalation potentials of perchlorate anions into graphite, which is approximately 4.5 V to 5.0 V vs. Li^+/Li , as reported previously in non-aqueous systems^{131,132}.

Once galvanostatic charge/discharge was performed, the maximum discharge capacity was achieved at a high cut-off potential of 1.64 V vs Ag/AgCl. The subsequent cycle life, stability, and Coulombic efficiency (C.E.) tests were performed under the same conditions of 200 mA g^{-1} current density and cut-off potential. The anion (de)intercalation into the graphite electrode in the WiSE demonstrated excellent stability for over 2000 cycles at the aforementioned current density, as shown **Figure 3.6**. The discharge capacity exhibited a slight improvement in the initial cycles, with a peak value of 35 mAh g^{-1} at the 50th cycle. The C.E. gradually improved throughout cycling, reaching a value of over 95% after 100 cycles. Even after 2000 cycles, the discharge capacity (26 mAh g^{-1}) remained higher than the initial value of 22 mAh g^{-1} , with a C.E. of approximately 98%.

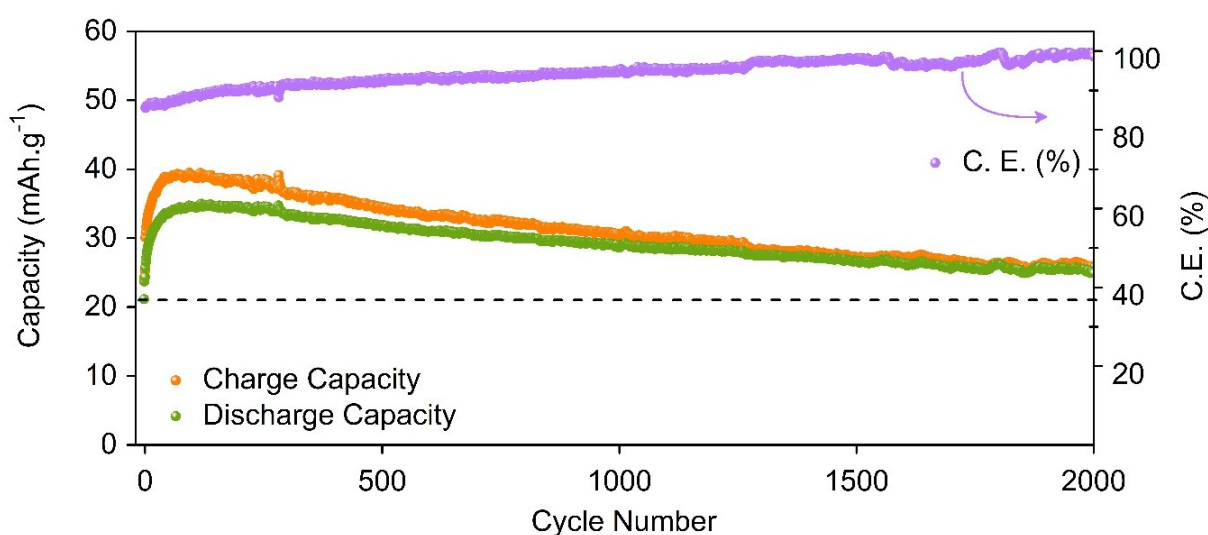


Figure 3.6. Long-cycling test up to 2000 cycles, at the cut-off potential of 1.64 V vs. Ag/AgCl at the current density of 200 mA g^{-1} .

Operando X-ray diffraction (XRD)

Operando-XRD investigations were conducted during the charging and discharging of a custom-made three-electrode half-cell. To enable the penetration of an X-ray beam, the cell-top was sealed with a KAPTON tape. The results of the *operando*-XRD measurements were presented using contour plots of the (002) and (004) characteristic reflections of graphite, as shown in **Figure 3.7**. The plots illustrate the reversible intercalation of ClO_4^- and structural changes of the HOPG electrode during the 4th and 5th (dis)charge cycles. The (002) characteristic peak position of HOPG exhibited a shift to lower and higher 2 theta angles with

reflection (00n+1) and (00n+2) during charging and discharging, respectively. However, the intensity of the (00n+2) reflection was observed to be very low. The splitting of the (004) reflection into two dominant peaks also signifies the intercalation of ClO_4^- in stages. Based on the ratio of the reflection peaks, a mixture of intercalation stages 4 and 5 was observed. This is between the theoretical values for stage 5 and stage 4. The gallery height (d_i), which represents the distance between two graphite layers with an intercalant layer in between, was found to be 7.08 Å, with a gallery expansion (Δd) of 3.76 Å. The relationship between the observed values of d_i , Δd and stages (n), and the periodic repeat distance (I_c), can be expressed by

$$I_c = d_i + 3.35\text{Å} \cdot (n - 1) = \Delta d + 3.35 \text{Å} \cdot n$$

By considering a mix of intercalation stages, the distance between two neighboring intercalation layers (I_c) was found to be between 17.14 Å to 20.48 Å.

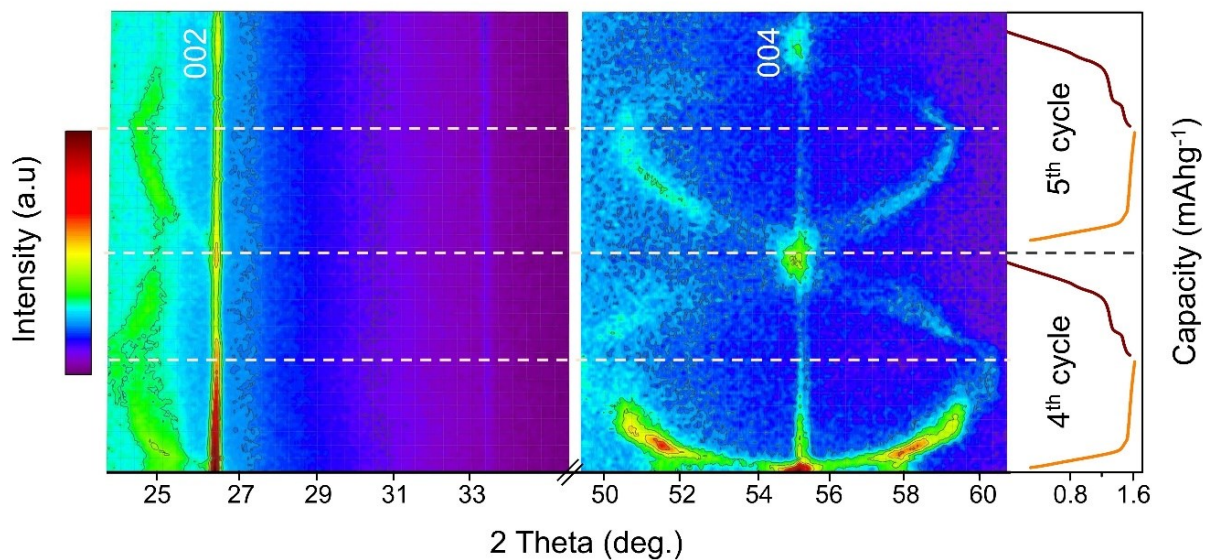


Figure 3.7. Operando- XRD for the 4th and 5th (dis)charge cycle at the current density of 20 mAh g⁻¹.

To identify the stages, theoretical stoichiometric models with single $[\text{C}_{18}\text{ClO}_4]$ and four intercalant sites $[\text{C}_{72}\text{ClO}_4]_4$ were used, as previously reported¹³³. Theoretical capacities were calculated for stages n , ($n = 1$ to 6) by using the following formula to determine which of the capacity contributions was closest to the experimental value¹³⁴,

$$\frac{F \cdot x\text{ClO}_4^-}{3.6 \cdot m_c \cdot \text{carbon atoms in unit cell} \cdot \text{stage } n}$$

where F is the Faraday constant, and m_c is the molar mass of the carbon. The multiplier 3.6 is the unit conversion factor from As g⁻¹ to mAh g⁻¹. The calculated theoretical discharge

capacities for stage 4 of 31.02 mAh g⁻¹ and stage 5 of 24.68 mAh g⁻¹ closely match the experimental values of 35 mAh g⁻¹ to 26 mAh g⁻¹, as shown in *Table 3.1*.

Table 3-1. The experimental and theoretical discharge capacities for different ClO₄⁻ intercalated graphite stages.

| Experimental | | Theoretical | | |
|--|-----------|--------------------|---|---|
| | | | C ₁₈ ClO ₄ 3 x 3 graphene sheet with 18 C-atoms | C ₇₂ (ClO ₄) ₄ 6 x 6 graphene sheet with 72 C-atoms |
| Discharged capacity (mAh g ⁻¹) | | | Capacity (mAh g ⁻¹) | |
| 1 st cycle | 22 | Stage 1 | 124.08 | 124.08 |
| 50 th cycle | 35 | Stage 2 | 62.04 | 62.04 |
| 1000 th cycle | 29 | Stage 3 | 41.36 | 41.36 |
| | | Stage 4 | 31.02 | 31.02 |
| | | Stage 5 | 24.81 | 24.81 |
| | | Stage 6 | 20.68 | 20.68 |

b) A case of natural graphite (NG) and kish graphite (KG) for ClO_4^- anion intercalation

As suggested in the literature, the degree of graphitization (DoG) can affect the anion intercalation into graphite^{3, 107, 115}. To investigate the role of crystallinity for the intercalation of ClO_4^- anion, natural graphite (NG) and kish graphite (KG) were used as the positive electrode in $\text{Al}(\text{ClO}_4)_3$ -based WiSE. The XRD was used to calculate the DoG of the considered materials. The XRD spectra of pristine NG and KG are shown in **Appendix II (Figure 1 (e))**, with the (002) reflection of NG and KG appearing at 26.53° and 26.54° , respectively, corresponding to interlayer spacings (d_{002}) of 3.35(6) and 3.35(5) Å. The DoG, was calculated for the out-of-plane direction (i.e., along the c-axis) using the following formula:

$$g (\%) = \frac{0.3440 - d_{002}}{0.34440 - 0.3354} \times 100$$

Where 0.3440 (nm) is for fully nongraphitized carbon, d_{002} (nm), is the interlayer spacing estimated from XRD measurements, and 0.3354 (nm) is the interlayer spacing of ideal graphite crystals. The degree of graphitization based on d_{002} was found to be 97.67% for NG and 98.84% for KG.

Electrochemical kinetics of the ClO_4^- anion intercalation

CV kinetics of NG and KG were investigated to gain a deeper understanding of the charge storage process during cycling and the effect of DoG. The results of the electrochemical kinetics study are presented in **Figure 3.8 (a-h)**. The analysis of the cyclic voltammograms involved separating the diffusion-controlled and surface-controlled electrochemical processes, following the methodology detailed in **Appendices (I -IV)**^{104, 135, 136}. The relationship between the peak current (i) and scan rate (v) was expressed as a power-law:

$$i = a v^b$$

The parameters a and b are adjustable in the power-law relationship between the peak current and the scan rate in CV. The slope of the $\log(i)$ vs $\log(v)$ plot provides the value of the parameter b , which is a measure of the dominant process controlling the charge/discharge process. A value of $b = 0.5$ indicates that diffusion is the main process, while $b = 1$ signifies a surface-controlled process. A value of b between 0.5 to 1.0 indicates the presence of both surface and diffusion-controlled processes.

The cyclic voltammograms of NG reveal an increase in the currents associated with the redox peaks (OA, O'A, RC, and R'C) with an increase in the scan rate from 1 mVs^{-1} to 7 mVs^{-1} (**Figure 3.8 (a)**). A similar trend is observed in the cyclic voltammograms of KG shown in **Figure 3.8 (b)**. In the case of NG (**Figure 3.8 (c)**), the fitted b values of 0.79, 0.96, and 0.94 for the oxidation peak OA and the reduction peaks RC and R'C, respectively, indicate the contribution of both ionic diffusion and surface-controlled processes. Similarly, there were fitted b values of 0.74, 0.88, and 0.95 for KG (**Figure 3.8 (d)**) for the oxidation peak OA and the reduction peaks RC and R'C, respectively, which also demonstrate the presence of both ionic diffusion and surface-controlled processes.

Since both surface and diffusion-controlled processes are present in NG and KG, their deconvolution can be performed from the cyclic voltammograms. Assuming the summation of purely surface and diffusion-controlled processes, the relation of the overall current and scan rate can be expressed as follows:

$$i = k_1 v + k_2 v^{1/2}$$

where the adjustable parameters $k_1 v$ and $k_2 v^{1/2}$ represent the contributions of surface-controlled and ionic diffusion processes, respectively. The values of k_1 and k_2 can be estimated by analyzing the $i/v^{1/2}$ vs. $v^{1/2}$ plot. By applying this approach, the deconvoluted currents arising solely from surface-controlled and ionic diffusion processes were obtained and overlapped with the experimentally recorded currents at a potential sweep rate of 1 mV s^{-1} , **Figure 3.8 (e-f)**. The analysis of different scan rates is presented in **Figure 3.8 (g-h)**. At a slow scan rate, the charge storage mechanism for both NG and KG were predominantly diffusion-controlled, with intercalation of ionic species in the interlayer spaces accounting for $\sim 95\%$ of the observed charge storage. However, at higher scan rates, the relative contributions of surface-controlled and diffusion-controlled processes changed. The drop in the contribution of the diffusion-controlled process from $\sim 95\%$ to $\sim 38\%$ with an increase in the sweep rate from 1 to 7 mVs^{-1} indicates that the surface-controlled process dominates over the diffusion-controlled process with an increase in scan rate.

The different electrochemical performance of NG and KG can be attributed to the DoG, and the defect density of the graphitic structure. Higher defect density could limit the coherent length of the charge carriers and their mobility, thereby mitigating the electrochemical performance. On the other hand, the degree of crystallinity and flake size are other crucial

factors that might influence capacity and ionic intercalation in the graphitic structure. In the case of NG, the higher defect density with less structural order accounts for its lower specific capacity. In contrast, the higher structural order (DoG) of KG enhances the possibility of ClO_4^- anion intercalation, resulting in more prominent CV redox peaks and a larger potential plateau and higher charge/discharge capacity compared to NG. The results of the charge/discharge analysis are presented in *Appendix II* (Figure 2 (b) and Figure 7).

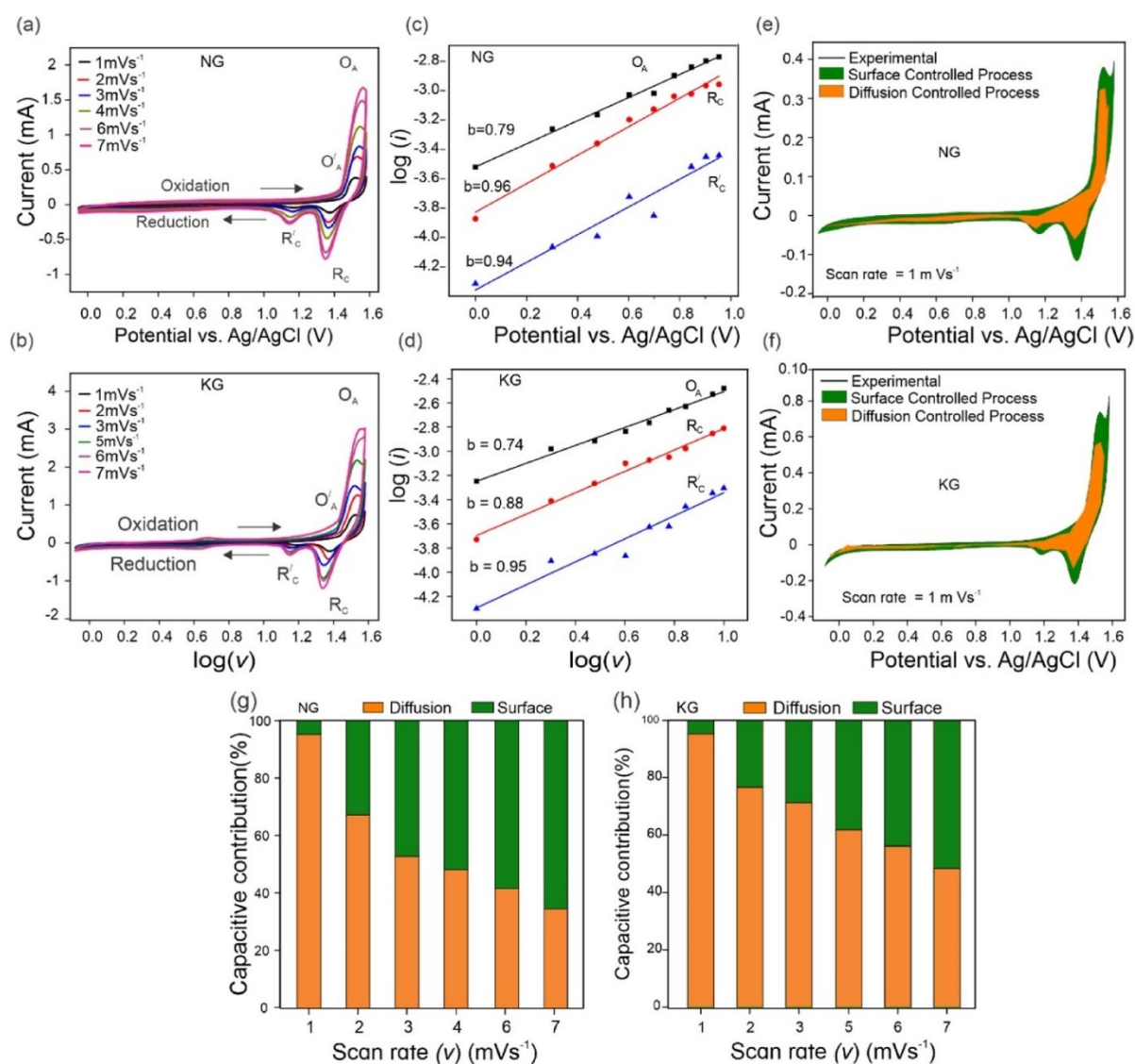


Figure 3.8 The CV kinetic analysis for ClO_4^- (de-)intercalation into NG and KG. cyclic voltammograms of (a) NG and, (b) KG at different scan rates (1–7 mV s^{-1}); a plot of $\log(i)$ vs. $\log(v)$ at the redox peaks for (c) NG, and (d) KG; the deconvolution of the surface and diffusion-controlled processes of charge storage in (e) NG, and (f) KG superimposed on the cyclic voltammogram recorded at a 1 mV s^{-1} ; and the relative contribution of the surface and diffusion-controlled processes of charge storage in NG and KG at various sweep rates (from 1 to 7 mV s^{-1}), (g) and (h), respectively.

c) Ultrasonicated natural graphite

To address the low capacity and low cycling stability in NG and other graphitic materials, a simple ultrasound treatment was done to enhance the reversibility and stability of (de)intercalation of ClO_4^- anions from $\text{Al}(\text{ClO}_4)_3$ system. The ultrasonication was done as described in detail in *Appendix III* and electrodes were prepared by the slurry method, as mentioned in *section 3.2* above. The pristine NG sample is further referred to as “NG” and the ultrasonicated NG as “US-NG”. The ultrasound treatment of graphite leads to an increase of the interlayer spacing and a partial disintegration of the bulk crystallites to flakes of varying thickness and lateral dimensions.

The electrochemical characteristics of the untreated and treated NG were studied in the same $\text{Al}(\text{ClO}_4)_3$ electrolyte. **Figure 3.9 (a)** shows the CV of NG and US-NG recorded at a sweep rate of 1 mV s^{-1} . The CVs show two redox peaks in both the cathodic and anodic regions. The prominent difference between the two systems is the visible discharge plateaus at around $\sim 1.4 \text{ V}$ vs Ag/AgCl (**Figure 3.9 (b)**) for US-NG. This could be due to the relatively smaller lateral crystallite size and expanded graphite plains of the US-NG compared to pristine NG. It also shows that ultrasound treatment can improve the mean discharge voltage.

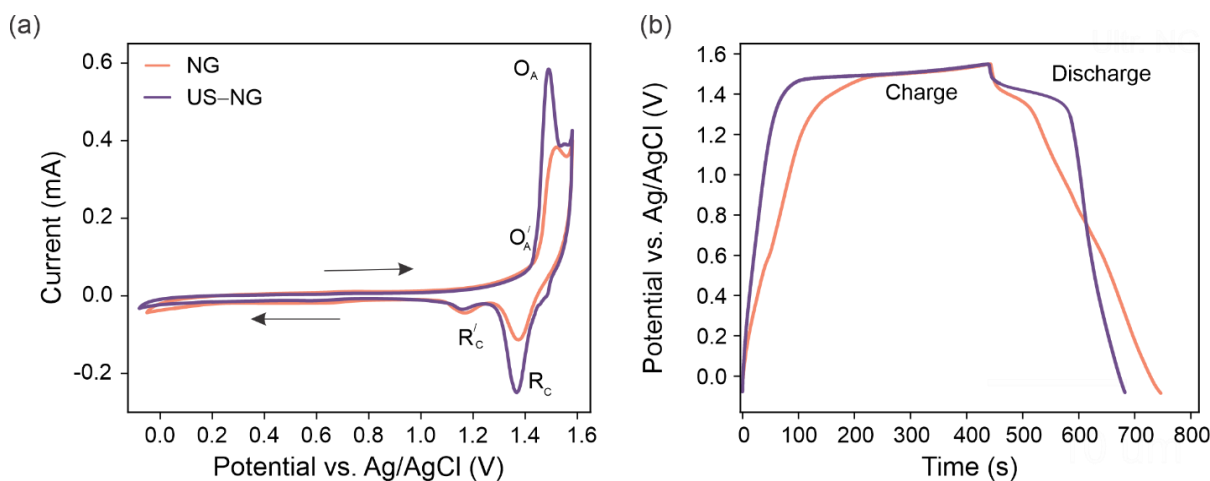


Figure 3.9. CV and (dis)charge curves of NG and US-NG in concentrated $\text{Al}(\text{ClO}_4)_3$ -electrolyte at 1 mV s^{-1} (a), and 250 mA g^{-1} , (b).

3.3 Zn-graphite dual-ion battery based on Zn-perchlorate WiSE

3.3.1 Stripping plating of Zn

To assess the feasibility of $\text{Zn}(\text{ClO}_4)_2$ -WiSE for use in a full-Zn-graphite dual-ion battery (ZnG-DIB), we carried out an investigation of Zn stripping/plating from/on a carbon and Cu substrate using a half cell. The results of this analysis are depicted in **Figure 3.10 (a-c)**. To enable reversible Zn plating/stripping on and from a carbon substrate (120 Toray Carbon paper), CV was conducted at a scan rate of 10 mV s^{-1} in a 3-electrode electrochemical cell with Zn metal serving as both the counter and reference electrode. The obtained results show that the process of Zn plating and stripping in the WiSE takes place within a narrow potential range of -0.1 to $0.2 \text{ V vs. Zn}^{2+}/\text{Zn}$. This range of Zn plating potential, which is close to $0 \text{ V vs. Zn}^{2+}/\text{Zn}$, is highly desirable for Zn batteries, as it helps to reduce the charge voltage and minimizes the electrolyte decomposition via hydrogen evolution or reduction reactions¹³⁷. Similarly, the Zn stripping potential close to $0 \text{ V vs. Zn}^{2+}/\text{Zn}$ provides a low overpotential in the cell, making it possible to use a wide range of positive cathode materials without compromising on cell output voltages.

To examine the deposited Zn morphology on the carbon substrate, the CV was stopped at $-0.1 \text{ V vs. Zn}^{2+}/\text{Zn}$. The electrode surface was subsequently examined using SEM after washing with deionized water (D.I.) and drying in air. The morphology of the deposited Zn layer with a hydrangea flower-like morphology and Zn elemental mapping are presented in **Figure 3.10 (b)**, revealing a uniform distribution of Zn on the carbon substrate.

Zn plating/stripping was also conducted on other substrates, including Cu, and in the dilute 0.5 m electrolyte (**Appendix IV**). The morphologies of the deposited Zn were different on Cu and carbon substrates in the WiSE and diluted electrolytes. This could be attributed to several factors, including different effective surface areas, structure, architecture, surface chemistry of the substrates, and the different salt concentrations in the electrolyte. Previous studies have also suggested that the nucleation overpotential and wetting ability of plating metal can result in different morphologies, sizes, and shapes of the deposited metal on a substrate¹³⁸. Thus, all of these factors should be carefully evaluated and controlled to achieve uniform Zn plating without dendrite formation.

A more rigorous analysis of Zn stripping/plating was performed in a Zn symmetric cell, $\text{Zn}|8 \text{ m Zn}(\text{ClO}_4)_2\text{-WiSE}|\text{Zn}$, to investigate the suitability of the $\text{Zn}(\text{ClO}_4)_2$ -WiSE for the ZnG-DIB.

The galvanostatic (dis)charging was conducted for 1 hour, with upper and lower cut-off voltages of

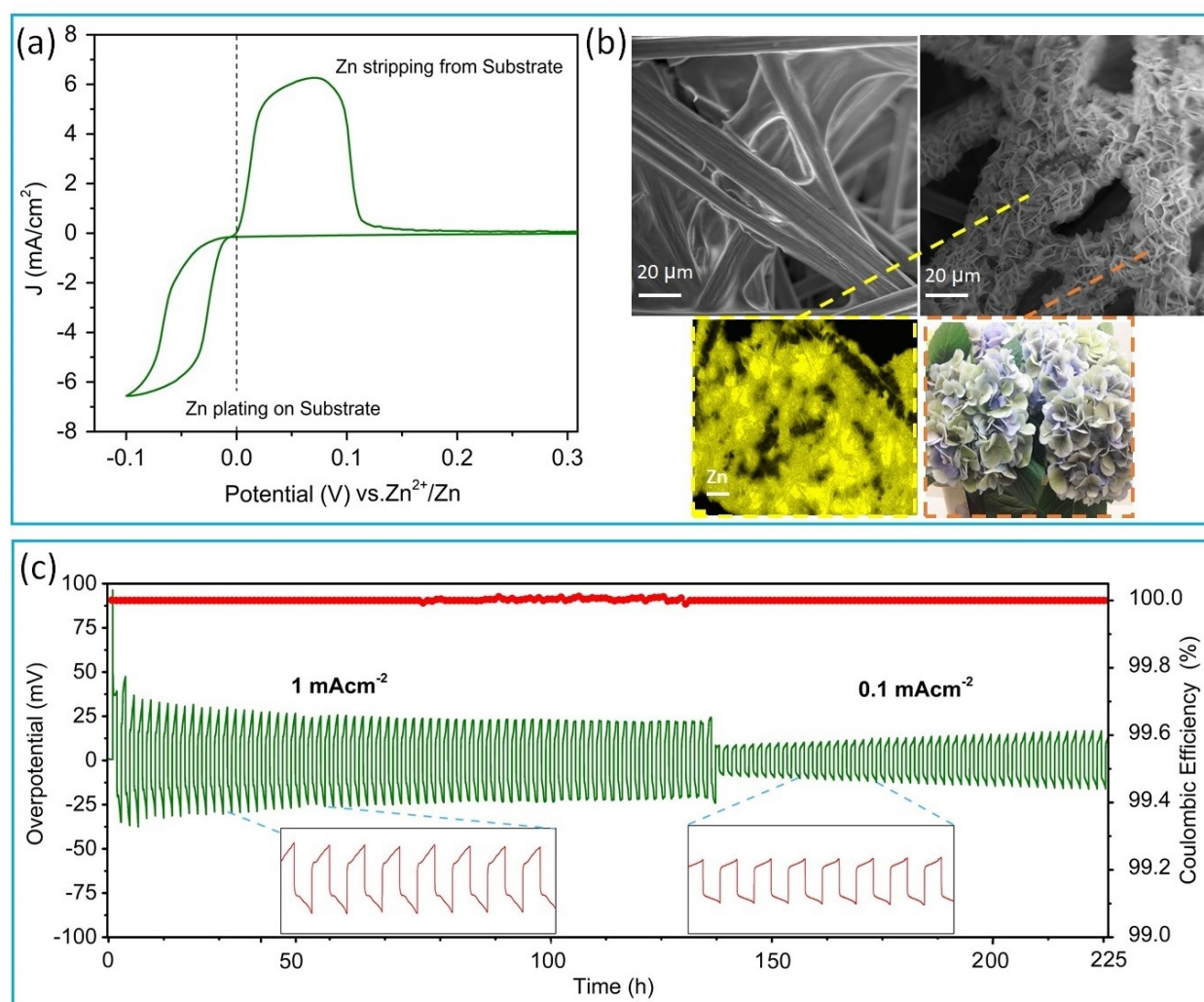


Figure 3.10. Stripping/plating analysis of Zn²⁺/Zn from 8 m Zn(ClO₄)₂-WiSE: (a) CV of Zn plating-stripping on a carbon substrate (120 Toray paper) at a scan rate of 10 mVs⁻¹, (b) SEM images showcasing the morphology of the original carbon substrate (left) and the Zn plated with a hydrangea flower-like structure (bottom right), and EDS mapping of Zn signals (bottom left), and (c) results of stripping-plating cycling and Coulombic efficiency of a Zn||Zn symmetric.

2 V and -2 V, respectively, to allow for visualization of the overpotential during plating (charging) and stripping (discharging). The cell was first cycled at a high current density of 1 mA cm⁻² with an areal capacity of 1 mAh cm⁻² for 140 hours, followed by a low current density of 0.1 mA cm⁻² for another 80 hours. Further, a high C.E. of 99.995% was achieved with a very low overpotential of less than 0.05 V and 0.025 V when cycled at high (1 mA cm⁻²) and low (0.1 mA cm⁻²) current densities, as shown in **Figure 3.10 (c)**.

Notably, the observed overpotential in the WiSE is significantly lower than that in the diluted electrolyte (**Appendix IV**). This result is promising since the high C.E. and low overpotential

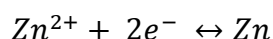
are crucial features for ensuring stable Zn stripping/plating and, consequently, the prolonged cycle life of the battery. In summary, the $Zn(ClO_4)_2$ -based WiSE possesses key characteristics that should ensure stable Zn stripping/plating in a ZnG-DIB, improving the battery performance and extending the cycle life.

3.3.2 Performance of full-cell

A schematic illustration of the working mechanism of the ZnG-DIB during the (dis)charge processes is presented in **Figure 3.11**. During charging, Zn^{2+} ions in the electrolyte migrate to the Zn anode and deposit on it, while ClO_4^- anions simultaneously migrate to the graphite paper (GP) cathode and intercalate between the graphite layers. Upon discharge, both ions are released back into the electrolyte.

The electrochemical reactions during (dis)charging are proposed as follows.

At anode:



At cathode:

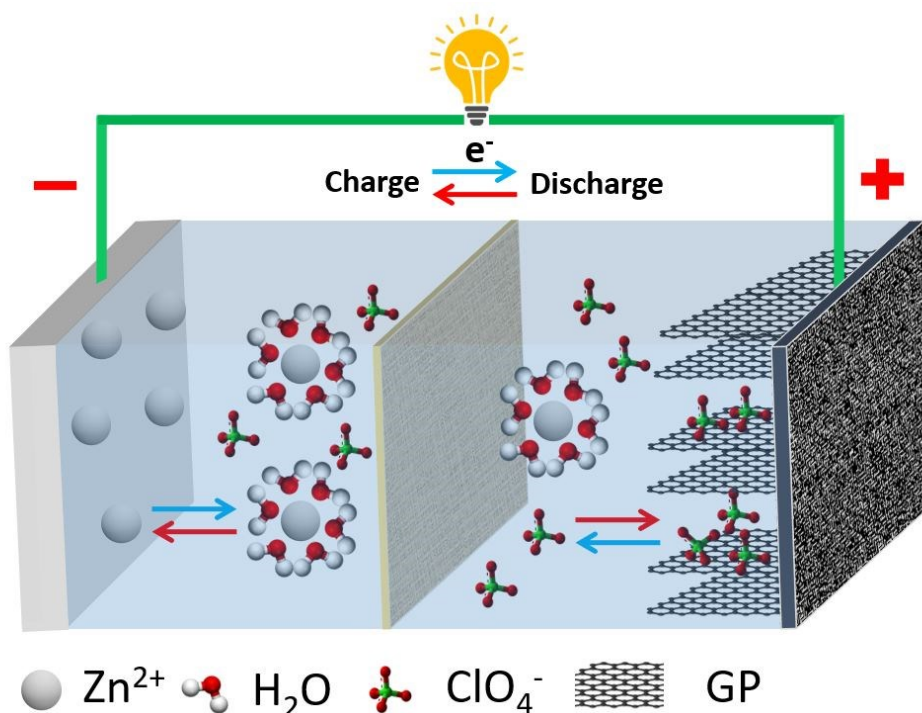
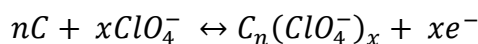


Figure 3.11. Schematic of a Zn-graphite dual-ion battery working mechanism.

The as-assembled ZnG-DIB and a practical demonstration of powering a red 2 V LED with this battery are demonstrated in *Appendix IV (Figure 3 (a))*. The fabrication of this two-electrode ZnG-DIB involved assembling a Zn metal anode, a GF/D glass microfiber separator, a low-cost and binder-free GP cathode, and an as-prepared zinc perchlorate WiSE. Detailed information on the experimental procedure is provided in the *Experimental section in Appendix IV*.

To modify the surface of the pristine GP, a Kapton tape was used to peel off the surface, as shown in *Appendix IV (Figure 3 (b))*, which presents photos and SEM images of the pristine GP before and after the peeling. Before the peeling, the GP surface was glossy, resembling a metal sheet, whereas, after the surface modification, it exhibited a 3D surface structure consisting of multilayers of crumpled graphene sheets with a matte appearance. One notable advantage of this surface modification strategy is the improved wettability and fast electrolyte saturation of the GP, as evidenced by the low contact angle of the modified GP (approximately 30°) compared to that of the pristine GP (approximately 60°). Due to the porous 3D surface and reduced hydrophobicity, a drop of the WiSE spread and was absorbed instantly on the surface of the modified GP.

The electrochemical characterization of a ZnG-DIB using CV is presented in *Appendix IV (Figure 3 (d))*. The CV was conducted at different scan rates and in the voltage range of 0.5 to 2.5 V vs. Zn²⁺/Zn to investigate the (de)intercalation of ClO₄⁻ anions into and from the graphite cathode. There were observed three redox peaks in the CV, which were similar to the results in *Figure 3.8*. The oxidation peak (I_{pa}) at 2.45 V is related to the intercalation of ClO₄⁻ anions into the graphite, while two reduction peaks I_{pc} (2.20 V) and I_{pc}' (2.0 V) are associated with the deintercalation of ClO₄⁻ anions from graphite. The ClO₄⁻ intercalation process appears to involve at least two steps, as suggested by the multiple reduction peaks observed.

The galvanostatic charge discharge (GCD) analysis of ZnG-DIB was performed at different cut-off potentials in the range of 2.2 V to 2.6 V vs. Zn²⁺/Zn at 100 mA g⁻¹. The GCD results are presented in *Figure 3.12 (a)*. The optimum upper cut-off potential of 2.5 V was determined based on a comparative graph of upper cut-off voltage vs. discharged capacity and C.E., as shown in *Appendix IV (Figure 4 (b))*. All subsequent long-term cycling and rate-capability tests were performed at this cut-off voltage. During the cycling tests, the discharged capacity gradually increased from around 30 mAh g⁻¹ at 100 mA g⁻¹ to 45 mAh g⁻¹ with an improved C.E., as shown in *Figure 3.12 (c)*. The highest C.E. of over 90% was achieved at a current

density of 300 mA g^{-1} but at the cost of reduced capacity, which decreased to 20 mAh g^{-1} . The battery showed a recoverable capacity profile and very small capacity decay when tested back at low current densities (300 to 100 mA g^{-1}). The ZnG-DIB performed stably at the cut-off potential of 2.5 V for up to 500 cycles. The battery also demonstrated a high and stable mean-discharge voltage of $\sim 1.95 \text{ V}$ vs. Zn^{2+}/Zn , which is higher than most reported Zn-ion batteries with conventional manganese and vanadium oxide cathodes and Li^+ chemistry-free ZnG-DIBs

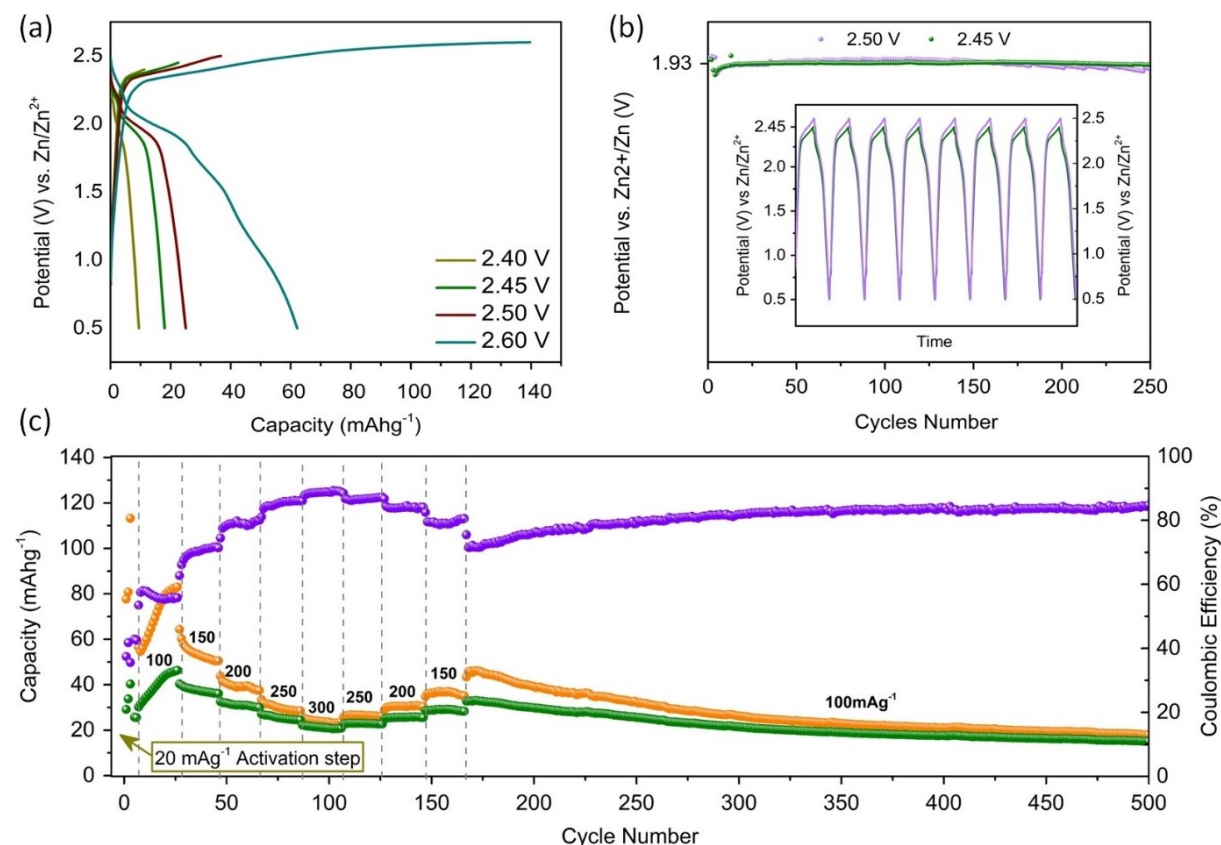


Figure 3.12 Charge-discharge curves at different cut-off potentials at 100 mA g^{-1} (a), demonstration of the mean-discharge voltage and charge-discharge profile (inset) of the ZnG-DIB at the cut-off potentials of 2.45 V (green) and 2.5 V (purple) vs. Zn^{2+}/Zn . (b), and rate-capability and long-cycling tests at a cut-off voltage of 2.5 V vs. Zn^{2+}/Zn (c).

Operando-XRD

Operando-XRD was utilized to investigate the (de)intercalation of ClO_4^- anions into GP electrode. The tests were performed using a homemade 2-electrode cell, as described in **Section 3.2**, and the results are presented in **Figure 3.13**. The operando-XRD findings were found to be consistent with those obtained from operando Raman spectroscopy in **Appendix IV** (**Figure 6 (a)**). The 002 peak (26.7°) of the graphite cathode gradually splits and shifts towards a lower 2θ angle ($\sim 25.2^\circ$) upon charging but recovers after discharging. The peak becomes broader,

and its intensity decreases, indicating the intercalation of anions into graphite. However, the presence of the 002-reflection peak in the fully charged cathode indicates a partial intercalation process, suggesting the formation of GICs of higher-stages. These results are also consistent with the kinetic analysis in *Appendix IV* (Figure 3 (e-g)), which suggests that both diffusion and adsorption processes contribute to the capacity. A schematic of anion (de)intercalation (from)into graphite on (dis)charging and *Operando*-XRD results of a ZnG-DIB are presented in *Figure 3.13*.

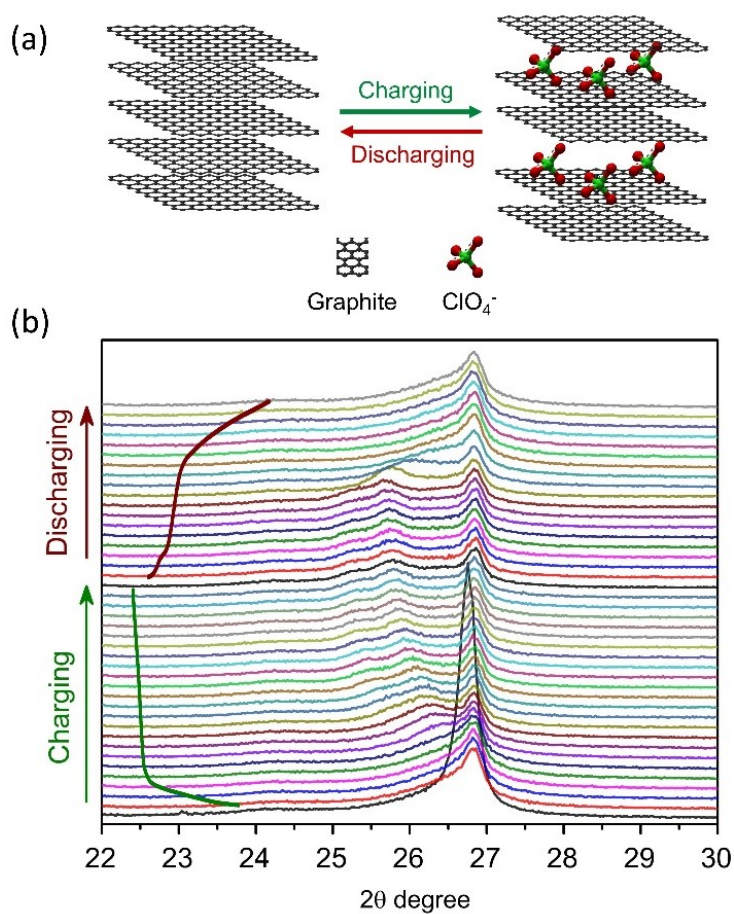


Figure 3.13. Schematic of anion (de)intercalation (from)into graphite on (dis)charging (a), and *Operando*-XRD results of a ZnG-DIB (b).

4 Conclusions

This thesis addresses the fundamental issue of a narrow electrochemical stability window in aqueous electrolytes and demonstrates a feasible strategy to widen it. Furthermore, it investigates the electrochemical energy storage mechanisms in high-voltage electrodes using water-in-salt electrolytes (WiSE). Finally, the thesis presents a high-voltage aqueous battery based on a Zn-metal anode and a high-voltage graphite cathode comprising a Zn-based WiSE. The results of the separate investigations are summarized in **Section 3** of this thesis.

Section 3.1 discusses multivalent zinc and aluminum perchlorate-based WiSE systems, their preparation and properties for energy storage applications. The electrochemical and physical properties of the WiSE, such as ESW and temperature dependence of ionic conductivity, are discussed. Both WiSE systems demonstrated high ionic conductivity in the wide temperature range of -30 to 60 °C. The WiSE based on aluminum- and zinc-perchlorate exhibited ESW of ~ 4 V and 2.8 V, respectively. The wide ESWs are attributed to the strong chaotropic nature of ClO_4^- anion and the localization of water at multivalent kosmotropic cations. Raman spectroscopy was used to examine the hydration of Zn^{2+} and Al^{3+} cations in the considered WiSE systems. It has been found that the chaotropic (hydrophobic) strength of the counter anion is a crucial factor in selecting suitable zinc or aluminum salts for WiSE to attain a wide electrochemical stability window (ESW). The study reveals that chaotropic ions in the Hofmeister series are promising candidates for developing high-voltage WiSE and graphite-based dual-ion batteries.

Section 3.2 presents the results of the anion (ClO_4^-) intercalation into various graphitic materials, including HOPG, NG, KG, and US-NG, that possess high oxidation potentials. The high oxidative stability >1.65 vs. Ag/AgCl or >2.60 V vs. Zn^{2+}/Zn in both Zn and Al-based WiSE enabled the anion intercalation into these graphitic materials, which was not feasible in dilute electrolytes due to their narrow ESW. Different electrochemical and *operando*-spectroscopy techniques were used to study the reversibility and stability of anion-intercalation into the graphitic materials. Additionally, the mechanism of charge storage was also investigated by the CV kinetic analysis. It was concluded that the capacity contribution in all the graphitic materials from the WiSE systems contains a mixture of pseudocapacitive and diffusion mechanisms. Furthermore, the degree of graphitization (DoG) and the effects of structural defects and ultrasonication treatment were investigated on anion-intercalation processes in the graphitic materials. It was found that higher DoG supports the anion-

intercalation (diffusion process) and helps to achieve a high-mean discharge voltage plateau. Additionally, ultrasonication helps in increasing the stability and long cycling in graphitic materials during the process of (de)intercalation. For instance, in the case of ultrasonicated highly crystallized HOPG (*Appendix I*), stable and reversible intercalation of perchlorate anions in a half-cell configuration was achieved in $\text{Al}(\text{ClO}_4)_2$ -WiSE for more than 2000 cycles, with a high Coulombic efficiency of over 95%.

Section 3.3 demonstrates the realization of a high-voltage Zn-graphite dual-ion battery using chaotropic anion-based $\text{Zn}(\text{ClO}_4)_2$ -WiSE, a Zn anode, and a low-cost free-standing and binder-free graphite cathode. The WiSE with a wide electrochemical stability window of 2.80 V allowed for stable and reversible Zn plating/stripping with very low overpotentials and high Coulombic efficiency. Additionally, the high oxidative stability of the electrolyte supported the efficient (de)intercalation of ClO_4^- anions into the graphite cathode at high potentials and allowed using a high upper cut-off potential of 2.5 V vs. Zn^{2+}/Zn . The battery demonstrated a maximum discharged capacity of 45 mAh g^{-1} at 100 mA h^{-1} and an average discharged capacity of 23.5 mA h g^{-1} for over 500 cycles, along with a high mean discharge voltage of approximately 1.95 V vs. Zn^{2+}/Zn .

In summary, WiSE based on chaotropic anion and multivalent metal cations offers a wide stability window and a suitable aqueous electrolyte system for designing high-voltage, non-flammable, and low-cost metal-graphite batteries. The battery is not suitable for mobile applications but might be used in grid storage applications. Although further optimization and improvements are still required, for instance, improvement of capacity. Also, the Coulombic efficiency of the battery was relatively low in Zn perchlorate-based WiSE, which suggests parasitic reactions occurring at high potentials. Another issue is the absence of the formation of stable SEI/CEI layers to prevent parasitic reactions on the electrode surfaces.

The following suggestions are proposed to address these issues and further improve the battery performance.

Capacity improvements: Graphitic materials with a higher degree of graphitization containing a highly edged surface area, small lateral size flakes, or 3D structures can be tested to fasten the kinetics by reducing the diffusion paths and providing more intercalation sites. Furthermore, other anion-intercalation hosting materials with open 3D structures or layered structures by π - π stacking can be investigated, such as PAH, MOFs, and other organic electrode materials (OEMs), which offer higher capacity and faster kinetics, e.g., due to fast surface

coordination reactions to store ions. Another interesting strategy might be designing special hybrid materials based on, for instance, hybrid intercalation-type (graphite, etc.) or conversion-type cathodes materials (sulfur, chalcogenides, etc.).

Mitigation of parasitic reactions and improvements of Coulombic efficiency: One of the reasons why the demonstrated battery has a low capacity could be a parasitic reaction at high potentials. This could also be because the anion intercalation in graphite happens at very high potentials, which are already at the limits of the oxidative stability of the WiSE. Therefore, one way could be to extend the ESW of the WiSE electrolyte further either by employing quasi-solid-state electrolytes (polymer-based), which can make water unavailable for decomposition. Another possibility might be designing *in-situ* or *ex-situ* SEI/CEI to prevent e-transfers from electrodes to the electrode to avoid its reduction at the anode side and oxidation at the cathode side. The formation of SEI/CEI can be achieved either through the sacrificial reduction of electrolyte additives or by physical means like molecular-layer deposition (MLD) or atomic-layer deposition (ALD).

References

1. R. Chen, R. Luo, Y. Huang, F. Wu and L. Li, *Advanced Science* 2016, **3**, 1600051.
2. J. J. H. Togonon, P.-C. Chiang, H.-J. Lin, W.-C. Tsai and H.-J. Yen, *Carbon Trends*, 2021, **3**, 100035.
3. T. Placke, A. Heckmann, R. Schmuch, P. Meister, K. Beltrop and M. Winter, *Joule*, 2018, **2**, 2528-2550.
4. L. Zhang, H. Wang, X. Zhang and Y. Tang, *Advanced Functional Materials*, 2021, **31**, 2010958.
5. S. Ko, Y. Yamada, K. Miyazaki, T. Shimada, E. Watanabe, Y. Tateyama, T. Kamiya, T. Honda, J. Akikusa and A. Yamada, *Electrochemistry Communications*, 2019, **104**, 106488.
6. H. Xu, H. Chen and C. Gao, *ACS Materials Letters*, 2021, **3**, 1221-1237.
7. L. Zhao, A. E. Lakraychi, Z. Chen, Y. Liang and Y. Yao, *ACS Energy Letters*, 2021, **6**, 3287–3306.
8. L. Gaines, K. Richa and J. Spangenberg, *MRS Energy & Sustainability*, 2018, **5**, 12.
9. L. da Silva Lima, L. Cocquyt, L. Mancini, E. Cadena and J. Dewulf, *Journal of Industrial Ecology*, 2022, **00**, 1– 18.
10. J. L. Matthew Li, *Science*, 2020, **367**, 978-979.
11. B. Dunn, H. Kamath and J.-M. Tarascon, *Science*, 2011, **334**, 928-935.
12. *IEA, Paris, 2022*, <https://www.iea.org/reports/global-ev-outlook-2022>, License: CC BY 4.0.
13. W. Manalastas, Jr., S. Kumar, V. Verma, L. Zhang, D. Yuan and M. Srinivasan, *ChemSusChem*, 2019, **12**, 379-396.
14. M. Li, J. Lu, X. Ji, Y. Li, Y. Shao, Z. Chen, C. Zhong and K. Amine, *Nature Reviews Materials*, 2020, **5**, 276-294.
15. Z. A. Zafar, G. Abbas, K. Knizek, M. Silhavič, P. Kumar, P. Jiricek, J. Houdkova, O. Frank and J. Cervenka, *Journal of Materials Chemistry A*, 2022, **10**, 2064-2074.
16. S. Wang, Y. Guan, F. Gan and Z. Shao, *ChemSusChem*, 2022, **16**, e202201373.
17. M.-x. Jing, H. Yang, H. Chong, F. Chen, L.-k. Zhang, X.-y. Hu, F.-y. Tu and X.-q. Shen, *Journal of The Electrochemical Society*, 2019, **166**, A3019.
18. Z. A. Zafar, G. Abbas, M. Silhavič, K. Knizek, O. Kaman, F. J. Sonia, P. Kumar, P. Jiricek, J. Houdková, O. Frank and J. Cervenka, *Electrochimica Acta*, 2022, **404**, 139754.

19. R. J. Brodd, K. R. Bullock, R. A. Leising, R. L. Middaugh, J. R. Miller and E. Takeuchi, *Journal of The Electrochemical Society*, 2004, **151**, K1.
20. D. Guyomard and J.-M. Tarascon, *Advanced Materials*, 1994, **6**, 408-412.
21. M. Wu, J. Liao, L. Yu, R. Lv, P. Li, W. Sun, R. Tan, X. Duan, L. Zhang, F. Li, J. Kim, K. H. Shin, H. Seok Park, W. Zhang, Z. Guo, H. Wang, Y. Tang, G. Gorgolis, C. Galiotis and J. Ma, *Chemistry an Asian Journal*, 2020, **15**, 995-1013.
22. P. Li, G. Zhao, X. Zheng, X. Xu, C. Yao, W. Sun and S. X. Dou, *Energy Storage Materials*, 2018, **15**, 422-446.
23. K. Huang, S. Bi, B. Kurt, C. Xu, L. Wu, Z. Li, G. Feng and X. Zhang, *Angewandte Chemie*, 2021, **60**, 19232-19240.
24. X. Zhou, Q. Liu, C. Jiang, B. Ji, X. Ji, Y. Tang and H. M. Cheng, *Angewandte Chemie*, 2019, **59**, 3802-3832.
25. J. Ma, Y. Li, N. S. Grundish, J. B. Goodenough, Y. Chen, L. Guo, Z. Peng, X. Qi, F. Yang, L. Qie, C.-A. Wang, B. Huang, Z. Huang, L. Chen, D. Su, G. Wang, X. Peng, Z. Chen, J. Yang, S. He, X. Zhang, H. Yu, C. Fu, M. Jiang, W. Deng, C.-F. Sun, Q. Pan, Y. Tang, X. Li, X. Ji, F. Wan, Z. Niu, F. Lian, C. Wang, G. G. Wallace, M. Fan, Q. Meng, S. Xin, Y.-G. Guo and L.-J. Wan, *Journal of Physics D: Applied Physics*, 2021, **54**, 183001.
26. X. Ou, D. Gong, C. Han, Z. Liu and Y. Tang, *Advanced Energy Materials*, 2021, **11**, 2102498.
27. W.-H. Li and X.-L. Wu, *Electrochemical Science Advances*, 2022, **2**, e2100127.
28. T. Placke, P. Bieker, S. F. Lux, O. Fromm, H.-W. Meyer, S. Passerini and M. Winter, *Zeitschrift für Physikalische Chemie*, 2012, **226**, 391-407.
29. M. Noel and R. Santhanam, *Journal of Power Sources*, 1998, **72**, 53-65.
30. W. Rüdorff and U. Hofmann, *Zeitschrift für Anorganische und Allgemeine Chemie*, 1938, **238**, 1-50.
31. P. T. MICHEL ARMAND, *Materials Science and Engineering*, 1977, **31**, 319-329.
32. J. S. Dunning, W. H. Tiedemann, L. Hsueh and D. N. Bennion, *Journal of The Electrochemical Society*, 1971, **118**, 1886.
33. F.P., L.C.A. McCullough, R.V.U.S. Snelgrove, *Patent*, 1989, **4**, 830-938.
34. R. T. Carlin, H. C. De Long, J. Fuller and P. C. Trulove, *Journal of The Electrochemical Society*, 1994, **141**, L73.
35. J. Li, K. S. Hui, D. A. Dinh, S. Wu, X. Fan, F. Chen and K. N. Hui, *Materials Today Sustainability*, 2022, **19**, 100188.
36. J. A. Read, A. V. Cresce, M. H. Ervin and K. Xu, *Energy & Environmental Science*, 2014, **7**, 617-620.

37. S. Rothermel, P. Meister, G. Schmuelling, O. Fromm, H.-W. Meyer, S. Nowak, M. Winter and T. Placke, *Energy & Environmental Science*, 2014, **7**, 3412-3423.
38. M. C. Lin, M. Gong, B. Lu, Y. Wu, D. Y. Wang, M. Guan, M. Angell, C. Chen, J. Yang, B. J. Hwang and H. Dai, *Nature*, 2015, **520**, 325-328.
39. Y. Li, Q. Guan, J. Cheng and B. Wang, *Energy & Environmental Materials*, 2022, **5**, 1285-1293.
40. D. Ma, D. Yuan, C. Ponce de León, Z. Jiang, X. Xia and J. Pan, *Energy & Environmental Materials*, 2022, **6**, e12301.
41. Y. Yu, Q. Zhang, J. Chen and S.-G. Sun, *Energy & Fuels*, 2021, **35**, 10945-10948.
42. N. Shpigel, F. Malchik, M. D. Levi, B. Gavriel, G. Bergman, S. Tirosh, N. Leifer, G. Goobes, R. Cohen, M. Weitman, H. Aviv, Y. R. Tischler, D. Aurbach and Y. Gogotsi, *Energy Storage Materials*, 2020, **32**, 1-10.
43. Y. Wang, R. Chen, T. Chen, H. Lv, G. Zhu, L. Ma, C. Wang, Z. Jin and J. Liu, *Energy Storage Materials*, 2016, **4**, 103-129.
44. J. Fan, Q. Xiao, Y. Fang, L. Li and W. Yuan, *Ionics*, 2018, **25**, 1303-1313.
45. X. Wu, Y. Xu, C. Zhang, D. P. Leonard, A. Markir, J. Lu and X. Ji, *Journal of American Chemical Society*, 2019, **141**, 6338-6344.
46. M. Guo, C. Fu, M. Jiang, Y. Bai, J. Zhang and B. Sun, *Journal of Alloys and Compounds*, 2020, **838**, 155640.
47. V. Soundharrajan, B. Sambandam, S. Kim, V. Mathew, J. Jo, S. Kim, J. Lee, S. Islam, K. Kim, Y.-K. Sun and J. Kim, *ACS Energy Letters*, 2018, **3**, 1998-2004.
48. H. D. Yoo, I. Shterenberg, Y. Gofer, G. Gershinsky, N. Pour and D. Aurbach, *Energy & Environmental Science*, 2013, **6**, 2265.
49. V. Koleva, M. Kalapsazova, D. Marinova, S. Harizanova and R. Stoyanova, *ChemSusChem*, 2023, **16**, e202201442.
50. L. Zhang, H. Fan and H. Wang, *Electrochimica Acta*, 2020, **342**, 135992.
51. B. Ji, W. Yao and Y. Tang, *Sustainable Energy & Fuels*, 2020, **4**, 101-107.
52. Y. Zhu, J. Yin, X. Zheng, A.-H. Emwas, Y. Lei, O. F. Mohammed, Y. Cui and H. N. Alshareef, *Energy and Environment Science*, 2021, **14**, 4463-4473.
53. H. Li, T. Kurihara, D. Yang, M. Watanabe and T. Ishihara, *Energy Storage Materials*, 2021, **38**, 454-461.
54. T. Ishihara, K. Inda and T. Kurihara, *ECS Meeting Abstracts*, 2019, **MA2019-04**, 3.
55. Y. Tian, Y. An, J. Feng and Y. Qian, *Materials Today*, 2022, **52**, 225-249.
56. P. Peljo and H. H. Girault, *Energy & Environmental Science*, 2018, **11**, 2306-2309.

57. M. Á. Muñoz-Márquez, M. Zarrabeitia, S. Passerini and T. Rojo, *Advanced Materials Interfaces*, 2022, **9**, 2101773.
58. J. Guo, Z. Wen, M. Wu, J. Jin and Y. Liu, *Electrochemistry Communications*, 2015, **51**, 59-63.
59. M. Liu, W. Zhang and W. Zheng, *ChemSusChem*, 2023, **16**, e202300148.
60. A. M. Haregewoin, A. S. Wotango and B.-J. Hwang, *Energy & Environmental Science*, 2016, **9**, 1955-1988.
61. Y. Matsuda and M. Morita, *Journal of Power Sources*, 1987, **20**, 273-278.
62. Q. Q. Liu, D. J. Xiong, R. Petibon, C. Y. Du and J. R. Dahn, *Journal of The Electrochemical Society*, 2016, **163**, A3010.
63. S. Miyoshi, H. Nagano, T. Fukuda, T. Kurihara, M. Watanabe, S. Ida and T. Ishihara, *Journal of The Electrochemical Society*, 2016, **163**, A1206.
64. T. Mukra, Y. Horowitz, I. Shekhtman, M. Goor, S. Drvarič Talian, L. Burstein, J. Kasnatscheew, P. Meister, M. Grünebaum, M. Winter, H.-D. Wiemhöfer, D. Golodnitsky and E. Peled, *Electrochimica Acta*, 2019, **307**, 76-82.
65. P. Hong, M. Xu, X. Zheng, Y. Zhu, Y. Liao, L. Xing, Q. Huang, H. Wan, Y. Yang and W. Li, *Journal of Power Sources*, 2016, **329**, 216-224.
66. E. R. Logan, E. M. Tonita, K. L. Gering, L. Ma, M. K. G. Bauer, J. Li, L. Y. Beaulieu and J. R. Dahn, *Journal of The Electrochemical Society*, 2018, **165**, A705.
67. X. Tong, X. Ou, N. Wu, H. Wang, J. Li and Y. Tang, *Advanced Energy Materials*, 2021, **11**, 2100151.
68. A. Heckmann, J. Thienenkamp, K. Beltrop, M. Winter, G. Brunklaus and T. Placke, *Electrochimica Acta*, 2018, **260**, 514-525.
69. Z. Guo, G. Cheng, Z. Xu, F. Xie, Y.-S. Hu, C. Mattevi, M.-M. Titirici and M. Crespo Ribadeneyra, *ChemSusChem*, 2023, **16**, e202201583.
70. T. Liu, X. Han, Z. Zhang, Z. Chen, P. Wang, P. Han, N. Ding and G. Cui, *Journal of Power Sources*, 2019, **437**, 226942.
71. J. Fan, Q. Xiao, Y. Fang, L. Li, W. Feng and W. Yuan, *ChemElectroChem*, 2019, **6**, 676-683.
72. B. Heidrich, A. Heckmann, K. Beltrop, M. Winter and T. Placke, *Energy Storage Materials*, 2019, **21**, 414-426.
73. Z. Lv, M. Han, J. Sun, L. Hou, H. Chen, Y. Li and M.-C. Lin, *Journal of Power Sources*, 2019, **418**, 233-240.
74. H. Sun, W. Wang, Z. Yu, Y. Yuan, S. Wang and S. Jiao, *Chemical communications*, 2015, **51**, 11892-11895.
75. Z. A. Zafar, S. Imtiaz, R. Li, J. Zhang, R. Razaq, Y. Xin, Q. Li, Z. Zhang and Y. Huang, *Solid State Ionics*, 2018, **320**, 70-75.

76. D. J. Kim, D.-J. Yoo, M. T. Otley, A. Prokofjevs, C. Pezzato, M. Owczarek, S. J. Lee, J. W. Choi and J. F. Stoddart, *Nature Energy*, 2018, **4**, 51-59.
77. D. Chao, W. Zhou, F. Xie, C. Ye, H. Li, M. Jaroniec and S. Z. Qiao, *Science Advances*, 2020, **6**, eaba4098.
78. P. Kulkarni, D. Ghosh and R. G. Balakrishna, *Sustainable Energy and Fuels*, 2021, **5**, 1619-1654.
79. C. Dong, F. Xu, L. Chen, Z. Chen and Y. Cao, *Small Structures*, 2021, **2**, 2100001.
80. Y. Sui and X. Ji, *Chemical Reviews*, 2021, **121**, 6654-6695.
81. W. Li, J. R. Dahn and D. S. Wainwright, *Science*, 1994, **264**, 1115-1118.
82. J. J. Shea and C. Luo, *ACS Applied Materials & Interfaces*, 2020, **12**, 5361-5380.
83. S. Dühnen, J. Betz, M. Kolek, R. Schmuch, M. Winter and T. Placke, *Small Methods*, 2020, **4**, 2000039.
84. L. Suo, O. Borodin, T. Gao, M. Olguin, J. Ho, X. Fan, C. Luo, C. Wang and K. Xu, *Science*, 2015, **350**, 938-943.
85. Y. Yamada, K. Usui, K. Sodeyama, S. Ko, Y. Tateyama and A. Yamada, *Nature Energy*, 2016, **1**, 16129.
86. C. Yang, J. Chen, X. Ji, T. P. Pollard, X. Lü, C.-J. Sun, S. Hou, Q. Liu, C. Liu, T. Qing, Y. Wang, O. Borodin, Y. Ren, K. Xu and C. Wang, *Nature*, 2019, **569**, 245-250.
87. Y. Yamada, J. Wang, S. Ko, E. Watanabe and A. Yamada, *Nature Energy*, 2019, **4**, 269-280.
88. X. Ou, D. Gong, C. Han, Z. Liu and Y. Tang, *Advanced Energy Materials*, 2021, **11**, 2102498.
89. P. E. Mason, F. Uhlig, V. Vaněk, T. Buttersack, S. Bauerecker and P. Jungwirth, *Nature Chemistry*, 2015, **7**, 250-254.
90. G. Wang, M. Yu, J. Wang, D. Li, D. Tan, M. Löffler, X. Zhuang, K. Müllen and X. Feng, *Advanced Materials*, 2018, **30**, 1800533.
91. W.-H. Li, Q.-L. Ning, X.-T. Xi, B.-H. Hou, J.-Z. Guo, Y. Yang, B. Chen and X.-L. Wu, *Advanced Materials*, 2019, **31**, 1804766.
92. H.-g. Wang, H. Wang, Z. Si, Q. Li, Q. Wu, Q. Shao, L. Wu, Y. Liu, Y. Wang, S. Song and H. Zhang, *Angewandte Chemie International Edition*, 2019, **58**, 10204-10208.
93. S. Xu, H. Dai, S. Zhu, Y. Wu, M. Sun, Y. Chen, K. Fan, C. Zhang, C. Wang and W. Hu, *eScience*, 2021, **1**, 60-68.
94. A. Byeon, M.-Q. Zhao, C. E. Ren, J. Halim, S. Kota, P. Urbankowski, B. Anasori, M. W. Barsoum and Y. Gogotsi, *ACS Applied Materials & Interfaces*, 2017, **9**, 4296-4300.
95. H. Zhang, Y. Yang, D. Ren, L. Wang and X. He, *Energy Storage Materials*, 2021, **36**, 147-170.

96. J. Liu, X. Li, Q. Wang, Y. Kawazoe and P. Jena, *Journal of Materials Chemistry A*, 2018, **6**, 13816-13824.
97. W. Zhou, W. Y. Tong, Y. Wang, D. Y. W. Yu and P. H. L. Sit, *The Journal of Physical Chemistry C*, 2019, **123**, 18132-18141.
98. K. I. Bolotin, K. J. Sikes, Z. Jiang, M. Klima, G. Fudenberg, J. Hone, P. Kim and H. L. Stormer, *Solid State Communications*, 2008, **146**, 351-355.
99. K. V. Kravchyk and M. V. Kovalenko, *MRS Energy & Sustainability*, 2020, **7**.
100. Y. Sui, C. Liu, R. C. Masse, Z. G. Neale, M. Atif, M. AlSalhi and G. Cao, *Energy Storage Materials*, 2020, **25**, 1-32.
101. P. Canepa, G. Sai Gautam, D. C. Hannah, R. Malik, M. Liu, K. G. Gallagher, K. A. Persson and G. Ceder, *Chemical Reviews*, 2017, **117**, 4287-4341.
102. J. Gao, S. Tian, L. Qi and H. Wang, *Electrochimica Acta*, 2015, **176**, 22-27.
103. M. Chugh, M. Jain, G. Wang, A. S. Nia, H. Mirhosseini and T. D. Kühne, *Materials Research Express*, 2021, **8**, 085502.
104. G. Abbas, F. J. Sonia, Z. A. Zafar, K. Knížek, J. Houdková, P. Jiříček, M. Bouša, J. Plšek, M. Kalbáč, J. Červenka and O. Frank, *Carbon*, 2022, **186**, 612-623.
105. G. Abbas, Z. A. Zafar, F. J. Sonia, K. Knizek, J. Houdkova, P. Jiricek, M. Kalbac, J. Cervenka and O. Frank, *Nanomaterials* , 2022, **12**, 3932.
106. T. Placke, S. Rothermel, O. Fromm, P. Meister, S. F. Lux, J. Huesker, H.-W. Meyer and M. Winter, *Journal of The Electrochemical Society*, 2013, **160**, A1979.
107. A. Heckmann, O. Fromm, U. Rodehorst, P. Münster, M. Winter and T. Placke, *Carbon*, 2018, **131**, 201-212.
108. G. Wang, M. Yu and X. Feng, *Chemical Society Reviews*, 2021, **50**, 2388-2443.
109. Z. Guo, Z. Xu, F. Xie, J. Feng and M. Titirici, *Advanced Energy and Sustainability Research*, 2021, **11**, 2100074.
110. G. G. Eshetu, G. A. Elia, M. Armand, M. Forsyth, S. Komaba, T. Rojo and S. Passerini, *Advanced Energy Materials*, 2020, **10**, 2000093.
111. C. Jiang, L. Xiang, S. Miao, L. Shi, D. Xie, J. Yan, Z. Zheng, X. Zhang and Y. Tang, *Advanced Materials*, 2020, **32**, e1908470.
112. K. Yang, Q. Liu, Y. Zheng, H. Yin, S. Zhang and Y. Tang, *Angewandte Chemie*, 2021, **60**, 6326-6332.
113. Y. Li, Y. Lu, P. Adelhelm, M. M. Titirici and Y. S. Hu, *Chemical Society Reviews*, 2019, **48**, 4655-4687.
114. A. Lerf, *Dalton Transactions*, 2014, **43**, 10276-10291.
115. W. H. Li and X. L. Wu, *Electrochemical Science Advances*, 2021, **2**, e2100127.

116. A. Heckmann, P. Meister, L.-Y. Kuo, M. Winter, P. Kaghazchi and T. Placke, *Electrochimica Acta*, 2018, **284**, 669-680.
117. R. Borah, F. R. Hughson, J. Johnston and T. Nann, *Materials Today Advances*, 2020, **6**, 100046.
118. C. Sole, N. E. Drewett and L. J. Hardwick, *Faraday Discussions*, 2014, **172**, 223-237.
119. B. Ji, F. Zhang, X. Song and Y. Tang, *Advanced Materials*, 2017, **29**, 1700519.
120. J. C. Chacon-Torres, L. Wirtz and T. Pichler, *ACS Nano*, 2013, **7**, 9249-9259.
121. A. M. Tripathi, W. N. Su and B. J. Hwang, *Chemical Society Reviews*, 2018, **47**, 736-.
122. M. S. Dresselhaus, *NATO ASI series. Series B, Physics*, 1986, **148**, ISBN 0306424835.
123. C. Yang, J. Chen, X. Ji, T. P. Pollard, X. Lu, C. J. Sun, S. Hou, Q. Liu, C. Liu, T. Qing, Y. Wang, O. Borodin, Y. Ren, K. Xu and C. Wang, *Nature*, 2019, **569**, 245-250.
124. J. Han, A. Mariani, S. Passerini and A. Varzi, *Energy & Environmental Science*, 2023, **16**, 1480-1501.
125. D. Reber, R. Grissa, M. Becker, R. S. Kühnel and C. Battaglia, *Advanced Energy Materials*, 2020, **11**, 2002913.
126. A. Salis and B. W. Ninham, *Chemical Society Reviews*, 2014, **43**, 7358-7377.
127. G. Yang, J. Huang, X. Wan, B. Liu, Y. Zhu, J. Wang, O. Fontaine, S. Luo, P. Hiralal, Y. Guo and H. Zhou, *EcoMat*, 2022, **4**, e12165 .
128. D. A. B. Schnyder, R. Kötz, H. Siegenthaler, *Applied Surface Science.*, 2001, **173**, 221-232.
129. W. W. Rudolph and C. C. Pye, *Journal of Solution Chemistry*, 1999, **28**, 1045-1070.
130. H. Zhang, G. Guo, H. Adenusi, B. Qin, H. Li, S. Passerini and W. Huang, *Materials Today*, 2022, **53**, 162-172.
131. M. Tebyetekerwa, T. T. Duignan, Z. Xu and X. Song Zhao, *Advanced Energy Materials*, 2022, **12**, 2202450.
132. B. Ji, F. Zhang, N. Wu and Y. Tang, *Advanced Energy Materials*, 2017, **7**, 1700920.
133. W. Zhou and P. H. Sit, *ACS Omega*, 2020, **5**, 18289-18300.
134. C. J. Pan, C. Yuan, G. Zhu, Q. Zhang, C. J. Huang, M. C. Lin, M. Angell, B. J. Hwang, P. Kaghazchi and H. Dai, *Proceedings of the National Academy of Sciences of the United States of America*, 2018, **115**, 5670-5675.
135. V. Augustyn, J. Come, M. A. Lowe, J. W. Kim, P.-L. Taberna, S. H. Tolbert, H. D. Abruña, P. Simon and B. Dunn, *Nature Materials*, 2013, **12**, 518-522.
136. H. Lindström, S. Södergren, A. Solbrand, H. Rensmo, J. Hjelm, A. Hagfeldt and S.-E. Lindquist, *The Journal of Physical Chemistry B*, 1997, **101**, 7717-7722.

137. L. Ma, M. A. Schroeder, O. Borodin, T. P. Pollard, M. S. Ding, C. Wang and K. Xu, *Nature Energy*, 2020, **5**, 743-749.
138. W. Liu, P. Liu and D. Mitlin, *Chemical Society Reviews*, 2020, **49**, 7284-7300.

Complete list of journal publications

1. **Z.A. Zafar**, G. Abbas, K. Knizek, M. Silhavič, P. Kumar, P. Jiricek, J. Houdková, et al., Chaotropic anion based “water-in-salt” electrolyte realizes a high voltage Zn–graphite dual-ion battery, *Journal of Materials Chemistry A*, 2022, **10**, 2064-2074.
2. **Z.A. Zafar**, G Abbas, M Silhavič, K Knizek, O Kaman, FJ Sonia, P Kumar et al. Reversible anion intercalation into graphite from aluminum perchlorate “water-in-salt” electrolyte, *Electrochimica Acta*, 2022, **404**, 139754.
3. **Z.A. Zafar**, S. Imtiaz, R. Razaq, S. Ji, T. Huang, Z. Zhang, Y. Huang, J. A. Anderson, Cathode materials for rechargeable Aluminum batteries. Current progress and future prospects, *Journal of Material Chemistry A*, 2017, **5**, 5646-5660.
4. **Z.A. Zafar**, S. Imtiaz, R. Razaq, S. Ji, Y. Huang, Z. Zhang, A Super-Long Life Rechargeable Aluminum Battery, *Solid State Ionic*, 2018, **320**, 70-75.
5. **Z.A. Zafar**, M. Jamil, M.A. Ahmed, S. Imtiaz, N. Abid, Evaluation of mixing cow dung with apple and banana peels on biogas yield, *World Applied Sciences Journal*, 2014, **29**, 903-907.
6. G Abbas, **Z.A. Zafar**, F.J. Sonia, K Knížek, *et al.*, The Effects of Ultrasound Treatment of Graphite on the Reversibility of the (De)Intercalation of an Anion from Aqueous Electrolyte Solution, *Nanomaterials*, 2022, **12**, 3932.
7. G Abbas, F. J. Sonia, **Z.A. Zafar**, K Knížek, J Houdková, P Jiříček, M Bouša, Influence of structural properties on (de-) intercalation of ClO_4^- anion in graphite from concentrated aqueous electrolyte, *Carbon* 2022, **186**, 612-623.
8. M Šilhavič, P Kumar, **Z.A. Zafar**, M Mišek, M Čičala, M Piliarik, J Červenka, Anomalous elasticity and damping in covalently cross-linked graphene aerogels, *Communications Physics*, 2022, **5**, 1.
9. M Šilhavič, P Kumar, **Z.A. Zafar**, J Červenka, High-Temperature Fire Resistance and Self-Extinguishing Behavior of Cellular Graphene, *ACS Nano*, 2022, **16**, 19403-19411.
10. P Kumar, M Šilhavič, **Z.A. Zafar**, J Červenka, Contact resistance based tactile sensor using covalently cross-linked graphene aerogels, *Nanoscale* 2022, **14** (4), 1440-1451.
11. S. Imtiaz, **Z.A. Zafar**, R. Razaq, D. Sun, Y. Xin, Q. Li, Z. Zhang, L. Zheng, Y. Huang, J. A. Anderson, Electrocatalysis on Separator Modified by Molybdenum Trioxide

- Nanobelts for Lithium–Sulfur Batteries, *Advanced Materials Interfaces* 2018, **5**, 1800243.
12. M. Kazazi, **Z.A. Zafar**, An Improved TiO₂/CNT Nanocomposite Anode Material for Aqueous Rechargeable Aluminum Batteries, *Solid State Ionic*, 2018, **320**, 64-69.
 13. S. Imtiaz, J. Zhang, **Z.A. Zafar**, S. Ji, T. Huang, J. A. Anderson, Z. Zhang, Y. Huang, Biomass-derived nanostructured porous carbons for lithium-sulfur batteries, *Science China Materials*, 2016, **59**, 389-407.

Conference proceedings

1. **Z.A. Zafar**, G. Abbas, A. Wahab, and J. Cervenka, A High Voltage Aqueous Zn-Graphite Battery Utilizing "Water-in-Salt" Electrolyte, *ECS Meet. Abstr.* 2023.
2. **Z.A. Zafar**, G. Abbas, O. Frank, and J. Cervenka, Chaotropic Anion-Based "Water-in-Salt" Electrolytes for Beyond Li-Ion Energy Storage Systems, *ECS, Meet. Abstr.* MA2022-02 2418.
3. **Z.A. Zafar**, K. Knizek, G. Abbas, M. Silhavik, and J. Cervenka, Perchlorate Based "Water -in-Salt" Electrolyte for Electrochemical Energy Storage Systems, *ECS, Meet. Abstr.* MA2021, 023.
4. **Z.A. Zafar**, G. Abbas, M. Silhavik and J. Cervenka, "Water-in-Salt" Electrolyte Promises Reversible Anion Intercalation into Graphite for Energy Storage Applications *ECS, Meet. Abstr.* MA2020,02, 3794.

Patents

1. **Z.A. Zafar**, M. Silhavik, and J. Cervenka, "An aqueous-based energy storage system containing an electrolyte of metal perchlorate", Luxembourg patent LU101731, 2021.
2. **Z.A. Zafar**, M. Silhavik, and J. Cervenka, "A secondary battery with a perchlorate-based electrolyte", European patent application, Reference No. EP21020206.5 (pending).
3. M. Silhavik, P. Kumar, **Z. A. Zafar**, J. Cervenka, "Highly thermally insulating and electrically conductive graphene aerogel and method of manufacturing thereof", Luxembourg patent application, Reference No. LU502730 (pending).

List of Appendices

1. **Z.A. Zafar**, G. Abbas, M. Silhavik, K. Knizek, O. Kaman, F.J. Sonia, P. Kumar, P. Jiricek, J. Houdková, O. Frank, J. Cervenka, Reversible anion intercalation into graphite from aluminum perchlorate “water-in-salt” electrolyte, *Electrochimimica Acta*, 2022, **404**, 139754.
2. G. Abbas, F.J. Sonia, **Z.A. Zafar**, K. Knížek, J. Houdková, P. Jiříček, M. Bouša, J. Plšek, M. Kalbáč, J. Červenka, O. Frank, Influence of structural properties on (de-)intercalation of ClO_4^- anion in graphite from concentrated aqueous electrolyte, *Carbon*, 2022, **186**, 612-623.
3. G. Abbas, **Z.A. Zafar**, F.J. Sonia K. Knížek, J. Houdková, P. Jiříček, M. Kalbáč, J. Červenka, O. Frank, The Effects of Ultrasound Treatment of Graphite on the Reversibility of (De)intercalation of Anion from Aqueous Electrolyte Solution, *Nanomaterials*, 2022, **12**, 3932.
4. **Z. A. Zafar**, G Abbas, K Knizek, M Silhavik, P Kumar, P Jiricek, J Houdková, et al., Chaotropic anion based “water-in-salt” electrolyte realizes a high voltage Zn–graphite dual-ion battery, *Journal of Materials Chemistry A*, 2022, **10**, 2064-2074

Appendix I

Reversible anion intercalation into graphite from aluminum perchlorate “water-in-salt” electrolyte

Z.A. Zafar, G. Abbas, M. Silhavič, K. Knizek, O. Kaman, F.J. Sonia, P. Kumar, P. Jiricek, J. Houdková, O. Frank, J. Cervenka

Annexed: Electrochimica Acta, 2022, 404, 139754



Reversible anion intercalation into graphite from aluminum perchlorate “water-in-salt” electrolyte

Zahid Ali Zafar^{a,b}, Ghulam Abbas^{b,c}, Martin Silhavič^a, Karel Knížek^d, Ondřej Kaman^d,
Farjana J. Sonia^e, Prabhat Kumar^a, Petr Jiríček^e, Jana Houdková^e, Otakar Frank^c,
Jiri Cervenka^{a,*}

^a Department of Thin Films and Nanostructures, FZU - Institute of Physics of the Czech Academy of Sciences, Cukrovarnicka 10/112 162 00 Prague 6, Czech Republic

^b Department of Physical Chemistry and Macromolecular Chemistry, Faculty of Science, Charles University, Hlavova 2030, 128 43 Prague 2, Czech Republic

^c J. Heyrovský Institute of Physical Chemistry of the Czech Academy of Sciences, Dolejškova 2155/3, 183 23 Prague 8, Czech Republic

^d Department of Magnetism and Superconductors, FZU - Institute of Physics of the Czech Academy of Sciences, Cukrovarnicka 10/112 162 00 Prague 6, Czech Republic

^e Department of Optical Materials, FZU - Institute of Physics of the Czech Academy of Sciences, Cukrovarnicka 10/112 162 00 Prague 6, Czech Republic



ARTICLE INFO

Article history:

Received 6 April 2021

Revised 2 November 2021

Accepted 15 December 2021

Available online 22 December 2021

ABSTRACT

Anion intercalated graphite has achieved tremendous attention for the application as cathode materials in dual-ion batteries due to their high working potentials, reversibility, and low cost. However, the process of anion intercalation into graphite requires high oxidative stability of the electrolytes and high reaction potentials above 1.4 V vs. Ag/AgCl (4.5 V vs. Li⁺). Reaching such high potentials is difficult with conventional aqueous electrolytes due to their limited electrochemical window. Here, we demonstrate a highly concentrated “water-in-salt” electrolyte of aluminum perchlorate that demonstrates a wide electrochemical stability window of 4.0 V. The “water-in-salt” electrolyte suppresses the dissociation of water at high potentials, facilitating a stable and reversible perchlorate (ClO₄⁻) anion intercalation into the graphite with a Coulombic efficiency of over 95% for more than 2000 cycles. The structural and chemical changes of the anion-intercalated graphite are studied by *Operando* Raman, *Operando* X-ray diffraction, and X-ray photoelectron spectroscopy. Our study provides an insight into ClO₄⁻ anion intercalation into graphite in the supersaturated aluminum perchlorate “water-in-salt” electrolyte, demonstrating a suitable platform for future high-voltage aqueous energy storage systems.

© 2021 Elsevier Ltd. All rights reserved.

1. Introduction

Graphite has played a crucial role in the development of a wide range of electrochemical energy storage systems (EESS), especially in supercapacitors and lithium-ion batteries [1–3]. It has been commonly employed as an anode material in Li-ion batteries because it allows efficient cation (Li⁺) intercalation and deintercalation. Graphite also tolerates anion intercalation due to its amphoteric redox nature [4–6]. Recently, a number of anion-based graphite intercalation compounds (GICs) have been reported as electrode materials for Li and post-Li EESS [7,8]. Graphite-based electrodes are particularly important for dual-ion batteries, which are emerging as high-voltage post-Li EESS with high energy density, safety, and low cost [7,9]. The ad-

vantage of dual-ion batteries is that they can combine multiple chemistries, including metal cations (Li⁺, Na⁺, K⁺, Ca²⁺, Mg²⁺, Zn²⁺, Al³⁺, etc.) and anions (hexafluorophosphate (PF₆⁻), tetrafluoroborate (BF₄⁻), bis(trifluoromethanesulfonyl)imide (TFSI⁻), bis(fluorosulfonyl)imide (FSI⁻), tetrachloroaluminate (AlCl₄⁻), perchlorate (ClO₄⁻), etc.) [10–16]. As both cations and anions in the electrolyte are involved in the energy storage mechanism of dual-ion batteries, it is important to develop new electrolytes which support the existence of various anion and cation chemistries.

Different types of electrolyte mixtures have been recently investigated for application in graphite-based dual-ion batteries, demonstrating promising results in terms of cycling stability, reversible capacity, and Coulombic efficiency (C.E.) [8,11,16–18]. However, most of the studies of anion intercalation into graphite have included organic electrolytes which are inherently prone to fire hazards and environmental issues [9,19,20]. Aqueous-based electrolytes can overcome safety and environmental issues, but they suffer from a small electrochemical window of 1.23 V [21–

* Corresponding author.

E-mail address: cervenka@fzu.cz (J. Cervenka).

23]. The electrochemical stability window of aqueous electrolytes is also outside the reaction potentials of most of the anion-based GICs, which occur at the ranges of 1.4–1.7 V vs. Ag/AgCl (4.5 V to 5.0 V vs. Li⁺) [24].

Recently, an interesting concept of “water-in-salt” electrolytes (WiSE) using highly concentrated aqueous solutions has been demonstrated [18,25]. The use of high salt concentrations in WiSE enabled expanding the electrochemical window of aqueous electrolytes well beyond the water dissociation limit [26–28]. The WiSE concept has recently led to significant improvements in energy storage performance of different aqueous battery systems, placing WiSE electrolytes on par with organic electrolytes [18,25,27].

Here, we report an electrochemical study of highly concentrated aluminum perchlorate [Al(ClO₄)₃]-based WiSE with a wide electrochemical stability window of 4.0 V. We demonstrate that the electrolyte provides high oxidative stability (> 2 V) and facilitates access to high potentials (above 1.6 V vs. Ag/AgCl) that are necessary to reversibly (de)intercalate ClO₄⁻ anions into graphite. We show that the ClO₄⁻ anion (de)intercalation into graphite is highly reversible in the demonstrated WiSE, similar to organic electrolytes [29–31]. The Al(ClO₄)₃-based WiSE offers stable cycling, high working voltage, and C.E., providing a promising electrolyte platform for high-voltage aqueous EESS.

2. Experimental section

2.1. Preparation of Al(ClO₄)₃ based wise

The Al(ClO₄)₃ based WiSE was prepared by mixing 36.5 g of Al(ClO₄)₃·9H₂O (Alfa-Aesar, 99.999%) into 5 ml of deionized water (conductivity < 0.26 μS cm⁻¹) in the mass ratio of 7.3:1 to get a 15 m (moles per kg) solution under continuous stirring, resulting in a supersaturated transparent solution.

2.2. Preparation of positive electrode

A highly oriented pyrolytic graphite (HOPG) was used as a model positive electrode material to elucidate the electrochemical anion intercalation into graphite due to its well-defined ordered crystal structure and high purity. To prepare a working electrode, a uniform HOPG slurry was fabricated to avoid the disintegration of the bulk HOPG upon the anion intercalation. HOPG was first exfoliated by tip-ultrasonication (Hielscher UP200S, 24 kHz, Germany) using 30 mg of HOPG flakes in 60 ml of *N*-methyl-2-pyrrolidone (NMP) (ROTH®, Germany) at 80% power (160 W) for 6 h. Fig. S1 (Supplementary Information) shows HOPG in NMP before and after the ultrasonication. The exfoliated HOPG flakes were separated by centrifugation and NMP was washed by ethanol. The as-collected micro flakes were mixed with a conductive carbon (Super P, Imerys, France) and polyvinylidene fluoride (PVDF) (Kynar® HSV 1800, Arkema, France) binder dissolved in an NMP disperser (25 mg ml⁻¹) in the mass ratio of 8:1:1 by a pestle in a mortar to get a homogenous slurry. The resulting HOPG slurry was pasted on a current collector made of polytetrafluoroethylene (PTFE) treated hydrophobic carbon paper (120 Toray Carbon paper, Fuel Cell Store, USA). The electrode films were dried in air at 80 °C overnight prior to the electrochemical measurements. Fig. S2 shows an SEM micrograph of the morphology of a HOPG cathode, depicting graphite micro-flakes of arbitrary shapes and sizes (mostly from 10 to 100 μm) embedded in the conductive carbon and PVDF binder matrix. The active mass density of the resulting HOPG electrodes was ~2.5 mg cm⁻².

2.3. Electrochemical performance measurements

All the electrochemical tests were performed in a three-electrode electrochemical half-cell setup. The HOPG cathodes were applied as working electrodes, platinum (Pt) as a counter electrode, and Ag/AgCl pseudo-reference electrode (potential 220 mV once measured against standard Ag/AgCl with 3 M KCl aqueous solution) as a reference electrode. The standard Ag/AgCl with 3 M KCl was found impractical in the highly concentrated WiSE, so Ag/AgCl wire-type pseudo-reference electrode was used instead. The measured potentials are presented with respect to the Ag/AgCl (3 M KCl aqueous solution) by adding the potential difference of 220 mV. The potentiostatic cyclic voltammetry (CV) and electrochemical impedance spectroscopy (EIS) were performed by using a potentiostat/galvanostat (Metrohm Autolab PGSTAT302N). The galvanostatic charge/discharge and cycle life tests were carried out using a battery tester (Neware, China) at constant (dis)charging current densities at room temperature.

2.4. Material characterization

Operando Raman spectroscopy was performed on a home-made electrochemical cell using a battery tester and a Renishaw inVia™ confocal Raman spectroscope equipped with an optical microscope, a He-Cd blue laser (442 nm excitation wavelength), and 2400 l/mm diffraction grating. A TESCAN scanning electron microscope (SEM) was used for the analysis of the surface morphology of the electrodes. The chemical nature of the intercalation species and electrodes was probed via X-ray photoelectron spectroscopy (XPS) by using an AXIS Supra photoelectron spectrometer (Kratos Analytical Ltd, UK) with a monochromated Al Kα (1486 eV) excitation source. To probe the bulk of the samples, the samples were sputtered using Ar ions. The Ar ion sputtering was carried out by a Minibeam 6 ion gun operating in a cluster mode with a raster area of 2 × 2 mm for 600 s. The Ar clusters were composed of roughly 1000 atoms with an ion energy of 5 keV. The base pressure during the XPS measurements was 2 × 10⁻⁸ Torr. *Operando* X-ray diffraction (XRD) was performed on a Bruker D8 Advance X-ray diffractometer (λ = 1.54 Å, Cu-K α radiation). All the XRD measurements were collected in the 2 theta angles of the range of 10–60° with the step rate of 0.02° using a Lynxeye detector and applying an accelerating voltage of 40 kV and a current of 40 mA. The total XRD scan time was set to 10 min to deliver a sufficient resolution while performing *Operando* (dis)charge using a home-made electrochemical cell equipped with a top KAPTON window.

3. Results and discussion

3.1. WiSE electrochemical stability window test

The electrochemical stability window of the as-prepared Al(ClO₄)₃-based WiSE was tested by linear cyclic voltammetry (LSV) by employing a glassy carbon as a working electrode, platinum as a counter electrode, and pseudo-reference Ag/AgCl as a reference electrode. Fig. 1(a) shows the LSV of the WiSE in comparison to the lower concentration (0.5 m, 10 m) aqueous electrolytes of the same salt at a scan rate of 5 mVs⁻¹. The Al(ClO₄)₃-based WiSE demonstrates a stable and wide electrochemical stability window in the voltage range of 2.0 to -2.0 V vs. Ag/AgCl. The electrochemical window of the WiSE is approximately double the window obtained with the diluted aqueous electrolytes. The electrochemical window of the Al(ClO₄)₃-based WiSE is wider than most of the other reported WiSE systems [32].

The wide electrochemical window in the as-reported WiSE is attributed to the multivalent aluminum ion, which has high charge density and tendency to make strong interactions with water

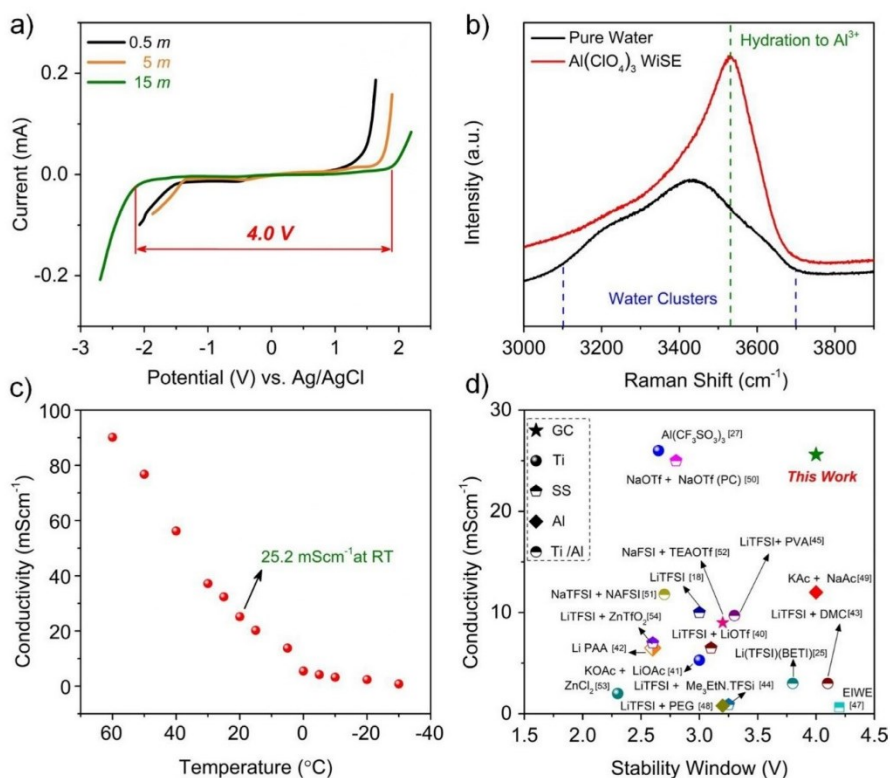


Fig. 1. Electrochemical stability window and conductivity tests of the $\text{Al}(\text{ClO}_4)_3$ WiSE: (a) Linear sweep voltammetry (LSV) of aluminum $\text{Al}(\text{ClO}_4)_3$ -based electrolytes showing the electrochemical stability window of 0.5 m, 10 m, and 15 m WiSE solutions at the scan rate of 5 mVs^{-1} , (b) Raman spectra in the wavenumber region corresponding to the OH stretching vibrations of pure water (black) vs. $\text{Al}(\text{ClO}_4)_3$ WiSE (red), (c) Conductivity vs. temperature plot of the as-prepared WiSE, (d) Comparison of the stability window and ionic conductivity of $\text{Al}(\text{ClO}_4)_3$ WiSE with previously reported WiSE systems in the literature at RT [18,25,40–54].

molecules, as well as the strong chaotropic nature of the perchlorate anion, which helps to keep water trapped inside water-cation solvation sheath [33]. Consequently, less free water in the electrolyte. The absence of free-water molecules in the WiSE is confirmed using Raman spectroscopy in Fig. 1(b). The Raman spectrum of the WiSE is showing a narrow peak at 3530 cm^{-1} that is typical for the bound water molecules to cations [33]. In contrast the Raman spectra of the pure water demonstrate a typical broadband peak of water molecules, which are arising from the OH stretching vibrations [34]. The absence of the free water molecules and the widening of the electrochemical window has also been observed in other WiSE systems [18,27,33,35].

3.2. Ionic conductivity measurements

The ionic-conductivity of an electrolyte is a crucial parameter to assess its potential applications in EESS. Ionic-conductivity of the as-prepared WiSE was measured by employing EIS, as mentioned elsewhere [17,35]. Briefly, the electrolyte resistance (R_s) was measured in an electrolytic tank with two symmetric Pt electrodes of a specific surface area at a fixed distance (L) in between them at a frequency range of $0.1\text{--}10^5 \text{ Hz}$. The ionic-conductivity (σ , mS cm^{-1}) was calculated by using

$$\sigma = L / (R_s * A)$$

where A is the area of the platinum electrode immersed in the electrolyte. The conductivity measurement system was calibrated by subjecting it to the standard conductivity calibration solutions of $12,880 \mu\text{S cm}^{-1}$ and $80,000 \mu\text{S cm}^{-1}$ (Atlas Scientific, LLC).

Fig. 1(c) shows the ionic conductivity of the $\text{Al}(\text{ClO}_4)_3$ -based WiSE as a function of the temperature in the range of $-30\text{--}60 \text{ }^\circ\text{C}$. The $\text{Al}(\text{ClO}_4)_3$ -based WiSE has a high ionic conductivity of $25.7 \pm 0.07 \text{ mS cm}^{-1}$ at room temperature, which is far higher than ionic liquids [36–39]. Interestingly, the ionic conductivity of the WiSE is relatively high even at extremely low temperatures (0.81 mS cm^{-1} at $-30 \text{ }^\circ\text{C}$), making it suitable for cold climate-energy storage applications. A comparison of the ionic conductivity and stability window of the $\text{Al}(\text{ClO}_4)_3$ WiSE with previously reported WiSE systems is presented in Fig. 1. (d). The graph shows that the $\text{Al}(\text{ClO}_4)_3$ WiSE reported in our study has both high ionic conductivity and a wide stability window.

3.3. Electrochemical testing and performance analysis of graphite electrodes in the WiSE

3.3.1. Cyclic voltammetry and electrochemical impedance spectroscopy

Fig. 2(a) shows the CV of a HOPG-based electrode and bare current collector in the $\text{Al}(\text{ClO}_4)_3$ -based WiSE at a scan rate of 10 mVs^{-1} . The oxidative stability of the carbon current collector is

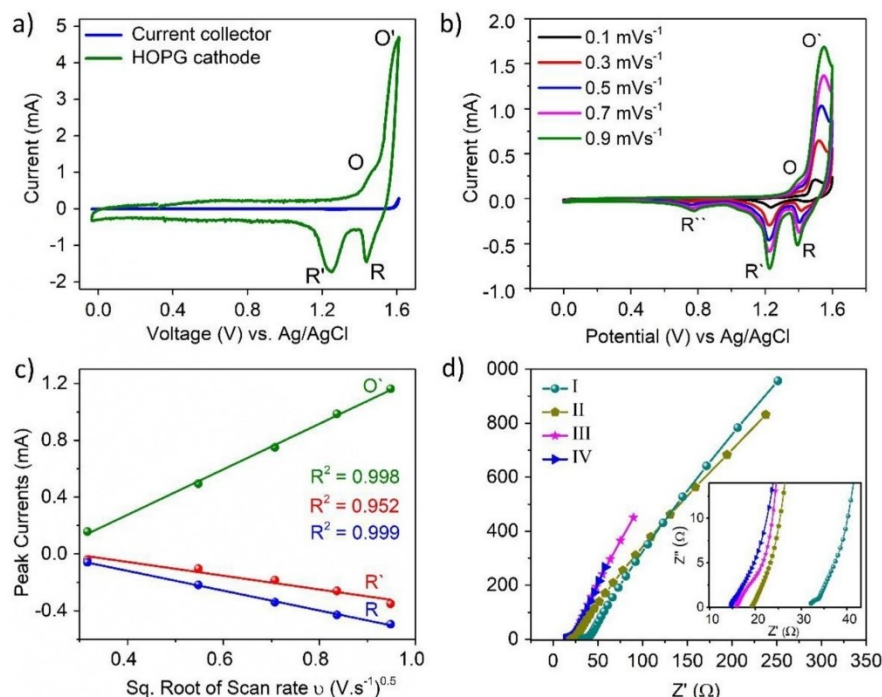


Fig. 2. Electrochemical performance tests of half-cells utilizing HOPG electrode vs. Ag/AgCl reference and Pt counter electrodes in 15 m Al(ClO₄)₃-based WiSE: (a) CV of HOPG cathode (green) and carbon current collector (blue) at a scan rate of 10 mVs⁻¹, (b) CV at low scan rates from 0.1 mVs⁻¹ to 9 mVs⁻¹, (c) graph of the linear relationship between the peak currents and the square root of scan rate, and, (d) Nyquist plots of HOPG in as-reported WiSE, I and II after soaking for 10 min and 20 min, III after 30 CV scans and IV after 180 cycles at 200 mAg⁻¹.

up to 1.64 V vs Ag/AgCl considering an onset current density of 0.1 mA/cm², which hinders the full usage of the available 4 V potential window of the Al(ClO₄)₃ - WiSE (Fig. 2(a)). However, the CV voltammogram for the HOPG electrode demonstrates two oxidation peaks (O and O') and two corresponding reduction peaks (R and R'). The oxidation peaks at around 1.48 V and 1.6 V vs. Ag/AgCl correspond to the intercalation potentials of perchlorate anions into graphite (approximately 4.5 V to 5.0 V vs. Li/Li⁺) as reported previously in non-aqueous systems [24]. The presence of more than one redox peak is attributed to different graphite intercalation stages [29,55].

The kinetic analysis of the perchlorate anion interaction with the HOPG electrode was conducted using low scan rate CV measurements. Fig. 2(b) shows CV of HOPG in the WiSE at low scan rates from 0.1 mVs⁻¹ to 0.9 mVs⁻¹. The peak currents were successively increased with the scan rates in the CV measurements. The unchanged position of the potentials of the cathodic and anodic peaks in the CV spectra at different scan rates provides evidence of reversible electrochemical processes. Further analysis of the oxidation and reduction peaks in the CV spectra shows a linear dependence of the peak currents as a function of the square root of the scan rates (Fig. 2(c)), providing a piece of evidence that the reversible electrochemical electron transfer processes involve freely diffusing redox species [56–58].

Electrochemical impedance spectroscopy was utilized to analyze the internal and interface impedance of the electrochemical half-cells. Fig. 2(d) presents the Nyquist plots of an HOPG electrode after immersing it in the electrolyte for 10 and 20 min, af-

ter performing 30 consecutive CV scans at 5 mVs⁻¹, and finally after 180 charge-discharge cycles at 200 mAg⁻¹. The shortly immersed (10 min) electrode demonstrates a higher charge transfer and diffusion impedance due to incomplete wetting by the electrolyte. The longer (20 min) immersing in the electrolyte improves wetting and results in a decrease of the impedance of the HOPG electrode. The electrode impedance, particularly, the Warburg impedance is significantly reduced after performing multiple CV scans and charge-discharge cycles. The observed decrease in impedance is attributed to the surface activation and expansion of the graphite layers in HOPG as a result of the anion intercalation [59].

3.3.2. Effect of different cut-off potentials and charge-discharge performance

The effects of different upper cut-off potentials on the discharge capacities, C.E., stability, and cycle life of the cells are presented in Fig. 3. The highest discharge capacity of 22 mAhg⁻¹ is obtained at a high cut-off potential of 1.64 V, while a significantly lower discharge capacity of 7 mAhg⁻¹ is obtained when charged to 1.54 V. The charge-discharge curves in Fig. 3(a) depict two clear charging plateaus at 1.45 V and 1.55 V, and two discharging plateaus at 1.5 V and 1.28 V. These plateaus are in line with the potentials of the redox peaks in the CV results in Fig. 2. There is also observed a minor third discharge plateau at ~ 0.8 V, which is only visible in the CVs at low scan rates < 1 mVs⁻¹. It is worth mentioning that the high oxidative stability of the as-prepared WiSE enabled charging the HOPG electrodes at much higher potentials without electrolyte

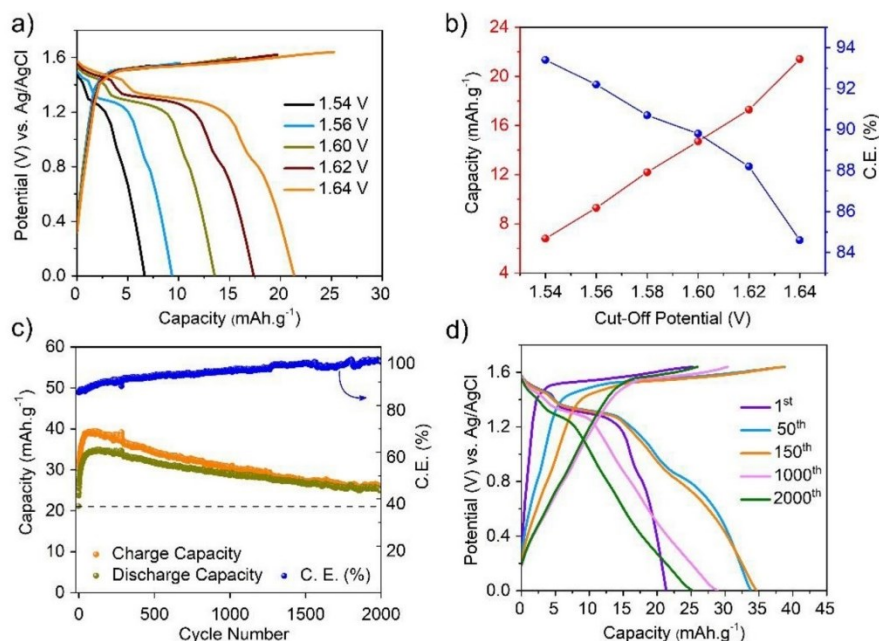


Fig. 3. (Dis)charge and long cycling performance tests: (a) charge-discharge curves at different cut-off potentials, discharged capacities and Coulombic efficiencies, (b) graph showing the relationship between cut-off potentials of 1.64 V vs. Ag/AgCl at the current density of 200 mA g^{-1} , (c) long-cycling test up to 2000 cycles, and (d) charge-discharge curves at different cycle numbers at the cut-off potential of 1.64 V vs. Ag/AgCl at the current density of 200 mA g^{-1} .

decomposition than in diluted aqueous electrolytes (Fig. S3). Further, to exclude any contribution of the graphitic current collector to the obtained capacity, a bare cell was assembled with the current collector as a working electrode and tested with the same parameters as the reported system. There was found no capacity contribution (<1 mA $h g^{-1}$) from the current collector (Fig. S4 (a) & (b)). Fig. 3(b) shows the relationship between cut-off potentials, C.E. and obtained capacities. At low cut-off potential higher C.E. was observed though discharged capacity was very low and vice versa at the high cut-off potentials. Since the highest discharge capacity has been obtained at a high cut-off potential of 1.64 V, the cycle life, stability, and C.E. performance tests were conducted at this cut-off potential and current density of 200 mA g^{-1} .

The cycle life, stability, and reversibility of the anion (de)intercalation into graphite electrode in as-reported WiSE shows stability for more than 2000 cycles at the current density of 200 mA g^{-1} (Fig. 3c). The (dis)charge capacity is observed to improve slightly in the first cycles, reaching a maximum discharge capacity of 35 mA $h g^{-1}$ at the 50th cycle (Fig. 3d). The C.E. gets gradually improved with an increasing number of cycles, raising even over 95% after 100 cycles. After 2000 cycles, the discharge capacity is reduced to 26 mA $h g^{-1}$ but it is still higher than the initial value of 22 mA $h g^{-1}$, and C.E. reached \sim 98%. A change in the (dis)charge curves shape can be seen for the various cycles from 1 to 2000 as presented in Fig. 3(d). Well-defined plateaus can be seen for the initial cycles. At later cycles, however, there is more capacitor-like behavior which suggests a more dominant surface contribution (non-Faradic process) to the capacity. This observation is also supported by the EIS analysis after 180 cycles (Fig. 2d), which confirms a gradual evolution of an electrochemical double layer.

The demonstrated electrochemical performance of the presented WiSE demonstrates a higher capacity, better stability, and

long cycle life than the previous reports on ClO $_4^-$ anions intercalation into graphite from organic solvents [38]. A comparison of the current work to the previously reported results in the literature is presented in Supplementary Information (Table S2).

3.4. Analysis of the structural and chemical changes related to anion intercalation

3.4.1. X-ray photoelectron spectroscopy

To probe the chemical nature of the intercalated species into HOPG, X-ray photoelectron spectroscopy (XPS) was performed on the charged and discharged HOPG electrodes and compared to the HOPG electrode unexposed to the electrolyte (Fig. 4). All the samples were thoroughly rinsed with deionized water to minimize the amount of trapped electrolyte and dried in an oven at 80 $^{\circ}C$ before the XPS measurements. To avoid any possible contamination of the sample surfaces, the XPS measurements were done on the Ar cluster sputtered samples (10 min, 5 keV Ar $_{1000}^+$ ions). Hence, the XPS spectra in Fig. 4 represent information about the changes in the bulk of the materials.

The XPS spectrum of the pristine electrode shows only the presence of C, O, and F elements. The F 1s peak is detected due to the presence of the PVDF binder in the electrodes. The XPS spectrum of the charged electrode demonstrates additional Cl and O peaks that were not present in the pristine electrode, providing evidence of the presence of perchlorate anions in the HOPG electrodes. The Cl 2p XPS spectrum in Fig. 4(b) comprises the characteristic doublet perchlorate peaks at 207.7 and 209.2 eV corresponding to ClO $_4^-$ 2p $^{3/2}$ and 2p $^{1/2}$ [60], while the peaks at 199.8 eV and 201.7 eV are attributed to C-Cl 2p $^{3/2}$ and 2p $^{1/2}$, respectively [61,62]. The C-Cl bonding is not visible in the C 1s spectrum most probably due to a high carbon to chlorine ratio in the samples. The in-

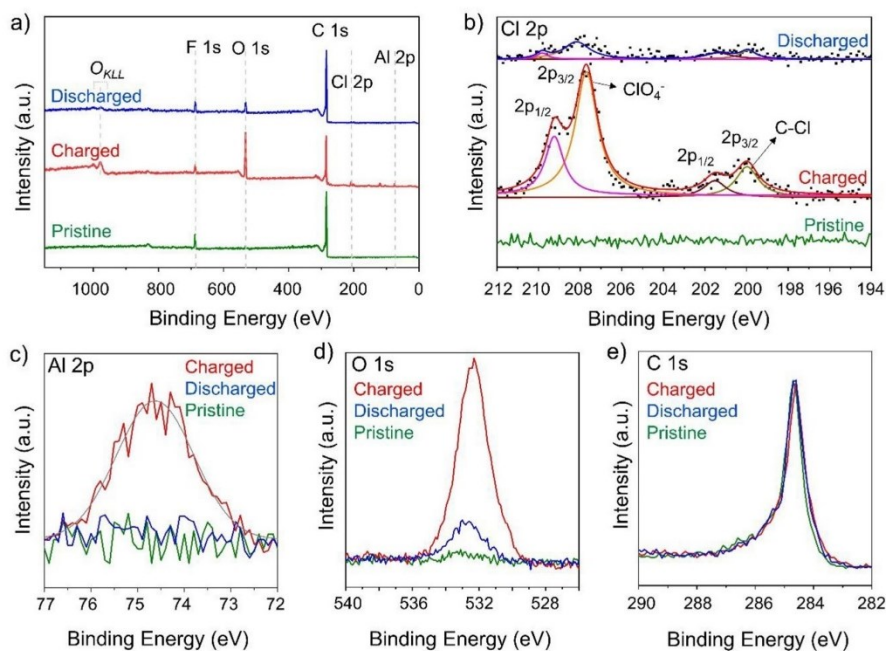


Fig. 4. Chemical Analysis of pristine (green), charged (red) and discharged (blue) HOPG cathodes by X-ray Photoelectron Spectroscopy (XPS) in $\text{Al}(\text{ClO}_4)_3$ -based WISE: (a) wide XPS scans (b) Cl 2p, (c) Al 2p, (d) O 1s, and (e) C 1s spectra. All XPS measurements were done after the Ar cluster sputtering (5 keV Ar_{1000}^+ ions) of the sample surfaces for 10 min.

tensity of the Cl and O peaks is significantly decreased in the discharged samples, in line with the deintercalation of the perchlorate ions from the HOPG electrode. The remaining small ClO_4^- and C-Cl peaks in the discharged samples suggest that the deintercalation process is not fully complete and a few intercalated species are remaining inside the HOPG electrodes. This can be one of the reasons why the measured C.E. has not reached 100%. The XPS spectra of the charged electrodes are also containing a small amount of Al, which might be a result of local co-intercalation of solvated cations [13,24]. The F 1s spectra of the charged and discharged samples presented in Fig. S5 suggest a side reaction of the WISE with the PVDF binder. The incompatibility of PVDF binder with acidic electrolytes has been reported before [63], and might be responsible for the observed electrolyte color change after long cycling (see Fig. S6). Hence, a binder-free electrode would be a more feasible choice for highly acidic electrolytes to avoid any possible side reactions.

3.4.2. Operando Raman spectroscopy

Operando Raman spectroscopy was conducted to probe the ClO_4^- anion (de)intercalation process (from)into graphite during (dis)charge. The Operando Raman spectra recorded at different (dis)charge voltages are presented in Fig. 5(a). The graphitic G-band at 1574 cm^{-1} was split into two Raman modes of a lower-frequency component $E_{2g}(i)$ and a higher-frequency component $E_{2g}(b)$ after the charging. This result suggests the formation of the perchlorate-graphite intercalation compound [24,29,31,64,65]. The $E_{2g}(i)$ represents the vibrations of the carbon atoms of the non-intercalated graphite layers, whereas $E_{2g}(b)$ represents the vibrations of the carbon atoms of the intercalated graphite layer.

The maximum Raman shift of the $E_{2g}(b)$ component was observed at 1612 cm^{-1} for the fully charged sample. The peaks are up-shifted and the intensity of the $E_{2g}(i)$ peak decreases with increasing charging voltage because more graphite layers are intercalated by ClO_4^- . The peaks shifted back during the discharge process, but they have not fully recovered their original position before the charging. This observation is consistent with the C.E. and XPS results, providing evidence of the sample evolution with the increasing number of cycles.

The intensity ratio of the $E_{2g}(i)$ to $E_{2g}(b)$ band (I_i/I_b) can be used to estimate the stage number (n) of GICs by using the following formula [29,66]

$$\frac{I_i}{I_b} = \frac{(\sigma_i) n - 2}{(\sigma_b) 2}$$

where σ_i/σ_b is the ratio of Raman scattering cross-sections, which is assumed to be unity and stage number $n \geq 2$ [49]. Fig. 5(b) shows a plot of I_i/I_b (n) against the (dis)charge potentials of the HOPG electrode, suggesting a stage 4 ClO_4^- -GIC is present in the fully charged electrodes in the $\text{Al}(\text{ClO}_4)_3$ -WISE. Nevertheless, I_i/I_b ratio is a laser-excitation wavelength dependent quantity as reported earlier [67], therefore, Operando XRD was considered for the validation of the stage number.

3.4.3. Operando X-ray diffraction

Operando XRD investigations were carried out while the charging and discharging of a homemade three electrodes half-cell. The cell-top was sealed with the KAPTON tape to allow the penetration of an X-ray beam. Fig. 5c presents the results of the Operando XRD measurements using contour plots of the characteristics (002) and (004) peaks of graphite. The plots show the reversible structural

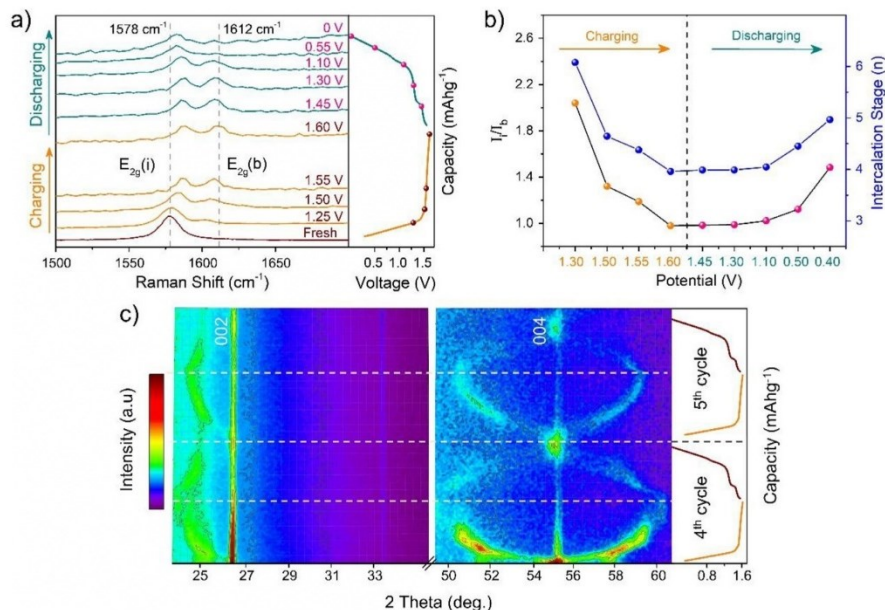


Fig. 5. Structural characterizations of charged and discharged HOPG cathodes in $\text{Al}(\text{ClO}_4)_3$ -based WISE using: (a) Operando Raman spectroscopy, (b) I/I_0 , and stage number vs. (dis)charge state plot determined using the Raman peak shifts, and (c) Operando XRD for the 4th and 5th (dis)charge cycle at the current density of 20 mAhg^{-1} .

changes of the HOPG electrode for the 4th and 5th (dis)charge cycle. The (002) characteristic peak position of HOPG demonstrates the shift to lower and higher 2 theta angles with reflection $(00n+1)$ and $(00n+2)$ during the charging and reversed during the discharging. However, the intensity of $(00n+2)$ reflection was observed very low possibly due to the absorption of X-rays by the electrolyte at low 2 theta. The splitting of the (004) reflection to two dominant peaks also manifests the intercalation of ClO_4^- based on staging. A mixture of stages 4 and 5 was observed on the basis of the ratio of the reflection peaks, which is between the theoretical values for stage 5 and stage 4 [68]. A gallery height (d_i), (i.e., the distance between two graphite layers with an intercalant layer in between) of 7.08 \AA was observed with the gallery expansion (Δd) of 3.76 \AA .

The relationship between the observed values of d_i , Δd and stages (n), and the periodic repeat distance (l_c), can be expressed by [69,70]

$$l_c = d_i + 3.35 \text{ \AA} \cdot (n - 1) = \Delta d + 3.35 \text{ \AA} \cdot n$$

The periodic repeat distance or the distance between two neighboring intercalation layers, l_c was found 17.14 \AA to 20.48 \AA considering a mix of intercalation stages. To elucidate the calculated stages, we adopted the previously reported theoretical stoichiometric models with single $[\text{C}_{18}\text{ClO}_4]$ and 4 intercalant sites $[\text{C}_{72}\text{ClO}_4)_4]$ [53]. The theoretical capacity was calculated for different stages (1 to 6) to determine which of the capacity contributions becomes as close as possible to the experimental value [71,72]. The calculated theoretical discharge capacities for stage 4 (31.02 mAhg^{-1}) and stage 5 (24.68 mAhg^{-1}) are in close agreement with the experimental values (35 mAhg^{-1} to 26 mAhg^{-1}), Table S1.

4. Conclusions

In summary, we have reported a highly concentrated water-in-salt electrolyte based on aluminum perchlorate which provides a wide electrochemical stability window of 4.0 V. The reported WISE has demonstrated stable and reversible intercalation of perchlorate anions into an HOPG electrode in a half-cell setup for more than 2000 cycles with high Coulombic efficiency of over 95%. Our study gives an insight into the processes of perchlorate (de)intercalation (from) into graphite in highly concentrated aqueous electrolytes, providing a suitable electrolyte platform for future high-voltage dual-ion batteries.

Declaration of Competing Interest

We wish to confirm that there are no known conflicts of interest associated with this publication and there has been no significant financial support for this work that could have influenced its outcome. We confirm that the manuscript has been read and approved by all named authors and that there are no other persons who satisfied the criteria for authorship but are not listed. We further confirm that the order of authors listed in the manuscript has been approved by all of us. We confirm that we have given due consideration to the protection of intellectual property associated with this work and that there are no impediments to publication, including the timing of publication, with respect to intellectual property. In so doing we confirm that we have followed the regulations of our institutions concerning intellectual property. We understand that the Corresponding Author is the sole contact for the Editorial process (including Editorial Manager and direct communications with the office). He is responsible for communicating with the other authors about progress, submissions of revisions and final approval of proofs. We confirm that we have

provided a current, correct email address which is accessible by the Corresponding Author. Signed by all authors as follows: • Zahid Ali Zafar; • Ghulam Abbas; • Martin Silhavič; • Karel Knezík; • Ondrej Kaman; • Farjana J. Sonia; • Prabhat Kumar; • Petr Jiricek; • Jana Houdková; • Otakar Frank; • Jiri Cervenka

Credit authorship contribution statement

Zahid Ali Zafar: Conceptualization, Methodology, Investigation, Formal analysis, Validation, Writing – original draft, Writing – review & editing. **Ghulam Abbas:** Investigation, Formal analysis, Validation, Writing – review & editing. **Martin Silhavič:** Investigation, Writing – review & editing. **Karel Knezík:** Investigation, Formal analysis, Writing – review & editing. **Ondrej Kaman:** Investigation, Formal analysis, Writing – review & editing. **Farjana J. Sonia:** Investigation, Formal analysis, Writing – review & editing. **Prabhat Kumar:** Investigation, Formal analysis, Writing – review & editing. **Petr Jiricek:** Investigation, Formal analysis, Writing – review & editing. **Jana Houdková:** Investigation, Formal analysis, Writing – review & editing. **Otakar Frank:** Conceptualization, Writing – review & editing, Supervision, Project administration, Funding acquisition. **Jiri Cervenka:** Conceptualization, Methodology, Investigation, Writing – original draft, Writing – review & editing, Supervision, Project administration, Funding acquisition.

Acknowledgment

We acknowledge funding support from the Czech Science Foundation (GACR – Grant No. 19-23986S) and the Operational Programme Research, Development and Education financed by European Structural and Investment Funds and the Czech Ministry of Education, Youth and Sports (Project No. SOLID21 – CZ.02.1.01/0.0/0.0/16_019/0000760). This work was further supported by the Ministry of Education, Youth and Sports of the Czech Republic and The European Union - European Structural and Investments Funds in the frame of Operational Programme Research Development and Education; OP RDE (Project: “Carbon allotropes with rationalized nanointerfaces and nanolinks for environmental and biomedical applications” No. CZ.02.1.01/0.0/0.0/16_026/0008382). This work was further supported by the project Strategy AV21, program Diagnostic Methods, and Techniques.

Supplementary materials

Supplementary material associated with this article can be found, in the online version, at doi:[10.1016/j.electacta.2021.139754](https://doi.org/10.1016/j.electacta.2021.139754).

References

- [1] J. Lee, J. Kim, T. Hyeon, Recent progress in the synthesis of porous carbon materials, *Adv. Mater.* 18 (2006) 2073–2094.
- [2] W. Wang, X. Wei, D. Choi, X. Lu, G. Yang, C. Sun, Chapter 1 Electrochemical cells for medium- and large-scale energy storage, ed. C. Menictas, M. Skyllas-Kazacos and T.M. Lim, Woodhead Publishing Ltd. (2015) 3–28.
- [3] S.W. Lee, B.M. Gallant, H.R. Byon, P.T. Hammond, Y. Shao-Horn, Nanostructured carbon-based electrodes: bridging the gap between thin-film lithium-ion batteries and electrochemical capacitors, *Energy Environ. Sci.* 4 (2011) 1972–1985.
- [4] J.H. Xu, D.E. Turney, A.L. Jadhav, R.J. Messinger, Effects of graphite structure and ion transport on the electrochemical properties of rechargeable aluminum-graphite batteries, *ACS App. Energy Mater.* 2 (2019) 7799–7810.
- [5] I.A. Rodríguez-Pérez, X. Ji, Anion hosting cathodes in dual-ion batteries, *ACS Energy Lett.* 2 (2017) 1762–1770.
- [6] S. Wang, S. Jiao, D. Tian, H.S. Chen, H. Jiao, J. Tu, Y. Liu, D.N. Fang, A novel ultrafast rechargeable multi-ions battery, *Adv. Mater.* 29 (2017) 1606349.
- [7] K. Beltrop, S. Beuker, A. Heckmann, M. Winter, T. Placke, Alternative electrochemical energy storage: potassium-based dual-graphite batteries, *Energy Environ. Sci.* 10 (2017) 2090–2094.
- [8] Y. Sui, C. Liu, R.C. Masse, Z.G. Neale, M. Atif, M. AlSalhi, G. Cao, Dual-ion batteries: the emerging alternative rechargeable batteries, *Energy Storage Mater.* 25 (2020) 1–32.
- [9] X. Jiang, L. Luo, F. Zhong, X. Feng, W. Chen, X. Ai, H. Yang, Y. Cao, Electrolytes for dual-carbon batteries, *ChemElectroChem* 6 (2019) 2615–2629.
- [10] M. Zhang, X. Song, X. Ou, Y. Tang, Rechargeable batteries based on anion intercalation graphite cathodes, *Energy Storage Mater.* 16 (2019) 65–84.
- [11] J. Fan, Q. Xiao, Y. Fang, L. Li, W. Yuan, A rechargeable Zn/graphite dual-ion battery with an ionic liquid-based electrolyte, *Ionics* 25 (2018) 1303–1313 (Kiel).
- [12] Z.A. Zafar, S. Imtiaz, R. Razaq, S. Ji, T. Huang, Z. Zhang, Y. Huang, J.A. Anderson, Cathode materials for rechargeable aluminum batteries: current status and progress, *J. Mater. Chem. A* 5 (2017) 5646–5660.
- [13] Q. Li, Y. Qiao, S. Guo, K. Jiang, Q. Li, J. Wu, H. Zhou, Both cationic and anionic co-(de)intercalation into a metal-oxide material, *Joule* 2 (2018) 1134–1145.
- [14] Y. Feng, S. Chen, J. Wang, B. Lu, Carbon foam with microporous structure for high performance symmetric potassium dual-ion capacitor, *J. Energy Chem.* 43 (2020) 129–138.
- [15] J. Zhu, Y. Li, B. Yang, L. Liu, J. Li, X. Yan, D. He, A dual carbon-based potassium dual ion battery with robust comprehensive performance, *Small* 14 (2018) 1801836.
- [16] J. Hao, X. Li, X. Song, Z. Guo, Recent progress and perspectives on dual-ion batteries, *EnergyChem* 1 (2019) 100004.
- [17] F. Gan, K. Chen, N. Li, Y. Wang, Y. Shuai, X. He, Low cost ionic liquid electrolytes for rechargeable aluminum/graphite batteries, *Ionics* 25 (2019) 4243–4249 (Kiel).
- [18] L. Suo, O. Borodin, T. Gao, M. Olguin, J. Ho, X. Fan, C. Luo, C. Wang, K. Xu, Water-in-salt[™] electrolyte enables high-voltage aqueous lithium-ion chemistries, *Science* 350 (2015) 938–943.
- [19] E. Zhang, W. Cao, B. Wang, X. Yu, L. Wang, Z. Xu, B. Lu, A novel aluminum dual-ion battery, *Energy Storage Mater.* 11 (2018) 91–99.
- [20] K. Xu, Electrolytes and interphases in Li-ion batteries and beyond, *Chem. Rev.* 114 (2014) 11503–11618.
- [21] D. Bin, F. Wang, A.G. Tamirat, L. Suo, Y. Wang, C. Wang, Y. Xia, Progress in aqueous rechargeable sodium-ion batteries, *Adv. Energy Mater.* 8 (2018) 1703008.
- [22] M. Kazazi, Z.A. Zafar, M. Delshad, J. Cervenka, C. Chen, TiO₂/CNT nanocomposite as an improved anode material for aqueous rechargeable aluminum batteries, *Solid State Ion.* 320 (2018) 64–69.
- [23] T. Zhai, S. Sun, X. Liu, C. Liang, G. Wang, H. Xia, Achieving insertion-like capacity at ultrahigh rate via tunable surface pseudocapacitance, *Adv. Mater.* 30 (2018) e1706640.
- [24] Y. Kondo, Y. Miyahara, T. Fukutsuka, K. Miyazaki, T. Abe, Electrochemical intercalation of bis(fluorosulfonyl)amide anions into graphite from aqueous solutions, *Electrochem. Commun.* 100 (2019) 26–29.
- [25] Y. Yamada, K. Usui, K. Sodeyama, S. Ko, Y. Tateyama, A. Yamada, Hydrate-melt electrolytes for high-energy-density aqueous batteries, *Nat. Energy* 1 (2016) 16129.
- [26] X. Bu, L. Su, Q. Dou, S. Lei, X. Yan, A low-cost “water-in-salt[™]” electrolyte for a 2.3V high-rate carbon-based supercapacitor, *J. Mater. Chem. A* 7 (2019) 7541–7547.
- [27] A. Zhou, L. Jiang, J. Yue, Y. Tong, Q. Zhang, Z. Lin, B. Liu, C. Wu, L. Suo, Y.S. Hu, H. Li, L. Chen, Water-in-salt electrolyte promotes high-capacity FeFe(CN)₆ cathode for aqueous Al-ion battery, *ACS Appl. Mater. Interfaces* 11 (2019) 41356–41362.
- [28] Q. Dou, Y. Lu, L. Su, X. Zhang, S. Lei, X. Bu, L. Liu, D. Xiao, J. Chen, S. Shi, X. Yan, A sodium perchlorate-based hybrid electrolyte with high salt-to-water molar ratio for safe 2.5 V carbon-based supercapacitor, *Energy Storage Mater.* 23 (2019) 603–609.
- [29] D. Reber, R. Grissa, M. Becker, R.S. Kühnel, C. Battaglia, Anion selection criteria for water-in-salt electrolytes, *Adv. Energy Mater.* 11 (2020) 2002913.
- [30] J. Gao, S. Tian, L. Qi, H. Wang, Intercalation manners of perchlorate anion into graphite electrode from organic solutions, *Electrochim. Acta* 176 (2015) 22–27.
- [31] D. Alliata, P. Haring, O. Haas, R. Kotz, H. Siegenthaler, Anion intercalation into highly oriented pyrolytic graphite studied by electrochemical atomic force microscopy, *Electrochem. Commun.* 1 (1999) 5–9.
- [32] M.S. Jagadeesh, G. Bussetti, A. Calloni, R. Yivilialin, L. Brambilla, A. Accogli, E. Gibertini, D. Alliata, C. Goletti, F. Ciccacci, L. Magagnin, C. Castiglioni, L. Duò, Incipient anion intercalation of highly oriented pyrolytic graphite close to the oxygen evolution potential: a combined X-ray photoemission and Raman spectroscopy study, *J. Phys. Chem. C* 123 (2018) 1790–1797.
- [33] T. Liang, R. Hou, Q. Dou, H. Zhang, X. Yan, The applications of water-in-salt electrolytes in electrochemical energy storage devices, *Adv. Funct. Mater.* 21 (2020) 2006749.
- [34] B.M. Auer, J.L. Skinner, IR and Raman spectra of liquid water: theory and interpretation, *J. Chem. Phys.* 128 (2008) 224511.
- [35] Y. Li, Z. Zhou, W. Deng, C. Li, X. Yuan, J. Hu, M. Zhang, H. Chen, R. Li, A super-concentrated water-in-salt hydrogel electrolyte for high-voltage aqueous K-ion batteries, *ChemElectroChem* 8 (2021) 1–5.
- [36] J. Li, H. Jiao, C. Wang, S. Jiao, Ternary AlCl₃-urea-[EMIm]Cl ionic liquid electrolyte for rechargeable aluminum-ion batteries, *J. Electrochem. Chem.* 164 (2017) A3093–A3100.
- [37] H. Wang, S. Gu, Y. Bai, S. Chen, N. Zhu, C. Wu, F. Wu, Anion-effects on electrochemical properties of ionic liquid electrolytes for rechargeable aluminum batteries, *J. Mater. Chem. A* 3 (2015) 22677–22686.
- [38] T. Mandai, P. Johansson, Al conductive haloaluminate-free non-aqueous room-temperature electrolytes, *J. Mater. Chem. A* 3 (2015) 12230–12239.
- [39] N. Jabeen, A. Hussain, Q. Xia, S. Sun, J. Zhu, H. Xia, High-performance 2.6V aqueous asymmetric supercapacitors based on operando formed Na_{0.5}MnO₂ nanosheet assembled nanowall arrays, *Adv. Mater.* 29 (2017) 1700804.

- [40] L. Suo, O. Borodin, W. Sun, X. Fan, C. Yang, F. Wang, T. Gao, Z. Ma, M. Schroeder, A. von Cresce, S.M. Russell, M. Armand, A. Angell, K. Xu, C. Wang, Advanced high-voltage aqueous lithium-ion battery enabled by "water-in-bisalt" electrolyte, *Angew. Chem. Int. Ed.* 55 (2016) 7136–7141.
- [41] M.R. Lukatskaya, J.I. Feldblyum, D.G. Mackanic, F. Lissel, D.L. Michels, Y. Cui, Z. Bao, Concentrated mixed cation acetate "water-in-salt" solutions as green and low-cost high voltage electrolytes for aqueous batteries, *Energy Environ. Sci.* 11 (2018) 2876–2883.
- [42] X. He, B. Yan, X. Zhang, Z. Liu, D. Bresser, J. Wang, R. Wang, X. Cao, Y. Su, H. Jia, C.P. Grey, H. Frielinghaus, D.G. Truhlar, M. Winter, J. Li, E. Paillard, Fluorine-free water-in-ionomer electrolytes for sustainable lithium-ion batteries, *Nat. Commun.* 9 (2018) 5320.
- [43] F. Wang, O. Borodin, M.S. Ding, M. Gobet, J. Vatamanu, X. Fan, T. Gao, N. Eidson, Y. Liang, W. Sun, S. Greenbaum, K. Xu, C. Wang, Hybrid aqueous/non-aqueous electrolyte for safe and high-energy Li-ion batteries, *Joule* 2 (2018) 927–937.
- [44] L. Chen, J. Zhang, Q. Li, J. Vatamanu, X. Ji, T.P. Pollard, C. Cui, S. Hou, J. Chen, C. Yang, L. Ma, M.S. Ding, M. Garaga, S. Greenbaum, H.S. Lee, O. Borodin, K. Xu, C. Wang, A 63m superconcentrated aqueous electrolyte for high-energy Li-ion batteries, *ACS Energy Lett.* 5 (2020) 968–974.
- [45] C. Yang, X. Ji, X. Fan, T. Gao, L. Suo, F. Wang, W. Sun, J. Chen, L. Chen, F. Han, L. Miao, K. Xu, K. Gerasopoulos, C. Wang, Flexible aqueous Li-ion battery with high energy and power densities, *Adv. Mater.* 29 (2017) 1701972.
- [46] P. Kulkarni, D. Ghosh, R.G. Balakrishna, Recent progress in "water-in-salt" and "water-in-salt"-hybrid-electrolyte-based high voltage rechargeable batteries, *Sustain. Energy Fuels* 5 (2021) 1619–1654.
- [47] Y. Shang, N. Chen, Y. Li, S. Chen, J. Lai, Y. Huang, W. Qu, F. Wu, R. Chen, An "ether-in-water" electrolyte boosts stable interfacial chemistry for aqueous lithium-ion batteries, *Adv. Mater.* 32 (2020) e2004017.
- [48] J. Xie, Z. Liang, Y.C. Lu, Molecular crowding electrolytes for high-voltage aqueous batteries, *Nat. Mater.* 19 (2020) 1006–1011.
- [49] J. Han, H. Zhang, A. Varzi, S. Passerini, Fluorine-free water-in-salt electrolyte for green and low-cost aqueous sodium-ion batteries, *ChemSusChem* 11 (2018) 3704–3707.
- [50] H. Zhang, B. Qin, J. Han, S. Passerini, Aqueous/nonaqueous hybrid electrolyte for sodium-ion batteries, *ACS Energy Lett.* 3 (2018) 1769–1770.
- [51] D. Reber, R.S. Kühnel, C. Battaglia, Suppressing crystallization of water-in-salt electrolytes by asymmetric anions enables low-temperature operation of high-voltage aqueous batteries, *ACS Mater. Lett.* 1 (2019) 44–51.
- [52] L. Jiang, L. Liu, J. Yue, Q. Zhang, A. Zhou, O. Borodin, L. Suo, H. Li, L. Chen, K. Xu, Y.S. Hu, High-voltage aqueous Na-ion battery enabled by inert-cation-assisted water-in-salt electrolyte, *Adv. Mater.* 32 (2020) e1904427.
- [53] C. Zhang, J. Holoubek, X. Wu, A. Daniyar, L. Zhu, C. Chen, D.P. Leonard, I.A. Rodriguez-Perez, J.X. Jiang, C. Fang, X. Ji, A ZnCl₂ water-in-salt electrolyte for a reversible Zn metal anode, *Chem. Commun.* 54 (2018) 14097–14099.
- [54] H. Zhang, X. Liu, B. Qin, S. Passerini, Electrochemical intercalation of anions in graphite for high-voltage aqueous zinc battery, *J. Power Sources* 449 (2020) 227594.
- [55] M.C. Lin, M. Gong, B. Lu, Y. Wu, D.Y. Wang, M. Guan, M. Angell, C. Chen, J. Yang, B.J. Hwang, H. Dai, An ultrafast rechargeable aluminium-ion battery, *Nature* 520 (2015) 325–328.
- [56] N. Elgrishi, K.J. Rountree, B.D. McCarthy, E.S. Rountree, T.T. Eisenhart, J.L. Dempsey, A practical beginner's guide to cyclic voltammetry, *J. Chem. Educ.* 95 (2017) 197–206.
- [57] S. Ghasemi, M.F. Mousavi, M. Shamsipur, Enhancement of electron transfer kinetics on a polyaniline-modified electrode in the presence of anionic dopants, *J. Solid State Electrochem.* 12 (2007) 259–268.
- [58] A. Subasri, K. Balakrishnan, E.R. Nagarajan, V. Devadoss, A. Subramania, Development of 2D La(OH)₃/graphene nanohybrid by a facile solvothermal reduction process for high-performance supercapacitors, *Electrochim. Acta* 281 (2018) 329–337.
- [59] M. Kazazi, M.R. Vaezi, A. Kazemzadeh, Enhanced rate performance of polypyrrole-coated sulfur/MWCNT cathode material: a kinetic study by electrochemical impedance spectroscopy, *Ionics* 20 (2013) 635–643 (Kiel).
- [60] M. Bonomo, D. Dini, A.G. Marrani, R. Zanon, X-ray photoelectron spectroscopy investigation of nanoporous NiO electrodes sensitized with Erythrosine B, *Colloid Surf. A Physicochem. Eng. Asp.* 532 (2017) 464–471.
- [61] T. Ishizaki, Y. Wada, S. Chiba, S. Kumagai, H. Lee, A. Serizawa, O.L. Li, G. Panomswan, Effects of halogen doping on nanocarbon catalysts synthesized by a solution plasma process for the oxygen reduction reaction, *Phys. Chem. Chem. Phys.* 18 (2016) 21843–21851.
- [62] Z. Yan, Z. Zhuxia, L. Tianbao, L. Xuguang, X. Bingshe, XPS and XRD study of FeCl₃-graphite intercalation compounds prepared by arc discharge in aqueous solution, *Spectrochim. Acta A Mol. Biomol. Spectrosc.* 70 (2008) 1060–1064.
- [63] H. Wang, Y. Bai, S. Chen, X. Luo, C. Wu, F. Wu, J. Lu, K. Amine, Binder-free V2O5 cathode for greener rechargeable aluminum battery, *ACS Appl. Mater. Interfaces* 7 (2015) 80–84.
- [64] D.Y. Wang, C.Y. Wei, M.C. Lin, C.J. Pan, H.L. Chou, H.A. Chen, M. Gong, Y. Wu, C. Yuan, M. Angell, Y.J. Hsieh, Y.H. Chen, C.Y. Wen, C.W. Chen, B.J. Hwang, C.C. Chen, H. Dai, Advanced rechargeable aluminium ion battery with a high-quality natural graphite cathode, *Nat. Commun.* 8 (2017) 14283.
- [65] C. Liu, Z. Liu, H. Niu, C. Wang, Z. Wang, B. Gao, J. Liu, M. Taylor, Preparation and Operando Raman characterization of binder-free u-GP@CFC cathode for rechargeable aluminum-ion battery, *MethodsX*, 6 (2019) 2374–2383.
- [66] Y. Kong, C. Tang, X. Huang, A.K. Nanjundan, J. Zou, A. Du, C. Yu, Thermal reductive perforation of graphene cathode for high-performance aluminum-ion batteries, *Adv. Funct. Mater.* 31 (2021) 2010569.
- [67] J.C. Chacon-Torres, L. Wirtz, T. Pichler, Manifestation of charged and strained graphene layers in the Raman response of graphite intercalation compounds, *ACS Nano* 7 (2013) 9249–9259.
- [68] X. Zhang, N. Sukpirom, M.M. Lerner, Graphite intercalation of bis(trifluoromethanesulfonyl) imide and other anions with perfluoroalkanesulfonyl substituents, *Mater. Res. Bull.* 34 (1999) 363–372.
- [69] G. Schmuelling, T. Placke, R. Kloepsch, O. Fromm, H.-W. Meyer, S. Passerini, M. Winter, X-ray diffraction studies of the electrochemical intercalation of bis(trifluoromethanesulfonyl)imide anions into graphite for dual-ion cells, *J. Power Sources* 239 (2013) 563–571.
- [70] M.S. Dresselhaus, G. Dresselhaus, Intercalation compounds of graphite, *Adv. Phys.* 51 (2002) 1–186.
- [71] W. Zhou, P.H. Sit, First-principles understanding of the staging properties of the graphite intercalation compounds towards dual-ion battery applications, *ACS Omega* 5 (2020) 18289–18300.
- [72] C.J. Pan, C. Yuan, G. Zhu, Q. Zhang, C.J. Huang, M.C. Lin, M. Angell, B.J. Hwang, P. Kaghazchi, H. Dai, An operando X-ray diffraction study of chloroaluminate anion-graphite intercalation in aluminum batteries, *Proc. Natl. Acad. Sci. U. S. A.* 115 (2018) 5670–5675.

Appendix II

Influence of structural properties on (de-)intercalation of ClO₄ anion in graphite from concentrated aqueous electrolyte

G. Abbas, F.J. Sonia, **Z.A. Zafar**, K. Knížek, J. Houdková, P. Jiríček, M. Bouša, J. Plšek, M. Kalbáč, J. Červenka, O. Frank

Annexed: Carbon, 2022, 186, 612-623



Influence of structural properties on (de-)intercalation of ClO_4^- anion in graphite from concentrated aqueous electrolyte



Ghulam Abbas^{a,b}, Farjana J. Sonia^{a,*}, Zahid Ali Zafar^{b,c}, Karel Knížek^d, Jana Houdková^e, Petr Jiríček^e, Milan Bouša^a, Jan Plšek^a, Martin Kalbáč^a, Jiří Červenka^c, Otakar Frank^{a,**}

^a J. Heyrovsky Institute of Physical Chemistry of the Czech Academy of Sciences, v.v.i, Doležalkova 2155/3, 183 23, Prague 8, Czech Republic

^b Department of Physical Chemistry and Macromolecular Chemistry, Faculty of Science, Charles University in Prague, Hlavova 2030, 128 43, Prague 2, Czech Republic

^c Department of Thin Films and Nanostructures, FZU - Institute of Physics of the Czech Academy of Sciences, Cukrovarnicka 10/112, 162 00, Prague 6, Czech Republic

^d Department of Magnetism and Superconductors, FZU - Institute of Physics of the Czech Academy of Sciences, Cukrovarnicka 10/112, 162 00, Prague 6, Czech Republic

^e Department of Optical Materials, FZU - Institute of Physics of the Czech Academy of Sciences, Cukrovarnicka 10/112, 162 00, Prague 6, Czech Republic

ARTICLE INFO

Article history:

Received 9 August 2021

Received in revised form

12 October 2021

Accepted 17 October 2021

Available online 18 October 2021

Keywords:

Structural properties

Graphite

Electrochemical intercalation

Graphite intercalation compounds

Aqueous electrolyte

Spectroelectrochemistry

ABSTRACT

Graphite intercalation compounds (GICs) are widely known for their remarkable multifold physico-chemical properties and their numerous state-of-the-art applications, such as energy storage, sensors, lubrication, catalysis, magneto-optics, superconductivity, etc. However, the properties of GICs largely depend on the synthesis technique, structure, and morphology of the graphite; the size and properties of the intercalant species and its concentration in the host material. Accordingly, in the field of electrochemical energy storage, the appearance of novel ionic systems and detailed investigations of GICs are highly desired. In this study, two different types of graphite, natural graphite (NG) and kish graphite (KG), were used to gain insights into the intercalation of ClO_4^- anion in graphite from a concentrated $\text{Al}(\text{ClO}_4)_3$ aqueous electrolyte solution through extensive electrochemical studies and various *in situ* and *ex situ* spectroscopic characterization techniques. An analysis of cyclic voltammograms indicated the presence of surface-controlled charge storage along with diffusion-controlled ion intercalation into the interlayer spaces in NG and KG. Additionally, a comparative study on the electrochemical behavior of these two types of graphite showed differences that can be correlated with their structural properties. These findings open new perspectives for GIC formation in concentrated aqueous electrolytes and applications in electrochemical energy storage.

© 2021 Elsevier Ltd. All rights reserved.

1. Introduction

Graphite is a widely known amphoteric material for intercalation of “guest” molecules and ions of different sizes and properties in the interlayer galleries of constituent graphene layers by chemical and electrochemical means and formation of acceptor/donor type graphite intercalation compounds (GICs) [1–3]. Due to their manifold exceptional physico-chemical properties, GICs have drawn attention as functional materials in various fields of research

and industrial usage [3,4]. For instance, GICs based on metal chlorides, pentafluorides, alkali metals, and others have been observed to have high electrical conductivity [5]. Graphite or graphene sheets are prepared at an industrial scale by the exfoliation of graphite from metal-based GICs or large ion/molecule-based GICs [6]. Easy shearing of the graphene layers upon ionic/molecular intercalation in the interlayer spaces makes GICs excellent lubricants [7]. The reversible electrochemical (de-)intercalation of lithium ions in graphite and excellent mechanical integrity have established graphitic carbon as the most commonly used anode material for state-of-art Li-ion batteries [3,8–11]. Additionally, the capability of storing even larger, negatively charged ions in the graphitic carbon structure has led to the introduction of graphite-based dual-ion battery (DIB) systems [12]. However, the progress

* Corresponding author.

** Corresponding author.

E-mail addresses: jaishmin.farjana@jh-inst.cas.cz (F.J. Sonia), otakar.frank@jh-inst.cas.cz (O. Frank).

<https://doi.org/10.1016/j.carbon.2021.10.051>

0008-6223/© 2021 Elsevier Ltd. All rights reserved.

of DIBs and other electrochemical applications strongly depends on the development of novel GICs and electrolytes that can support mixed ion chemistries.

Recently, a wide range of anions has been extensively investigated for electrochemical intercalation into graphite using different electrolyte salts in organic solvents, ionic liquids, and water. The intercalation mechanism has been explored for various redox-active anionic species, such as BF_4^- , ClO_4^- , PF_6^- , AlCl_4^- , bis (trifluoromethanesulfonyl) imide (TFSI⁻), bis (fluorosulfonyl) imide (FSI⁻), fluorosulfonyl- (trifluoromethanesulfonyl) imide (FTFSI⁻), or bis (fluorosulfonyl) amide (FSA⁻) [13–21]. Among them, the aqueous electrolytes have recently received tremendous attention for dual ion batteries due to their multifold advantages, including low cost, non-corrosiveness, easy handling (even the suitability of handling in open air), high ionic conductivity, and safety due to their non-flammable nature, over ionic liquid and organic electrolytes [20–24]. However, hydrogen evolution reactions (HERs) and oxygen evolution reactions (OERs) at the graphite surface limit the workable potential window of aqueous electrolytes below the theoretical potential of water-splitting (1.23 V). They are a serious concern for the development of aqueous-based DIBs, which require high intercalation potential for anions [25–27]. To circumvent this issue, highly concentrated water-in-salt aqueous electrolyte solutions have been utilized to enlarge the operational window [28,29]. Such an extended potential window not only reduces electrolyte decomposition but also provides a better chance for redox-active ionic species to intercalate deeper into layers of the host graphite material and the formation of more concentrated and lower indexed “stage” GICs, resulting in high charge storage capacity and high Coulombic efficiency [30–32]. However, the intercalation mechanisms of most of the anions, mentioned above, are yet to be investigated in aqueous electrolyte systems. Among them, the ClO_4^- anion has been chosen for the current study in a concentrated aqueous solution of $\text{Al}(\text{ClO}_4)_3$ salt, which is an electrolyte that has not previously been explored for graphite intercalation.

Additionally, the physico-chemical properties of GICs depend largely upon the size and properties of the intercalant species, their concentration in the host material, and the synthesis technique, the structure, and the morphology of the graphite [33–35]. For instance, Placke et al. [34] showed that the electrochemical intercalation behavior of TFSI⁻ ions in various types of commercially available graphite differs significantly, predominantly due to the varied particle sizes and surface areas. Ishihara et al. [35] showed that the intercalation of PF_6^- ions also varies when graphitic carbon materials of different interlayer spaces and crystallinity are used. Ejigu et al. [36] reported variations in the intercalation of AlCl_4^- ions in expanded graphite materials, prepared via different methods. Our previous studies also confirmed that the electrochemical storage of alkali metal ions in graphitic/graphenic carbon is strongly influenced by its preparation methods, dimensionality, and physical/structural properties [3,9,11,37].

Herein, we report a comparative study on the reversible (de-) intercalation of the ClO_4^- anion in natural (NG) and kish graphite (KG) using a concentrated $\text{Al}(\text{ClO}_4)_3$ aqueous electrolyte solution. By means of extensive material characterization, electrochemical studies, and *in situ* and *ex situ* spectroscopic characterizations, we unveil the intercalation process of the ClO_4^- anion and establish the correlation between the structural properties and the electrochemical behavior of NG and KG. The results also provide a useful insight into the electrochemical energy storage processes in perchlorate anion intercalated graphite electrodes, which is in particular important for the future development of aqueous-based DIBs and understanding the intercalation of large ionic species in layered materials, graphite and beyond.

2. Material and methods

2.1. Electrolyte preparation

A 2.4 M aqueous $\text{Al}(\text{ClO}_4)_3$ electrolyte solution was prepared by dissolving 29.24 g of $\text{Al}(\text{ClO}_4)_3 \cdot 9\text{H}_2\text{O}$ (Alfa Aesar) in 10 ml of deionized water and stirring at room temperature for 30 min.

2.2. Electrode preparation

For the preparation of electrodes, a slurry consisting of commercial NG (Nacional de Grafite, Ltda) or KG (Graphene Supermarket) powder, conducting carbon black, polyvinylidene difluoride (PVDF) binder (75:15:10 wt ratio), and *N*-methyl-2-pyrrolidone (NMP) was tape-casted on a current collector made of polytetrafluoroethylene (PTFE)-treated hydrophobic carbon paper that was 150–200 μm thick (120 Toray Carbon paper, Fuel Cell Store, USA). The as-prepared electrodes were dried at 80 °C under a vacuum in an oven for 12 h prior to electrochemical testing; such electrodes are called *pristine* in the following text.

2.3. Electrochemical cycling

A standard three-electrode electrochemical cell was used for cycling the electrodes prepared from NG and KG in concentrated $\text{Al}(\text{ClO}_4)_3$ electrolyte using an Ag/AgCl reference electrode and a platinum (Pt) wire as a counter electrode. The electrochemical measurements were performed using a μ -Autolab type III workstation. The cyclic voltammetry (CV) tests were conducted in the potential window of –0.08 to 1.58 V (vs. Ag/AgCl) at various sweep rates (from 1 to 7 mVs^{-1}), and the galvanostatic charge/discharge tests were performed from –0.08 to 1.55 V (vs. Ag/AgCl).

2.4. Materials characterization

X-Ray diffraction (XRD) was performed on Bruker D8 Advance equipped with Lynxeye XE-T position sensitive detector with $\text{Cu } \alpha_1$ ($\lambda = 1.5406 \text{ \AA}$). In order to improve the accuracy of the measured peak positions, XRD spectra were recorded with a very slow scan rate (*i.e.*, 0.01° per step) and with slit width of 0.6 mm. Fourier transform infrared spectra (FTIR) in attenuated total reflection (ATR) mode were recorded using a Nicolet FTIR-6700 spectrophotometer in the region of 4000–650 cm^{-1} (resolution of 4 cm^{-1}) with a laser wavelength of 633 nm. The samples were in contact with a zinc selenide (ZnSe) ATR crystal, and the spectra were averaged over 64 scans. Scanning electron microscopy (SEM) images were obtained using a Hitachi S4800 microscope. For the *ex situ* characterizations, all the samples were discharged till –0.08 V and charged till 1.55 V (vs. Ag/AgCl), washed in DI water, and dried prior to the measurements; such electrodes are called *discharged* and *charged*, respectively, in the following text.

X-Ray Photoelectron Spectroscopy (XPS) of the pristine, charged, and discharged graphite electrode materials was performed using an AXIS Supra photoelectron spectrometer (Kratos Analytical Ltd.) with an Al $K\alpha$ monochromatic energy source. The spectra were recorded after sputter etching of the samples with Ar^+ ion clusters (the number of Ar atoms in the cluster was 1000) of 5 keV energy for 10 min.

The *in situ* Raman spectroelectrochemistry measurements were carried out in homemade glass spectroelectrochemical cells, as shown in Fig. S1, using NG or KG as the working electrode, Ag/AgCl as the reference electrode, and Pt as the counter electrode. The Raman spectra were recorded using Horiba Lab-RAM HR equipped with an Olympus microscope using a 633 nm laser operated at

1 mW power by 600 lines/mm grating and 100× long working distance objective connected to an Autolab PGSTAT30. The same Raman setup was used for the *ex situ* Raman characterization.

3. Results and discussion

3.1. Structural and morphological characterization of the pristine graphite samples

The SEM images of the pristine NG in Fig. 1a and b and the pristine KG in Fig. 1c and d shows the difference in the graphite structure. The XRD spectra of the pristine NG and the KG are shown in Fig. 1e. The XRD (002) peak of the NG and KG (Fig. 1e) was recorded at 26.53(7)° and 26.54(6)° respectively, corresponding to the interlayer spacing (d_{002}) of 3.356 and 3.355 Å, respectively. Additionally, as the degree of graphitization is a very important

parameter for determining the structural properties of the graphitic material, the graphitization degree for out of plane, i.e., along c-axis (g) was calculated as follows [38]:

$$g (\%) = \frac{0.3440 - d_{002}}{0.3440 - 0.3354} \times 100, \quad (1)$$

where 0.3440 (nm) is the interlayer spacing of fully non-graphitized carbon, d_{002} (nm) is the interlayer spacing estimated from XRD and 0.3354 (nm) is the interlayer spacing of the ideal graphite crystals. The degree of graphitization based on d_{002} was estimated to be 97.67% for the case of NG and 98.84% for KG, as shown in Table 1.

Furthermore, the probability of the adjacent hexagonal layer planes having the graphitic AB stacking relation which is also known as degree of graphitization (i.e., P_1) and accounts for the

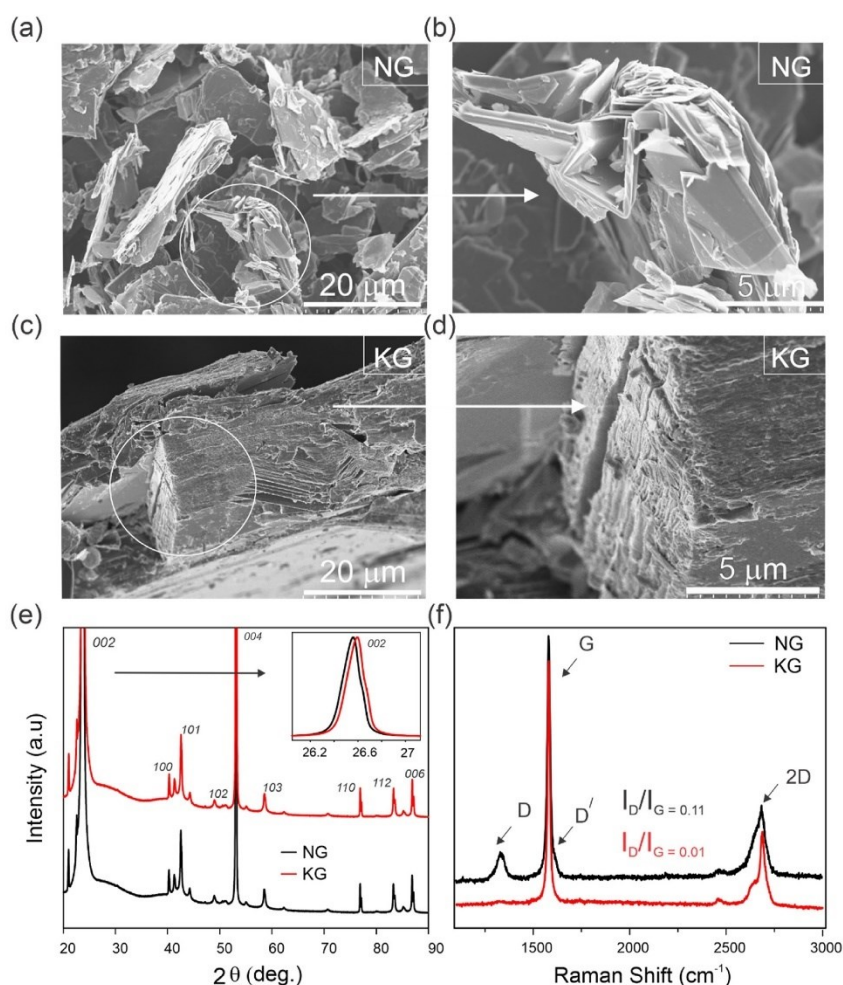


Fig. 1. Characterization of the pristine NG and KG: (a) SEM image and (b) zoomed-in SEM image of NG; (c) SEM image and (d) zoomed-in SEM image of KG; and (e) XRD and (f) Raman spectra of NG (black) and KG (red). (A colour version of this figure can be viewed online.)

Table 1
The quantification of structural parameters for NG and KG.

| Material | g (%) | $P_1(10)$ | $P_1(11)$ | L_c (nm) | L_D (nm) | n_D (cm ⁻²) | L_a (nm) |
|-----------------------|-------|-----------|-----------|------------|------------|---------------------------|------------|
| Natural graphite (NG) | 97.67 | 0.92 | 1.00 | 46.12 | 51.25 | 12.33×10^9 | 350.29 |
| Kish graphite (KG) | 98.84 | 0.93 | 1.00 | 46.13 | 170.00 | 1.12×10^9 | 3853.24 |

evolution of graphitic structure in the a and b-axis (i.e., in-plane direction) was also determined from the Fourier coefficients of both 10 and 11 diffraction profiles (i.e., $A_1(10)$ and $A_1(11)$, respectively) [39–41] following the relation:

$$P_1(10) = -2A_1(10), \quad (2)$$

$$P_1(11) = A_1(11). \quad (3)$$

The Fourier coefficient $A_n(hk)$ for each (hk) diffraction line was calculated following equation (4).

$$A_n(hk) = \frac{\sum q(2\theta) \cdot \cos \left[2\pi n (\sin^2\theta - \sin^2\theta_0)^{1/2} \cdot 2d_{002} / \lambda \right]}{\sum q(2\theta)}, \quad (4)$$

where $\sum q(2\theta)$ is a summation of integrated intensity of diffraction angle for $hk0$ to $hk2$ and θ_0 is the peak position of $hk0$ line and λ is the wavelength of incident X-rays. The estimated values of P_1 for NG are $P_1(10) = 0.92$ and $P_1(11) = 1.00$ and for KG are $P_1(10) = 0.93$ and $P_1(11) = 1.00$, as mentioned in Table 1.

The coherent domain size (L) of the polycrystalline hexagonal graphitic structure can be calculated by using the Scherrer equation when analyzing the X-ray diffraction peaks [42]:

$$L = \frac{k\lambda}{\beta \cos\theta}, \quad (5)$$

where the Scherrer constant (k) is 0.89 for the c -axis domain size L_c (002) and β (radian) is the full width at half maximum (FWHM) of the respective XRD peak, and θ is the Bragg's angle. Using Eq. (5), the L_c (002) along c -axis were calculated to be 46.12 nm and 46.13 nm for NG and KG respectively, as shown in Table 1.

Furthermore, as shown in Fig. 1f, the Raman spectra of both the NG and the KG exhibit a Raman active feature of the doubly degenerate E_{2g} phonon mode (the G band) at 1582 cm^{-1} [43]. However, the NG has more pronounced disorder-induced D and D[□] bands at 1350 cm^{-1} and 1620 cm^{-1} , respectively, compared to the KG. Similarly, the 2D band at $2500\text{--}2700 \text{ cm}^{-1}$ shows differences between the two materials, where the higher intensity of the lower frequency component in the NG indicates a lower structural order [44]. Hence, the average inter-defect distance (L_D) and the defect density of graphite (n_D) can be quantified from the D to G intensity ratio (I_D/I_G) by the following equations [45]:

$$L_D^2 (\text{nm}^2) = (1.8 \pm 0.5) \times 10^{-9} \lambda_L^4 \left(\frac{I_D}{I_G} \right)^{-1}, \quad (6)$$

$$n_D (\text{cm}^{-2}) = \frac{(1.8 \pm 0.5) \times 10^{22}}{\lambda_L^4} \left(\frac{I_D}{I_G} \right), \quad (7)$$

where λ_L is the wavelength of the laser used to measure the Raman spectra. The smaller I_D/I_G ratio of the KG ($I_D/I_G = 0.01$) corresponds to a larger L_D of 170.00 nm in comparison to the NG ($I_D/I_G = 0.11$, $L_D = 51.25$ nm), as mentioned in Table 1. Consequently, the n_D is estimated to be higher in the NG ($12.33 \times 10^9 \text{ cm}^{-2}$) compared to the KG ($1.12 \times 10^9 \text{ cm}^{-2}$). The low defect density in the KG illustrates a higher structural order and higher degree of graphitization.

Furthermore, the crystallite size (L_a) can be estimated from the following equation [46]:

$$L_a (\text{nm}) = 2.4 \times 10^{-10} \lambda_L^4 \left(\frac{I_D}{I_G} \right)^{-1}, \quad (8)$$

This leads to determination of the L_a as 3853.24 nm for the KG while it was 350.29 nm for the NG (Table 1). This is again in line with the previous observation of the lower degree of graphitization of the NG, compared to KG. The differences in domain size and crystallinity of the NG and the KG also play a significant role in the electrochemical performance and the anion intercalation process, which are discussed in the following sections.

3.2. Electrochemical intercalation/deintercalation of ClO_4^- anions

The cyclic voltammograms of the NG and the KG in a 2.4 M aqueous solution of $\text{Al}(\text{ClO}_4)_3$ were recorded at a sweep rate of 5 mVs^{-1} . Fig. 2a shows a set of two redox peaks, both in the cathodic and anodic regimes. The oxidation peaks at 1.43 V (O^{\square}_A) and 1.55 V (O_A) and the reduction peaks at 1.15 V (R^{\square}_C) and 1.35 V (R_C) indicate intercalation and deintercalation (respectively) of the ClO_4^- ions in the graphite samples and the formation of the perchlorate-based GICs [47,48]. The galvanostatic charge/discharge potential profiles obtained with the NG and the KG at a current density of 250 mA/g are shown in Fig. 2b. This also shows the presence of prominent potential plateaus at around 1.55 V during charge and 1.35 V during discharge, as well as a less discernible one at 1.15 V during discharge, in agreement with the peaks observed in the CVs. The prominent redox peaks and difference in galvanostatic charge/discharge potential profile in the case of the KG is due to its higher structural order, with a larger crystallite domain size than that in the NG.

3.3. Anion intercalation/deintercalation process

To describe the process of the anion intercalation/deintercalation in more detail, various *ex situ* techniques, such as XRD, FTIR-ATR, XPS and Raman spectroscopy, accompanied by *in situ* Raman spectroelectrochemistry, were used on the pristine, charged, and discharged electrodes (see section 2. Material and methods).

As shown in Fig. 3a-e, upon charging, the XRD peak at 26.5° of the pristine NG (Fig. 3c) splits into two peaks (Fig. 3a, b and d) at 2θ of 25.9° ($d = 3.44 \text{ \AA}$) and 26.6° ($d = 3.35 \text{ \AA}$) along with the appearance of an additional peak at 18.1° ($d = 4.90 \text{ \AA}$). The enhanced interlayer spacing of the charged NG indicates the intercalation of ClO_4^- ions [47]. The splitting of the (002) peak due to the intercalation of the large ClO_4^- anion was also previously observed by other research groups [49,50]. It should also be mentioned here that the intercalation of anions deeper in the graphite and formation of Stage I occurs at high potentials of $\sim 4.5\text{--}5.5 \text{ V vs. Li/Li}^+$ [27,51,52]. However, for our case, due to the limitation of water-splitting and OER in the aqueous $\text{Al}(\text{ClO}_4)_3$ electrolyte, the charging of the NG was restricted to comparatively lower potential 1.55 V vs. Ag/AgCl (i.e., 4.60 V vs. Li/Li^+). The splitting of the (002) peak thus indicates a partial/incomplete intercalation of ClO_4^- ions in the NG, mainly at the edge sites of the

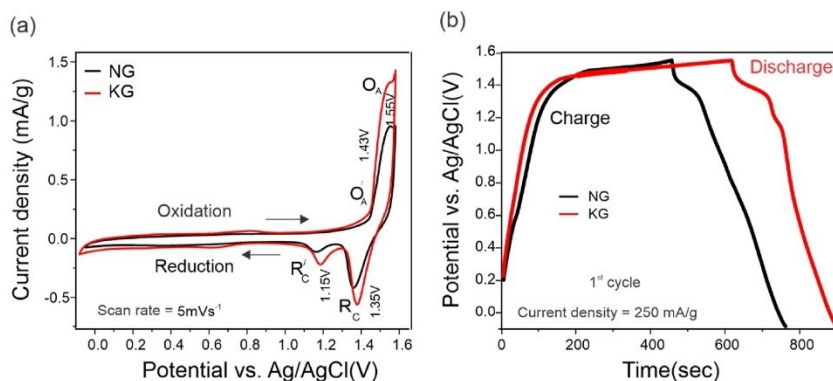


Fig. 2. Electrochemical performance of NG and KG using concentrated aqueous $\text{Al}(\text{ClO}_4)_3$ electrolyte solution: (a) cyclic voltammogram of NG and KG at 5 mVs^{-1} ; (b) galvanostatic charge/discharge potential profile of NG and KG obtained at a current density of 250 mA/g (1st cycle). (A colour version of this figure can be viewed online.)

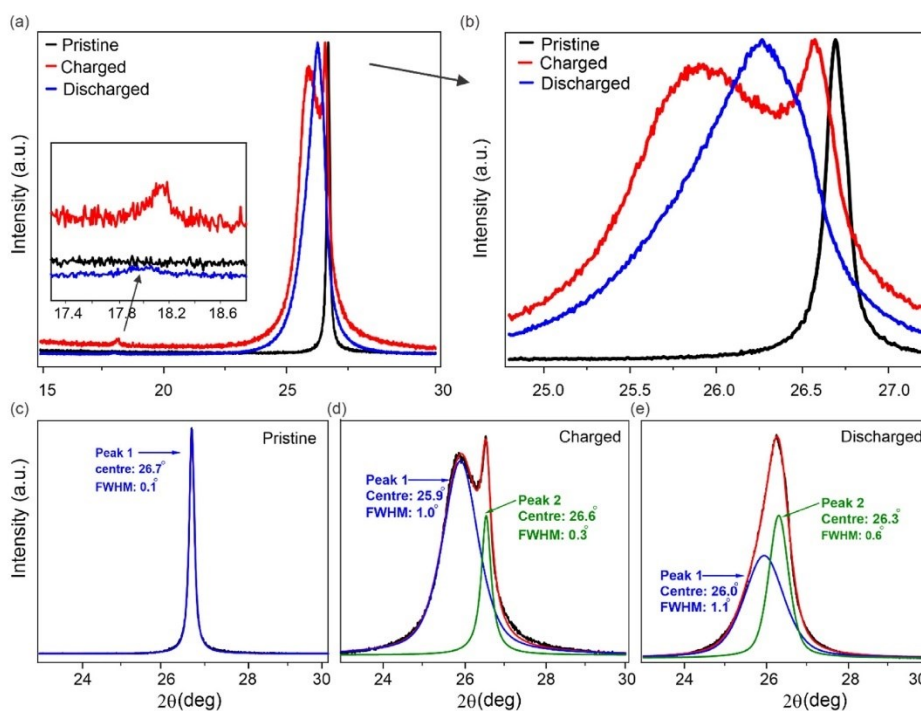


Fig. 3. X-ray diffractograms of NG: (a) broader range XRD and (b) zoomed-in view of (002) peak of pristine, charged and discharged NG. The deconvolution of the (002) XRD peak for (c) pristine, (d) charged, and (e) discharged NG. (A colour version of this figure can be viewed online.)

graphite crystallites.

After discharge, the intensity of the peak at 18.1° decreases, and the two major peaks merge into an asymmetric peak that could be deconvoluted into two peaks at $\sim 26.0^\circ$ ($d = 3.42 \text{ \AA}$) and $\sim 26.3^\circ$ ($d = 3.38 \text{ \AA}$) (Fig. 3a, b and e). The slightly enhanced interlayer spacing of the NG even after the discharge (Fig. 3e) in comparison to the pristine NG (Fig. 3c) might be due to the irreversibility or

decomposition of the ClO_4^- ion during deintercalation in the discharge half cycle. Furthermore, the L_c of the charged NG was observed to be 8.07 nm and 26.92 nm for peak 1 and 2, respectively, while it was 7.33 nm and 13.45 nm for peak 1 and 2, respectively, in the discharged state, which also reflects the decrease in the gallery height of the (002) plane upon the deintercalation of the ClO_4^- ion during the discharging process.

The *ex situ* Raman spectra (Fig. 4a) show the increased ratio of the Raman D and G band intensities ($I_D/I_G \sim 0.73$) in the charged NG, compared to the discharged NG ($I_D/I_G \sim 0.53$) and pristine NG ($I_D/I_G \sim 0.43$), indicating a higher degree of structural disorder due to the intercalation of ionic species, which is consistent with the *ex situ* XRD studies [47]. The *ex situ* Raman measurement of the KG (Fig. 4b) also demonstrates an increase of the I_D/I_G ratio to ~ 0.41 in the charged state, compared to the discharged ($I_D/I_G \sim 0.20$) and pristine KG ($I_D/I_G \sim 0.05$).

Furthermore, to gain deeper insights into the ionic intercalation and charge transfer processes in the NG and the KG, *in situ* Raman spectroelectrochemistry was performed. *In situ* Raman spectroelectrochemistry has been proved to be a useful tool in studying carbon materials, ranging from graphene and carbon nanotubes to bulk graphite. The Raman modes of these materials are dependent on defects, strain, and doping, which typically change during

electrochemical charging [53–57]. The Raman G band of graphitic carbons is known to be sensitive to the interaction of ionic species in the interlayer galleries and the formation of GICs [36,53]. A series of selected Raman spectra of NG collected during the first charge/discharge cycle is shown in Fig. 5a. During the charging half cycle, at approximately 1.45 V (vs. Ag/AgCl), the G peak splits into two components. The low-frequency ($\sim 1584 \text{ cm}^{-1}$) $E_{2g}(i)$ mode arises from the vibration of the sp^2 carbon atoms of the non-intercalated (interior) graphite layers, and the high-frequency ($\sim 1616 \text{ cm}^{-1}$) $E_{2g}(b)$ mode corresponds to the vibration of the carbon atoms from the boundary layers that accommodate intercalated ClO_4^- ions. Upon a further increase in the potential, the intensity of the $E_{2g}(b)$ peak increases due to the gradual enhancement of the ClO_4^- ion concentration in the graphite interlayer spaces. As shown before, the intercalation stage (n) of GICs can be estimated using the intensity ratio of the $E_{2g}(i)$ and $E_{2g}(b)$ (I_i/I_b) [58,59,60]:

$$\frac{I_i}{I_b} = \frac{(\sigma_i)}{(\sigma_b)} \frac{n-2}{2} \quad (9)$$

where σ_i/σ_b is the ratio of Raman scattering cross-sections, which is assumed to be unity [36]. Following eq. (9), at 1.55 V, the NG could be estimated to be in stage III ($I_i/I_b = 0.17$) upon the intercalation of ClO_4^- . The *in situ* Raman spectroelectrochemistry of the KG (Fig. 5b) shows a similar trend of the G band splitting into two components during the charging half cycle and the formation of stage III GIC, albeit with a higher $I_i/I_b = 0.51$ compared to the NG. Taking into consideration the highest achievable potential with our 2.4 M $\text{Al}(\text{ClO}_4)_3$ aqueous electrolyte of 1.55 V vs. Ag/AgCl (i.e., 4.6 V vs. Li/Li⁺) and the observation of only partial intercalation of the ClO_4^- ion in the NG and the KG, as also mentioned previously in this section, the stage number evaluated following Eq. (9) might be overestimated (see also Section 3.5). Furthermore, the presence of the $E_{2g}(b)$ at a low potential in the discharge cycle, together with a perceptible hysteresis in the $E_{2g}(i)$ shift, indicates again partial irreversibility in the (de-) intercalation process of ClO_4^- .

The chemical composition of pristine, charged, and discharged graphite electrode materials were studied by XPS (Figs. S2 and S3 and Tables S2 and S3). To suppress the contribution of adsorbed species on the surface, the samples were etched by Ar^+ ion clusters. The XPS survey spectra of the electrodes reveal the presence of Cl, Al, O, C, and F (Fig. S2a), among which F originates from the electrode binder (see section 2). The high-resolution Cl 2p core-level spectra (Fig. S2b, d and S3c, d) indicate the presence of two chemical states. The high-energy component at 208.1 eV corresponds to ClO_4^- and the low-energy component at 200.1 eV corresponds to Cl covalently bonded to sp^2 carbon [61,62]. The evidence for the intercalation of the ClO_4^- ion could be found in the increased atomic ratios of ClO_4^-/C or ClO_4^-/Al for charged samples (see Table S1). The concentration of ClO_4^- ions in the charged KG was approximately twice larger than that in the discharged sample (Table S1). Although Al was also detected for the discharged KG, the increased ClO_4^-/C or ClO_4^-/Al ratio indicates the presence of intercalated ClO_4^- ions in the charged KG. For the NG, the concentration of ClO_4^- ions seemed to be higher for the discharged sample. The presence of the ClO_4^- anion in the discharged NG (Fig. S2c) might be indicative of remaining ClO_4^- ions on the surface or in the graphite interlayer galleries. A complete discussion on the XPS characterization of the NG and the KG is provided in the supplementary information.

The *ex situ* FTIR measurements of the pristine, charged, and discharged NG are shown in Fig. S4. The peak at 1630 cm^{-1} , which is observed in the discharged NG but is absent in the case of the charged and pristine NG, can be tentatively assigned to the AlCl_2^+ ion [63] or O–H bending vibrations [64]. However, it is difficult to

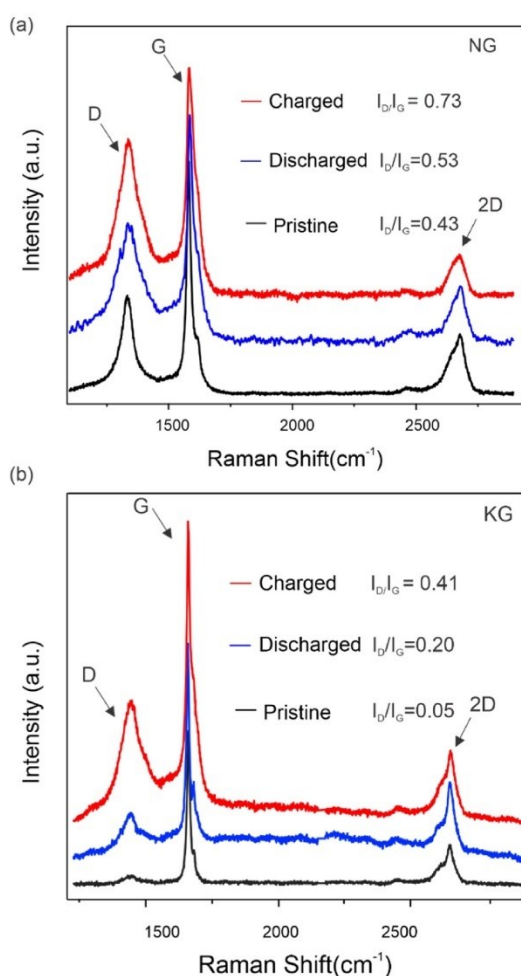


Fig. 4. *Ex situ* Raman spectroscopy of pristine, charged, and discharged (a) NG and (b) KG. (A colour version of this figure can be viewed online.)

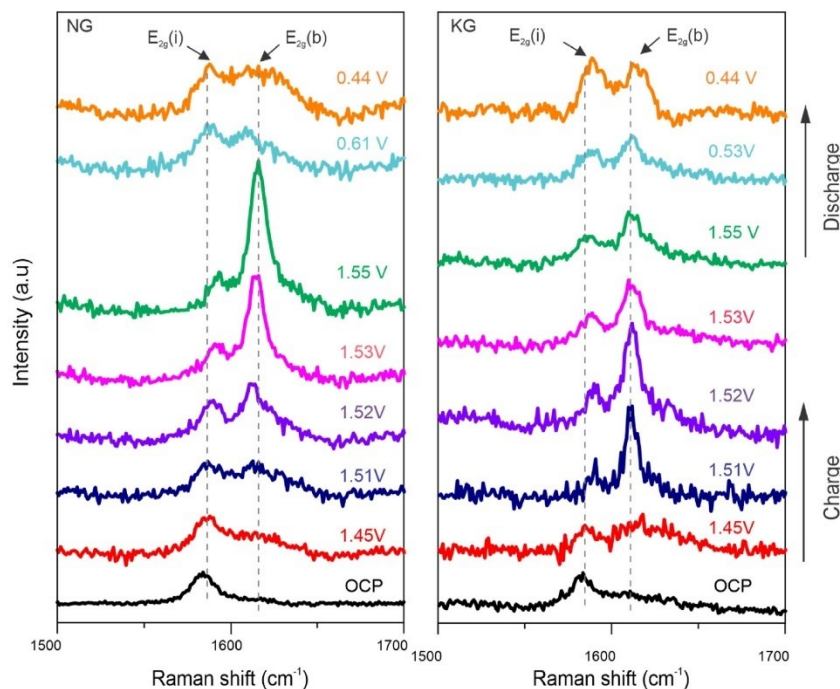


Fig. 5. *In situ* Raman spectroelectrochemistry of (a) NG and (b) KG during the charge/discharge process in concentrated $\text{Al}(\text{ClO}_4)_3$ aqueous electrolyte. (A colour version of this figure can be viewed online.)

make a strong conclusion here due to the overlapping position of these vibrations. The intense peaks corresponding to the O–H stretching and C–O asymmetric vibrations were also observed in the discharged NG (compared to the charged and pristine NG). These species originate from the decomposition of ClO_4^- ions during discharge, in agreement with the analysis of the XPS measurements (Note 1 in [supplementary information](#)).

3.4. Electrochemical kinetics of the ClO_4^- anion intercalation

To gain more insight into the process of charge storage in graphite when cycled in a concentrated $\text{Al}(\text{ClO}_4)_3$ aqueous electrolyte, the CV kinetics are depicted for the case of the NG and the KG in Fig. 6. Following the methodology described in detail in our previous publications [3,11,65], the diffusion and surface-controlled electrochemical processes have been disentangled through the analyses of cyclic voltammograms, as also discussed below. The power-law relationship of the peak current (i) and scan rate (ν) can be written as follows:

$$i = a \nu^b, \quad (10)$$

where a and b are adjustable parameters. The b value can be obtained from the slope of the $\log(i)$ vs. $\log(\nu)$ plot. The value of $b = 0.5$ indicates that the charge/discharge process is controlled by ion diffusion, while $b = 1$ indicates a purely surface-controlled process. The b value between 0.5 and 1.0 corresponds to the presence of both surface and diffusion-controlled processes [11,65].

The CVs of the NG in Fig. 6a show that the currents of the

corresponding redox peaks (O_A , O_A^\square , R_C and R_C^\square) increase with the increasing scan rate from 1 mVs^{-1} to 7 mVs^{-1} . The KG shows a similar trend of increase in the current with the scan rate (Fig. 6b). The CV kinetics of the NG, as shown in Fig. 6c, illustrates the fitted b value 0.79 for the oxidation peak O_A and 0.96 and 0.94 for the R_C and R_C^\square reduction peaks, respectively, which indicate the contribution of both ionic diffusion and surface-controlled processes. Furthermore, for the case of the KG, the CV kinetics of the fitted b value, as shown in Fig. 6d, is 0.74 for the oxidation peak O_A and 0.88 and 0.95 for the R_C and R_C^\square reduction peaks, respectively, which also indicate the contribution of both ionic diffusion and surface-controlled processes.

As both surface and diffusion-controlled processes of charge storage are present in NG and KG, their deconvolution can be performed from cyclic voltammograms. Based on the assumption of the summation of purely surface and diffusion-controlled processes, the relation of the overall current and the scan rate can be written as follows:

$$i = k_1 \nu + k_2 \nu^{1/2}, \quad (11)$$

where $k_1 \nu$ represents the surface-controlled process, and $k_2 \nu^{1/2}$ is the ionic diffusion [11,65]. The values of the adjustable parameters k_1 and k_2 can be determined from the slope and intercept, respectively, of the $i/\nu^{1/2}$ vs. $\nu^{1/2}$ plot. Thus, the deconvoluted currents for the NG and the KG (arising solely from the ionic diffusion and purely surface-controlled processes) are shown in Fig. 6e and f, overlapping with the experimentally recorded current at a potential sweep rate of 1 mVs^{-1} . At a scan rate of 1 mVs^{-1} , the charge

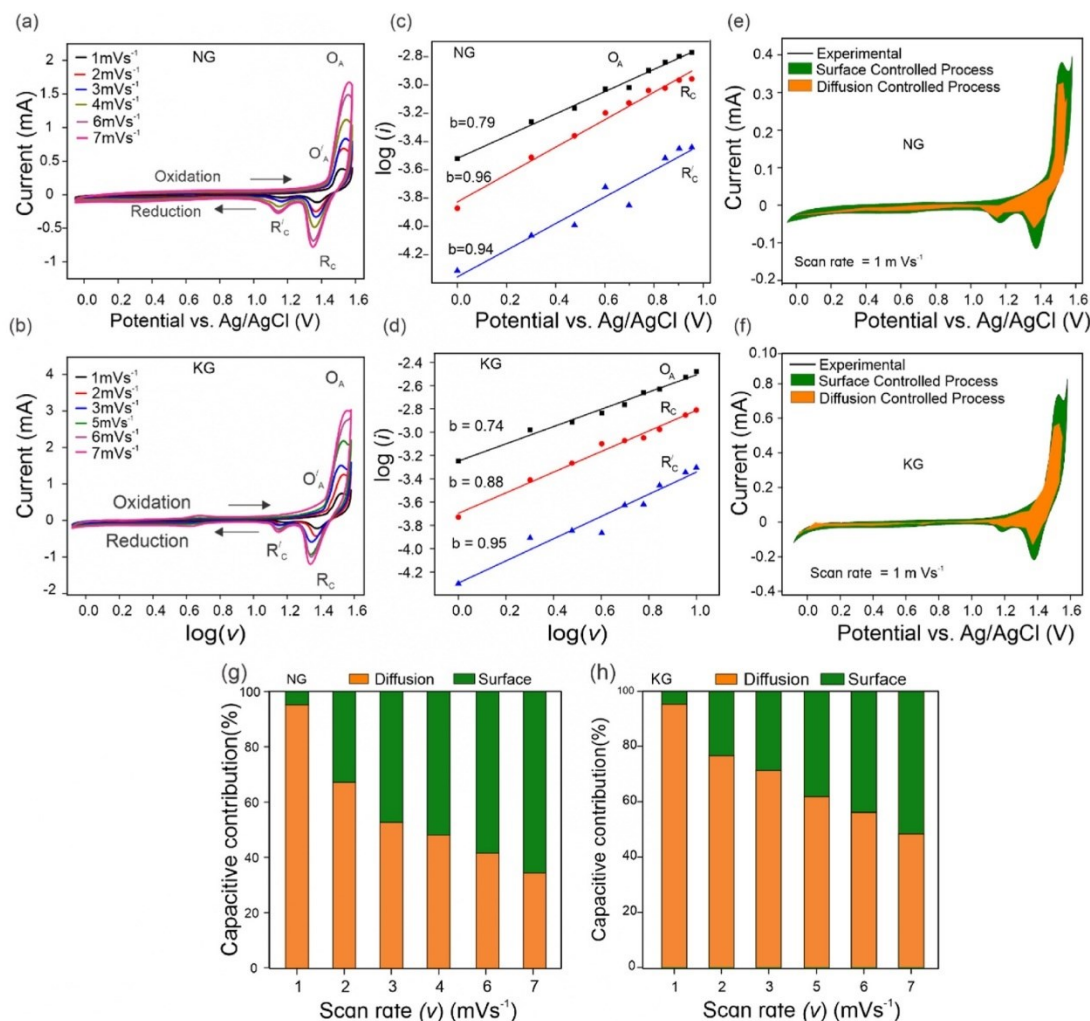


Fig. 6. Electrochemical kinetics analysis for ClO_4^- (de-)intercalation into NG and KG: (a–b) cyclic voltammograms of (a) NG and (b) KG at different scan rates (1–7 mVs^{-1}); (c–d) electrochemical kinetic plot of $\log(i)$ vs. $\log(v)$ at the redox peaks for (c) NG and (d) KG; (e–f) deconvolution of the surface and diffusion-controlled processes of charge storage in (e) NG and (f) KG superimposed on the cyclic voltammogram recorded at a sweep rate of 1 mVs^{-1} ; (g–h) the relative contribution of the surface and diffusion-controlled processes of charge storage in (g) NG and (h) KG at various sweep rates (from 1 to 7 mVs^{-1}). (A colour version of this figure can be viewed online.)

storage corresponds to a diffusion-controlled process; i.e. intercalation of the ionic species in the interlayer spaces has been observed to be ~95% for both types of graphite. However, the difference appeared at the higher scan rates, as shown in Fig. 6g and h, representing the relative contributions of charge storage with respect to the surface and diffusion-controlled processes, as calculated from the deconvoluted currents of CV for various scan rates (1–7 mVs^{-1}). The drop in contribution of the diffusion-controlled process from ~95% to ~38% with an increase in the sweep rate from 1 to 7 mVs^{-1} indicates that the surface-controlled process dominates over the diffusion with the increase in scan rate. In the case of the KG, the contribution of the diffusion-controlled

process dropped to a slower pace, to ~45% at 7 mVs^{-1} . This might be because of the larger crystallite size, lower defect content, and higher structural order of the KG, in comparison to the NG.

3.5. Specific capacity, rate capability, and reversibility of ClO_4^- anion storage

Fig. 7a–d shows the galvanostatic charge/discharge performance of the NG and the KG in a concentrated $\text{Al}(\text{ClO}_4)_3$ aqueous solution at a current density of 250 mA/g for 100 cycles. Fig. 7b indicates a relatively stable discharge capacity of ~20 mAhg^{-1} , even after 100 cycles, with Coulombic efficiency larger than 80%, whereas an

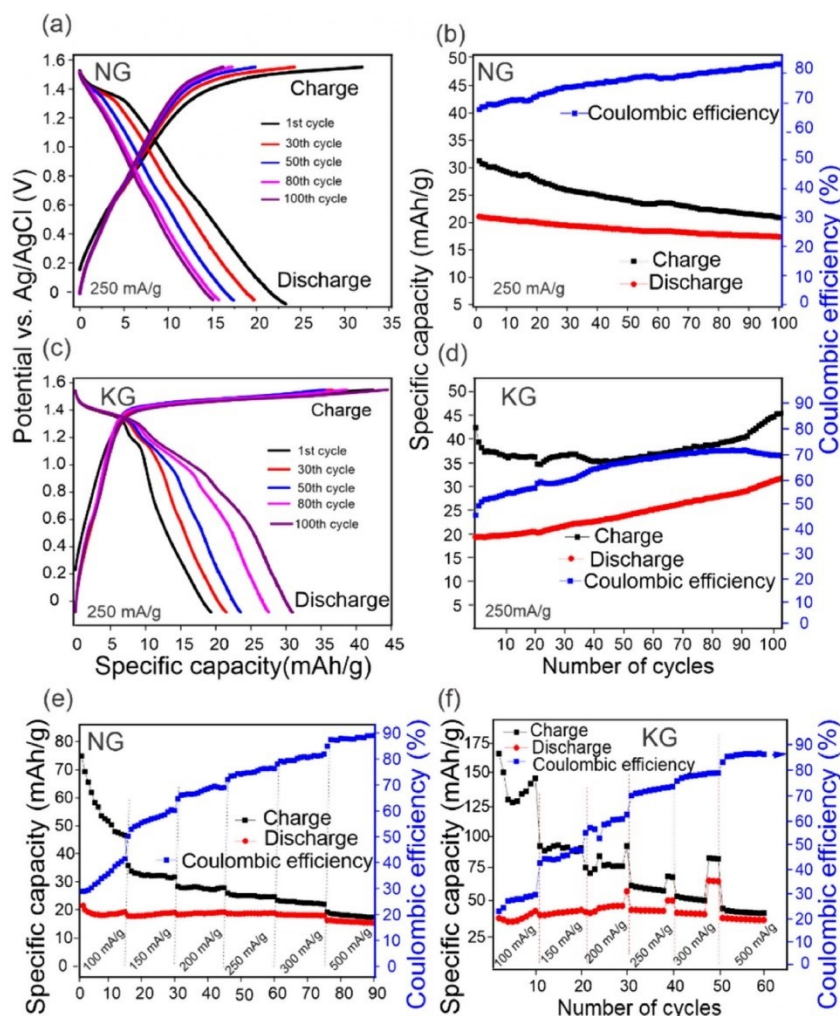


Fig. 7. The galvanostatic charge/discharge performance of NG and KG using concentrated aqueous $\text{Al}(\text{ClO}_4)_3$ electrolyte: (a) galvanostatic charge/discharge potential profile and (b) variation of specific capacity with the number of cycles obtained at a current density of 250 mA/g with NG and (c–d) with KG; (e–f) specific capacity recorded at various current densities (100 mA/g to 500 mA/g) for (e) NG and (f) KG. (A colour version of this figure can be viewed online.)

increase in discharge capacity from $\sim 18 \text{ mAhg}^{-1}$ to $\sim 30 \text{ mAhg}^{-1}$ is observed for the KG in 1–100 galvanostatic charge/discharge cycles with a comparatively stable charge capacity of $\sim 35 \text{ mAhg}^{-1}$ throughout (Fig. 7d). It needs to be emphasized here that the demonstrated capacity is comparable with the previous reports on ClO_4^- anion intercalation into graphitic materials, however, from organic electrolyte solutions [20]. Moreover, as the potential window for the aqueous electrolytes is limited due to HER and OER, the high cutoff voltage (e.g. 5.5 V vs. Li/Li^+) for complete anion intercalation is inaccessible [66]. Hence obtaining higher charge storage capacity from an aqueous electrolyte becomes difficult [66]. Following the previously reported theoretical and experimental studies on anionic intercalation, the obtained reversible capacity may correspond to the

formation of stage IV–V [14,27,52], which differs from the stage number estimated by the analysis of *in situ* Raman spectrum, as explained in Section 3.3. Furthermore, the difference in the electrochemical performance of NG and KG can be understood as originating from the variation in the defect density and the crystallinity of the graphitic structure. The increase in the defect density could limit the coherent length of the charge carriers and their mobility, which in turn mitigates the electrochemical performance [67]. The degree of crystallinity is another prominent factor that influences the capacity [68] and ionic intercalation in the graphitic structure [9,11]. For the case of the NG, higher defect density with less structural order might be the reason for its lower specific capacity, whereas the higher structural order of the KG enhancing the possibility for ClO_4^-

anion intercalation might be the reason for more prominent CV redox peaks (Fig. 2a), the larger potential plateau (Fig. 2b), and the higher charge/discharge specific capacity (Fig. 7a–d), in comparison to the NG. However, due to the larger crystalline size, the KG requires time for the stabilization of the charge/discharge capacity and also possesses lower Coulombic efficiency (~70%); i.e., faces a hurdle in the deintercalation of ClO_4^- anions.

Additionally, as shown in Fig. 7e, the NG also possesses good rate capability during the discharge process in the concentrated $\text{Al}(\text{ClO}_4)_3$ aqueous electrolyte solution. The discharge capacity obtained with the NG at a current density of 500 mA g^{-1} is 85% with respect to the capacity obtained at the lowest current density (100 mA g^{-1}), and the Coulombic efficiency increases with increasing current densities (Fig. 7e). One of the possible reasons is the suppression of some of the side reactions at higher current densities leading to more reversible charge storage. The charge/discharge of the KG measured at increasing current densities (shown in Fig. 7f) also reveals an increase in Coulombic efficiency, the same as in the NG. However, in contrast to NG, irregularities in the cyclic performance have been observed in KG at different current densities, which might be because of the time required for the stabilization of capacity in KG, as shown in Fig. 7d.

4. Conclusions

A comparative in-depth study on the reversible electrochemical (de-)intercalation of ClO_4^- anions in the NG and the KG using a concentrated $\text{Al}(\text{ClO}_4)_3$ aqueous electrolyte and its correlation with the structural properties is reported here. The characterizations of the pristine materials indicated lower degree of graphitization (g and P_1), smaller crystallite domain size (L_c and L_a) and higher defect content (i.e., higher n_D and smaller L_D) in the NG, compared to the KG. The process of the electrochemical charge storage in the graphite samples was revealed by extensive *ex situ* and *in situ* characterizations along with analytical and electrochemical studies. The prominent oxidation/reduction peaks corresponding to intercalation/deintercalation of ClO_4^- anions into the NG and the KG were observed in the cyclic voltammograms. Furthermore, the splitting of the XRD (002) peak, the change in the crystallite domain size upon charge/discharge, the appearance of an E_{2g} (b) Raman mode during the charging process, the increase of the I_D/I_G ratio, and the occurrence of the peaks related to ClO_4^- ion in the XPS spectra in charged state confirmed the intercalation of the ClO_4^- ions in the NG and the KG. Additionally, the analysis of the cyclic voltammograms indicated the presence of both surface and diffusion-controlled processes of charge storage for both the NG and the KG. The ionic intercalation/deintercalation in the NG resulted in a stable electrochemical performance (discharge capacity of $\sim 20 \text{ mAh g}^{-1}$ at a current density of 250 mA g^{-1}) with high Coulombic efficiency (>80%). However, we observed a higher discharge capacity of $\sim 30 \text{ mAh g}^{-1}$ at a current density of 250 mA g^{-1} for the KG, which can be attributed to the higher structural order and the lower defect content. Furthermore, the KG possesses slightly lower Coulombic efficiency (~70%) and has shown instability in the cyclic performance, which might be because of the larger crystallite size of KG compared to NG, making it difficult for the large size ClO_4^- anions to deintercalate from KG. Therefore, the detailed discussion on anion intercalation in NG and KG, the difference in their structural properties, and the variation in associated electrochemical behavior pave the way for smartly designed layered intercalation compounds and their applications in various fields, including environmentally friendly, non-flammable, and low-cost aqueous energy storage systems.

CRediT authorship contribution statement

Ghulam Abbas: Conceptualization, Methodology, Validation, Formal analysis, Investigation, Data curation, Writing – original draft, Funding acquisition. **Farjana J. Sonia:** Conceptualization, Methodology, Validation, Formal analysis, Investigation, Data curation, Writing – original draft. **Zahid Ali Zafar:** Conceptualization, Methodology, Validation, Investigation, Writing – review & editing. **Karel Knížek:** Validation, Formal analysis, Investigation, Writing – review & editing. **Jana Houdková:** Validation, Investigation. **Petr Jiríček:** Validation, Investigation. **Milan Bouša:** Validation, Investigation. **Jan Plšek:** Validation, Formal analysis, Investigation, Writing – review & editing. **Martin Kalbáč:** Validation, Writing – review & editing, Supervision, Funding acquisition. **Jirí Červenka:** Conceptualization, Methodology, Validation, Writing – review & editing, Supervision, Funding acquisition. **Otakar Frank:** Conceptualization, Methodology, Validation, Formal analysis, Data curation, Writing – original draft, Supervision, Funding acquisition.

Declaration of competing interest

The authors declare that they have no known competing financial interests or personal relationships that could have appeared to influence the work reported in this paper.

Acknowledgment

We acknowledge funding support from the Czech Science Foundation (GACR – Grant No. 19-23986S), the European Regional Development Fund; OP RDE; Project: “Carbon allotropes with rationalized nanointerfaces and nanolinks for environmental and biomedical applications” (No. CZ.02.1.01/0.0/0.0/16_026/0008382), Charles University Grant Agency (GAUK, project No. 371621), and LTAUSA19001 by the Ministry of Education, Youth and Sports of the Czech Republic. This work was also supported by the project Strategy AV21, program Diagnostic Methods, and Techniques. We are also thankful to M. Remzová and R. Zouzelka for assistance with FTIR measurements, V.L.P. Guerra for help with XRD measurements, and A. Rodriguez for help with CV analysis.

Appendix A. Supplementary data

Supplementary data to this article can be found online at <https://doi.org/10.1016/j.carbon.2021.10.051>.

References

- [1] M. Nobel, R. Santhanam, Review Electrochemistry of graphite intercalation compounds, *J. Power Sources* 72 (1998) 53–65.
- [2] M.S. Dresselhaus, G. Dresselhaus, Intercalation compounds of graphite, *Adv. Phys.* 51 (2002) 1–186.
- [3] F.J. Sonia, M.K. Jangid, M. Aslam, P. Johari, A. Mukhopadhyay, Enhanced and faster potassium storage in graphene with respect to graphite: a comparative study with lithium storage, *ACS Nano* 13 (2019) 2190–2204.
- [4] T. Enoki, M. Endo, M. Suzuki, Graphite Intercalation Compounds and Applications, Oxford University Press, 2003, <https://doi.org/10.1093/oso/9780195128277.001.0001>. ISBN-13: 9780195128277.
- [5] M. Inagaki, Applications of graphite intercalation compounds, *J. Mater. Res.* 4 (1989) 1560–1568.
- [6] M. Yi, Z. Shen, A review on mechanical exfoliation for the scalable production of graphene, *J. Mater. Chem. A* 3 (2015) 11700–11715.
- [7] P. Sutor, Solid lubricants: overview and recent developments, *MRS Bull.* 16 (1991) 24–30.
- [8] J.B. Goodenough, K.S. Park, The Li-ion rechargeable battery: a perspective, *J. Am. Chem. Soc.* 135 (2013) 1167–1176.
- [9] F.J. Sonia, M. Aslam, A. Mukhopadhyay, Understanding the processing-structure-performance relationship of graphene and its variants as anode

- [65] M.K. Jangid, A.S. Lakhnot, A. Vemulapally, F.J. Sonia, S. Sinha, R.O. Dusane, A. Mukhopadhyay, Crystalline core/amorphous shell structured silicon nanowires offer size and structure dependent reversible Na-storage, *J. Mater. Chem. A* 6 (2018) 3422–3434.
- [66] Y. Kondo, Y. Miyahara, T. Fukutsuka, K. Miyazaki, T. Abe, Electrochemical intercalation of bis(fluorosulfonyl)amide anions into graphite from aqueous solutions, *Electrochem. Commun.* 100 (2019) 26–29.
- [67] K.S. Kim, Y. Zhao, H. Jang, S.Y. Lee, J.M. Kim, K.S. Kim, J.H. Ahn, P. Kim, J.Y. Choi, B.H. Hong, Large-scale pattern growth of graphene films for stretchable transparent electrodes, *Nature* 457 (2009) 706–710.
- [68] C. Zhang, R. He, J. Zhang, Y. Hu, Z. Wang, X. Jin, Amorphous carbon-derived nanosheet-bricked porous graphite as high-performance cathode for aluminum-ion batteries, *ACS Appl. Mater. Interfaces* 10 (2018) 26510–26516.

Appendix III

The Effects of Ultrasound Treatment of Graphite on the Reversibility of (De)intercalation of Anion from Aqueous Electrolyte Solution

G. Abbas, **Z.A. Zafar**, F.J. Sonia K. Knižek, J. Houdková, P. Jiříček, M. Kalbáč, J. Červenka, O. Frank.

Annexed: Nanomaterials, 2022, 12, 3932



Article

The Effects of Ultrasound Treatment of Graphite on the Reversibility of the (De)Intercalation of an Anion from Aqueous Electrolyte Solution

Ghulam Abbas ^{1,2}, Zahid Ali Zafar ^{2,3}, Farjana J. Sonia ¹, Karel Knížek ³, Jana Houdková ³, Petr Jiříček ³, Martin Kalbáč ¹, Jiří Červenka ³ and Otakar Frank ^{1,*}

¹ J. Heyrovsky Institute of Physical Chemistry, Czech Academy of Sciences, Dolejskova 2155/3, 183 23 Prague, Czech Republic

² Department of Physical Chemistry and Macromolecular Chemistry, Faculty of Science, Charles University in Prague, Hlavova 2030, 128 43 Prague, Czech Republic

³ FZU—Institute of Physics of the Czech Academy of Sciences, Cukrovarnicka 10/112, 162 00 Prague, Czech Republic

* Correspondence: otakar.frank@jh-inst.cas.cz



Citation: Abbas, G.; Zafar, Z.A.; Sonia, F.J.; Knížek, K.; Houdková, J.; Jiříček, P.; Kalbáč, M.; Červenka, J.; Frank, O. The Effects of Ultrasound Treatment of Graphite on the Reversibility of the (De)Intercalation of an Anion from Aqueous Electrolyte Solution. *Nanomaterials* **2022**, *12*, 3932. <https://doi.org/10.3390/nano12223932>

Academic Editor: Rosario Pereira

Received: 6 October 2022

Accepted: 3 November 2022

Published: 8 November 2022

Publisher's Note: MDPI stays neutral with regard to jurisdictional claims in published maps and institutional affiliations.



Copyright: © 2022 by the authors. Licensee MDPI, Basel, Switzerland. This article is an open access article distributed under the terms and conditions of the Creative Commons Attribution (CC BY) license (<https://creativecommons.org/licenses/by/4.0/>).

Abstract: Low cycling stability is one of the most crucial issues in rechargeable batteries. Herein, we study the effects of a simple ultrasound treatment of graphite for the reversible (de)intercalation of a ClO_4^- anion from a 2.4 M $\text{Al}(\text{ClO}_4)_3$ aqueous solution. We demonstrate that the ultrasound-treated graphite offers the improved reversibility of the ClO_4^- anion (de)intercalation compared with the untreated samples. The ex situ and in situ Raman spectroelectrochemistry and X-ray diffraction analysis of the ultrasound-treated materials shows no change in the interlayer spacing, a mild increase in the stacking order, and a large increase in the amount of defects in the lattice accompanied by a decrease in the lateral crystallite size. The smaller flakes of the ultrasonicated natural graphite facilitate the improved reversibility of the ClO_4^- anion electrochemical (de)intercalation and a more stable electrochemical performance with a cycle life of over 300 cycles.

Keywords: ultrasonication; graphite; intercalation; in situ Raman spectroelectrochemistry; operando XRD; aqueous electrolyte

1. Introduction

Overwhelming energy demand has propelled paramount interest in discovering the best ways to store energy in an environmentally friendly and sustainable manner [1]. For the development of more efficient and stable energy storage technologies, it is vital to explore different possible electrochemical charge storage mechanisms [2]. Graphite is one of the most studied electrode materials for batteries and supercapacitors, and has been extensively used in many lithium-ion, metal-ion, and nonmetal-ion energy storage devices [3,4]. The advantages of graphite are its high abundance, low cost, and versatility. Graphite allows the formation of many different types of graphite intercalation compounds (GICs) using both cations and anions [5,6]. For this reason, graphite is one of the most explored electrode materials in dual-ion batteries (DIBs).

DIBs are the trending contender in energy storage systems because they offer a wide variety of viable intercalation chemistries. Graphite-based electrodes are also favorable for DIBs because of the mechanical integrity of GICs. Graphite can accommodate even large ions and provide high cutoff voltages (e.g., 2.0–5.2 V vs. K/K^+ or 2.4–3.7 V vs. Al/Al^{3+}) and specific capacities (50–300 mAh g^{-1}) in organic and ionic liquid electrolytes [7]. GICs can be formed using metal cations, such as Li^+ , Na^+ , K^+ , Zn^{2+} , Al^{3+} , and anions such as bis(trifluoromethanesulfonyl) imide TFSI^- , hexafluorophosphate PF_6^- , tetrafluoroborate BF_4^- , tetrachloroaluminate AlCl_4^- , and perchlorate ClO_4^- [8–16]. Even though graphite-based DIBs based on ionic liquid and organic electrolytes are promising in terms of stable

and reversible electrochemical performance, they have demerit points, such as flammability, high cost, environmental issues, or unsuitability for an open-air environment. These issues severely hinder their applicability across a wide variety of technology fields [17,18].

Aqueous electrolytes can potentially overcome the issues of organic and ionic liquid electrolytes in DIBs due to their inherent nonflammability, high ionic conductivity, and easy-to-handle nature in an open-air environment [19,20]. However, aqueous electrolytes suffer from small electrochemical potential windows of hydrogen and oxygen evolution reactions (~1.23 V) [21]. Highly concentrated aqueous electrolytes have recently enabled enlarging the electrochemical potential window by suppressing free water and reducing electrolyte decomposition [22]. Increased salt concentration in aqueous electrolytes has also enabled researchers to obtain lower-stage GICs and improve the reversibility of ionic (de)intercalation [23].

One of the highest electrochemical stabilities has been reported in highly concentrated $\text{Al}(\text{ClO}_4)_3$ and $\text{Zn}(\text{ClO}_4)_2$ aqueous electrolytes that offer an electrochemical window in the range of 3–4 V and the facile intercalation of the ClO_4^- anion in graphite [14,23]. However, the cycling stability and reversible ionic de(inter)calation in graphite during the discharge process are still key issues in ClO_4^- -based electrolytes, limiting the cycling stability of perchlorate-based aqueous DIBs [14].

Over the years, researchers have investigated several different approaches for improving the reversibility of graphite intercalation in aqueous electrolytes [24–26]. Ultrasound treatment has changed the structural properties of graphite by inducing defects in the lattice structure and reducing its crystallite size [24–26]. The impact of the crystallite domain size (L_a) and degree of graphitization (g) on anion intercalation in graphite has been reported by Heckmann et al. [27], and also in our previous publication [28]. It has been found that a smaller crystallite domain size enhances ionic transport kinetics, which in turn improves the reversibility during the electrochemical (dis)charge process [29]. Generally, the reversibility of the intercalation process and kinetics at the electrode surface can be monitored by cyclic voltammetry (CV). However, to gain deeper insights into electrochemical ionic intercalation and to understand its correlation with the incurred structural modifications, various in situ studies featuring techniques such as X-ray diffraction (XRD), transmission electron microscopy (TEM), Raman spectroscopy, and X-ray photoelectron spectroscopy (XPS) are required [30,31]. Ostwald et al. performed in situ XPS to investigate the surface evolution of a graphite electrode material during the intercalation process in a Li-ion battery [32]. However, due to depth limitations, in situ XPS can only provide information about the first few nanometers from the surface of the material. TEM can provide atomically resolved pictures of the insertion/extraction process of the reactive ion [33], but the experiments are extremely demanding and cannot be routinely performed. Therefore, in situ Raman spectroelectrochemistry (SEC) and operando XRD are the most prominent tools that have been utilized to explore structural changes during the ion storage mechanism in detail [34,35]. Operando XRD reveals the lattice changes (contraction/expansion) in bulk during the electrochemical ionic intercalation process [36–39]. The operando XRD can be complemented by more surface-sensitive in situ Raman SEC, to provide information from the first tens to hundreds of nanometers depending on the studied material. It can also provide information about the reversibility of the charge/discharge process and the disorder induced in the material [23,28].

In this study, we report the effects of the mild ultrasound treatment of graphite on the reversibility of the (de)intercalation of the ClO_4^- anion using a 2.4 M $\text{Al}(\text{ClO}_4)_3$ aqueous solution. The intercalation process is characterized by electrochemistry (galvanostatic charge/discharge and CV) and by various in situ and ex situ techniques, including Raman spectroscopy, SEC, XRD, and XPS. The obtained results provide insight into the ClO_4^- anion intercalation mechanism in graphite, demonstrating a positive correlation between the (de)intercalation reversibility and the decrease in the lateral crystallite size by the ultrasound treatment.

2. Material and Methods

2.1. Material Preparation

A total of 200 mg of natural graphite (NG) (Nacional de Grafite, Ltda, Itapecerica, Brazil) was added into 60 mL of N-methyl-2-pyrrolidone (NMP) (Roth, Karlsruhe, Germany, $\geq 99.8\%$ purity) solvent and ultrasonicated (Elmasonic P 00037510, 30 kHz, Singen, Germany) for 3 h. The micro flakes of NG were separated by centrifugation at 2500 rpm (Frontier Centrifuge FC5706, Parsippany, NJ, USA), collected, washed by ethanol, and dried under vacuum at 80 °C for 12 h. The ultrasonicated highly oriented pyrolytic graphite (HOPG) (NT-MDT, Moscow, Russia) was prepared using the same method. The pristine NG sample is further referred to as “NG” and the ultrasonicated NG and HOPG samples are referred to as “US-NG” and “US-HOPG”.

2.2. Electrode Preparation

The graphite electrodes were prepared by casting a slurry onto a current collector of polytetrafluoroethylene (PTFE)-treated hydrophobic carbon paper of 150–200 μm thickness (120 Toray Carbon paper, Fuel Cell Store, College Station, TX, USA). The slurry was prepared by manually mixing the US-NG with conducting carbon black (Super-P, Imerys, Paris, France), polyvinylidene difluoride (PVDF) (Kynar[®] HSV 1800, Arkema, Colombes, France) as a binder, and NMP (75:15:10 wt. ratio) in a mortar. The as-prepared electrodes were dried at 80 °C under vacuum in an oven for 12 h prior to electrochemical testing.

2.3. Electrolyte Preparation

The 2.4 M $\text{Al}(\text{ClO}_4)_3$ aqueous electrolyte solution was prepared by dissolving 29.24 g of $\text{Al}(\text{ClO}_4)_3 \cdot 9\text{H}_2\text{O}$ (Alfa Aesar, Haverhill, MA, USA) in 10 mL of deionized (DI) water. The solution was stirred for 30 min at room temperature to obtain a clear solution.

2.4. Electrochemical Cycling

The galvanostatic charge/discharge cycling was performed from -0.08 to 1.55 V (vs. Ag/AgCl) in a three-electrode standard electrochemical cell by using an Ag/AgCl pseudo-reference electrode and a platinum wire as a counter electrode in the concentrated $\text{Al}(\text{ClO}_4)_3$ aqueous electrolyte. A μ -Autolab type III workstation (Metrohm, Herisau, Switzerland) was used for electrochemical measurements. Cyclic voltammetry (CV) tests were conducted in the potential window of -0.08 to 1.58 V (vs. Ag/AgCl) at various sweep rates from 1 to 9 mVs^{-1} . For the ex situ characterizations, all the samples were washed in DI water and dried in a vacuum oven at 70 °C for 2 h prior to the measurements. The electrodes were discharged to -0.08 V and charged till 1.55 V (vs. Ag/AgCl), and subsequently referred to as “discharged” and “charged”, respectively, and those without any electrochemical activity were referred to as “fresh”.

2.5. Material Characterization

Scanning electron microscopy (SEM) images were obtained using a TESCAN MAIA3 microscope (Brno, Czech Republic). X-ray diffraction (XRD) was performed on Bruker D8 (Bruker, Karlsruhe, Germany) with $\text{Cu K}\alpha$ radiation ($\lambda = 1.5418 \text{ \AA}$). The X-ray diffractogram was recorded at 0.01° per step with a slit width of 0.6 mm in order to improve the accuracy of the XRD measurement. A Horiba Lab-RAM HR (Lille, France) equipped with an Olympus microscope, a 633 nm He-Ne excitation laser operated at 1 mW power by 600 lines/mm grating (1.8 cm^{-1} point-to-point spectral resolution), and a $100\times$ long working distance objective, was used to record the Raman spectra.

The in situ Raman spectroelectrochemistry measurements were performed in a home-made cell, using the same setup with the potential held for about 1000 s for each step. The prepared samples served as the working electrodes, a chlorinated Ag wire was used as the reference electrode, and Pt was used as the counter electrode; Autolab PGSTAT30 (Metrohm, Herisau, Switzerland) was used for the Raman-SEC measurement. The operando XRD analysis was performed using the same setup and conditions as the ex situ analyses. The

X-rays penetrate through the KAPTON tape (Tob Xiamen, Xiamen, China) window from the top. The XRD was connected with a battery tester (Neware, Hong Kong, China) for galvanostatic charge/discharge in a two-electrode setup at $20 \mu\text{Ag}^{-1}$ current density. All the measurements were recorded at 2θ in the range of $10\text{--}60^\circ$ with a step of 0.02° using a Lynxeye XE-T detector and applying a voltage of 40 kV and 30 mA current.

The ex situ XPS of the fresh, charged, and discharged samples were performed using an AXIS Supra photoelectron spectrometer (Kratos Analytical Ltd., Manchester, UK) with an Al K α monochromatic energy source. The XPS analysis of US-NG material was performed by ADES 400 (VG Scientific, London, UK) with an Al K α monochromatic energy source. The spectra were recorded after sputter-etching the samples with Ar⁺ ion clusters (the number of Ar atoms in the cluster was 1000) of 5 keV energy for 10 min. The elemental composition was calculated from the high-resolution core level spectra with respect to the relative sensitivity factor. The determined uncertainties in concentration correspond to the deviation in the measured atomic % of the elements, and were calculated by ESCApe 1.4.0 software (Kratos analytical Ltd., Manchester, UK).

3. Results and Discussion

3.1. Structural Properties of Graphite and Electrochemical (De)Intercalation of ClO₄⁻ Anion

The SEM images of the US-NG (Figure S1c,d in the Supplementary Materials) show more disjointed and crumpled structures in comparison to NG (Figure S1a,b). The ultrasound treatment of graphite leads to a partial disintegration of the bulk crystallites to flakes of varying thickness and lateral dimensions. Figure 1a displays the XRD patterns of the NG and US-NG. The resulting structural parameters are summarized in Table 1. The XRD (002) peaks of the NG and US-NG were recorded at 2θ of $26.53(8)^\circ$ and $26.54(4)^\circ$, corresponding to the interlayer spacing (d_{002}) of $3.35(6) \text{ \AA}$ and $3.35(5) \text{ \AA}$, respectively. For comparison, the XRD (002) peak of the US-HOPG (Figure S2a) recorded at 2θ of $26.53(1)^\circ$ corresponds to the interlayer spacing of $3.35(6) \text{ \AA}$. The degree of graphitization (g), calculated on the basis of d_{002} (see Supplementary Materials Equation (S1)) was also found to be very similar, and close to perfectly crystalline graphite for NG, US-NG, (Table 1) and US-HOPG (Table S1). The coherent domain size (L_c) for the stacking along the c-axis for the hexagonal graphitic structure was calculated using the Scherrer equation (Supplementary Materials Equation (S2)) [40]. The calculated L_c was 52.20 nm to 84.89 nm for NG and US-NG, respectively (Table 1), and 97.50 nm for the US-HOPG (Table S1).

Figure 1b shows the Raman spectra of NG and US-NG. The Raman G band at 1583 cm^{-1} and the 2D band at $2500\text{--}2700 \text{ cm}^{-1}$ are the typical Raman signatures of graphite [41]. In addition, disorder-related D and D' bands at 1350 cm^{-1} and 1620 cm^{-1} , respectively, can be seen in all the spectra. Importantly, the ultrasonication results in higher intensities of the D and D' bands, thereby pointing to a more defective crystalline structure (Figure 1b). The inter-defect distance (L_D), defect density (n_D) and lateral domain size (L_a) were calculated from the ratio of the D and G band intensities (I_D/I_G) by the equations as reported by Cancado et al. (Supplementary Materials Equations (S3)–(S5)) [42]. The calculated structural parameters are summarized in Table 1. The larger I_D/I_G ratio of the US-NG ($I_D/I_G = 0.18$) corresponds to lattice changes with a smaller inter-defect distance (L_D) of $\sim 44 \text{ nm}$ in comparison to the NG ($I_D/I_G = 0.11$, $L_D \sim 51 \text{ nm}$). The other two structural parameters, defect density (n_D) and crystallite size (L_a), follow the same trend as L_D (Table 1). The US-HOPG ($I_D/I_G = 0.04$) (Figure S2b) shows smaller lattice changes with an L_D of $\sim 84 \text{ nm}$ (Table S1). L_a refers to the mean lateral crystallite size, an important parameter to describe the structural properties of the graphite. As can be seen from the data above, the ultrasonication treatment of NMP does not have a substantial influence on the interlayer spacing (and graphitization degree). However, the coherent domain size L_c of NG increases with the treatment. The increase in L_c might be caused by the relaxation of the carbon hexagons as the lateral dimensions of the graphitic planes become smaller. The ultrasound cleaves the layers at the weaker defective sites, which might have been imposing stress, thereby lowering the L_c in the pristine material. Similar behavior was observed for carbon fibers [43]. Moreover, the

increase in I_D/I_G after ultrasonication corresponds to more functional groups' decorated defects at the edges of graphite, which in turn provide more active sites and enhance the electrochemical activity [44]. The Raman spectra-derived parameters corroborate the data obtained by XRD, evidencing the increase in structural damage caused by the ultrasonication treatment which has, consequently, a substantial influence on electrochemical performance and will be discussed in detail in the following sections.

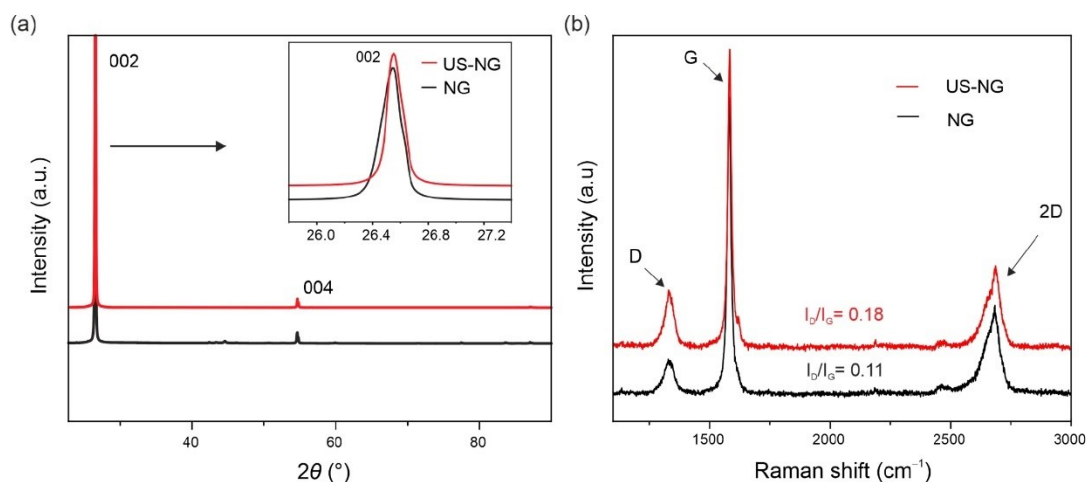


Figure 1. Structural characterization: (a) XRD and (b) Raman spectra of NG (black curves) and US-NG (red curves).

Table 1. Quantification of structural parameters of NG and US-NG from XRD and Raman spectroscopy.

| Material | g (%) | L_c (nm) | L_D (nm) | n_D (cm ⁻²) | L_a (nm) |
|----------|---------|------------|--------------|----------------------------------|------------|
| NG | 97.67 | 52.20 | 51.26 ± 0.14 | (12.33 ± 0.27) × 10 ⁹ | 350.29 |
| US-NG | 98.58 | 84.89 | 44.43 ± 0.02 | (20.20 ± 0.11) × 10 ⁹ | 214.07 |

The electrochemical characteristics of US-NG were studied in 2.4 M Al(ClO₄)₃ aqueous electrolyte concerning the (de)intercalation of the ClO₄⁻ anion. Figure 2a shows the cyclic voltammograms (CVs) of NG and US-NG recorded at a sweep rate of 1 mVs⁻¹. The CVs show two redox peaks in both the cathodic and anodic regions. The electrochemical intercalation of the ClO₄⁻ ions in the graphite is attributed to the two oxidation peaks at 1.43 V (O_A) and 1.55 V (O_A) (~4.7 to 4.8 V vs. Li/Li⁺) and the reduction peaks at 1.16 V (R_C) and 1.35 V (R_C) [45,46]. The different multiple peaks during the intercalation/deintercalation of the anion into graphite correspond to the different staging mechanisms [47,48]. The visible plateaus at around 1.55 V during galvanostatic charge, and at 1.35 V and 1.16 V during the discharge of NG and US-NG (Figure 2b), correspond to the intercalation and (de)intercalation of ClO₄⁻ ions, respectively, which is in line with the CV profile. Likewise, the CV of US-HOPG (Figure S3a) shows similar redox peaks (O_A, O_A, R_C, and R_C). The difference in the galvanostatic charge/discharge profile of NG and US-NG (Figure 2b) could be due to the relatively smaller lateral crystallite size of the US-NG compared to NG.

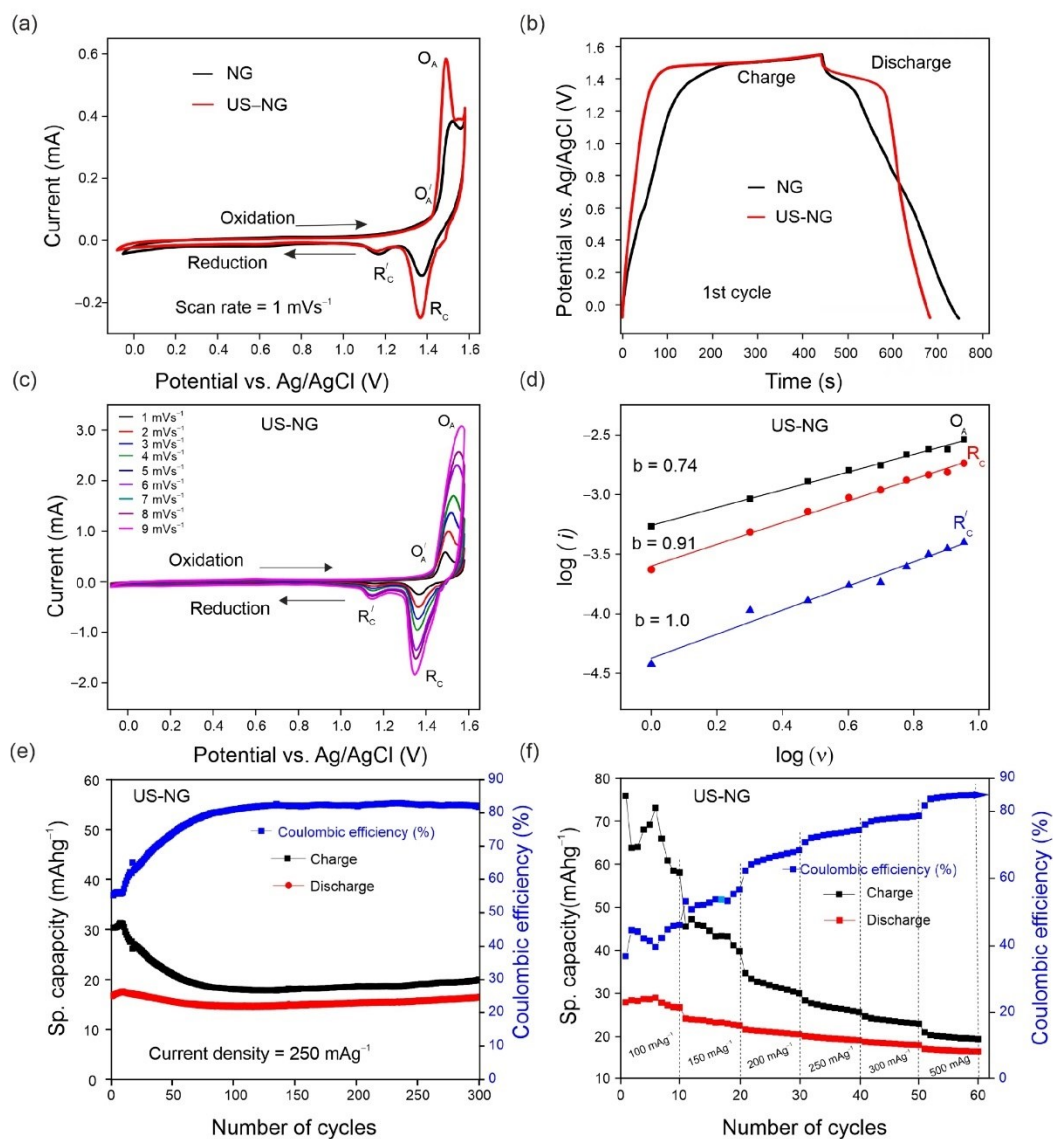


Figure 2. Electrochemical performance of US-NG using 2.4 M Al(ClO₄)₃ aqueous electrolyte solution: (a) CVs of NG and US-NG at 1 mVs⁻¹; (b) galvanostatic charge/discharge potential profile of NG and US-NG at a current density of 250 mA g⁻¹ (1st cycle); (c) CVs of US-NG at different scan rates (1 to 9 mVs⁻¹); (d) electrochemical kinetic of log(*i*) vs. log(*t*) at the redox peaks for US-NG; (e) galvanostatic cycling charge/discharge performance of US-NG obtained at a current density of 250 mA g⁻¹; (f) the rate capability of US-NG for specific capacities at various current densities ranging from 100 mA g⁻¹ to 500 mA g⁻¹ using 2.4 M Al(ClO₄)₃ aqueous electrolyte solution.

To reveal the nature of the electrochemical process of US-NG in detail, the analysis of CVs with varying scan rates (Figure 2c) can unbraided the contributions of diffusion and surface-controlled processes by using the power-law relationship of the peak current (i) and scan rate (v) (SI Equation (S6)) [49,50]. Figure 2d shows the CV kinetics of US-NG, where the fitted b values of 0.74 for the oxidation peak O_A and 0.91 for the reduction peak R_C indicate the contribution of both ionic diffusion and surface-controlled processes, while the b value of 1.0 for the R'_C reduction peak evidences the contribution of purely surface-controlled processes.

The galvanostatic charge/discharge cycling curves of US-NG were recorded in 2.4 M $\text{Al}(\text{ClO}_4)_3$ aqueous electrolyte at a current density of 250 mA g^{-1} . The US-NG shows a stable discharge capacity of $\sim 18 \text{ mAh g}^{-1}$ for 300 cycles, with Coulombic efficiency larger than 80% (Figure 2e). The discharge capacity of $\sim 18 \text{ mAh g}^{-1}$ for US-HOPG in 2.4 M $\text{Al}(\text{ClO}_4)_3$ aqueous electrolyte at a current density of 250 mA g^{-1} was also observed for 125 cycles, as shown in Figure S3c. A similar charge/discharge performance for graphitic electrode materials in both aqueous and non-aqueous electrolytes has been reported previously [23,39,51].

Ultrasound treatment leads to smaller crystallites (larger surface) and more active sites at the surface, which enhances electrochemical activity [52]. The smaller lateral crystallite size might have a substantial influence on the cyclic stability, as well as on the reversibility of the (de)intercalation of the ClO_4^- anion in US-NG. It is well known that defects are introduced into the lattice structure of graphite due to the attachment of functional groups during the ultrasound treatment in different solvents [53–55]. Skaltsas et al. reported that the ultrasonication of graphite in NMP induces the formation of defects accompanied by the increase in the concentration of the oxygenated species (COOH, COO) in the material [53]. Here, we observed the presence of the hydroxyl and carboxyl oxygen-containing functional groups attached to the graphitic carbon of US-NG by XPS analysis, as shown in Figure S4. We note that the analysis was performed after Ar^+ ion etching to minimize the potential influence of airborne contamination. The elemental analysis for US-NG is presented in Table S2. The oxygenated species at the graphite lattice could originate from the decomposition of NMP or surface oxidation during the ultrasound treatment [26]. The functional groups decorating the graphite surface could facilitate the large-size ions accessing the graphite interlayer galleries through surface adsorption during the electrochemical process [56–60]. Figure 2f displays the specific capacity of US-NG recorded at various current densities from 100 mA g^{-1} to 500 mA g^{-1} . It also shows a stable electrochemical performance with an increase in Coulombic efficiency at high current density (500 mA g^{-1}). Figure S3d shows the rate capability of US-HOPG from 100 mA g^{-1} to 500 mA g^{-1} .

3.2. In Situ Characterization

In order to obtain deeper insights on the ionic (de)intercalation into US-NG, in situ Raman SEC was performed. Figure 3a displays the Raman spectra of US-NG acquired in situ during the charge/discharge cycle. The G peak, being the most sensitive to the interaction of ions with the graphite planes, splits into two components. The low-frequency ($\sim 1584 \text{ cm}^{-1}$) G(*i*) mode and high-frequency ($\sim 1613 \text{ cm}^{-1}$) G(*b*) mode appear due to the formation of GICs with the anions inside the interlayer galleries [25,61,62]. The splitting of the G peak at 1.40 V (vs. Ag/AgCl) during the charging process, accompanied by a further intensity increase in the G(*b*) peak, corresponds to the gradual intercalation of the ClO_4^- ion in the interlayer spaces of graphite. The complete disappearance of the G(*b*) mode during the discharge process is attributed to a fully reversible deintercalation [63–65]. This observation is in line with the stable discharge capacity in the case of US-NG over long cycles, as shown in Figure 2e. In spite of the hysteresis in the G peak position during the charge/discharge cycle, Figure 3b shows that the graphite lattice is completely restored after the (de)intercalation of the ClO_4^- anion. Comparatively, during a galvanostatic discharge, in the case of untreated NG, the persistence of the G(*b*) mode during the discharge process

was attributed to the only partial reversibility of the (de)intercalation of the ClO_4^- anion, as shown in our previous publication [28].

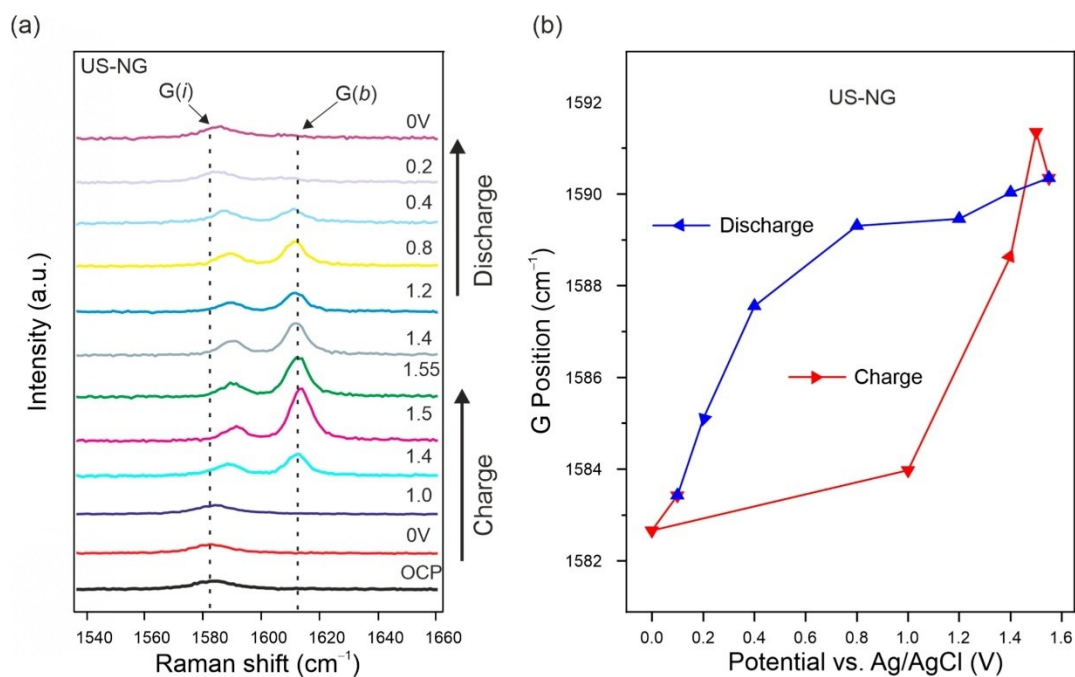


Figure 3. In situ Raman SEC of US-NG during charge/discharge cycle in 2.4 M $\text{Al}(\text{ClO}_4)_3$ aqueous electrolyte. (a) Evolution of the Raman spectra in the G peak spectral region. (b) Raman G peak position evolution fitted as one Lorentzian line shape. The applied potentials were held for 1000 s for each step.

Operando XRD proved to be an efficient tool to monitor the structural lattice modifications taking place alongside the GIC formation during the charge/discharge process [66,67]. Figure 4 shows the evolution of the (002) and (004) reflections of US-NG during one charge/discharge cycle. The characteristic graphitic (002) reflection broadens and splits during the charge process due to the intercalation of the ClO_4^- anion [23]. The emerged reflection has 2θ of $\sim 25.5^\circ$, corresponding to d_{002} of ~ 3.49 Å. Analogous behavior can be observed in the (004) reflection. Decreases in broadening and intensity in the main reflections were observed upon charging, which also depicts the ionic intercalation into graphite. The peaks were fully recovered during the discharge process (Figure 4).

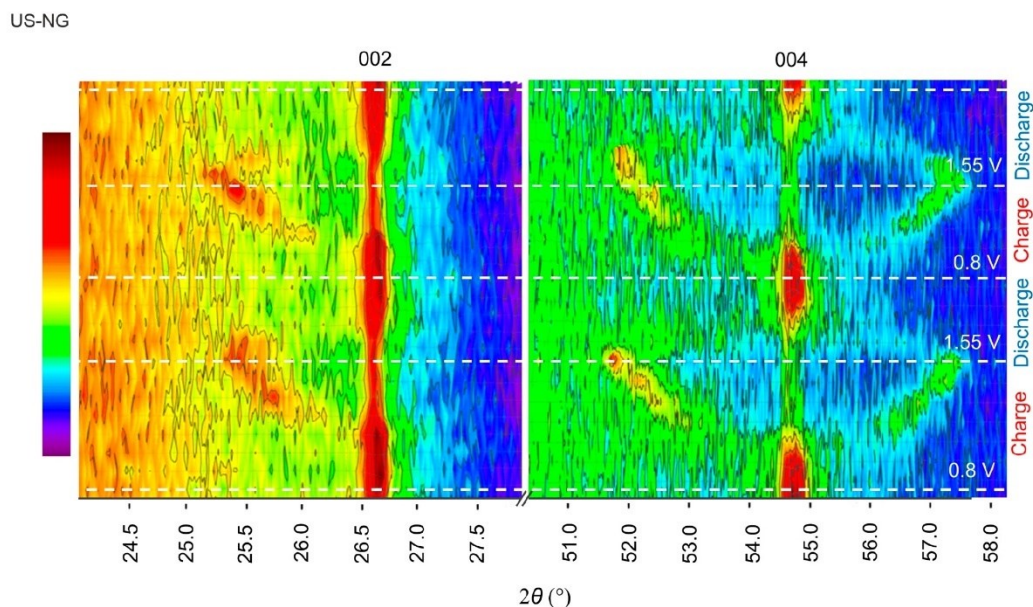


Figure 4. Operando XRD analysis of US-NG during charge/discharge process in 2.4 M $\text{Al}(\text{ClO}_4)_3$ aqueous electrolyte solution.

3.3. Ex Situ Spectroscopic Characterization

To describe the (de)intercalation process in more detail, additional ex situ spectroscopic techniques, such as ex situ Raman spectroscopy and ex situ XPS, were performed on the fresh, charged, and discharged US-NG electrodes.

The ex situ Raman spectra of US-NG show an increase in the intensity ratio of the D to G peaks (I_D/I_G) during the charged state (0.31) in comparison to the discharged (0.24) and fresh (0.17) states (Figure S5a), illustrating the reversible structural changes during the intercalation of the ClO_4^- anion [39]. Similarly, the ex situ Raman spectra of US-HOPG (Figure S5b) also show an increase in I_D/I_G ratio (0.17) during charging in comparison to the discharged (0.15) and fresh (0.03) states. The incomplete recovery of the small D peak intensity points to the partial irreversibility of the intercalation in US-HOPG.

The chemical composition of fresh, discharged, and charged US-NG electrode materials were analyzed by XPS (Figure 5). Figure 5a shows the survey XPS spectra of the electrodes, with the lines assigned to Cl, Al, O, C, and F labelled. The presence of F comes from the electrode binder [68]. Figure 5c,d shows the high-resolution Cl 2p core-level XPS spectra of US-NG during the charged/discharged state, demonstrating the presence of the two chemical states of Cl. The lower-energy component at ~200 eV corresponds to Cl covalently bonded to carbon atoms (C-Cl) [69]; the peaks at 201.9 eV and 200.1 eV belong to the $2p_{1/2}$ and $2p_{3/2}$ energy levels, respectively. The higher-energy state at ~208 eV corresponds to ClO_4^- . The peaks at 209.6 eV and 208.0 eV correspond to Cl $2p_{1/2}$ and Cl $2p_{3/2}$, respectively, attributed to the adsorbed ClO_4^- , possibly originating from the electrolyte presence at the surface of the electrode [70,71]. Cl $2p_{1/2}$ and Cl $2p_{3/2}$ at 208.0 eV and 206.4 eV, respectively, reveal the intercalated ClO_4^- ion [14,72]. The elemental composition (Table S3) and selected ratios of the atoms or ions (Table 2) evidence that higher amounts of ClO_4^- were present in the charged than in the discharged US-NG. Importantly, the ratio of intercalated/adsorbed ClO_4^- was observed to be significantly higher for the charged state than for the discharged state (Figure 5c,d). We noted that an exact quantification of the intercalated/adsorbed ClO_4^- is not possible due to the overlap of the spin-split

peaks at the binding energy of 208.0 eV (Cl 2p_{1/2} of the intercalated ClO₄⁻ and Cl 2p_{3/2} of the adsorbed ClO₄⁻). Nevertheless, the amount of intercalated ClO₄⁻ is very low in the discharged state, also taking into account the very low Cl content (Table S3), which can explain the structural reversibility seen in Raman SEC and XRD. Figure 5b shows the Al 2p core level at 75.5 eV binding energy. The concentration of Al (Table S3) was observed to be higher for the charged US-NG electrodes, compared to the discharged one. Additionally, the Al to C ratio in the charged US-NG is higher than in the discharged US-NG (Table 2), which might correspond to the trapped electrolyte in the US-NG electrode.

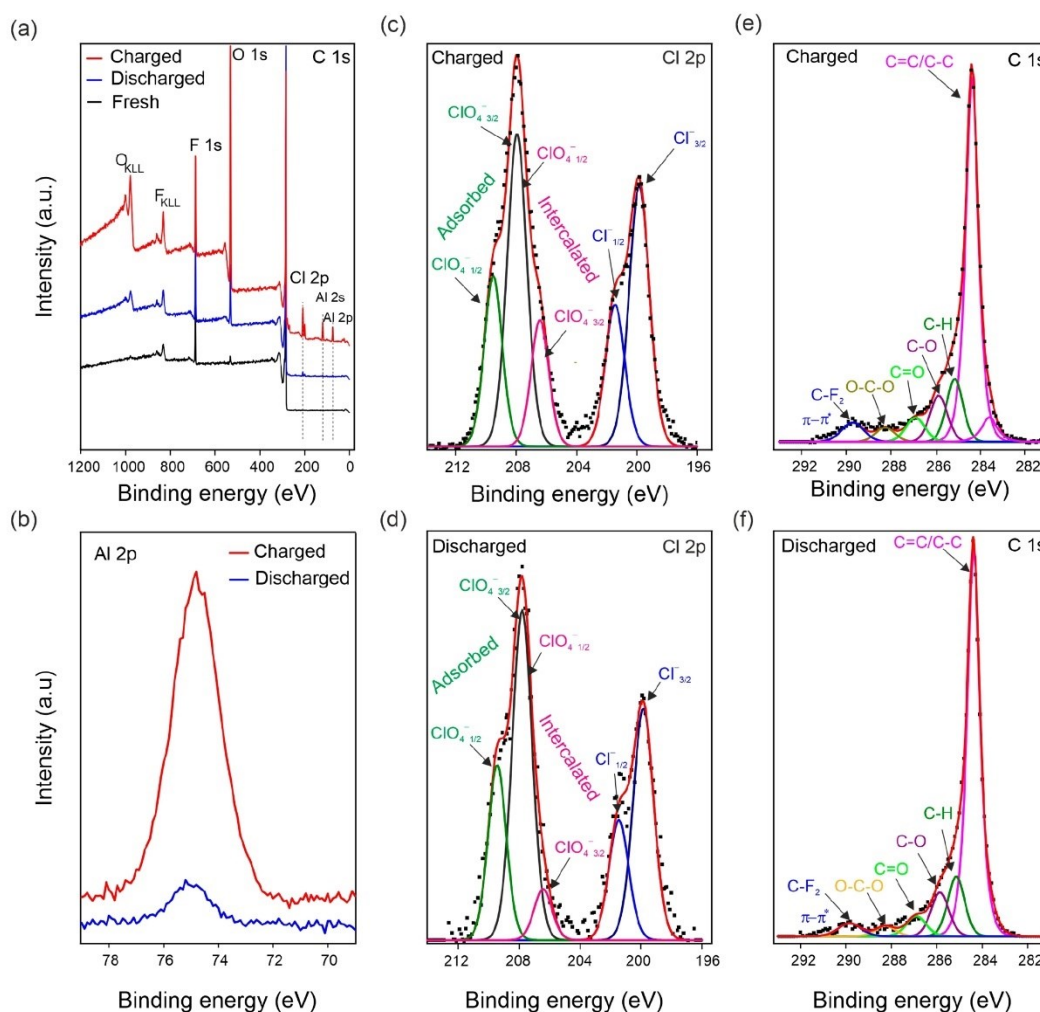


Figure 5. Ex situ XPS analysis of US-NG in fresh, charged, and discharged states using 2.4 M Al(ClO₄)₃ aqueous electrolyte solution. (a) Survey XPS spectrum; (b) high-resolution XPS spectra of the Al 2p core levels in the charged and discharged states; deconvoluted high-resolution XPS spectra of the Cl 2p core levels in the charged (c) and discharged states (d) (note, the Cl 2p_{1/2} of intercalated ClO₄⁻ and Cl 2p_{3/2} of adsorbed ClO₄⁻ overlap at 208.0 eV); deconvoluted high-resolution XPS spectra of the C 1s core levels in the charged (e) and discharged states (f).

Table 2. Concentration ratios of ClO_4^- and Cl and Al and C for US-NG derived from XPS.

| Sample | US-NG | |
|---------------------------|---------|------------|
| | Charged | Discharged |
| Cl/C | 0.059 | 0.010 |
| ClO_4^-/C | 0.335 | 0.080 |
| Al/ ClO_4^- | 0.227 | 0.080 |
| Al/C | 0.076 | 0.010 |

4. Conclusions

The effect of the ultrasound treatment of natural and highly oriented pyrolytic graphite on the reversibility of electrochemical (de)intercalation of the ClO_4^- anion was studied in aqueous $\text{Al}(\text{ClO}_4)_3$ electrolyte solution. The ultrasonication of graphite in NMP induced the formation of defects accompanied by a reduction in its crystallite size, L_a . The smaller L_a of US-NG in comparison to pristine NG facilitated the easier escape of the large-size ions from the graphite interlayer galleries, thereby enhancing the reversibility and cyclic stability. The in situ Raman SEC and operando XRD of US-NG confirmed the reversibility of the structural changes in the graphite induced by the ClO_4^- intercalation, although a remaining signal of the intercalated ClO_4^- species was detected by ex situ XPS. The study shows that ultrasound treatment offers a practical approach for improving the reversibility of electrochemical intercalation processes in graphite, which can also help in designing novel functional graphite intercalation materials for energy storage systems.

Supplementary Materials: The following supporting information can be downloaded at: <https://www.mdpi.com/article/10.3390/nano12223932/s1>, Figure S1: Characterization of NG and US-NG by SEM; Figure S2: Characterization of US-HOPG by XRD and Raman spectroscopy; Figure S3: Electrochemical characteristics of US-HOPG using aqueous $\text{Al}(\text{ClO}_4)_3$ electrolyte solution; Figure S4: XPS analysis of fresh US-NG after Ar^+ ion etching; Figure S5: *Ex-situ* Raman spectra of graphite; Table S1: Quantification of structural parameters of US-HOPG from XRD and Raman spectroscopy; Table S2: XPS elemental analysis of fresh US-NG material; Table S3: XPS elemental analysis of fresh, charged, and discharged US-NG; References [40,42,49,50,73–82] are cited in the Supplementary Materials.

Author Contributions: Conceptualization, G.A., F.J.S. and O.F.; methodology, G.A., F.J.S. and O.F.; software, G.A., K.K. and J.H.; validation, P.J., K.K., M.K., J.Č. and O.F.; formal analysis G.A., Z.A.Z. and F.J.S.; resources, G.A., Z.A.Z. and F.J.S.; data curation, G.A., F.J.S. and O.F.; writing—original draft, G.A. and O.F.; writing—review and editing, G.A., F.J.S., Z.A.Z., J.Č. and O.F.; visualization, F.J.S., P.J., K.K., M.K., J.Č. and O.F.; supervision, F.J.S. and O.F.; project administration, O.F.; funding acquisition; G.A., J.Č., M.K. and O.F. All authors have read and agreed to the published version of the manuscript.

Funding: This research was funded by Charles University Grant Agency (GAUK, project No. 371621), the European Regional Development Fund; OP RDE; Project: “Carbon allotropes with rationalized nanointerfaces and nanolinks for environmental and biomedical applications” (No. CZ.02.1.01/0.0/0.0/16_026/0008382) and SOLID21 (No. CZ.02.1.01/0.0/0.0/16_019/0000760) and the Czech Science Foundation (GACR—Grant No. 19-23986S). This work was also supported by the project Strategy AV21, programs Study of the atomically thin quantum materials by advanced microscopic/spectroscopic techniques applying machine learning and Sustainable energy.

Data Availability Statement: The data presented in this study are available on request from the corresponding author. The data are not publicly available due to IP protection revision of related studies.

Conflicts of Interest: The authors declare no conflict of interest.

References

- Dunn, B.; Kamath, H.; Tarascon, J.M. Electrical energy storage for the grid: A battery of choices. *Science* **2011**, *334*, 928–935. [[CrossRef](#)] [[PubMed](#)]
- Thackeray, M.M.; Wolverton, C.; Isaacs, E.D. Electrical energy storage for transportation—Approaching the limits of, and going beyond, lithium-ion batteries. *Energy Environ. Sci.* **2012**, *5*, 7854–7863. [[CrossRef](#)]

3. Rothermel, S.; Meister, P.; Schmuelling, G.; Fromm, O.; Meyer, H.W.; Nowak, S.; Winter, M.; Placke, T. Dual-graphite cells based on the reversible intercalation of bis(trifluoromethanesulfonyl)imide anions from an ionic liquid electrolyte. *Energy Environ. Sci.* **2014**, *7*, 3412–3423. [[CrossRef](#)]
4. Rodríguez-Pérez, I.A.; Zhang, L.; Wrogemann, J.M.; Driscoll, D.M.; Sushko, M.L.; Han, K.S.; Fulton, J.L.; Engelhard, M.H.; Balasubramanian, M.; Viswanathan, V.V.; et al. Enabling Natural Graphite in High-Voltage Aqueous Graphite || Zn Metal Dual-Ion Batteries. *Adv. Energy Mater.* **2020**, *10*, 2001256. [[CrossRef](#)]
5. Inagaki, M. Applications of graphite intercalation compounds. *J. Mater. Res.* **1989**, *4*, 1560–1568. [[CrossRef](#)]
6. Dresselhaus, M.S.; Dresselhaus, G. Intercalation compounds of graphite. *Adv. Phys.* **2002**, *51*, 1–186. [[CrossRef](#)]
7. Ji, B.; Zhang, F.; Song, X.; Tang, Y. A Novel Potassium-Ion-Based Dual-Ion Battery. *Adv. Mater.* **2017**, *29*, 1700519. [[CrossRef](#)]
8. Rodríguez-Pérez, I.A.; Ji, X. Anion Hosting Cathodes in Dual-Ion Batteries. *ACS Energy Lett.* **2017**, *2*, 1762–1770. [[CrossRef](#)]
9. Placke, T.; Fromm, O.; Rothermel, S.; Schmuelling, G.; Meister, P.; Meyer, H.-W.; Passerini, S.; Winter, M. Electrochemical Intercalation of Bis(Trifluoromethanesulfonyl) Imide Anion into Various Graphites for Dual-Ion Cells. *ECS Trans.* **2013**, *50*, 59–68. [[CrossRef](#)]
10. Kondo, Y.; Miyahara, Y.; Fukutsuka, T.; Miyazaki, K.; Abe, T. Electrochemical intercalation of bis(fluorosulfonyl)amide anions into graphite from aqueous solutions. *Electrochem. Commun.* **2019**, *100*, 26–29. [[CrossRef](#)]
11. Zhu, D.; Wang, H. Hexafluorophosphate Anion Intercalation into Graphite Electrodes from Propylene Carbonate/Gamma-Butyrolactone Solutions. *Langmuir* **2021**, *37*, 10797–10805. [[CrossRef](#)] [[PubMed](#)]
12. Wang, Y.; Li, J.; Huang, Y.; Wang, H. Anion Storage Behavior of Graphite Electrodes in LiBF₄/Sulfone/Ethyl Methyl Carbonate Solutions. *Langmuir* **2019**, *35*, 14804–14811. [[CrossRef](#)] [[PubMed](#)]
13. Lv, Z.; Han, M.; Sun, J.; Hou, L.; Chen, H.; Li, Y.; Lin, M.C. A high discharge voltage dual-ion rechargeable battery using pure (DMP1+)(AlCl₄⁻) ionic liquid electrolyte. *J. Power Sources* **2019**, *418*, 233–240. [[CrossRef](#)]
14. Zafar, Z.A.; Abbas, G.; Knizek, K.; Silhavič, M.; Kumar, P.; Jiricek, P.; Houdková, J.; Frank, O.; Cervenka, J. Chaotropic anion based “water-in-salt” electrolyte realizes a high voltage Zn-graphite dual-ion battery. *J. Mater. Chem. A* **2022**, *10*, 2064–2074. [[CrossRef](#)]
15. Bordet, F.; Ahlbrecht, K.; Tübke, J.; Ufheil, J.; Hoes, T.; Oetken, M.; Holzapfel, M. Anion intercalation into graphite from a sodium-containing electrolyte. *Electrochim. Acta* **2015**, *174*, 1317–1323. [[CrossRef](#)]
16. Zhu, J.; Li, Y.; Yang, B.; Liu, L.; Li, J.; Yan, X.; He, D. A Dual Carbon-Based Potassium Dual Ion Battery with Robust Comprehensive Performance. *Small* **2018**, *14*, 1801836. [[CrossRef](#)]
17. Xu, K. Electrolytes and interphases in Li-ion batteries and beyond. *Chem. Rev.* **2014**, *114*, 11503–11618. [[CrossRef](#)]
18. Jiang, X.; Luo, L.; Zhong, F.; Chen, W.; Ai, X.; Yang, H.; Cao, Y. Electrolytes for Dual-Carbon Batteries. *ChemElectroChem* **2019**, *6*, 2615–2629. [[CrossRef](#)]
19. Wang, P.; Chen, Z.; Wang, H.; Ji, Z.; Feng, Y.; Wang, J.; Liu, J.; Hu, M.; Fei, J.; Gan, W.; et al. A high-performance flexible aqueous Al ion rechargeable battery with long cycle life. *Energy Storage Mater.* **2020**, *25*, 426–435. [[CrossRef](#)]
20. Nandi, S.; Das, S.K. Realizing a Low-Cost and Sustainable Rechargeable Aqueous Aluminum-Metal Battery with Exfoliated Graphite Cathode. *ACS Sustain. Chem. Eng.* **2019**, *7*, 19839–19847. [[CrossRef](#)]
21. Liu, Z.; Huang, Y.; Huang, Y.; Yang, Q.; Li, X.; Huang, Z.; Zhi, C. Voltage issue of aqueous rechargeable metal-ion batteries. *Chem. Soc. Rev.* **2020**, *49*, 180–232. [[CrossRef](#)] [[PubMed](#)]
22. Liang, T.; Hou, R.; Dou, Q.; Zhang, H.; Yan, X. The Applications of Water-in-Salt Electrolytes in Electrochemical Energy Storage Devices. *Adv. Funct. Mater.* **2021**, *31*, 2006749. [[CrossRef](#)]
23. Zafar, Z.A.; Abbas, G.; Silhavič, M.; Knizek, K.; Kaman, O.; Sonia, F.J.; Kumar, P.; Jiricek, P.; Houdková, J.; Frank, O.; et al. Reversible anion intercalation into graphite from aluminum perchlorate “water-in-salt” electrolyte. *Electrochim. Acta* **2022**, *404*, 139754. [[CrossRef](#)]
24. Ng, K.L.; Malik, M.; Buch, E.; Glossmann, T.; Hintennach, A.; Azimi, G. A low-cost rechargeable aluminum/natural graphite battery utilizing urea-based ionic liquid analog. *Electrochim. Acta* **2019**, *327*, 135031. [[CrossRef](#)]
25. Liu, C.; Liu, Z.; Niu, H.; Wang, C.; Wang, Z.; Gao, B.; Liu, J.; Taylor, M. Preparation and in-situ Raman characterization of binder-free u-GF@CFC cathode for rechargeable aluminum-ion battery. *MethodsX* **2019**, *6*, 2374–2383. [[CrossRef](#)]
26. Kokai, F.; Sorin, R.; Chigusa, H.; Hanai, K.; Koshio, A.; Ishihara, M.; Koga, Y.; Hasegawa, M.; Imanishi, N.; Takeda, Y. Ultrasonication fabrication of high quality multilayer graphene flakes and their characterization as anodes for lithium ion batteries. *Diam. Relat. Mater.* **2012**, *29*, 63–68. [[CrossRef](#)]
27. Heckmann, A.; Fromm, O.; Rodehorst, U.; Münster, P.; Winter, M.; Placke, T. New insights into electrochemical anion intercalation into carbonaceous materials for dual-ion batteries: Impact of graphitization degree. *Carbon N. Y.* **2018**, *131*, 201–212. [[CrossRef](#)]
28. Abbas, G.; Sonia, F.J.; Zafar, Z.A.; Knizek, K.; Houdková, J.; Jiříček, P.; Bouša, M.; Plšek, J.; Kalbáč, M.; Cervenka, J.; et al. Influence of structural properties on (de-)intercalation of ClO₄⁻ anion in graphite from concentrated aqueous electrolyte. *Carbon N. Y.* **2022**, *186*, 612–623. [[CrossRef](#)]
29. Kaewmala, S.; Limphirat, W.; Yordsri, V.; Kim, H.; Muhammad, S.; Yoon, W.S.; Srilomsak, S.; Limthongkul, P.; Meethong, N. Structural and Electrochemical Kinetic Properties of 0.5Li₂MnO₃·0.5LiCoO₂ Cathode Materials with Different Li₂MnO₃ Domain Sizes. *Sci. Rep.* **2019**, *9*, 427. [[CrossRef](#)]
30. Zou, J.; Sole, C.; Drewett, N.E.; Velický, M.; Hardwick, L.J. In Situ Study of Li Intercalation into Highly Crystalline Graphitic Flakes of Varying Thicknesses. *J. Phys. Chem. Lett.* **2016**, *7*, 4291–4296. [[CrossRef](#)]

31. Li, N.; Su, D. In-situ structural characterizations of electrochemical intercalation of graphite compounds. *Carbon Energy* **2019**, *1*, 200–218. [[CrossRef](#)]
32. Oswald, S.; Nikolowski, K.; Ehrenberg, H. Quasi in situ XPS investigations on intercalation mechanisms in Li-ion battery materials. *Anal. Bioanal. Chem.* **2009**, *393*, 1871–1877. [[CrossRef](#)] [[PubMed](#)]
33. Zhang, Y.; Lu, F.; Pan, L.; Xu, Y.; Yang, Y.; Bando, Y.; Golberg, D.; Yao, J.; Wang, X. Improved cycling stability of NiS₂ cathodes through designing a “kiwano” hollow structure. *J. Mater. Chem. A* **2018**, *6*, 11978–11984. [[CrossRef](#)]
34. Fan, H.; Qi, L.; Wang, H. Intercalation Behavior of Hexafluorophosphate into Graphite Electrode from Propylene/Ethylmethyl Carbonates. *J. Electrochem. Soc.* **2017**, *164*, A2262–A2267. [[CrossRef](#)]
35. Wang, B.; Wang, Y.; Huang, Y.; Zhang, L.; Ma, S.; Wang, H. Hexafluorophosphate Intercalation into the Graphite Electrode from Mixed Cyclic Carbonates. *ACS Appl. Energy Mater.* **2021**, *4*, 5316–5325. [[CrossRef](#)]
36. Wang, D.Y.; Huang, S.K.; Liao, H.J.; Chen, Y.M.; Wang, S.W.; Kao, Y.T.; An, J.Y.; Lee, Y.C.; Chuang, C.H.; Huang, Y.C.; et al. Insights into dynamic molecular intercalation mechanism for Al[Sbnd]C battery by operando synchrotron X-ray techniques. *Carbon N. Y.* **2019**, *146*, 528–534. [[CrossRef](#)]
37. Zhu, D.; Huang, Y.; Zhang, L.; Fan, H.; Wang, H. PF₆—Intercalation into Graphite Electrode from Gamma-butyrolactone/ethyl Methyl Carbonate. *J. Electrochem. Soc.* **2020**, *167*, 070513. [[CrossRef](#)]
38. Seel, J.A.; Dahn, J.R. Electrochemical Intercalation of PF₆ into Graphite. *J. Electrochem. Soc.* **2000**, *147*, 892. [[CrossRef](#)]
39. Gao, J.; Tian, S.; Qi, L.; Wang, H. Intercalation manners of perchlorate anion into graphite electrode from organic solutions. *Electrochim. Acta* **2015**, *176*, 22–27. [[CrossRef](#)]
40. Akikubo, K.; Kurahashi, T.; Kawaguchi, S.; Tachibana, M. Thermal expansion measurements of nano-graphite using high-temperature X-ray diffraction. *Carbon N. Y.* **2020**, *169*, 307–311. [[CrossRef](#)]
41. Ferrari, A.C.; Meyer, J.C.; Scardaci, V.; Casiraghi, C.; Lazzeri, M.; Mauri, F.; Piscanec, S.; Jiang, D.; Novoselov, K.S.; Roth, S.; et al. Raman spectrum of graphene and graphene layers. *Phys. Rev. Lett.* **2006**, *97*, 18740. [[CrossRef](#)] [[PubMed](#)]
42. Cançado, L.G.; Jorio, A.; Ferreira, E.H.M.; Stavale, F.; Achete, C.A.; Capaz, R.B.; Moutinho, M.V.O.; Lombardo, A.; Kulmala, T.S.; Ferrari, A.C. Quantifying defects in graphene via Raman spectroscopy at different excitation energies. *Nano Lett.* **2011**, *11*, 3190–3196. [[CrossRef](#)] [[PubMed](#)]
43. Lim, S.; Yoon, S.H.; Mochida, I.; Chi, J.H. Surface modification of carbon nanofiber with high degree of graphitization. *J. Phys. Chem. B* **2004**, *108*, 1533–1536. [[CrossRef](#)]
44. Wu, C.; Cheng, Q.; Wu, K. Electrochemical Functionalization of N-Methyl-2-pyrrolidone-Exfoliated Graphene Nanosheets as Highly Sensitive Analytical Platform for Phenols. *Anal. Chem.* **2015**, *87*, 3294–3299. [[CrossRef](#)] [[PubMed](#)]
45. Liu, T.; Zhu, C.; Kou, T.; Worsley, M.A.; Qian, F.; Condes, C.; Duoss, E.B.; Spadaccini, C.M.; Li, Y. Ion Intercalation Induced Capacitance Improvement for Graphene-Based Supercapacitor Electrodes. *ChemNanoMat* **2016**, *2*, 635–641. [[CrossRef](#)]
46. Bu, X.; Su, L.; Dou, Q.; Lei, S.; Yan, X. A low-cost “water-in-salt” electrolyte for a 2.3 V high-rate carbon-based supercapacitor. *J. Mater. Chem. A* **2019**, *7*, 7541–7547. [[CrossRef](#)]
47. Schmuelling, G.; Placke, T.; Kloepsch, R.; Fromm, O.; Meyer, H.W.; Passerini, S.; Winter, M. X-ray diffraction studies of the electrochemical intercalation of bis(trifluoromethanesulfonyl)imide anions into graphite for dual-ion cells. *J. Power Sources* **2013**, *239*, 563–571. [[CrossRef](#)]
48. Xu, J.H.; Turney, D.E.; Jadhav, A.L.; Messinger, R.J. Effects of Graphite Structure and Ion Transport on the Electrochemical Properties of Rechargeable Aluminum-Graphite Batteries. *ACS Appl. Energy Mater.* **2019**, *11*, 7799–7810. [[CrossRef](#)]
49. Sonia, F.J.; Jangid, M.K.; Ananthoju, B.; Aslam, M.; Johari, P.; Mukhopadhyay, A. Understanding the Li-storage in few layers graphene with respect to bulk graphite: Experimental, analytical and computational study. *J. Mater. Chem. A* **2017**, *5*, 8662–8679. [[CrossRef](#)]
50. Sonia, F.J.; Jangid, M.K.; Aslam, M.; Johari, P.; Mukhopadhyay, A. Enhanced and faster potassium storage in graphene with respect to graphite: A comparative study with lithium storage. *ACS Nano* **2019**, *13*, 2190–2204. [[CrossRef](#)]
51. Zhang, E.; Cao, W.; Wang, B.; Yu, X.; Wang, L.; Xu, Z.; Lu, B. A novel aluminum dual-ion battery. *Energy Storage Mater.* **2018**, *11*, 91–99. [[CrossRef](#)]
52. Son, D.K.; Kim, J.; Raj, M.R.; Lee, G. Elucidating the structural redox behaviors of nanostructured expanded graphite anodes toward fast-charging and high-performance lithium-ion batteries. *Carbon N. Y.* **2021**, *175*, 187–201. [[CrossRef](#)]
53. Skaltsas, T.; Ke, X.; Bittencourt, C.; Tagmatarchis, N. Ultrasonication induces oxygenated species and defects onto exfoliated graphene. *J. Phys. Chem. C* **2013**, *117*, 23272–23278. [[CrossRef](#)]
54. Shibaev, A.A.; Mal'tsev, L.I.; Petrov, V.M.; Maksimovskii, E.A.; Ukhina, A.V.; Prosanov, I.Y.; Popov, M.V.; Bannov, A.G. Studies of ultrasonication of exfoliated graphite. *Prot. Met. Phys. Chem. Surf.* **2017**, *53*, 261–267. [[CrossRef](#)]
55. Xu, J.H.; Schoetz, T.; McManus, J.R.; Subramanian, V.R.; Fields, P.W.; Messinger, R.J. Tunable Pseudocapacitive Intercalation of Chloroaluminate Anions into Graphite Electrodes for Rechargeable Aluminum Batteries. *J. Electrochem. Soc.* **2021**, *168*, 060514. [[CrossRef](#)]
56. Liu, C.; Liu, Z.; Li, Q.; Niu, H.; Wang, C.; Wang, Z.; Gao, B. Binder-free ultrasonicated graphite flakes@carbon fiber cloth cathode for rechargeable aluminum-ion battery. *J. Power Sources* **2019**, *438*, 226950. [[CrossRef](#)]
57. Kim, J.; Raj, M.R.; Lee, G. High-Defect-Density Graphite for Superior-Performance Aluminum-Ion Batteries with Ultra-Fast Charging and Stable Long Life. *Nano-Micro Lett.* **2021**, *13*, 171. [[CrossRef](#)]

58. Peng, Y.; Chen, Z.; Zhang, R.; Zhou, W.; Gao, P.; Wu, J.; Liu, H.; Liu, J.; Hu, A.; Chen, X. Oxygen-Containing Functional Groups Regulating the Carbon/Electrolyte Interfacial Properties Toward Enhanced K^+ Storage. *Nano-Micro Lett.* **2021**, *13*, 192. [[CrossRef](#)]
59. Xiong, D.; Li, X.; Shan, H.; Zhao, Y.; Dong, L.; Xu, H.; Zhang, X.; Li, D.; Sun, X. Oxygen-containing Functional Groups Enhancing Electrochemical Performance of Porous Reduced Graphene Oxide Cathode in Lithium Ion Batteries. *Electrochim. Acta* **2015**, *174*, 762–769. [[CrossRef](#)]
60. Cao, H.; Peng, X.; Zhao, M.; Liu, P.; Xu, B.; Guo, J. Oxygen functional groups improve the energy storage performances of graphene electrochemical supercapacitors. *RSC Adv.* **2018**, *8*, 2858–2865. [[CrossRef](#)]
61. Tian, S.; Qi, L.; Wang, H. Difluoro(oxalato)borate anion intercalation into graphite electrode from ethylene carbonate. *Solid State Ionics* **2016**, *291*, 42–46. [[CrossRef](#)]
62. Lin, M.C.; Gong, M.; Lu, B.; Wu, Y.; Wang, D.Y.; Guan, M.; Angell, M.; Chen, C.; Yang, J.; Hwang, B.J.; et al. An ultrafast rechargeable aluminium-ion battery. *Nature* **2015**, *520*, 325–328. [[CrossRef](#)] [[PubMed](#)]
63. Flores, E.; Novák, P.; Berg, E.J. In situ and Operando Raman spectroscopy of layered transition metal oxides for Li-ion battery cathodes. *Front. Energy Res.* **2018**, *6*, 82. [[CrossRef](#)]
64. Wang, D.Y.; Wei, C.Y.; Lin, M.C.; Pan, C.J.; Chou, H.L.; Chen, H.A.; Gong, M.; Wu, Y.; Yuan, C.; Angell, M.; et al. Advanced rechargeable aluminium ion battery with a high-quality natural graphite cathode. *Nat. Commun.* **2017**, *8*, 14283. [[CrossRef](#)]
65. Julien, C.M.; Mauger, A. In situ Raman analyses of electrode materials for Li-ion batter. *AIMS Mater. Sci.* **2018**, *5*, 650–698. [[CrossRef](#)]
66. Liang, H.J.; Hou, B.H.; Li, W.H.; Ning, Q.L.; Yang, X.Y.; Gu, Z.Y.; Nie, X.J.; Wang, G.; Wu, X.L. Staging Na/K-ion de-/intercalation of graphite retrieved from spent Li-ion batteries: In operando X-ray diffraction studies and an advanced anode material for Na/K-ion batteries. *Energy Environ. Sci.* **2019**, *12*, 3575–3584. [[CrossRef](#)]
67. Pan, C.J.; Yuan, C.; Zhu, G.; Zhang, Q.; Huang, C.J.; Lin, M.C.; Angell, M.; Hwang, B.J.; Kaghazchi, P.; Dai, H. An operando X-ray diffraction study of chloroaluminate anion-graphite intercalation in aluminum batteries. *Proc. Natl. Acad. Sci. USA* **2018**, *115*, 5670–5675. [[CrossRef](#)]
68. Wang, H.; Bai, Y.; Chen, S.; Luo, X.; Wu, C.; Wu, F.; Lu, J.; Amine, K. Binder-free V_2O_5 cathode for greener rechargeable aluminum battery. *ACS Appl. Mater. Interfaces* **2015**, *7*, 80–84. [[CrossRef](#)]
69. Sheet, D.; Bera, A.; Fu, Y.; Desmecht, A.; Riant, O.; Hermans, S. Carbon-Nanotube-Appended PAMAM Dendrimers Bearing Iron(II) α -Keto Acid Complexes: Catalytic Non-Heme Oxygenase Models. *Chem.—A Eur. J.* **2019**, *25*, 9191–9196. [[CrossRef](#)]
70. Takehira, H.; Karim, M.R.; Shudo, Y.; Fukuda, M.; Mashimo, T.; Hayami, S. Modulating the Work Function of Graphene by Pulsed Plasma Aided Controlled Chlorination. *Sci. Rep.* **2018**, *8*, 17392. [[CrossRef](#)]
71. Jagadeesh, M.S.; Bussetti, G.; Calloni, A.; Yivlialin, R.; Brambilla, L.; Accogli, A.; Gibertini, E.; Alliata, D.; Goletti, C.; Ciccacci, F.; et al. Incipient Anion Intercalation of Highly Oriented Pyrolytic Graphite Close to the Oxygen Evolution Potential: A Combined X-ray Photoemission and Raman Spectroscopy Study. *J. Phys. Chem. C* **2019**, *123*, 1790–1797. [[CrossRef](#)]
72. Schnyder, B.; Alliata, D.; Kötz, R.; Siegenthaler, H. Electrochemical intercalation of perchlorate ions in HOPG: An SFM/LFM and XPS study. *Appl. Surf. Sci.* **2001**, *173*, 221–232. [[CrossRef](#)]
73. Zou, L.; Huang, B.; Huang, Y.; Huang, Q.; Wang, C. An investigation of heterogeneity of the degree of graphitization in carbon-carbon composites. *Mater. Chem. Phys.* **2003**, *82*, 654–662. [[CrossRef](#)]
74. Warren, B.E. X-ray Diffraction in Random Layer Lattices. *Phys. Rev.* **1941**, *59*, 693–698. [[CrossRef](#)]
75. Cançado, L.G.; Takai, K.; Enoki, T.; Endo, M.; Kim, Y.A.; Mizusaki, H.; Jorio, A.; Coelho, L.N.; Magalhães-Paniago, R.; Pimenta, M.A. General equation for the determination of the crystallite size L_a of nanographite by Raman spectroscopy. *Appl. Phys. Lett.* **2006**, *88*, 163106. [[CrossRef](#)]
76. Jayaramulu, K.; Dubal, D.; Nagar, B.; Ranc, V.; Tomanec, O.; Petr, M.; Datta, K.K.R.; Zboril, R.; Gómez-Romero, P.; Fischer, R.A. Ultrathin Hierarchical Porous Carbon Nanosheets for High-Performance Supercapacitors and Redox Electrolyte Energy Storage. *Adv. Mater.* **2018**, *30*, e1705789. [[CrossRef](#)]
77. Pei, S.; Cheng, H.M. The reduction of graphene oxide. *Carbon N. Y.* **2012**, *50*, 3210–3228. [[CrossRef](#)]
78. Stobinski, L.; Lesiak, B.; Malolepszy, A.; Mazurkiewicz, M.; Mierzwa, B.; Zemek, J.; Jiricek, P.; Bieloshapka, I. Graphene oxide and reduced graphene oxide studied by the XRD, TEM and electron spectroscopy methods. *J. Electron Spectrosc. Relat. Phenom.* **2014**, *195*, 145–154. [[CrossRef](#)]
79. Yang, D.; Velamakanni, A.; Bozoklu, G.; Park, S.; Stoller, M.; Piner, R.D.; Stankovich, S.; Jung, I.; Field, D.A.; Ventrice, C.A., Jr.; et al. Chemical analysis of graphene oxide films after heat and chemical treatments by X-ray photoelectron and Micro-Raman spectroscopy. *Carbon N. Y.* **2009**, *47*, 145–152. [[CrossRef](#)]
80. Fan, L.-Z.; Liu, J.-L.; Ud-Din, R.; Yan, X.; Qu, X. The effect of reduction time on the surface functional groups and supercapacitive performance of graphene nanosheets. *Carbon* **2012**, *50*, 3724–3730. [[CrossRef](#)]
81. Yoshida, A.; Tanahashi, I.; Nishino, A. Effect of concentration of surface acidic functional groups on electric double-layer properties of activated carbon fibers. *Carbon* **1990**, *28*, 611–615. [[CrossRef](#)]
82. Bokare, A.; Nordlund, D.; Melendrez, C.; Robinson, R.; Keles, O.; Wolcott, A.; Erogbogbo, F. Surface functionality and formation mechanisms of carbon and graphene quantum dots. *Diam. Relat. Mater.* **2020**, *110*, 108101. [[CrossRef](#)]

Appendix IV

Chaotropic Anion Based “Water-in-Salt” Electrolyte Realizes A High Voltage Zn–Graphite Dual-Ion Battery

Z.A. Zafar, G Abbas, K Knizek, M Silhavik, P Kumar, P Jiricek, J Houdková, O. Frank, J. Cervenka

Annexed: Journal of Materials Chemistry A, 2022, 10, 2064-2074



Cite this: DOI: 10.1039/d1ta10122f

Chaotropic anion based “water-in-salt” electrolyte realizes a high voltage Zn–graphite dual-ion battery†

Zahid Ali Zafar,^{ab} Ghulam Abbas,^{bc} Karel Knizek,^d Martin Silhavyk,^{ea} Prabhath Kumar,^a Petr Jiricek,^e Jana Houdková,^e Otakar Frank,^c and Jiri Cervenka^{ab*}

Aqueous Zn-based batteries are promising candidates for grid energy storage due to their low cost, intrinsic safety, and environmental friendliness. Nevertheless, they suffer from limited energy density due to the utilization of low-voltage cathodes and electrolytes. Graphite could be a viable high-voltage cathode material owing to its high redox potential (2.1–3.1 V vs. Zn/Zn²⁺). However, finding a suitable aqueous electrolyte with high anodic stability remains a fundamental challenge. This work realizes a high-voltage and low-cost aqueous Zn–graphite dual-ion battery based on a Zn(ClO₄)₂ water-in-salt electrolyte with a wide electrochemical window of 2.80 V. The implementation of the supersaturated Zn(ClO₄)₂ water-in-salt electrolyte containing strong chaotropic ClO₄[−] anions expands the oxidative stability of the aqueous electrolyte beyond 1.65 V vs. Ag/AgCl or 2.60 V vs. Zn/Zn²⁺, and facilitates reversible plating/stripping of Zn²⁺ with a low overpotential of <50 mV at 1 mA cm^{−2} and a high upper cut-off potential of 2.5 V vs. Zn/Zn²⁺. Consequently, the Zn–graphite dual-ion battery delivers a maximum discharge capacity of 45 mA h g^{−1} at 100 mA g^{−1} with a mean discharge voltage of ~1.95 V and cycle life of over 500 cycles.

Received 26th November 2021
Accepted 27th December 2021

DOI: 10.1039/d1ta10122f

rsc.li/materials-a

1. Introduction

Grid energy storage is a key component in the integration and smooth utilization of intermittent renewable energy sources, such as solar and wind power.¹ Cost, safety, and cycling life are the most important performance metrics of the battery systems for grid energy storage.² Rechargeable aqueous zinc batteries have recently attracted significant attention for potential applications in grid energy storage owing to their high abundance, high theoretical capacity (820 mA h g^{−1} and 5854 mA h cm^{−3}), high safety, and good compatibility with aqueous electrolytes.^{3–6} However, the critical challenges associated with aqueous Zn batteries lie in low cell voltage and limited

cyclability, which result from the lack of high-voltage electrolyte/cathode materials and dendrite formation on the Zn anode.⁷ For instance, conventional aqueous Zn-ion batteries based on metal oxide- or sulfide-based cathode materials and dilute aqueous electrolytes can deliver a cell voltage of only ~1.5 V due to low redox-potentials of the cathodes and a narrow thermodynamic electrochemical stability window (ESW) of water (1.23 V).^{8,9}

Graphite, thanks to its high natural abundance, affordability, sustainability, and structural stability, is an excellent candidate for high-voltage and high-power cathodes for dual-ion batteries.¹⁰ It is cheap and offers a high redox potential of 4.4–5.4 V vs. Li/Li⁺ or 2.1–3.1 V vs. Zn/Zn²⁺.¹¹ These properties are in particular attractive for the development of high-voltage Zn–graphite dual-ion batteries.^{7,11–14} Dual-ion batteries promise safe and low-cost alternative energy storage technology to the state-of-the-art Li-ion technology. Dual-ion batteries, in contrast to the Li-ion batteries, can avoid the use of critical materials which are precious, environmentally harmful, or difficult to recycle, such as nickel and cobalt.^{15,16} Such batteries also use a different electrochemical mechanism for energy storage than the “rocking-chair” Li-ion batteries, which offers researchers many possibilities for employing new materials.² In dual-ion batteries, the electrolyte functions as an active material, and both cations and anions of the electrolyte are incorporated into the anode and cathode, respectively, during

^aDepartment of Thin Films and Nanostructures, FZU – Institute of Physics of the Czech Academy of Sciences, Cukrovarnicka 10/112, 162 00 Prague 6, Czech Republic. E-mail: cervenka@fzu.cz

^bDepartment of Physical Chemistry and Macromolecular Chemistry, Faculty of Science, Charles University in Prague, Hlavova 2030, 128 43 Prague 2, Czech Republic

^cJ. Heyrovsky Institute of Physical Chemistry of the Czech Academy of Sciences, Dolejskova 2155/3, 183 23 Prague 8, Czech Republic

^dDepartment of Magnetism and Superconductors, FZU – Institute of Physics of the Czech Academy of Sciences, Cukrovarnicka 10/112, 162 00 Prague 6, Czech Republic

^eDepartment of Optical Materials, FZU – Institute of Physics of the Czech Academy of Sciences, Cukrovarnicka 10/112, 162 00 Prague 6, Czech Republic

† Electronic supplementary information (ESI) available. See DOI: 10.1039/d1ta10122f

charging and released from the electrodes into the electrolyte during discharging.¹⁷ However, most of the electrolytes are not compatible with graphite-based dual-ion batteries because they have limited oxidative stability to access the high redox potentials of graphite cathodes.^{10,13} The low oxidative stability of electrolytes poses a serious obstacle in the realization of high-voltage Zn-graphite dual-ion batteries.

Other important issues in the development of high-voltage Zn-ion batteries are on the Zn anode side. Zn anodes have been shown to suffer from dendrite issues, H₂ evolution, irreversible zincates formation, high overpotentials, and low coulombic efficiency (C.E.).¹⁸ Recently, several strategies have been demonstrated to enhance the cycle life and reversibility of Zn anodes.¹⁹ These strategies have included Zn-alloying with other metals,^{20,21} applying coatings and interfaces on Zn anodes,^{22–24} modifying Zn structure,²⁵ and novel electrolyte design.^{26,27} Among these, the electrolyte design is considered the most cost-effective and viable solution because it can potentially improve both the reversibility of the Zn metal anode as well as the stability window of aqueous electrolytes.²⁶

The recently reported electrolyte design strategies for Zn-ion batteries involve additions of additives,²⁸ adjustment of pH,^{19,29} and use of gel,^{5,29–31} deep eutectic,^{32,33} hybrid,^{34,35} and concentrated aqueous electrolytes.^{36–40} The development of highly concentrated, “water-in-salt” (WiS) electrolytes has been demonstrated as an effective way to overcome the limitations of the narrow voltage window of aqueous electrolytes and enhance the energy density of different aqueous-based battery systems.^{38,41} This strategy is based on an extremely high concentration of salts dissolved in water. At these supersaturated salt conditions, ions disrupt the well-structured hydrogen-bonding network of water and bound water within their solvation sheath. As a result, the WiS electrolytes exhibit special features that are fundamentally different from bulk water, demonstrating a wider ESW (>1.5 V) and modified ionic conductivity and dynamics at electrode interfaces.^{38,41} The effect of ions on the water environment has been studied well in the past and given in the empirical Hofmeister series.^{42–44} The Hofmeister series provides a ranking of the relative influence of ions on the physical behavior of the aqueous solution. Ions grouped in the kosmotrope (structure-maker) series have a high charge density (*e.g.*, SO₄²⁻, PO₄³⁻, Al³⁺, Mg²⁺, Co²⁺, Ni²⁺, Zn²⁺, *etc.*) and the ability to strengthen the hydrogen-bonding network of water molecules beyond their first solvation shell. Whereas ions grouped in chaotrope series have a low charge density (*e.g.*, NH₄⁺, SCN⁻, I⁻, ClO₄⁻, *etc.*), and are known as structure-breakers that lack this quality.^{42–44} A recent study by D. Reber *et al.* has found a strong correlation between the position of an anion in the Hofmeister series and the resulting ESW of the highly concentrated aqueous electrolytes.⁴³ It has been shown that kosmotropic anions had a negative impact on the ESW by disturbing the solvation shell of the counter cations. On the other hand, chaotrope anions had increased the ESW by limiting the fraction of free water in the electrolytes by pushing water molecules in the solvation shells of the cations.⁴³ This means that a key property for choosing suitable zinc salts for WiS electrolytes is the chaotrope strength of the counter anion.

Therefore, a high-voltage WiS electrolyte should comprise a strong chaotrope anion to make the electrolyte less prone to hydrolysis and attain a wide ESW. As the perchlorate anion is one of the most chaotrope ions in the Hofmeister series and has been demonstrated to form reversible intercalation compounds with graphite,^{43,45,46,60} it is one of the most suitable candidates for the development of high-voltage WiS electrolytes and Zn-graphite dual-ion batteries.

In this work, we report a high-voltage and low-cost aqueous Zn-graphite dual-ion battery based on a WiS electrolyte of zinc perchlorate. It is shown that the high concentration of the salt and the chaotrope nature of ClO₄⁻ anions in the WiS electrolyte efficiently suppress the free water in the electrolyte by trapping water molecules in the Zn²⁺ cation solvation sheath. As a result, the WiS electrolyte demonstrates a wide ESW of 2.80 V. Furthermore, a high concentration of Zn²⁺ is shown to inhibit etching and spontaneous-corrosion of the Zn anode in the WiS electrolyte and to facilitate highly reversible plating/stripping of Zn²⁺ with a low overpotential (50 mV) and 99.995% C.E. The WiS electrolyte offers high oxidative stability of 2.61 V *vs.* Zn/Zn²⁺ (4.89 V *vs.* Li/Li⁺) which brings the additional benefit of increased capacity of graphite cathode and higher upper cut-off voltage.¹¹ Consequently, the reported chaotrope anion based WiS-electrolyte enables the construction of a high voltage aqueous Zn-graphite dual-ion battery delivering a high cut-off voltage of 2.5 V Zn/Zn²⁺, a mean discharge voltage of 1.95 V Zn/Zn²⁺, a maximum discharged capacity of 45 mA h g⁻¹ at 100 mA h g⁻¹, and cycle life of over 500 cycles.

2. Results and discussion

The electrochemical stability windows of differently concentrated Zn(ClO₄)₂-based electrolytes were assessed by linear sweep voltammetry (LSV) in a 3-electrode electrolytic cell on a glassy carbon electrode, with a platinum counter electrode, and a pseudo-reference Ag/AgCl electrode. Fig. 1(a) shows LSV spectra of the supersaturated 8 *m* Zn(ClO₄)₂-WiS electrolyte in comparison to the diluted 0.5 *m* Zn(ClO₄)₂-based aqueous electrolyte and supersaturated 8 *m* ZnSO₄-WiS-electrolyte at a scan rate of 5 mV s⁻¹. The LSV spectra were compensated for the iR potential drop. The physical appearance of the supersaturated electrolytes is shown in Fig. S2 (ESI[†]). The ZnSO₄ WiS-electrolyte was considered for comparison because it constitutes a highly kosmotropic (SO₄²⁻) anion, which lies on the opposite side of the Hofmeister series (SO₄²⁻ > HPO₄²⁻ > F⁻ > CH₃COO⁻ > Cl⁻ > Br⁻ > NO₃⁻ > I⁻ > ClO₄⁻) to the chaotrope ClO₄⁻ anion. The LSV results show that the oxygen evolution reaction (OER) is efficiently shifted with the increasing concentration of zinc perchlorate salt in the aqueous media. As a result, an extended electrochemical stability window of nearly 2.80 V is observed for the Zn(ClO₄)₂ WiS electrolyte compared to the diluted electrolyte (~2 V). The supersaturated ZnSO₄ WiS electrolyte (~2.32 V) has a lower ESW than the supersaturated Zn(ClO₄)₂ WiS electrolyte with the same concentration. This result shows that the chaotrope ion plays an important role in the expansion of the ESW of WiS electrolytes. An important feature of the Zn(ClO₄)₂-based WiS electrolyte is the high

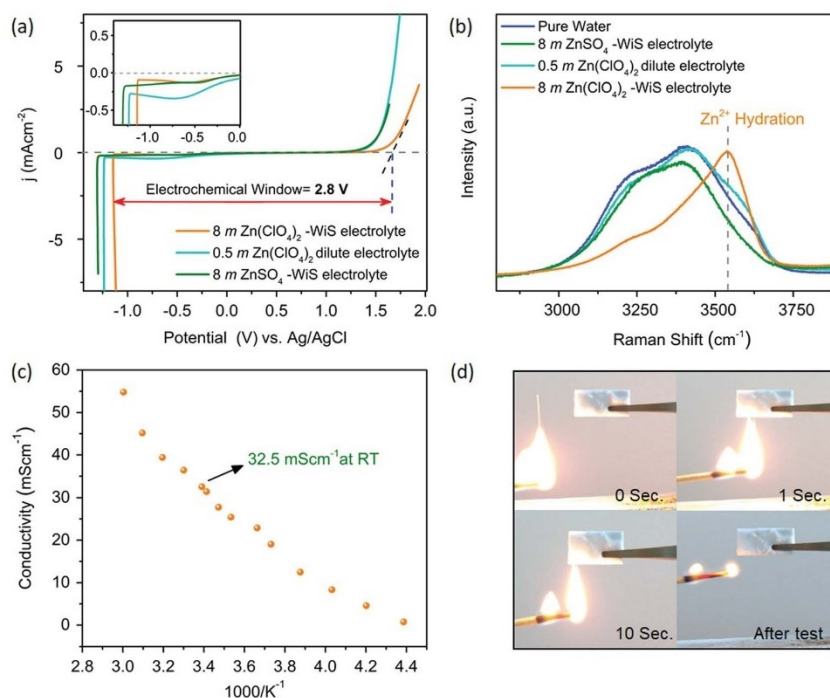


Fig. 1 Electrochemical stability window (ESW), ionic-conductivity and flammability tests of an 8 *m* Zn(ClO₄)₂-WiS electrolyte: (a) iR-drop corrected linear sweep voltammetry (LSV) of 8 *m* Zn(ClO₄)₂-WiS electrolyte in comparison to 0.5 *m* diluted Zn(ClO₄)₂ electrolyte and 8 *m* ZnSO₄-WiS electrolyte at a scan rate of 5 mV s⁻¹ on a glassy carbon working electrode (W.E.), Pt counter electrode (C.E.) and Ag/AgCl reference electrode (R.E.). (b) Raman spectra in the wavenumber region corresponding to the OH-stretching vibrations of 8 *m* WiS-electrolyte, diluted electrolyte, and pure water, and 8 *m* ZnSO₄-WiS electrolyte. (c) Ionic conductivity test of WiS-electrolyte and physical appearance at room temperature (inset). (d) Flammability test of WiS-electrolyte.

oxidative stability of 4.89 V vs. Li/Li⁺ or 2.61 V vs. Zn/Zn²⁺ that is sufficiently high to enable anion intercalation into graphite, which typically occurs at ≥ 4.5 V vs. Li/Li⁺ or 2.1 V to 3.1 V Zn/Zn²⁺.^{11,43} However, the reductive stability is nearly the same as for the diluted electrolyte. This is most probably because the hydrogen evolution reaction (HER) is limited by the standard reduction potential of the Zn/Zn²⁺ redox couple, and, further, it does not depend on the concentration of electrolyte.¹³ The observed electrochemical stability window of the Zn(ClO₄)₂-WiS electrolyte is larger than of many previously reported concentrated and organic/ionic liquid-based electrolytes used in Zn battery systems.^{13,14,47,48} Such a wide electrochemical stability window is attributed to the multivalent nature of the Zn²⁺ ion and the strong chaotropic nature of the perchlorate anion,⁴³ which strongly affect the water-cation solvation sheath, and, consequently, lead to less free water in the WiS electrolyte.

The hydration to Zn²⁺ cations in the Zn(ClO₄)₂-WiS electrolyte was probed by Raman spectroscopy in Fig. 1(b) and S1, ESI.† Unlike in water, dilute Zn(ClO₄)₂ electrolyte and ZnSO₄-WiS electrolyte with the kosmotropic SO₄²⁻ anion, a narrow peak at 3530 cm⁻¹ is observed for the Zn(ClO₄)₂-WiS electrolyte with the

chaotropic ClO₄⁻ anion. The small linewidth of the peak suggests that water molecules are mostly present in the solvation sheath of Zn²⁺ cations.⁴³ In contrast, the Raman spectra of the pure water, dilute Zn(ClO₄)₂ electrolyte and ZnSO₄-WiS electrolyte demonstrate a typical broad peak with both the O-H symmetric (3200 cm⁻¹) and asymmetric (3400 cm⁻¹) stretching vibration modes of water molecules, which are arising from free water.⁴⁹ The Raman spectroscopy results demonstrate that the chaotropic anion strongly modifies the hydrogen-bonding network of water and pushes water molecules towards the cation, where they are bound within its solvation sheath. Consequently, there is no free water in the Zn(ClO₄)₂-WiS electrolyte, and the ESW is widened. A similar phenomenon demonstrating the absence of the free-water molecules and the widening of the stability window has also been observed in recently reported WiS electrolyte systems.^{41,43,50,51}

Fig. 1(c) displays the temperature-dependent ionic conductivity of the Zn(ClO₄)₂-WiS electrolyte in the temperature range of -45 °C to 60 °C. The Zn(ClO₄)₂-based WiS electrolyte has a high ionic conductivity of 32.5 ± 0.07 mS cm⁻¹ at room temperature. Interestingly, the ionic conductivity of the WiS

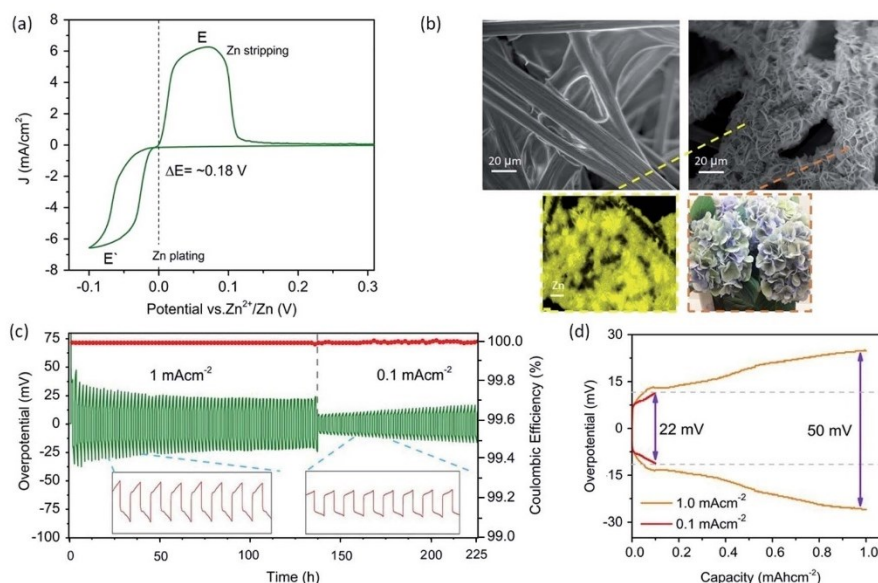


Fig. 2 Stripping/plating analysis of Zn/Zn^{2+} : (a) cyclic voltammetry of the Zn^{2+} plating–stripping reaction at a carbon substrate (120 Toray paper) at a scan rate of 10 mV s^{-1} in 8 m WiS electrolyte; (b) SEM images showing the morphology of the pristine carbon substrate (left), and the as-plated Zn with hydrangea flower like morphology (bottom right), corresponding energy dispersive spectrometry (EDS) mapping of Zn signals (bottom left); (c) stripping–plating cycling along with coulombic efficiency results of a $\text{Zn}||\text{Zn}$ symmetric cell in 8 m WiS electrolyte; and (d) stripping–plating profiles showing overpotential and corresponding capacity.

electrolyte at extremely low temperatures is still relatively high (0.81 mS cm^{-1} at $-30 \text{ }^\circ\text{C}$), making it a suitable electrolyte for cold climate-energy storage applications. The physical appearance and non-flammability test results are presented in Fig. 1(c) inset and Fig. 1(d), respectively, where the perchlorate-based WiS electrolyte has been shown to be non-combustible when exposed to open flame.

To study the suitability of the $\text{Zn}(\text{ClO}_4)_2$ -WiS electrolyte for Zn–graphite dual-ion battery, we first analyzed Zn/ Zn^{2+} stripping/plating from/on a carbon substrate. The results of the Zn stripping/plating analysis in the WiS electrolyte are presented in Fig. 2(a–c). To reversibly plate/strip (Zn/Zn^{2+}) on and from a carbon substrate (120 Toray Carbon paper), cyclic voltammetry (CV) was conducted at a scan rate of 10 mV s^{-1} in a 3-electrode electrochemical cell with Zn metal as both counter and reference electrode, Fig. 2(a). The results of the Zn plating and stripping in the WiS electrolyte show that the process happens within a narrow potential range of -0.1 to $0.2 \text{ V vs. Zn}/\text{Zn}^{2+}$, respectively.⁵² The Zn plating potential close to $0 \text{ V vs. Zn}/\text{Zn}^{2+}$ is ideal for Zn batteries to reduce the charge voltage and minimize the electrolyte decomposition *via* hydrogen evolution or reduction reactions.⁵² Similarly, the Zn stripping potential close to $0 \text{ V vs. Zn}/\text{Zn}^{2+}$ provides a low overpotential in the cell, enabling the implementation of a broad range of positive cathode materials without compromising on cell output voltages.⁵²

To showcase the morphology of the deposited Zn on the carbon substrate, CV was stopped at the $-0.1 \text{ V vs. Zn}/\text{Zn}^{2+}$, and the electrode surface was subjected to scanning electron microscopy (SEM) after washing with deionized water (D.I.) and drying in air. Fig. 2(b) (left) shows the morphology of the pristine carbon substrate wherein the deposited Zn layer with a hydrangea flower-like morphology can be seen on the right. Zn elemental mapping is presented bottom of Fig. 2(b), revealing a homogeneous distribution of Zn on the carbon substrate. Zn plating/stripping was also performed on other substrates, such as Cu (Fig. S3, ESI†) as well as in the dilute 0.5 m electrolyte (Fig. S4 and S5, ESI†). The morphologies of the deposited Zn were different on Cu and carbon substrates in the WiS and dilute electrolytes. This could be caused by many possible factors, including different effective surface area, structure, architecture, surface chemistry of the substrates, as well as by the different concentrations of the salt in the electrolyte. Previous studies have also shown that the nucleation overpotential and wetting ability of plating metal (zincophilic or zincophobic substrate) can also lead to different morphologies, sizes, and shapes of the deposited metal on a substrate.⁶⁴ All of these factors need to be carefully evaluated and controlled to obtain uniform Zn plating without dendrite formation.

Long cycle and more rigorous Zn stripping/plating analysis was done in a Zn symmetric cell, $\text{Zn}||8 \text{ m Zn}(\text{ClO}_4)_2\text{-WiS electrolyte}|\text{Zn}$. The galvanostatic (dis)charging was set for 1 h with

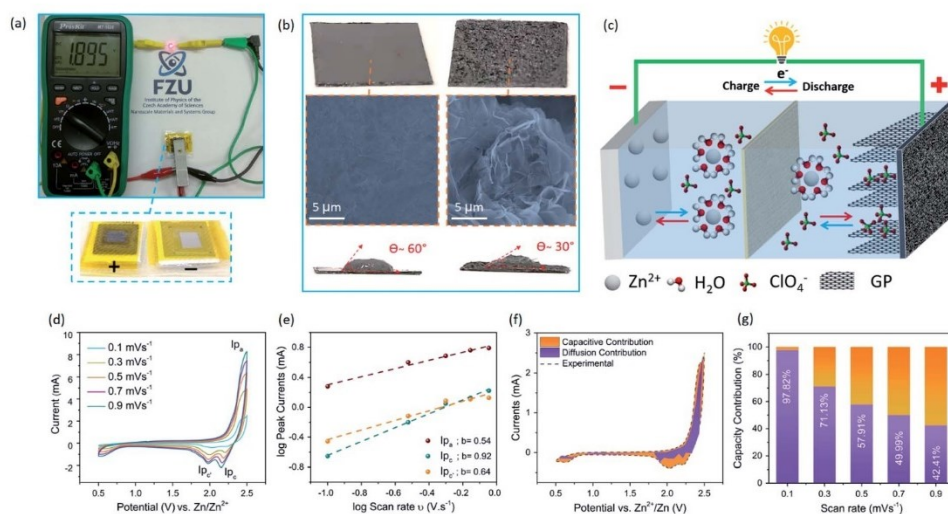


Fig. 3 Zn-graphite dual-ion battery demonstration, schematic and electrochemical kinetic analysis: (a) demonstration of a Zn-graphite dual-ion battery powering a 2 V red LED with a multimeter showing the discharge voltage and a digital photo of the assembly of the battery; (b) digital photos of pristine graphite paper (GP), corresponding SEM image and contact angle experiment with a drop of the as-prepared WiS electrolyte (left), surface modified GP (right); (c) schematics of a Zn-graphite dual-ion battery; (d) CV at different scan rates from 0.1 to 0.9 mV s^{-1} ; (e) corresponding $\log(i_p)$ versus $\log(\nu)$ plots at specific peak currents and calculated b -values by linear-fit; (f) CV curve with the pseudocapacitive fraction shown by the shaded area at a scan rate of 0.1 mV s^{-1} ; and (g) bar chart showing the percent of pseudocapacitive contribution at different scan rates.

upper and lower cut-off voltages of 2 and -2 V so that sufficient time can be given to visualize the overpotential during plating (charging) and stripping (discharging). Firstly, the cell was cycled for 140 h at a high current density of 1 mA cm^{-2} with an areal capacity of 1 mA h cm^{-2} and then a low current density of 0.1 mA cm^{-2} was employed for other 80 h (Fig. 2(c)). High coulombic efficiency of 99.995% was recorded with a very low overpotential of less than 0.05 V and 0.025 V when cycled at high (1 mA cm^{-2}) and low (0.1 mA cm^{-2}) current densities, as presented in Fig. 2(d). A comparison of the overpotentials in the WiS and diluted electrolytes is given in Fig. S6, ESI†. Comparatively, a high overpotential was observed in the dilute electrolyte. The demonstrated overpotential is far lower than in many previously reported electrolytes for Zn batteries including those with $\text{Zn}(\text{ClO}_4)_2$ based gel, organic, and hybrid electrolytes.^{13,14,29,35,47,53} The high coulombic efficiency and low overpotential are the key characteristics of the as-prepared WiS electrolyte which overall guarantee that the Zn-based battery will have stable Zn stripping/plating, and consequently, lead to the prolonged cycle life of the battery.

As the $\text{Zn}(\text{ClO}_4)_2$ -WiS-electrolyte is highly acidic ($\text{pH} \sim 1$), Zn metal reactivity test was performed in the freshly prepared $\text{Zn}(\text{ClO}_4)_2$ -WiS-electrolyte to evaluate the compatibility of the electrolyte with Zn metal. For comparison, perchloric acid of the same pH and dilute $0.5 \text{ M Zn}(\text{ClO}_4)_2$ electrolyte ($\text{pH} \sim 5$) were tested as well. HClO_4 acid contains ClO_4^- anions similarly to the $\text{Zn}(\text{ClO}_4)_2$ -WiS-electrolyte but no Zn^{2+} cations whereas the dilute electrolyte is deficient in ionic species compared to the

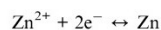
WiS-electrolyte. Zn metal sheets of the same dimensions were immersed in identical volumes of WiS-electrolyte, dilute electrolyte, and perchloric acid for 10 days. Interestingly, the Zn foil was neither corroded nor etched in the highly acidic environment of the WiS-electrolyte, unlike in HClO_4 of the same pH. Zn metal was significantly dissolved in HClO_4 , resulting in salt sediments and H_2 gas evolution (Fig. S6, ESI†). The surface morphology of the Zn metal was also changed in the dilute electrolyte due to corrosion (Fig. S7, ESI†). The surface morphology of the Zn metal was also changed after the corrosion test in the dilute electrolyte. The morphology of the Zn metal remained unchanged in the WiS electrolyte. This difference is attributed to the higher deprotonation rate of the free-water at higher pH which generates hydroxyl species and consequently leads to the reduction of the perchlorate anions, HER, and formation of Zn corrosion products in the diluted electrolyte.⁶² Additionally, the supersaturation of Zn^{2+} ions in the WiS-electrolyte efficiently minimizes these corrosion processes and Zn dissolution by balancing the concentration gradient of Zn across the solid-liquid interface.

The as-assembled Zn-graphite dual-ion battery and a practical demonstration of powering a red 2 V LED using such a battery are presented in Fig. 3(a). The two-electrode Zn-graphite dual-ion battery was fabricated by assembling Zn metal anode, GF/D glass microfiber separator, a low-cost and binder-free graphite paper (GP) cathode, and the as-prepared zinc perchlorate WiS electrolyte (for details see, Experimental section in ESI†). The surface of the pristine GP was modified by

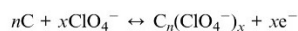
peeling off with a Kapton tape. Fig. 3(b) shows photos and SEM images of the surface of the pristine GP before and after the peeling. The surface of the GP before the peeling was glossy like a metal sheet, while it was mat after the surface modification showing a 3D surface structure made of multilayers of crumpled graphene sheets. A distinct feature of this strategy is an improved wettability and fast electrolyte saturation of the GP, as proven by the low contact angle of the modified GP of $\sim 30^\circ$ compared to the pristine GP of $\sim 60^\circ$ (Fig. 3(b)). A drop of the WIS electrolyte was instantly spread and absorbed on the surface of the modified GP due to the porous 3D surface and decreased hydrophobicity.

A schematic illustration of the working mechanism during the (dis)charge processes of the Zn-graphite dual-ion battery is depicted in Fig. 3(c). During the charging process, Zn^{2+} ions in the electrolyte migrate to the Zn anode and deposit on it, while the ClO_4^- anions in the electrolyte simultaneously migrate to the GP cathode and intercalate between the graphite layers. Upon discharge, both the ions are released back into the electrolyte. The electrochemical reactions during (dis)charging are proposed as follows.

At anode:



At cathode:



Electrochemical characterization of the Zn-graphite dual-ion battery using cyclic voltammetry (CV) is shown in Fig. 3(d). CV was performed at different scan rates from 0.1 to 0.9 mV s^{-1} in the voltage range of 0.5 to 2.5 V vs. Zn/Zn^{2+} for the kinetic analysis of (de)intercalation of ClO_4^- anions (from) into the graphite cathode, Fig. 3(d–g). The oxidation peak (Ip_a) at 2.45 V (4.73 V vs. Li/Li^+) is associated with the ClO_4^- intercalation into the graphite. Two reduction peaks Ip_c (2.20 V) and Ip_d (2.0 V) are related to the deintercalation of ClO_4^- anions from graphite. Multiple reduction peaks suggest that the ClO_4^- intercalation involves at least two step processes. The kinetic analysis studies were carried out to assess whether the process is diffusion or adsorption (surface) controlled. For this purpose, plots of the log of the scan rate (ν) vs. log of peak currents (i) were plotted and analyzed using the equation

$$i = a\nu^b$$

where a and b are fitted coefficients. The value of the coefficient b provides information about the dominating reaction mechanism. If the value of it is 0.5 then the kinetics is diffusion-controlled. If the b value is 1.0 then the process is surface or adsorption-controlled.⁵⁴ However, a b value in between 0.5 and 1.0 suggests both processes are contributing to the capacity or pseudocapacitive behavior.^{13,48,54} The calculated b values of the anodic (Ip_a) and cathodic peaks (Ip_c and Ip_d) of the Zn-graphite dual-ion battery in Fig. 3(c) are 0.54, 0.92 and 0.64, respectively,

indicating that both processes take part in the redox reactions. The contribution of both processes to the capacity can be deconvoluted from the cyclic voltammograms.⁵⁴ The relation of the overall current and scan rate can be written based on the assumption of the summation of the purely surface and diffusion-controlled processes as follows⁴¹

$$i = k_1\nu + k_2\nu^{1/2}$$

where $k_1\nu$, and $k_2\nu^{1/2}$ represent the surface- and diffusion-controlled processes. The values of the adjustable parameters k_1 and k_2 can be estimated from the slope and intercept of the $i/\nu^{1/2}$ vs. $\nu^{1/2}$ plot, respectively. The deconvoluted voltammogram for the redox peaks of the ClO_4^- (de)intercalation (from) in GP at a scan rate of 0.1 mV s^{-1} is presented in Fig. 3(f). A bar-chart graph for other scan rates is presented in Fig. 3(g), which shows that at low scan rates the dominant reaction mechanism of the (de)intercalation is diffusion-controlled while at high scan rates capacitive contribution prevails.

The electrochemical performance of the Zn-graphite dual-ion battery is demonstrated in Fig. 4(a–e). Fig. 4(a) presents the curves of the battery at different cut-off voltages in the range of 2.0 to 2.6 V vs. Zn/Zn^{2+} at a current density of 100 mA g^{-1} . A low capacity ($<18 \text{ mA h g}^{-1}$) and steep galvanostatic charge/discharge (GCD) profiles are observed at low cut-off voltages. Capacitor-like GCD curves were obtained especially at cut-off potentials of 2.0 and 2.2 V, which suggest a dominant capacity contribution without any intercalation process. The observed C.E. of $>100\%$ at these cut-off potentials indicate a possible occurrence of parasitic processes, which may include the deposition or intercalation of solvated Zn^{2+} cations at low potentials near 0.5 V vs. Zn/Zn^{2+} , as supported by the CV results in Fig. 3(d). Whereas a high discharge capacity of 26 and 65 mA h g^{-1} with plateau-like GCD curves is observed for upper cut-off potentials of 2.5 and 2.6 V vs. Zn/Zn^{2+} , respectively. The optimum upper cut-off potential of 2.5 V was determined by plotting a comparative graph of upper cut-off voltage vs. discharged capacity and C.E., Fig. 4(b). Consequently, all the following long-term cycling and rate-capability tests were performed at the optimum upper cut-off voltage of 2.5 V vs. Zn/Zn^{2+} . All batteries were initially activated for 4 cycles at a small current density of 20 mA g^{-1} up to a cut-off voltage of 2.45 V vs. Zn/Zn^{2+} . After activation, the batteries were (dis)charged at various current densities (100 to 300 mA g^{-1}). At the start of the cycling, the discharged capacity was around 30 mA h g^{-1} at the current density of 100 mA g^{-1} and C.E. was below 60% but it gradually raised to 45 mA h g^{-1} with an improved C.E. The highest C.E. of over 90% was achieved at the current density of 300 mA g^{-1} but it was at the cost of the reduced capacity, which decreased to 20 mA h g^{-1} . It is worth mentioning that a recoverable capacity profile and very small capacity decay were observed once the battery was tested back at the low current densities (300 to 100 mA g^{-1}). The Zn-graphite dual-ion battery performed stable at the cut-off potential of 2.5 V up to 500 cycles, Fig. 4(c). Rate-capability and cycling performance at the lower cut-off potential of 2.45 V is presented in Fig. S8, ESI,† Fig. S9, ESI,† presents the battery with the dilute electrolyte (0.5

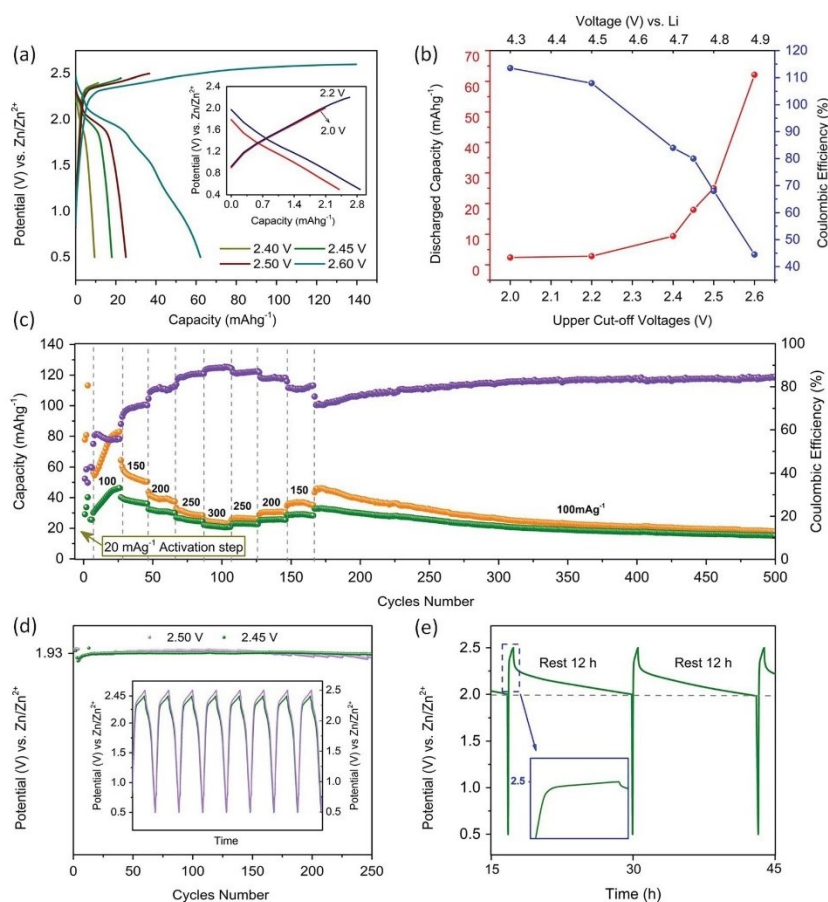


Fig. 4 (Dis)charge and long cycling performance tests of Zn-graphite dual-ion battery: (a) charge-discharge curves at different cut-off potentials; (b) graph showing the relationship between cut-off potentials, discharged capacities and coulombic efficiencies; (c) rate-capability and long-cycling tests at the cut-off voltage of 2.5 V vs. Zn/Zn²⁺; (d) demonstration of the mean-discharge voltage of the battery at the cut-off potentials of 2.45 V (green), 2.5 V (purple) vs. Zn/Zn²⁺ and (e) discharge profiles (inset); (e) self-discharge test of the battery after a rest period of 12 h.

m), which could not reach the upper-cut off potential even after charging for 19 h due to electrolyte decomposition at high potentials. Another important characteristic of the Zn-graphite dual-ion battery with WiS electrolyte is the high and stable mean-discharge voltage of ~ 1.95 V vs. Zn/Zn²⁺, as depicted in Fig. 4(d). The demonstrated mean-discharge voltage is higher than most of the reported Zn-ion batteries with conventional manganese and vanadium oxide cathodes and Li⁺ chemistry-free Zn-graphite dual-ion batteries.^{5,9,14,29,31,34,48,55} A comparison with most relevant literature is presented in Table S1, ESI.† The self-discharge test of the battery was carried out by fully charging to 2.5 V and then resting for 12 h. Even after the long resting time, a high voltage of 2.0 V was observed (Fig. 4(e)).

After the electrochemical tests, *ex situ* XPS and EDS analyses of the battery electrodes were performed to confirm the chemical composition of the intercalated species into the binder-free graphitic cathode. The batteries were disassembled at fully charged and discharged states and GP cathodes were collected after rinsing with D.I. water and drying in the air before conducting the measurements. The morphology and corresponding XRD of the pristine, charged, and discharged GP cathodes and Zn anodes are presented in Fig. S11 and S12 in ESI.† To avoid any possible contamination of the sample surfaces, the XPS measurements were done on the Ar cluster sputtered samples (10 min, 5 keV Ar¹⁰⁰⁰⁺ ions). Hence, the XPS spectra in Fig. (5) represent information about the composition changes

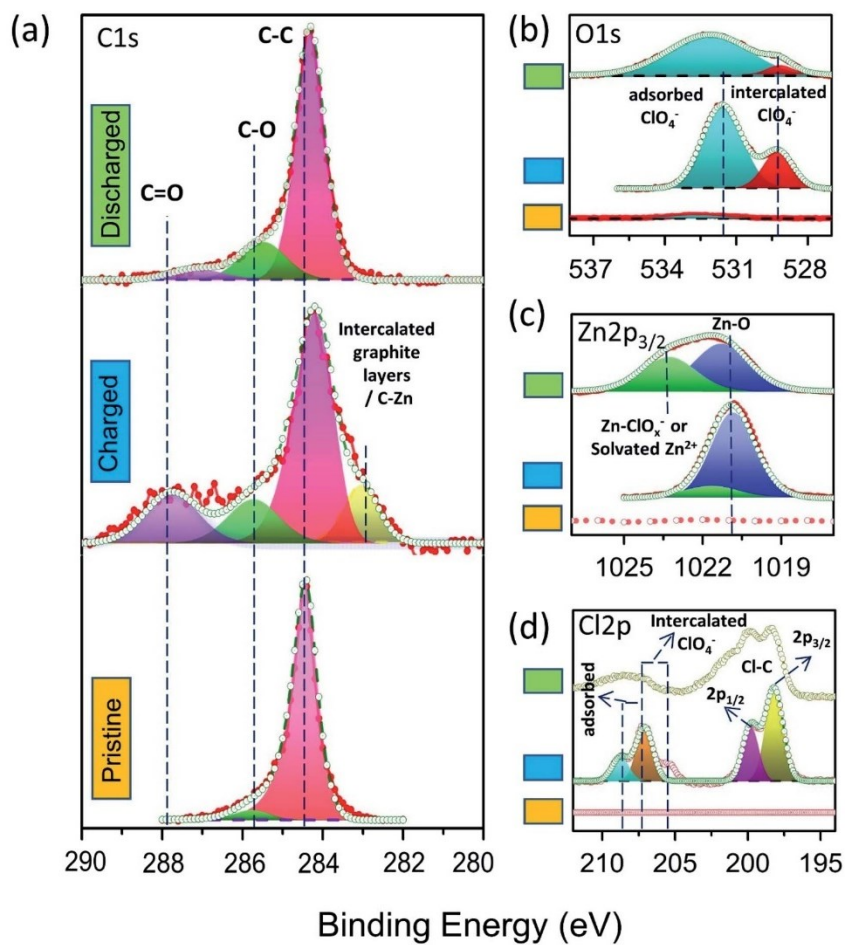


Fig. 5 *Ex situ* XPS analysis of pristine, charged, and discharged GP cathodes: C1s spectra (a), O1s spectra (b), Zn 2p and Cl 2p, (c and d), respectively.

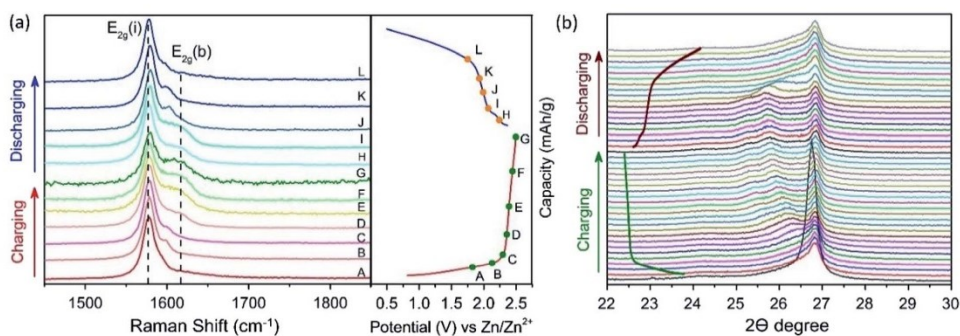


Fig. 6 *Operando*-Raman spectroscopy (a), and XRD (b) of Zn-graphite dual-ion batteries.

in the bulk (under-surface) of the electrode materials. Fig. 5(a) presents deconvoluted C 1s spectra of the pristine, charged, and discharged GP. The pristine sample shows a significant (93.1%) C–C sp² component of C at 284.4 eV, and minor components of (4.8%) C–C sp³ and (1.4%) C–O at 285.4 and 286.1 eV, respectively. The charged GP electrode, however, contained significant C–O and C=O components which are originating from the intercalation of ClO₄[−] anions and the surface oxidation of GP electrode. The deconvoluted C 1s component at ~283 eV in the charged GP electrode is assigned to the intercalated graphite layers and C–Zn.^{56,57} The C 1s spectrum of the discharged GP sample looks like the pristine sample, except for the oxygen-bearing species at higher binding energies that are caused most probably by the incomplete deintercalation. O 1s spectra are given in Fig. 5(b). They show double peaks, where the high energy component at 532.6 eV arises from the oxygen species of adsorbed ClO₄[−] and H₂O, whereas the lower energy component is assigned to the intercalated oxygen of ClO₄[−] and H₂O.^{56,58} In the discharged sample, the oxygen component of the ClO₄[−] intercalation was decreased but did not fully disappear. This result is in line with the observed irreversible capacity and lower C.E. The XPS spectra of Zn 2p show the presence of Zn in the charged graphite electrode. There is also found the C–Zn bond after deconvoluting of peaks in the C 1s spectra in the charged graphite electrode.⁵⁶ This could originate either from the trapped electrolyte inside the structure of the graphite electrode or it can be caused by the co-intercalation of the solvated Zn²⁺ cations. However, the increased Zn signals in the discharged samples suggest more solvated Zn²⁺ ions were intercalated at low potential (*i.e.*, 0.5 V vs. Zn/Zn²⁺) due to charge-gradient at GP cathode. The presence of Zn in the GP electrodes was also spotted by EDS mapping (Fig. S13, ESI†). The Cl 2p XPS spectra in Fig. 5(d) clearly show the intercalation of ClO₄[−] anions in the graphite electrode during charging and partial deintercalation during discharging. This result is in line with the earlier report by Schnyder *et al.*⁵⁶ The peaks at 198.2 eV and 199.8 eV are attributed to C–Cl 2p_{3/2} and 2p_{1/2}, respectively. The characteristic doublet perchlorate peaks at 207.1 and 208.7 eV correspond to ClO₄[−] 2p_{3/2} and 2p_{1/2}. Further, an additional spin-split peak at 205.4 eV is assigned to intercalated ClO₄[−] anions.³³ It is observed that the Cl 2p of the intercalated perchlorate is shifted by ~1.7 eV with respect to the adsorbed perchlorate (207.1 eV). The same shift is found also in the corresponding peaks in the O 1s spectra. However, the peaks of the intercalated species overlap with the peaks of the adsorbed perchlorate as the Cl 2p_{3/2} of the adsorbed species have the same peak position as the Cl 2p_{1/2} peak of the intercalated species, Fig. 5(d).⁵⁶ Further, the ratios of Cl/C, Zn/C, and O/C of the charged samples were found higher than in the discharged samples, providing evidence of the intercalation/adsorption process (Table S2, ESI†).

Operando Raman spectroscopy and XRD were further utilized to probe the (de)intercalation of ClO₄[−] anions (from) into graphite cathode. The tests were conducted in the homemade 2-electrode cells. The results of the *operando* Raman spectroscopy and XRD are presented in Fig. 6(a and b). During the charging of the battery, the graphitic G band (1578 cm^{−1}) of the pristine GP was gradually split into two Raman modes of a lower-frequency

component E_{2g}(i) and a higher-frequency component E_{2g}(b) and reversed during the discharging, Fig. 6(a). This result suggests that there is a formation of a reversible perchlorate-based graphite intercalation compound (GIC).⁵⁹ The obtained *operando* XRD results are in line with the *operando* Raman spectroscopy results. They show that the characteristic 002 peak (26.7°) of the graphite cathode gradually splits and shifts towards a lower 2θ angle (~25.2°) upon charging. The peaks were recovered after the cell was discharged. The peak was broadened and its intensity was also decreased, indicating the intercalation of anions into graphite.⁵⁹ However, the presence of the E_{2g}(i) band and the 002 peak in the fully charged cathode suggest only a partial intercalation process, in other words, the formation of GICs of mixed-stage. These results are in agreement with the kinetic analysis, which suggests that there is a capacity contribution from both diffusion and adsorption processes.

3. Conclusions

In summary, we have demonstrated a high-voltage Zn–graphite dual-ion battery based on Zn(ClO₄)₂ water-in-salt electrolyte and a low-cost binder-free graphite cathode. The water-in-salt electrolyte provides a wide electrochemical stability window of 2.80 V due to the utilization of high concentration of zinc perchlorate salt and chaotropic nature of ClO₄[−] anion. Accordingly, the zinc perchlorate WiS electrolyte facilitates stable and reversible Zn plating/stripping with very low overpotentials (<50 mV) and 99.995% coulombic efficiency at 1 mA cm^{−2}. Furthermore, high oxidative stability of WiS-electrolyte alleviates the intercalation of ClO₄[−] anions into graphite cathode at high potentials (4.8 V vs. Li/Li⁺) in the aqueous electrolyte while allowing a higher upper cut-off potential of 2.5 V vs. Zn/Zn²⁺. The demonstrated Zn–graphite dual-ion battery can deliver a maximum discharged capacity of 45 mA h g^{−1} at 100 mA h g^{−1} and an average discharged capacity of 23.5 mA h g^{−1} for over 500 cycles. Moreover, it exhibits a high mean discharge voltage of ~1.95 V vs. Zn/Zn²⁺. This work provides a feasible strategy for designing high-voltage, non-flammable, and low-cost Zn–graphite batteries. Although the Zn–graphite dual-ion batteries demonstrate encouraging results for large grid storage applications they still require further optimization and improvements.

Author contributions

Zahid Ali Zafar: conceptualization, methodology, investigation, formal analysis, writing – original draft, writing – review & editing. Ghulam Abbas: investigation, formal analysis, validation, writing – review & editing. Martin Silhavič: investigation, writing – review & editing. Karel Knizek: investigation, formal analysis, writing – review & editing. Prabhat Kumar: investigation, formal analysis, writing – review & editing. Petr Jiricek: investigation, formal analysis, writing – review & editing. Jana Houdková: investigation, formal analysis, writing – review & editing. Otakar Frank: conceptualization, writing – review & editing, supervision, project administration, funding

acquisition. Jiri Cervenka: conceptualization, methodology, investigation, writing – original draft, writing – review & editing, supervision, project administration, funding acquisition.

Conflicts of interest

The authors declare no conflicts of interest.

Acknowledgements

We acknowledge funding support from the Czech Science Foundation (GACR – Grant No. 19-23986S) and the Operational Programme Research, Development and Education financed by European Structural and Investment Funds and the Czech Ministry of Education, Youth and Sports (Project No. SOLID21 – CZ.02.1.01/0.0/0.0/16_019/0000760 and Project: “Carbon allotropes with rationalized nanointerfaces and nanolinks for environmental and biomedical applications” No. CZ.02.1.01/0.0/0.0/16_026/0008382). This work was further supported by the Charles University Grant Agency (GAUK) project No. 371621 and the MEYS project LTAUSA19001.

References

- R. Chen, R. Luo, Y. Huang, F. Wu and L. Li, *Adv. Sci.*, 2016, **3**, 1600051.
- M. Wang and Y. Tang, *Adv. Energy Mater.*, 2018, **8**, 1703320.
- C. Li, X. Xie, S. Liang and J. Zhou, *Energy Environ. Mater.*, 2020, **3**, 146–159.
- L. Wang and J. Zheng, *Mater. Today Adv.*, 2020, **7**, 100078.
- H. Li, L. Ma, C. Han, Z. Wang, Z. Liu, Z. Tang and C. Zhi, *Nano Energy*, 2019, **62**, 550–587.
- Z. A. Zafar, S. Intiaz, R. Razaq, S. Ji, T. Huang, Z. Zhang, Y. Huang and J. A. Anderson, *J. Mater. Chem. A*, 2017, **5**, 5646–5660.
- G. Wang, B. Kohn, U. Scheler, F. Wang, S. Oswald, M. Löffler, D. Tan, P. Zhang, J. Zhang and X. Feng, *Adv. Mater.*, 2020, **32**, e1905681.
- J. Ming, J. Guo, C. Xia, W. Wang and H. N. Alshareef, *Mater. Sci. Eng., R*, 2019, **135**, 58–84.
- X. Jia, C. Liu, Z. G. Neale, J. Yang and G. Cao, *Chem. Rev.*, 2020, **120**, 7795–7866.
- I. A. Rodríguez-Pérez and X. Ji, *ACS Energy Lett.*, 2017, **2**, 1762–1770.
- Z. Chen, Y. Tang, X. Du, B. Chen, G. Lu, X. Han, Y. Zhang, W. Yang, P. Han, J. Zhao and G. Cui, *Angew. Chem., Int. Ed.*, 2020, **59**, 21769–21777.
- T. Placke, A. Heckmann, R. Schmich, P. Meister, K. Beltrop and M. Winter, *Joule*, 2018, **2**, 2528–2550.
- I. A. Rodríguez-Pérez, L. Zhang, J. M. Wrogemann, D. M. Driscoll, M. L. Sushko, K. S. Han, J. L. Fulton, M. H. Engelhard, M. Balasubramanian, V. V. Viswanathan, V. Murugesan, X. Li, D. Reed, V. Sprenkle, M. Winter and T. Placke, *Adv. Energy Mater.*, 2020, **10**, 2001256.
- H. Zhang, X. Liu, B. Qin and S. Passerini, *J. Power Sources*, 2020, **449**, 227594.
- J. Dewulf, G. Van der Vorst, K. Denturck, H. Van Langenhove, W. Ghysels, J. Tytgat and K. Vandepitte, *Resour., Conserv. Recycl.*, 2010, **54**, 229–234.
- J. L. Matthew Li, *Science*, 2020, **367**, 978–979.
- L. Haneke, J. E. Frerichs, A. Heckmann, M. M. Lerner, T. Akbay, T. Ishihara, M. R. Hansen, M. Winter and T. Placke, *J. Electrochem. Soc.*, 2020, **167**, 140526.
- J. Shin, J. Lee, Y. Park and J. W. Choi, *Chem. Sci.*, 2020, **11**, 2028–2044.
- J. Wang, Y. Yang, Y. Zhang, Y. Li, R. Sun, Z. Wang and H. Wang, *Energy Storage Mater.*, 2021, **35**, 19–46.
- Z. Cai, Y. Ou, J. Wang, R. Xiao, L. Fu, Z. Yuan, R. Zhan and Y. Sun, *Energy Storage Mater.*, 2020, **27**, 205–211.
- S. B. Wang, Q. Ran, R. Q. Yao, H. Shi, Z. Wen, M. Zhao, X. Y. Lang and Q. Jiang, *Nat. Commun.*, 2020, **11**, 1634.
- Z. Yi, G. Chen, F. Hou, L. Wang and J. Liang, *Adv. Energy Mater.*, 2020, **11**, 2003065.
- J. Han, H. Euchner, M. Kuenzel, S. M. Hosseini, A. Groß, A. Varzi and S. Passerini, *ACS Energy Lett.*, 2021, **6**, 3063–3071.
- S. Zhou, Y. Wang, H. Lu, Y. Zhang, C. Fu, I. Usman, Z. Liu, M. Feng, G. Fang, X. Cao, S. Liang and A. Pan, *Adv. Funct. Mater.*, 2021, **31**, 2104361.
- Y. Du, X. Chi, J. Huang, Q. Qiu and Y. Liu, *J. Power Sources*, 2020, **479**, 228808.
- L. Qian, W. Yao, R. Yao, Y. Sui, H. Zhu, F. Wang, J. Zhao, C. Zhi and C. Yang, *Adv. Funct. Mater.*, 2021, **31**, 2105736.
- X. Zeng, J. Mao, J. Hao, J. Liu, S. Liu, Z. Wang, Y. Wang, S. Zhang, T. Zheng, J. Liu, P. Rao and Z. Guo, *Adv. Mater.*, 2021, **33**, e2007416.
- S. J. Zhang, J. Hao, D. Luo, P. F. Zhang, B. Zhang, K. Davey, Z. Lin and S. Z. Qiao, *Adv. Energy Mater.*, 2021, **11**, 2102010.
- S. Chen, R. Lan, J. Humphreys and S. Tao, *ACS Appl. Energy Mater.*, 2020, **3**, 2526–2536.
- Z. Wu, C. Lu, Y. Wang, L. Zhang, L. Jiang, W. Tian, C. Cai, Q. Gu, Z. Sun and L. Hu, *Small*, 2020, **16**, e2000698.
- H. Zhang, X. Liu, H. Li, B. Qin and S. Passerini, *ACS Appl. Mater. Interfaces*, 2020, **12**, 15305–15312.
- W. Yang, X. Du, J. Zhao, Z. Chen, J. Li, J. Xie, Y. Zhang, Z. Cui, Q. Kong, Z. Zhao, C. Wang, Q. Zhang and G. Cui, *Joule*, 2020, **4**, 1557–1574.
- H. Qiu, X. Du, J. Zhao, Y. Wang, J. Ju, Z. Chen, Z. Hu, D. Yan, X. Zhou and G. Cui, *Nat. Commun.*, 2019, **10**, 5374.
- J. Q. Huang, X. Guo, X. Lin, Y. Zhu and B. Zhang, *Research*, 2019, **2019**, 2635310.
- C. Li, W. Wu, H. Y. Shi, Z. Qin, D. Yang, X. Yang, Y. Song, D. Guo, X. X. Liu and X. Sun, *Chem. Commun.*, 2021, **57**, 6253–6256.
- P. Kulkarni, D. Ghosh and R. G. Balakrishna, *Sustainable Energy Fuels*, 2021, **5**, 1619–1654.
- Y. Shen, B. Liu, X. Liu, J. Liu, J. Ding, C. Zhong and W. Hu, *Energy Storage Mater.*, 2021, **34**, 461–474.
- T. Liang, R. Hou, Q. Dou, H. Zhang and X. Yan, *Adv. Funct. Mater.*, 2020, **31**, 2006749.
- P. Ruschhaupt, S. Pohlmann, A. Varzi and S. Passerini, *Batteries Supercaps*, 2020, **3**, 698–707.

- 40 X. Wu, Y. Xu, C. Zhang, D. P. Leonard, A. Markir, J. Lu and X. Ji, *J. Am. Chem. Soc.*, 2019, **141**, 6338–6344.
- 41 A. Zhou, L. Jiang, J. Yue, Y. Tong, Q. Zhang, Z. Lin, B. Liu, C. Wu, L. Suo, Y. S. Hu, H. Li and L. Chen, *ACS Appl. Mater. Interfaces*, 2019, **11**, 41356–41362.
- 42 Y. Marcus, *Chem. Rev.*, 2009, **109**, 1346–1370.
- 43 D. Reber, R. Grissa, M. Becker, R. S. Kühnel and C. Battaglia, *Adv. Energy Mater.*, 2020, **11**, 2002913.
- 44 R. E. Vera, F. Salazar-Rodriguez, R. Marquez and A. M. Forgiarini, *J. Surfactants Deterg.*, 2020, **23**, 603–615.
- 45 J. Gao, S. Tian, L. Qi and H. Wang, *Electrochim. Acta*, 2015, **176**, 22–27.
- 46 G. Abbas, F. J. Sonia, Z. A. Zafar, K. Knížek, J. Houdková, P. Jiříček, M. Bouša, J. Plšek, M. Kalbáč, J. Červenka and O. Frank, *Carbon*, 2022, **186**, 612–623.
- 47 J. Fan, Q. Xiao, Y. Fang, L. Li and W. Yuan, *Ionics*, 2018, **25**, 1303–1313.
- 48 B. Ji, W. Yao and Y. Tang, *Sustainable Energy Fuels*, 2020, **4**, 101–107.
- 49 B. M. Auer and J. L. Skinner, *J. Chem. Phys.*, 2008, **128**, 224511.
- 50 L. Suo, O. Borodin, T. Gao, M. Olguin, J. Ho, X. Fan, C. Luo, C. Wang and K. Xu, *Science*, 2015, **350**, 938–943.
- 51 Y. Li, Z. Zhou, W. Deng, C. Li, X. Yuan, J. Hu, M. Zhang, H. Chen and R. Li, *ChemElectroChem*, 2021, **8**, 1451–1454.
- 52 L. Ma, M. A. Schroeder, O. Borodin, T. P. Pollard, M. S. Ding, C. Wang and K. Xu, *Nat. Energy*, 2020, **5**, 743–749.
- 53 Z. Liu, G. Li, T. Cui, A. Borodin, C. Kuhl and F. Endres, *J. Solid State Electrochem.*, 2017, **22**, 91–101.
- 54 J. H. Xu, T. Schoetz, J. R. McManus, V. R. Subramanian, P. W. Fields and R. J. Messinger, *J. Electrochem. Soc.*, 2021, **168**, 060514.
- 55 Y. Zhu, J. Yin, X. Zheng, A.-H. Emwas, Y. Lei, O. F. Mohammed, Y. Cui and H. N. Alshareef, *Energy Environ. Sci.*, 2021, **14**, 4463–4473.
- 56 D. A. B. Schnyder, R. Koëtzi and H. Siegenthaler, *Appl. Surf. Sci.*, 2001, **173**, 221–232.
- 57 J. J. Beltran, C. A. Barrero and A. Punnoose, *Phys. Chem. Chem. Phys.*, 2019, **21**, 8808–8819.
- 58 M. S. Jagadeesh, G. Bussetti, A. Calloni, R. Yivlialin, L. Brambilla, A. Accogli, E. Gibertini, D. Alliata, C. Goletti, F. Ciccacci, L. Magagnin, C. Castiglioni and L. Duò, *J. Phys. Chem. C*, 2018, **123**, 1790–1797.
- 59 Y. Wang, L. Zhang, F. Zhang, X. Ding, K. Shin and Y. Tang, *J. Energy Chem.*, 2021, **58**, 602–609.
- 60 Z. A. Zafar, G. Abbas, M. Silhavik, K. Knizek, O. Kaman, F. J. Sonia, P. Kumar, P. Jiricek, J. Houdková, O. Frank and J. Cervenka, *Electrochim. Acta*, 2022, **404**, 139754.
- 61 W. Liu, P. Liu and D. Mitlin, *Chem. Soc. Rev.*, 2020, **49**, 7284–7300.
- 62 L. Sziráki, Á. Cziráki, I. Geröcs, Z. Vértesy and L. Kiss, *Electrochim. Acta*, 1998, **43**, 175–186.






Curriculum Vitae

Zahid Ali Zafar

Researcher at the FZU-Institute of Physics of the Czech Academy of Sciences

*Department of Thin Films & Nanostructures,
Cukrovarnická 10/112 162 00 Prague, Czech Republic*

✉ zafar@fzu.cz

 [0000-0002-1155-2674](https://orcid.org/0000-0002-1155-2674)
 [Google Scholar-Profile](#)
 [F-9231-2016](#)
 [@zahidalizafar](#)
 [zahidalizafar](#)

Results-driven, enthusiastic, and reliable professional with skills in nanotechnology and electrochemistry, material synthesis and physical and chemical characterization, battery applications, product engineering, and performance analysis.

Current Status

Doctoral-Researcher

Group of Nanoscale Materials and Systems (NMS)

FZU - Institute of Physics of the Czech Academy of Sciences in Prague, Czech Republic

Research Interests: Electrode/electrolyte interphases, concentrated (Water-in-Salt) and quasi-solid electrolytes, multivalent/dual-ion batteries; novel battery/energy storage concepts.

Academic History

- **Charles University in Prague, Czech Republic** **Oct. 2017- Jun 2023**
PhD fellow in Physical Chemistry
Research Project: *Water-in-Salt Electrolytes of Dual-ion Batteries*
Supervisor: Ing. Dr. Jiri Cervenka
Sept. 2014- Jun.2017

 - **University of Jinan (UJN), Shandong, P. R. China**
Master of Science in Chemical Engineering
Research Project: *Advanced Materials for Rechargeable Aluminum Batteries*
Advisor: Prof. Zhaoliang Zhang
Cumulative Percentage: 4.52/5.0

 - **University of Gujrat (UOG), Gujrat, Pakistan** **Sept. 2008–Aug. 2012**
Bachelor of Science in Chemical Engineering
Design Project: *Production of Absolute Ethanol from Molasses*
Advisor: Prof. Salman Haider
CGPA: 3.26/4.0
-

Experience

- **Bachelor's Thesis Supervisor** (FZU- Czech Academy of Sciences)
March 2021 to present
 - Successfully supervised a bachelor's thesis on "Si-anodes" for lithium-ion batteries
 - Supervising another thesis on "supercapacitors" based on concentrated electrolytes

- **Researcher** Contract-based at FZU- Czech Academy of Sciences **Dec 2017 to Present**
 - Pioneered battery research at FZU.
 - Successfully, procured, and commissioned battery research-related equipment and materials, including, potentiostats, battery tester systems, coin-cell, and pouch cell fabrication units, chemicals, and materials.
 - *Developed in-house Operando-XRD, and Raman Spectroscopy* for battery research.
 - Established safety and lab procedures to ensure smooth working in the battery research lab.
 - Aided in the recruitment of new group members, including, advertisement, screening, short-listing of candidates, and arrangement of interviews.

- **Teaching Assistant of Inorganic Chemistry**
School of International Education & Exchange, University of Jinan, China **Spring-2015**

- **Production Engineer (Chemical)**
Service Industries Limited, Pakistan **Jun. 2013 - Aug. 2014**

Research & Training Background

- **Research Training on the Design, Fabrication and Characterization of Batteries**
Group: Prof. Yunhui Huang at Huazhong University of Science & Technology (HUST), Wuhan, China. **Jan.2015 - Feb.2015**

- **Junior Research Assistant** at the Department of Chemical Engineering, University of Gujrat, Pakistan **Sep. 2012 – May 2013**

Technical Skills

- **Characterization:** *Operando-XRD, and -Raman, Spectroscopy, SEM, XPS, etc.*
- **Electrochemical Testing:** Galvanostatic Charge-Discharge, CV, LSV, and EIS; Battery Safety and Performance Analysis and Failure Tests, etc.
- **Fabrication and characterization of batteries** (Coin Cells, Pouch Cells, Electrolytic Tank Cells)

- **Laboratory Skills:** Hydrothermal/Solvothermal Method, Precipitation and Co-precipitation Method, and High Temperature Furnace Operations (3000 °C, home-built), Cryodesiccation (home-built), Glove box, *ALD (R200 Advanced, Picosun)*.

Honors and Awards

- ECS Battery Division Travel Grant **Aug 2021**
Issued by Electrochemical Society (ECS)
- Nominated for Pakistan Foreign Minister's Honors-List 2021 **July 2021**
(Category: Science and Innovation; Country: Czech Republic)
- Research Award (Publications) **Jan. 2017**
University of Jinan, China
- CSC-Scholarship **2014-2017**
Fully funded Chinese Scholarship Council Award for Master Studies
- Honored over all 2nd position in the Punjab province in Engineering and IT Exhibition and won the prize money of **100,000.00 PKR.** **Aug. 2012**
Government of Punjab, Pakistan
- Laptop award from Chief Minister Punjab on merit basis **Mar. 2012**
Government of Punjab, Pakistan

Certificates

- **“Risk and safety Management in process industries”** from University of Engineering & Technology (UET), Lahore, Pakistan **(2010)**

Volunteer

- Editor at PakSciComm forum, Pakistan **Mar 2021- Sep 2022**
- Managing Editor, Materials Innovation, Hexa Publishers, Pakistan **Jan 2022- Feb 2023**
- Organized special Zinc-Battery Symposium (virtual), **Feb. 2023**

Memberships

- Materials Science Society of Pakistan (MSSP) Student-membership
- Electrochemical Society (ECS) Student-membership
- Materials Research Society (MRS)
- Member of Pakistan Engineering Council (PEC) (Reg. No. Chem/10449)